

nature

CANCER FUTURES

Advances in tumour biology,
genomics and therapy

LABORATORY ANIMALS

The next top model

REGENERATIVE MEDICINE

Worm-free iPSC cells

CATALYTIC CONVERTERS

Can nanowires rob?

www.nature.com



Abstracts



LAST AUTHOR

Even with a lower food intake, many dieters just can't seem to lose weight — perhaps because their bodies aren't burning it off. Yi Zhang, a biochemist at the University of North

Carolina at Chapel Hill, and his colleagues have discovered that loss of a specific enzyme causes obesity in mice by snuffing out the body's ability to burn energy but leaving appetite unaffected. On page 757, the authors show that the enzyme, *Jhdm2a*, helps to control the expression of metabolic genes. Loss of the enzyme's function causes a metabolic defect that makes mice accumulate fat. Zhang tells *Nature* about finding a new pathway involved in obesity.

How did you discover this enzyme's function in metabolism?

We study the role that the modification of histone proteins has in the regulation of gene expression. Histones are a class of proteins required to organize DNA into chromosomes, and *Jhdm2a* is an enzyme that modifies histones by removing methyl groups from specific locations. By testing mice in which the *Jhdm2a* gene had been knocked out, we had previously learned that the *Jhdm2a* protein is required for sperm maturation. To our surprise, when these knockout mice got older, they grew much fatter than their littermates. We began to notice this when they were about three months old, and by six months old they were significantly obese.

How did you connect the obese animals' condition to defects in metabolism?

First, we checked whether the knockout mice eat more than their littermates, and found that they don't. So then we turned to thinking about energy expenditure — we figured that the obese mice must be expending less energy. We found that the expression of certain metabolic genes was defective in these mice, leading to lowered fat-burning.

Was reduced energy expenditure the only result of the enzyme's absence?

No, the mice also exhibited defective heat generation, or thermogenesis. Normally, mammals have a mechanism for maintaining body temperature in a cold environment. But *Jhdm2a*-knockout mice cannot maintain their body temperature in the cold.

What do your results mean for human dieters?

Some people say that even if they just drink water they gain weight. There might be a good reason; maybe such people have a low basal metabolic rate because they have a defect in this gene, or in genes performing a similar function. An agonist that can enhance the function of this protein could potentially be useful in increasing basal metabolism. ■

MAKING THE PAPER

Wenjie Shen

Altering the shape of catalyst particles can boost their activity.

Chemical catalysts that mop up toxic pollutants created by vehicle use and other human activities have made a difference to the environment, but there is still ample room for improvement. For example, the metal oxides currently used to catalyse the oxidation of carbon monoxide (CO) to carbon dioxide (CO₂) are only active at temperatures much higher than ambient. Wenjie Shen, a physical chemist at the Chinese Academy of Sciences' Dalian Institute of Chemical Physics, has found that changing the shape of one metal-oxide catalyst renders it practical for use at low temperatures. The discovery may lead to ways of producing more efficient catalysts for a broad range of reactions.

Researchers have known since the 1970s that tricobalt tetraoxide (Co₃O₄) can catalyse CO oxidation at low temperatures, but only under artificially dry conditions. The catalyst works by binding CO at its active sites, which contain Co³⁺ cations, so that CO can react with nearby oxygen molecules. But, explains Shen, "at low temperatures, the active sites eventually become occupied by water molecules and can no longer bind CO". This severely limits most practical applications of this catalyst.

Most metal-oxide particles are spherical, with their active sites located in 'dents' on the sphere's surface. "The exposed active sites are limited in these particles," says Shen, who several years ago had the idea that changing the particles' shape might increase the number of active sites. "I had been following the material sciences field. There were many reports of metal and metal-oxide particles designed with different shapes that had altered properties," he explains. "I thought that the same concept could be applied to the design of solid catalysts."

Shen and his colleagues tested a number of strategies for synthesizing Co₃O₄ particles



under various conditions in the hope of building different shapes. They eventually produced tiny rods, 5–15-nanometres wide by 200–300-nanometres long. "We immediately tested these in CO oxidation," says Shen. "Right away we were surprised by the results."

In contrast to the spherical particles, which perform poorly at low temperatures, the nanorods could convert 100% of CO in a flowing stream of gas. The rods' activity lasted for 6 hours at very low temperatures — down to -77°C. Importantly, the nanorods maintained their high level of activity and stability at temperatures up to 400°C, as well as in gases containing a lot of water and CO₂ — conditions that mimic the exhausts of cars.

Excited by the results, Shen and his co-workers examined why the nanorods were so active. Detailed transmission electron microscope images revealed that the nanorod shape exposes one specific crystal plane that makes up about 41% of the total surface area of the particle and consists primarily of Co³⁺ active sites.

The work not only paves the way for designing the next generation of catalysts for reducing CO in the air but, more generally, demonstrates that particle shape is a crucial parameter to consider in the design of high-efficiency metal-oxide catalysts. "This discovery is very exciting. Until now, researchers emphasized the importance of particle size in making catalysts more effective," says Shen. "But now we know that morphology should also be considered. By controlling the morphology you can quantitatively design and enrich the active sites." ■

FROM THE BLOGOSPHERE

Preliminary data are in for a *Nature Neuroscience* peer-review experiment (<http://tinyurl.com/cs95jo>). Last year, the journal joined the Neuroscience Peer Review Consortium, a group of journals that have agreed to offer authors the option to transfer peer reviews of manuscripts to another journal when a manuscript is no longer under consideration at the first journal. The consortium's goals

include speeding up publication and reducing the burden on reviewers.

In an April editorial, the journal's editors share that only a handful of transfers have taken place, all of them from *Nature Neuroscience* to the *Journal of Neuroscience*. The transfers represent less than 1% of manuscripts rejected after review. Authors who participated reported a saving

of time and effort for papers that were eventually published, even when new referees were chosen. There were no transfers to *Nature Neuroscience* from other journals.

More data will be needed to determine whether the group is meeting its goals, but the editors hope that transfer rates may increase as more authors become aware of the consortium. ■

Visit *Nautilus* for regular news relevant to *Nature* authors ▶ <http://blogs.nature.com/nautilus> and see Peer-to-Peer for news for peer reviewers and about peer review ▶ <http://blogs.nature.com/peer-to-peer>.

Early warnings

Screening programmes for cancer detection are not always as effective at saving lives as might be hoped. Improving the situation will require a concerted effort on a broad front.

Early detection of cancer is broadly seen as key to successful treatment, but many screening programmes are coming under fire for being relatively ineffectual. On 18 March, for example, *The New England Journal of Medicine* published online two studies of screening programmes for prostate cancer, which look for the biomarker prostate-specific antigen (PSA). One found that the screening programme had no effect on mortality rates for prostate cancer (G. L. Andriole *et al.* *N. Engl. J. Med.* **360**, 1310–1319; 2009), the other found that screening reduced the rate of death from prostate cancer by 20% but was associated with a high risk of overdiagnosis (F. H. Schröder *et al.* *N. Engl. J. Med.* **360**, 1320–1328; 2009). Both found that a large number of men received unnecessary medical treatment as a result of the screening programmes.

Hard on the heels of these studies came another that looked at the gene-expression profile of ovarian cancers detected early, and found that they would probably advance more slowly and be less deadly than those detected later. If screening is to succeed, the authors conclude, we need other, better tests that can detect the virulent forms earlier (A. Berchuck *et al.* *Clin. Cancer Res.* **15**, 2448–2455; 2009). Then earlier this month, researchers reported that screening for ovarian cancer by measuring levels of the protein CA125 and performing transvaginal ultrasound detected mostly advanced cancers, not the early-stage tumours that could presumably be treated more effectively (E. Partridge *et al.* *Obstet. Gynecol.* **113**, 775–782; 2009).

These studies highlight a problem that has also been seen in other cancers, such as breast and lung: slower-growing cancers are easier to detect, but less likely to be fatal, precisely because they are less aggressive. But the early stages of more virulent cancers still elude today's tests, which themselves can bring risks when false-positive results lead to unnecessary medical interventions.

It is clear that, although some screening programmes are very effective at saving lives — cervical and breast cancer being prime examples — many others are not. This doesn't mean that early detection

is worthless, simply that some current methods are not as good as they could be.

Researchers are now trying to improve tests by gaining a better molecular understanding of cancer. They are looking for biomarkers that can distinguish aggressive tumours from slow-growing ones (see <http://tinyurl.com/naturecancer>). They are studying the cancer genome to devise better screening tests and more targeted therapies (see page 719). And they are learning how to give doctors genetic information to guide the use of drugs in the clinic (see *Nature* **458**, 131–132; 2009).

A better molecular understanding of cancer is unlikely to cure cancer on its own. For example, scientists are still unravelling the complex biology of angiogenesis inhibitors, which once promised to starve tumours to death by choking off their blood supply. Researchers have now found that the drugs can actually increase the spread of cancer in mouse models in certain situations (see page 686). And although the researchers hope that their studies will eventually lead to better angiogenesis inhibitors, the fact remains that every previous cancer 'breakthrough' — be it a targeted therapy or a marker for early detection — has also hit roadblocks.

Given that reality, the best strategy is to continue working on a broad front, improving these methods along with every other intervention in the cancer-fighting tool kit — even those that seem outside a basic biologist's remit. Nobel laureate Roger Tsien at the University of California, San Diego, for example, is trying to devise probes that could light up tumour cells to help surgeons do a more thorough job of removing them. Helping surgeons probably doesn't hold the same appeal for basic biologists as discovering a groundbreaking cancer pathway. But it may be that the most effective treatments for cancer will come, not from some major conceptual breakthrough, but from the steady refinement of the tools we already have. ■

"The early stages of more virulent cancers still elude today's tests."

Tough climate

The US National Academy of Sciences faces a difficult balancing act over global warming.

The US Congress has put the National Academy of Sciences (NAS) in an awkward position. In asking for the academy's advice on what to do about global climate change, it has left the NAS with a difficult balancing act if the academy wants to be effective and remain respected.

The question of efficacy is in large part a matter of timing: things are moving very quickly in the climate arena, and the political

world won't necessarily wait for the academy's methodical review. In the past two weeks, for example, as the NAS was gathering information on the science and policy of climate change at a high-level workshop in Washington DC, two congressmen — Henry Waxman (Democrat, California) and Edward Markey (Democrat, Massachusetts) — introduced a 648-page bill that would commit the United States to a cap-and-trade programme to curb greenhouse-gas emissions. In Bonn, Germany, meanwhile, international negotiators were meeting as part of the lengthy process of hammering out a climate treaty, which is expected to be adopted in Copenhagen this December.

The NAS study committee, under the banner of America's Climate Choices, is not scheduled to release its first set of findings until the

end of the year — by which time the national and international strategies on climate change may well have been decided.

The concern over respect comes from the scope of the studies. Congress specifically asked the NAS committee — which includes top scientists, corporate leaders, environmentalists and industry representatives — to “make recommendations regarding what steps must be taken and what strategies must be adopted in response to global climate change, including the science and technology challenges thereof”.

On the face of it, this sounds as though Congress was asking the NAS for specific policy choices — a request that could lead the academy into dangerous territory. Although it has recommended specific policies in the past, the academy runs the risk of politicizing itself and weakening its standing should it advocate policies such as the stabilization of carbon dioxide at a particular atmospheric concentration, or the adoption of a US cap-and-trade programme. These are not scientific decisions: they depend on how much society is willing to spend on curbing CO₂ emissions versus how much it is willing to live with the results — a fundamentally political problem.

Leaders of the NAS study say that they are not overly concerned. On timing, they point out that any bill moving through Congress this year will be only the first of many. And the same could be said of any treaty that emerges from Copenhagen. NAS studies are meant to provide sound and comprehensive advice that could inform policies over the long term. That laudable goal should not stop the academy from providing Congress with more immediate guidance, should Congress ask for it. For example, the academy could produce an interim report within a few months summarizing its most important findings so far.

As for politicization, the NAS can avoid the pitfalls by its usual practice of outlining the pluses and minuses of different policy options without choosing specific ones. In particular, the committee should examine both carbon taxes and a cap-and-trade programme, even though politicians avoid talking about the former and have lined up behind the latter. If the NAS eschews politics, as it should, then it should have a much greater impact than any advocate ever could, simply by providing a trusted and dispassionate analysis of each strategy's relative merits. ■

Welcome, *Nature Chemistry*

Chemistry is not only a core scientific discipline, it is also of key relevance to others. Many research breakthroughs in physics and the development of sophisticated drug therapies would not have happened without using the principles and methods of chemistry. And our understanding of biology and of our environment would be limited indeed if it were not for the vital contributions from this branch of science.

Such issues persist: it is essential for chemistry to develop new tools, materials and processes to help us take on the problems and challenges of the twenty-first century. The creativity, ingenuity and perseverance of chemists will be crucial in successfully meeting the need for efficient and affordable medicines, for alternative energy and fuel sources, or for smart materials to improve modern technologies.

Happily, the chemistry research community is delivering. Examples range from ever more sophisticated and efficient syntheses for formidably complex organic molecules of interest to biology and medicine, to rationally designed catalysts that could render industrial processes greener and more efficient. A plethora of materials are being designed at the molecular level to optimize their function, whether for capturing carbon dioxide, harnessing sunlight to generate useful chemicals or energy, or delivering and releasing a drug at just the right place in the body.

Meanwhile, an ever-growing array of chemistry-based tools is enabling researchers to probe, at the atomic level and on the timescale of molecular vibrations, the structure and properties of molecules and the processes that involve them. These technical developments are all the more rich and exciting because theorists have delivered the computational and simulation capabilities that are needed to translate

sophisticated data into detailed microscopic pictures of molecular interactions, properties and processes.

With all that in mind, *Nature's* publishers are this month launching *Nature Chemistry*: the fifteenth *Nature* research journal. (The first in the series, *Nature Genetics*, was launched in 1992.)

As with other *Nature* research journals, the editors of *Nature Chemistry* aim to present its readers with stimulating science as well as informative commentaries and debates. But in doing so, they will also make use of the Internet to publish scientific information in ways that conventional paper journals cannot. One example is the linking of research articles to pages containing information about the compounds being discussed, including interactive three-dimensional models of the chemical structures. Another is the use of pop-up windows to display chemical structures when the cursor hovers over a compound number in the main text of an article.

The journal will also adopt compound identifiers that, by enabling online searching for chemicals, aim to provide global and efficient access to chemical information and assist communication between chemists. These facilities will be adopted by *Nature* and other journals in the stable in due course.

Of course, *Nature's* own ambition is to continue publishing papers that have the deepest or broadest impact on chemistry, or that have particularly exciting application possibilities. Judging by past experience in other disciplines, the new journal will indirectly help to strengthen the impact and range of *Nature's* own papers in the field. And *Nature*, in turn, will make use of its media expertise to provide exposure to exciting chemistry published in both journals.

We invite readers to take a look at the first issue of *Nature Chemistry* at www.nature.com/naturechemistry and enjoy the read. ■

***Nature Chemistry* will make use of the Internet to publish scientific information in ways that conventional paper journals cannot.**

RESEARCH HIGHLIGHTS

Flights of fancy

Proc. R. Soc. B. doi:10.1098/rspb.2009.0182 (2009)

Biologists believe that some butterflies send mixed signals. Wings with brightly coloured topsides attract mates, for example, whereas camouflaged undersides protect against predators.

Jeffrey Oliver of Yale University and his colleagues compared the rates of wing-pattern evolution in 54 species of the genus *Bicyclus* (pictured, *Bicyclus anynana*). Because eyespots are evolving at different rates on the upper and lower surfaces of *Bicyclus* wings, the team concludes that markings on different parts of the wings are probably used for different purposes and suggest this separation of signals allows butterflies to be simultaneously attractive to mates and safe from predators.



W. PIEL

ECOLOGY**Equality in dirt**

Glob. Biogeochem. Cycles

doi:10.1029/2008GB003250 (2009)

Soil is the same all around the world — at least in terms of its capacity to break down certain nutrients. Davey Jones of Bangor University in Gwynedd, UK, and his colleagues reached this conclusion after analysing soil samples collected at 40 locations around the globe, from the Arctic to the equatorial zone to Antarctica.

The researchers found that all of the soil samples contained similar concentrations of amino acids. And, when maintained at the same conditions, microbes resident in the different samples all broke down amino acids at roughly the same rate. The results suggest that even though global ecosystems are complex and distinct, soil microbes are similar in their ability to convert amino acids into smaller molecules.

QUANTUM DOTS**Pillars progress**

Appl. Phys. Lett. **94**, 121102 (2009)

The interplay between a photon and a quantum dot — a semiconducting blob of atoms — held inside a small cavity creates a device that can act as a qubit, the data-carrying building block of quantum computing.

Materials scientists would like to study information transfer between many such solid-state qubits. However, current construction techniques can create only a few unpredictable cavities and dots, thwarting attempts to build regular arrays.

Adrien Dousse and his colleagues at the Laboratory for Photonics and Nanostructures

in Marcoussis, France, have now used laser-guided etching to create, in one process, a dozen pillar-shaped cavities less than 3 micrometres wide, each containing an accurately tuned and positioned quantum dot. The technique could be scaled to create an assembly of identical qubits.

ATMOSPHERIC SCIENCE**Bolt from the storm**

Nature Geosci. doi:10.1038/ngeo477 (2009)

Although forecasters can anticipate hurricane trajectories fairly well, successful prediction of storm intensification lags behind. Lightning may provide the warning needed to predict that a tropical cyclone is about to become more powerful.

Colin Price of Tel Aviv University and his colleagues compared data from the World Wide Lightning Location Network with data on all 58 category-4 and category-5 tropical

cyclones that occurred between 2005 and 2007. In all but two storms, peak lightning activity preceded peak hurricane intensity by roughly one day.

The researchers say that they don't know the exact mechanism, but note that lightning serves as an indicator of the kind of in-storm convection that can lead to vortex intensification.

ASTRONOMY**Slow and steady**

Astrophys. J. **694**, 1171-1199 (2009)

Most nearby galaxies in the Universe are massive and filled with middle-aged stars, but how and when the galaxies formed is a topic of hot debate.

To estimate galactic ages, Edward Taylor of Leiden University in the Netherlands and his colleagues studied 7,840 galaxies using the Multiwavelength Survey by Yale-Chile (MUSYC), which in total covers one square degree of the southern sky. They looked at the age of stars in galaxies as far away as 10 billion light years, and discerned that about one-fifth of large galaxies formed within the Universe's first 4 billion years; 50% of the galaxies had formed by the time the Universe was 7 billion years old, about half its current age.

The new survey data suggest that massive galaxies develop at a slower, steadier rate than previously believed.

BIOPHYSICS**DNA made for walking**

Science **324**, 67-71 (2009)

Researchers have designed a DNA molecule that can 'walk' for two-and-a-half steps in a predetermined direction along a DNA track.



GETTY

Nadrian Seeman at New York University and his colleagues created a 49-nanometre-long track of bound DNA strands with loops, and a single-stranded DNA 'walker' molecule. The walker ratchets itself along when its front 'leg' binds to the next loop on the track, triggering a reaction that frees the back leg. Chemical analyses showed the walker took a step 74% of the time.

The team is exploring other chemical reactions besides base-pair binding to drive the walkers. If such constructs can be designed to carry cargo, they could be used to build molecular complexes, the researchers say.

IMMUNOLOGY

Inflaming the problem

Nature Immunol. doi:10.1038/ni.1722 (2009)

A common genetic mutation may contribute to a painful autoimmune disease by interfering with the production of the anti-inflammatory protein IL-10.

The mutation, in a gene called *NOD2*, is associated with up to half of all cases of Crohn's disease in the West, but how it contributes to the disease has been controversial, in part because mice with the mutation have normal IL-10 production. Xiaojing Ma at Weill Medical College of Cornell University in New York and his colleagues found that cells from patients with Crohn's disease who have the mutation produce less IL-10.

Furthermore, the mutation prevents activation of a protein called hnRNP-A1, which normally binds to a region near the IL-10 gene and stimulates its expression. The authors suggest that the altered *NOD2* protein functions differently in humans and mice.

DEVELOPMENT

The trouble with alcohol

Dis. Model. Mech. doi:10.1242/dmm.001420 (2009)

Excess alcohol consumed during pregnancy starves embryos of retinoic acid, causing deformities such as small head size and missing brain structures.

Abraham Fainsod at the Hebrew University in Jerusalem and his colleagues had previously developed a laboratory frog model of the effects of alcohol. Given alcohol, the frog embryos recapitulate some of the developmental defects of fetal alcohol syndrome.

Fainsod and Hadas Kot-Leibovich now show that alcohol competes with vitamin A, a precursor of retinoic acid, for an enzyme called RALDH2. Increasing RALDH2 levels allows the embryos to tolerate higher doses of alcohol.

CHEMISTRY

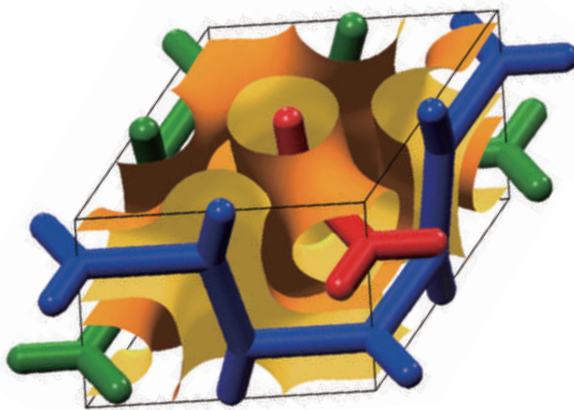
Three in one

Nature Chem. doi:10.1038/nchem.166 (2009)

The most complicated porous nanomaterial ever made is reported by Jackie Ying at the Institute of Bioengineering and Nanotechnology in Singapore, Xiaodong Zou at Stockholm University and their colleagues.

Made from silica, the material has three separate but interwoven continuous porous channels (pictured below). Until now, scientists have only managed to construct mesoporous silica materials containing at most two independent pore systems.

The authors generated the intertwined porous material using a specially designed template made from a positively charged surfactant. The structure contains both ultrashort and ultralong silica channels, and could be used as a molecular sieve to separate different molecules at different rates.



GEOLOGY

Flooding on the Silk Road

Geology 37, 243–246 (2009)

Increased flooding in northwestern China along a section of the old 'Silk Road' trade route is due to accelerated glacier melting, indicating that climate warming is affecting arid communities and their water resources.

Jian Sheng Chen of Hohai University in Nanjing, China, and Chi-yuen Wang of the University of California, Berkeley, analysed oxygen and hydrogen isotopes in the unusually high spring upwelling in a portion of the Hexi Corridor that abuts the Badian Jaran Desert. They traced the water's origin to glaciers four kilometres above sea level in the Qilian Mountains, 40 kilometres away.

The researchers suspect that earthquakes starting in 2003 are responsible for releasing stored groundwater. They also estimate that, at current melting rates, most of the Qilian Mountains' glaciers could disappear by 2050, ultimately depleting the valley aquifer.

JOURNAL CLUB

Michael Heckenberger
University of Florida, Gainesville

An archaeologist looks at South America's early complex societies.

What leads to the rise and fall of civilizations? In coastal Peru, early urban societies based on maritime fishing thrived from 5,800 to 3,600 years ago. Daniel Sandweiss at the University of Maine in Orono and his colleagues report that climate and environmental changes were critical to the rise of these societies (D. H. Sandweiss *et al. Proc. Natl Acad. Sci. USA* 106, 1359–1363; 2009). They find that environmental shifts are well recorded in coastal geological features, which correlate to high Andes glacial cores, notably in the sixth millennium BP, when small urban centres also emerged in southwestern Asia — the 'cradle of civilization'. But as the Peruvian coastal embayments disappeared, around 3,600 years ago, so too did the societies that depended on them.

This paper particularly interested me as our work in the southern Amazon has revealed integrated towns and villages thriving several millennia later on similar resources as the early Andeans — fish, fruit and tubers. Although not as marked as coastal Peru, climatic fluctuations recorded in glacial records, notably the 'Medieval Warming' around 1100–1300 AD, coincided with the emergence of these small territorial polities.

The early complex societies of South America prompt debate over what constitutes urbanism and 'civil society' in its earliest and most minute forms, and make us reconsider the traits and typologies developed from classical civilizations and Western experience. Notably, in some South American cases, corporate labour and civic organization were not based on agricultural intensification and administration of crop surpluses.

Whether we call them urban or not, these societies show unique properties of self-organization and dynamics of the relationship of humans with natural systems.

Discuss this paper at <http://blogs.nature.com/nature/journalclub>

NEWS

Obama's nuclear-weapons-free vision

The 1986 Reykjavik summit between Ronald Reagan and Mikhail Gorbachev marked a turning point in the history of the nuclear-arms race between the two superpowers, with subsequent discussions leading to unprecedented reductions in their nuclear arsenals. The ambitious speech on disarmament that President Barack Obama delivered in Prague on 5 April might be a similar milestone on the way to his stated goal of “a world without nuclear weapons”.

“If his administration can achieve half of it we will look back on this as an historic speech,” says Jessica Tuchman Mathews, president of the Carnegie Endowment for International Peace in Washington DC. Pavel Podvig, an expert on Russian nuclear affairs at the Center for International Security and Cooperation at Stanford University in California, adds that “it is a great commitment and a very good start, but will very much depend on the specifics of implementation”.

The key elements of Obama's speech were arms reductions; ratification of the Comprehensive Nuclear-Test-Ban-Treaty; new powers of international inspection and control over civilian nuclear fuel; controls on the production of weapons-grade materials; new efforts to round up uncontrolled nuclear materials; and new military attitudes. What are the prospects, and obstacles, facing each of these aspirations? **● A new Strategic Arms Reduction Treaty (START), to be expanded to include all nuclear-weapons states.** The Reykjavik discussions led in 1991 to the signing of the START I treaty, which limited the arsenals of the United States and Russia to 6,000 strategic warheads and 1,600 delivery systems. But this treaty, dramatic at the time, expires in December and its successor treaties were never ratified.

Obama and his Russian counterpart Dmitry Medvedev say they will thrash out a new START treaty by the end of the year; it is reported to involve slimming the arsenals to 1,500 strategic warheads, and later to just 1,000, while also halving the numbers of missiles and bombers that can deliver them. As to the other acknowledged nuclear powers, the United Kingdom has said this month that it is open to multilateral discussions, but France has made no similar declaration, although it has announced unilateral cuts. China has historically claimed to favour reduction to zero, as long as the United States and Russia act on a similar commitment.

The new bilateral START negotiations will take place against a backdrop of continuing acrimony over US proposals for a missile-defence shield in Europe. “Any discussion with



President Obama wants to reduce the nuclear threat to zero.

P. JOSEK/REUTERS

Russia would have to start with a removal of US nuclear weapons from Europe,” says Podvig, a move that that would be controversial within NATO. But both the United States and Russia are old hands at the complexities of disarmament deals and, given political will, a treaty along these lines seems quite possible.

● US Ratification of the Comprehensive Nuclear-Test-Ban-Treaty (CTBT). Since it was signed in 1996, 148 states have ratified the CTBT; the United States and China are the only acknowledged nuclear-weapons states not to have done so. The US Senate rejected ratification of the CTBT in 1999, but some technical concerns voiced then have since been alleviated. In terms of verifiability, the worldwide seismic monitoring network has proved able to detect explosions less than a tenth of the size of the Hiroshima blast, and progress has been made in the atmospheric monitoring of ‘smoking gun’ signatures from noble gases and radionuclides. The ‘stockpile stewardship’ programme aimed at ensuring the integrity of US weapons without any need for nuclear tests seems so far to have been largely successful.

The US National Academies, which threw their weight behind the CTBT in a 2002 report chaired by John Holdren, now Obama's science adviser, are one of many influential bodies that support US ratification. Prominent US statesmen, including George Shultz and Henry Kissinger, former Republican secretaries of state, have also come out in favour. The Republican voices could be of particular salience to Obama. Although he will need only 8 Republican votes

to pass the treaty, compared with the 22 that Bill Clinton needed in 1999, he will probably want a more broadly bipartisan vote in favour.

● More resources and authority to strengthen international inspections. Despite an increasing workload, the budget for the International Atomic Energy Agency (IAEA), which carries out international inspections, has been flat for much of the past two decades. The IAEA's outgoing director-general, Mohamed ElBaradei, says that its US\$400-million budget should double if the agency is to do its job. Resources are not the only constraint. The IAEA is limited to inspecting declared nuclear facilities, and cannot seek out clandestine sites. A 1997 ‘additional protocol’ to the IAEA's safeguards agreement gives it extra powers in this respect, but many countries — including Iran, where it might have important effects — have yet to sign it.

● A fuel-bank framework for civil cooperation. This proposal gives support to plans by the IAEA to offer countries access to nuclear fuel from facilities that would be put under multilateral control, thus decoupling the use of nuclear power from national enrichment facilities that can also be used for weapons-grade material — as they have been for example, in North Korea (which tested a satellite launcher/long-range missile on the day of Obama's speech — see page 685).

Such a scheme might help to ease the systemic tension between the IAEA's goals of limiting proliferation and allowing the spread of peaceful nuclear power. The tension was clearly



G20 SUMMIT
World leaders fail to
kickstart green economy.
www.nature.com/news

AP

visible in the failure of the agency's member states to agree on a successor to ElBaradei last month. Yukiya Amano of Japan was perceived as focused on safeguards whereas Abdul Samad Minty of South Africa was seen as the candidate for extending nuclear power in the developing world. The member states will now put forward new names in the search for a consensus candidate, with a vote likely to be held in May.

● **A new treaty to end the production of fissile materials for use in nuclear weapons.** A Fissile Material Cut-off Treaty was originally proposed in 1993 by the United Nations General Assembly. It would commit all signatories to stop producing weapons-grade material. According to Jean du Preez, an arms expert at the Monterey Institute of International Studies in California, this may be a way to cap weapons production in the unofficial weapons states — India, Pakistan, North Korea and Israel — which are currently not members of the 1968 Nuclear Non-Proliferation Treaty (NPT). Such a treaty would pose huge logistical and political challenges in terms of access, inventory and control, but it will be put back on the table at the 2010 NPT review conference, and might in time be a big step towards a nuclear-weapons-free world.

● **A new international effort to secure all vulnerable nuclear material.** Obama proposed a Global Summit on Nuclear Security, hosted by the United States, with an agenda to include the transformation of two existing programmes — the 2003 Proliferation Security Initiative, an international coalition targeting nuclear trafficking, and the 2006 Global Initiative to Combat Nuclear Terrorism — into permanent international institutions. The IAEA has no clear remit yet in this area.

● **Reducing the role of nuclear weapons in US national security strategy.** What might seem one of the most mundane disarmament proposals in Obama's speech may be more important even than arms reductions, and may come to underwrite all his non-proliferation proposals. So far, the five nuclear-weapons states recognized by the NPT have largely ignored the treaty's central bargain; that they should disarm just as others refrain from proliferating. Instead, they have maintained, and often extended, the 'crucial' role nuclear weapons have in their policy. By committing to using nuclear weapons only in the event of a nuclear attack, they could go a long way to creating an environment more conducive to broader non-proliferation measures. ■

Declan Butler

Korean satellite misses orbit

It was meant to broadcast a booming anthem to leader Kim Jong-il, but if it did it was heard only by sea nymphs ringing its knell. On 5 April, North Korea's third attempt at a satellite launch, like its predecessors, dropped its payload into the Pacific Ocean. Preliminary analyses point to a failure in the rocket's third and final stage, which either did not ignite or did not separate properly from the second stage.

North Korea had hoped to join a growing club of entry-level space-farers. In February, Iran successfully launched a small satellite into low-Earth orbit using the Safir-2 rocket, and last September, a private company, Space-X of Hawthorne, California, launched a satellite aboard a booster it had designed from scratch, the Falcon 1.

Most observers believe that North Korea's rocket, known as TaepoDong-2, was more primitive than either of these, as it is based on the decades-old Russian and Chinese technology behind the Scud missile. Assuming that heritage, says David Wright, an arms-control analyst with the Union of Concerned Scientists, a non-profit group based in Cambridge, Massachusetts, the booster would weigh about 80 tonnes, three times the weight of Iran's rocket. Its engines probably used a relatively low-impulse combination of kerosene fuel and nitric-acid oxidizer, whereas the Falcon uses liquid oxygen.

Those limitations do not mean that such a rocket could not work; it simply didn't work this time. The newest version of the TaepoDong-2 lifted off from the Musudan-ri launch site at around 2:30 a.m. GMT. Shortly after the launch, the state-run Korean Central News Agency reported that the rocket's payload, a communication satellite, had successfully reached orbit and begun transmitting the "Song of General Kim Jong-il". But a terse statement by the US Northern Command six hours later — by which time any satellite should have circled Earth a few times — said that "no object entered orbit". Citing diplomatic sources, the South Korean newspaper *Chosun Ilbo* reported that the rocket's first stage had landed in the Sea of Japan, whereas its remaining stages crashed some 2,700

kilometres farther out in the Pacific (see graphic). The launch's trajectory did not lend itself to the amateur observations from the United States and Europe that often provide corroboration of military launches.

The fact that it got 3,200 kilometres downrange suggests that the first stage of the rocket delivered, according to Wright. That would probably require the synchronized firing of four powerful engines, he says, and "the fact that it worked is a big deal".

A failure between the second and third stages is not uncommon, adds Brian Weeden, a technical consultant with the Secure World Foundation, a non-profit



group based in Superior, Colorado. The separation of stages is a "very delicate operation" that requires explosive bolts and the third stage to ignite in careful sequence.

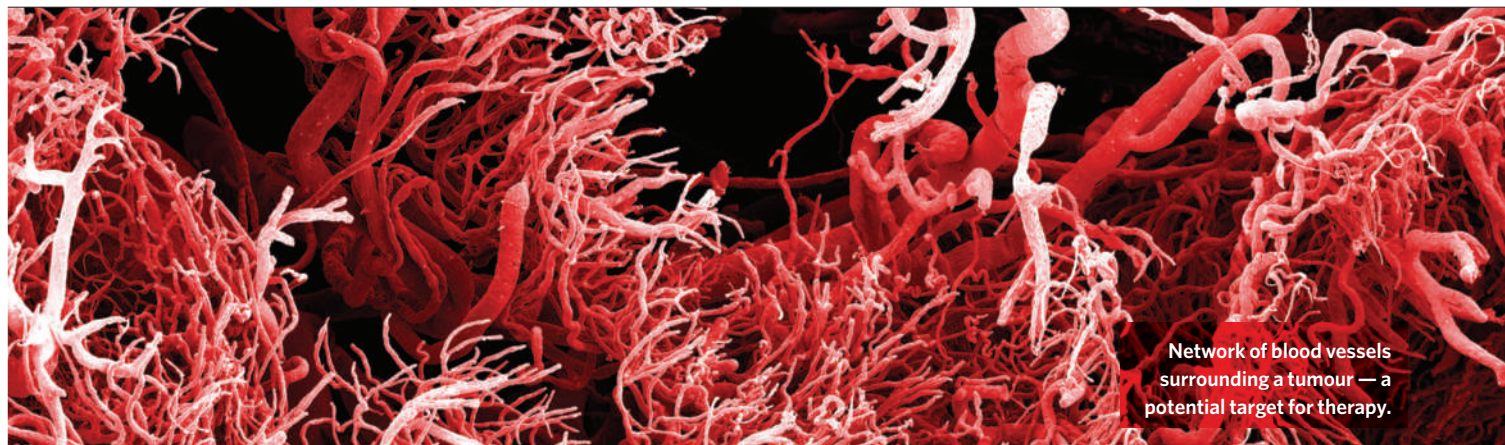
Whether North Korea can learn from its mistakes depends largely on what its developers gleaned from the rocket before it went down, says Jonathan McDowell, an astronomer at the Harvard-Smithsonian Center for Astrophysics in Cambridge, Massachusetts, who keeps tabs on rocket launches. No direct telemetry could have been received back in Korea after the rocket disappeared over the horizon. A support vessel in the Pacific tracking the flight would have solved that problem, but it is not clear whether North Korea has this capability. If it does not, then "it's just really hard for them to figure out what happened to their own rocket", McDowell says.

Given America's superior monitoring capabilities, "I'm almost sure that the United States knows more about what caused it to fail than they do," says Geoffrey Forden, an international security researcher at the Massachusetts Institute of Technology in Cambridge. ■

Geoff Brumfiel

SPECIAL REPORT

CLOUDS HILL IMAGING LTD/SPL



Network of blood vessels surrounding a tumour — a potential target for therapy.

Cutting off cancer's supply lines

Targeting the blood vessels that feed tumours is not the silver bullet once hoped for, but refinements to the strategy may suggest further ways to treat the disease. **Erika Check Hayden** reports.

Drugs that aim to choke off a tumour's blood supply, known as angiogenesis inhibitors, have been hailed as opening a new era in cancer therapy. But a flurry of animal studies suggests that such drugs may in certain situations actually accelerate the spread of cancer.

"We're just finding the limitations of these types of agents in the clinic," says John Ebos, a cancer researcher at the University of Toronto, Canada. "I don't think it's unique — various types of therapies, such as chemotherapy and radiation, also have limitations. It's just a question of how we can overcome it."

This is a key time in the long and controversial history of these drugs. In May, the US Food and Drug Administration (FDA) is expected to decide whether to expand use of bevacizumab, the first angiogenesis inhibitor. This monoclonal antibody, sold as Avastin by South San Francisco-based Genentech, was approved in 2004 for treating metastatic colon cancer in combination with chemotherapy. It has since been approved in the United States and elsewhere for other uses, and on 31 March an FDA advisory committee recommended the drug also be approved for glioblastoma, a deadly brain cancer for which few other treatments are available. The agency's decision is expected in May.

According to regulatory papers filed in January, Genentech may before then reveal results of a clinical trial to test the use of bevacizumab as an 'adjuvant' used with chemotherapy in patients whose colon tumours have been surgically removed. The 2,710-patient

phase III trial investigated whether those who take bevacizumab are more likely to survive without recurrence of their disease than patients who do not take the drug.

"There are tens of thousands of patients with early colorectal cancer who don't get Avastin right now," says Geoffrey Porges, an analyst with Sanford C. Bernstein in New York City. Success as an adjuvant therapy "would open up a market at least as large as the current metastatic market", he thinks, noting that trials testing the drug as an adjuvant for other cancers are under way. Last year, the drug racked up \$4.8 billion worldwide in sales; its wholesale price is about \$50,000 per year of treatment.

The original idea behind bevacizumab and other angiogenesis inhibitors was championed by Judah Folkman of Harvard Medical School. In 1971, Folkman wrote in the *New England Journal of Medicine*¹ that all tumours depend on the constant growth of new blood vessels, a process called angiogenesis, and that blocking it should eliminate the cancer. The popularity of the idea waned in the early 2000s following disappointing results in clinical trials of two anti-angiogenic compounds, angiostatin and endostatin, that were discovered in Folkman's lab. It regained ground when bevacizumab was approved.

Since 2004, two other angiogenesis inhibitors have been approved in major markets worldwide: sunitinib, sold as Sutent by Pfizer, for use in advanced kidney cancer and gastrointestinal stromal tumours, and sorafenib, sold as Nexavar by Bayer, for use in kidney and liver cancer. Both are small-molecule drugs that

target kinases, in particular vascular endothelial growth factor, or VEGF, which is also targeted by bevacizumab. Many more such compounds are in late-stage clinical trials (see table).

But these drugs have not been the magic bullet that Folkman envisaged. In major cancers, such as breast and colon, they have helped patients to survive longer when given with chemotherapy, but not when given alone. The drugs seem to grant most patients slower progression and a few extra months of survival — a real benefit, but not a cure.

The tumours fight back

That has led researchers to ask whether the drugs are working as Folkman hypothesized. Some, such as Rakesh Jain of the Massachusetts General Hospital in Boston, have suggested that the drugs "normalize" blood-vessel growth around tumours. Cancer blood vessels are normally leaky and chaotic; by correcting this, angiogenesis inhibitors may turn the vessels into a more efficient pipeline for delivering chemotherapy, Jain suggests.

Some physicians who treat patients with cancer have also noticed that when the disease does return after treatment aimed at angiogenesis, it is more aggressive than in patients not treated with the drugs. Other researchers now have evidence that may validate this observation. In mouse studies^{2,3}, researchers have reported that the drugs can speed the spread of tumours to nearby tissues and distant organs.

Reporting recently in *Cancer Cell*, two teams investigated the effects of angiogenesis-inhibiting drugs and of knocking out the gene encoding VEGF. One team, led by Douglas Hanahan of the University of California, San Francisco,

"I think there's been that growing feeling of why aren't they working better, and we're now uncovering some explanations."



ISLAM AND SCIENCE
Muslim students weigh in on evolution.
www.nature.com/news

PUNCHSTOCK

and Oriol Casanovas of the Catalan Institute of Oncology in Barcelona, Spain, reported that tumours spread faster and more often to both near and distant organs in mice treated with drugs or lacking the *VEGF* gene². The other group, led by Robert Kerbel of the University of Toronto, reported similar effects³, and found that in some situations the treated mice actually died earlier than untreated animals.

Kerbel's group further studied how metastasis changed depending on when the drugs were given. When given either before or long after metastatic tumour cells were injected into the mice, or after primary tumours had been surgically removed, the drugs hastened metastasis. But when given while the mice were still carrying primary tumours — those that had yet to metastasize — the drugs actually helped shrink the tumours. If the data hold true in humans, they suggest that the timing of drug delivery can have a major impact on a patient's response.

A third paper⁴, published online in *Nature Medicine* on 22 March, suggested that such effects might also occur for a class of drugs called integrin inhibitors. These block the activity of integrins, which are proteins that trigger angiogenesis, among other things. Researchers led by Kairbaan Hodivala-Dilke at Queen Mary, University of London, studied the effects of two integrin inhibitors, one of which, cilengitide, is in phase III clinical trials to treat brain cancer. They found that, when given in low doses in mice, the drugs paradoxically seemed to promote angiogenesis and tumour growth.

Ebos, the first author on the Kerbel-group paper, says that, taken together, these studies don't mean anti-angiogenesis drugs are a disappointment, simply that they have limitations. "I think there's been that growing feeling of why aren't they working better, and I think we're

now uncovering some of the explanations," he says.

For instance, Hanahan and Casanovas's team studied whether choking off some blood vessels, and thereby inducing oxygen deprivation (hypoxia), might be driving the tumours to search elsewhere for sustenance. When they stained cancer cells in mice with a marker for hypoxia, it showed up in the cancer cells of animals treated with angiogenesis inhibitors.

The oxygen connection

To Casanovas, this provides a link to earlier studies indicating that hypoxia can boost tumour invasiveness, and shows that the lack of oxygen caused by angiogenesis inhibitors actually induces cancerous cells to leave the tumour site in search of it. Casanovas says that his and Kerbel's teams have together found enough evidence to suggest that such effects probably occur with many angiogenesis inhibitors in many different tumour types. "Between us, we have tested five different compounds, including small molecules and antibodies, so we think the effect could be more general than strictly what we've seen in these two papers, and the same thing applies for different types of tumours," Casanovas says.

Donald McDonald, a vascular biologist at the University of California, San Francisco, suggests that the new studies are delivering a broader message. "What they're telling us is that there are other targets [in addition to VEGF] that need to be considered if you're going to mess with the blood supply." Drug companies are already developing compounds that may address

some of the problems raised by the papers.

McDonald notes that researchers six years ago reported⁵ that hypoxic cancer cells ramped up production of a protein called Met, which binds and activates another protein called hepatocyte growth factor. This growth factor also goes by the name of scatter factor because it triggers cells to move — precisely the effect seen in the *Cancer Cell* papers. Administered with anti-angiogenesis drugs, Met inhibitors — the focus of development by drug and biotechnology companies — might offset the effects reported in the *Cancer Cell* papers, McDonald suggests.

And Hodivala-Dilke's team noted that simply using some drugs differently might improve their effectiveness. Clinical trials of

"What they're telling us is that there are other targets that need to be considered if you're going to mess with the blood supply."

cilengitide have delivered mixed results so far, and the team says its study points to a possible reason for this. They found that integrin inhibitors slowed the degradation of proteins that promote angiogenesis. These longer-lived proteins then recruited cells that make up blood-vessel

walls to the tumour site, where they built new blood pipelines to the tumour. Because the effect occurred only at very low doses, the team suggests that the drugs should be delivered continuously, rather than at a high dose followed by drug-free days, as was done in the clinical trials. That way, levels would stay above those that seemed to promote angiogenesis in the study.

Porges says that the new studies have not dampened enthusiasm among drug companies who are developing angiogenesis inhibitors, integrin inhibitors and inhibitors of other growth factors thought to be involved in cancer. They expect that eventually patients will be given combinations of inhibitors, with or without chemotherapy.

Because of this, McDonald says that the angiogenesis-inhibitor story is far from over. "We have learned that what these drugs do is more complicated than the original idea, which was that they would stop tumour growth by stopping blood-vessel growth," he says. "Avastin is chapter one of angiogenesis inhibition, and we're going to move on to chapter two and chapter three. And with each chapter there will be more clinical benefit as we get a better understanding of the underlying biology." ■

1. Folkman, J. *N. Engl. J. Med.* **285**, 1182-1186 (1971).
2. Páez-Ribes, M. *et al. Cancer Cell* **15**, 220-231 (2009).
3. Ebos, J. M. L. *et al. Cancer Cell* **15**, 232-239 (2009).
4. Reynolds, A. R. *et al. Nature Med.* doi:10.1038/nm.1941 (2009).
5. Pennacchietti, S. *et al. Cancer Cell* **3**, 347-361 (2003).

See Editorial, page 679.

ANGIOGENESIS INHIBITORS IN LATE-STAGE CLINICAL DEVELOPMENT*

Drug	Maker	Being tested in which cancers
Bevacizumab (Avastin)	Genentech	Kidney, ovarian, brain, prostate, liver, pancreas, lymphoma, gastric, gastro-oesophageal
Sunitinib (Sutent)	Pfizer	Breast, kidney, liver, lung
Sorafenib (Nexavar)	Bayer	Lung, melanoma, pancreas
Pazopanib	GlaxoSmithKline	Kidney, soft-tissue sarcoma, lung, ovarian
Axitinib	Pfizer	Kidney (pancreas suspended)
XL184	Exelixis	Medullary thyroid cancer
BIBF1120	Boehringer Ingelheim	Lung, gallbladder
Cediranib (Recentin)	AstraZeneca	Colorectal, brain, ovarian
Aflibercept (VEGF Trap)	Regeneron, Sanofi-Aventis	Lung, prostate, pancreatic, colorectal
Brivanib	Bristol-Myers Squibb	Liver, colorectal
Vandetanib (Zactima)	AstraZeneca	Lung

*Phase III trials that target the VEGF pathway. Drugs shown in colour are already FDA approved for some cancers; see text for details.

Open-access policy flourishes at NIH

Researchers, institutions and publishers have complied with the mandate, but it still has its opponents.

One year on, advocates of free public access to scientific literature are calling a law that requires researchers at the US National Institutes of Health (NIH) to make their manuscripts publicly available at the PubMed Central repository a success. At the same time, the measure continues to be challenged by a senior congressman and some publishers.

Since the legal requirement that NIH-funded researchers make their manuscripts publicly available after acceptance for journal publication came into effect last April, the number of articles being approved by their authors for processing by the repository has more than tripled. In March 2009, 6,425 such original articles were approved by their authors for processing; a year earlier, the number was 1,852 (see graph). The articles become available through PubMed Central no more than a year after their journal publication. Author compliance “has been dramatically altered” by converting an “anaemic” voluntary policy into law, says former NIH director Harold Varmus, now president of the Memorial Sloan Kettering Cancer Center in New York and a keen supporter of open-access initiatives.

But the policy still has opponents. “This so-called ‘open access’ policy was not subject to open hearings, open debate or open amendment in Congress,” John Conyers (Democrat, Michigan), chairman of the House Judiciary



Congressman John Conyers has tabled a bill to challenge the NIH open-access requirement.

Committee, wrote on *The Huffington Post* website last month (he declined to be interviewed for this article). In February, Conyers re-introduced a bill from the last congressional session that would amend US copyright law to forbid the NIH making funding conditional on manuscripts being publicly accessible. However, congressional observers say that the bill has little chance of going anywhere this year.

Open-access policies have caught on around the world in recent years. Britain’s Wellcome Trust, the Italian National Institute of Health (ISS), the European Research Council and many others have implemented similar mandates, including all seven UK research councils. Disease groups such as the high-profile

US foundation Autism Speaks have done the same, as have the Massachusetts Institute of Technology and the Faculty of Arts and Sciences at Harvard University.

The reason that the policy has succeeded at the NIH “is that there has been cooperation — whether they wanted to [comply] or not — by grantees, by extramural staff, by the universities and by publishers”, says David Lipman, director of the NIH’s National Center for Biotechnology Information in Bethesda, Maryland. He believes that the new requirement is at least partly responsible for the increased use of PubMed Central; there were approximately 550,000 articles downloaded from the site in March 2008, and 680,000 last month.

Much of the increase in author participation has occurred since the autumn, when the NIH began e-mailing reminders about the new requirement to investigators submitting grant proposals or progress reports that cited agency-funded papers lacking PubMed Central identifiers. “We expect every paper falling under the NIH public-access policy to be posted to PubMed Central, and we are reviewing every NIH award to make sure that happens,” says Neil Thakur, who oversees the policy for the NIH’s Office of Extramural Research.

However, opposition to the law persists among some publishers. “What is being done by this policy is imposing a specific model of

M. WILSON/GETTY IMAGES

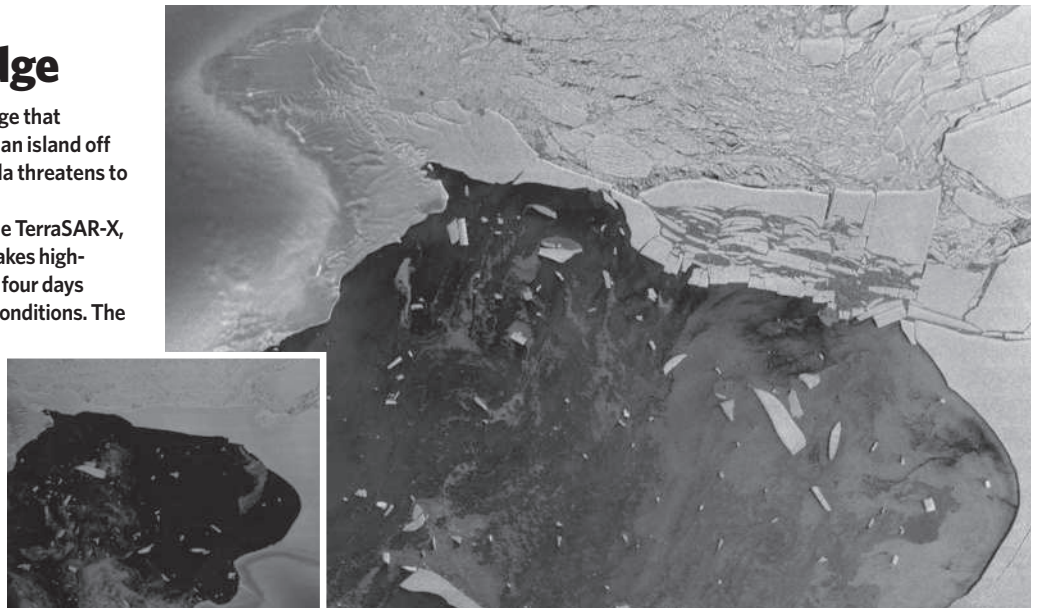
SNAPSHOT

Gapping the bridge

The collapse on 4 April of an ice bridge that connected the Wilkins ice shelf with an island off the southwestern Antarctic peninsula threatens to speed up the shelf’s disintegration.

The synthetic-aperture radar on the TerraSAR-X, a German remote-sensing satellite, takes high-resolution images of the region every four days regardless of cloud cover or lighting conditions. The main image, taken on 5 April, shows the broken bridge. The inset shows the bridge intact. Warming temperatures could still lead to the shelf’s demise, and as the shelf seems to hold back the flow of continental glaciers, it could eventually lead to a loss of ice from the continent itself. ■

Quirin Schiermeier



A. HUMBERT



SILVER LINING
Bright halo around clouds affects climate models.
www.nature.com/news

PUNCHSTOCK

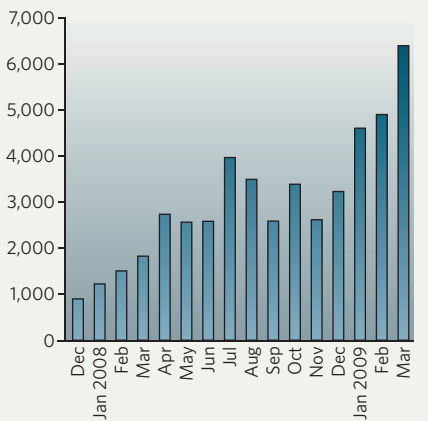
publication that we think the government has no business imposing,” says Allan Adler, legal counsel for the Association of American Publishers (AAP) in Washington DC. (*Nature* is a member of the AAP but cooperates with and supports the NIH on open access.)

Because of the delay of up to a year on NIH uploads to PubMed Central, it is difficult at this stage to gauge the impact of the policies on societies and other publishers that rely heavily on subscriptions for revenue. The recession is driving down endowments and with them library budgets, leading independently to some degree of subscription cancellations.

Heather Joseph, executive director of the Scholarly Publishing and Academic Resources Coalition (SPARC), an advocacy group in Washington DC with an open-access agenda, says that the consortium’s members are reporting large-scale cuts in journal subscriptions. “But they are across disciplines, completely due to the economic meltdown and not the NIH policy,” she adds.

But Martin Frank, executive director of the American Physiological Society in Bethesda, says that “in an environment where access is

ARTICLES APPROVED BY AUTHORS FOR PROCESSING BY PUBMED CENTRAL



readily available whether after 12 months or 6 months or immediately, the subscription model starts wobbling”. Frank predicts that, as subscription revenues tank, publishers will be forced to levy stiff fees on authors for publishing. He notes that the open-access journal group the Public Library of Science has boosted its publication fees for *PLoS Medicine* and *PLoS*

Biology from US\$1,500 in 2006 to \$2,950 today; the author fees for four of its other five journals have risen to \$2,300.

And last week, the formerly open-access *Journal of Visualized Experiments* (JoVE) abruptly switched to a subscription model, charging individuals \$99 per month and larger institutions up to \$2,400 per year. “While we do support open access — we think it’s a great idea — we simply cannot survive with the open-access model, at least now,” says Moshe Pritsker, JoVE’s editor-in-chief and co-founder.

Scientists seem to be coping with the changes, although there are some grumblings. “I don’t have any complaints about the procedures. They are pretty user-friendly,” says Carol Mason, a neuroscientist at Columbia University in New York. When she published a paper in the *Journal of Neuroscience* last month, the journal submitted the paper to PubMed Central for her. After receiving an e-mail from the NIH, it took her “a couple of minutes” to click through a step-by-step guide and log into the processing system, and another 15 minutes to review the attached PDF of her paper before hitting ‘approve’.

Meredith Wadman

NATL LIB. MED.

Sagging economy clips clean tech's wings

Despite fervent government interest in pursuing renewable energy, worldwide venture-capital investment in the clean-technology sector has fallen sharply for a second successive quarter, according to data released on 1 April by analysts Cleantech Group and Deloitte.

The sector includes renewable-energy, waste, water and materials technologies as well as the development of less destructive coal- and oil-extraction methods. The influx of venture capital fell from a high of US\$2.6 billion in the third quarter of 2008 to \$1.7 billion in last year's final quarter as the depth of the ongoing financial crisis became clear (see chart). This year's first quarter saw a further decline to \$1 billion,

more than one-third of which went into the solar industry.

G20 nations have, however, earmarked an estimated \$400 billion for green projects as part of their individual economic-stimulus plans (see *Nature* 458, 562; 2009).

Europe revises animal-research proposals

Apparently heeding researchers' warnings, politicians last week altered controversial provisions in European draft legislation on animal experiments (see box in *Nature* 458, 394–395; 2009).

The European Parliament's agriculture committee removed language that would have restricted research on non-human primates to work on "life-threatening or debilitating" conditions. And it stipulated that researchers may now reuse animals in procedures that cause "moderate" — rather than "mild" — pain.

The committee also called for feasibility studies on ending the use of captured wild animals in research, amid concerns about shortages in supply if this move were pushed through too quickly.

Having passed the committee, the draft legislation will be voted on by the full parliament in May before being considered

by the European Council and European Commission. It then heads back to parliament for a second reading.

For a longer version of this story, see <http://tiny.cc/animals12>.

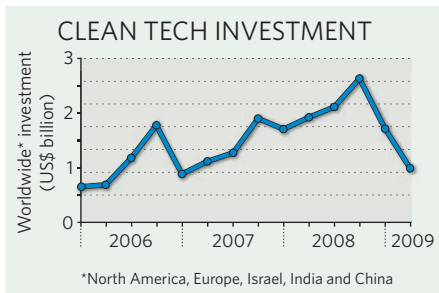
Skeleton transfer to Native Americans put on hold

An attempt by officials at the University of California, San Diego, to give a pair of nearly 10,000-year-old skeletons to a local Native American tribe has been halted. This may ultimately save the specimens for scientific study.

Under federal law, bones can be returned to a tribe that can prove 'cultural affiliation'. But the skeletons, found on the campus 33 years ago, are too old to be culturally linked to a tribe, say university scientific panels (see *Nature* 458, 265; 2009).

University chancellor Marye Anne Fox and president Mark Yudof nonetheless requested permission in February from federal officials to offer the Kumeyaay tribe the bones, which have been in dispute for more than two years (*Nature* 455, 1156–1157; 2008). But Fox has now cancelled that request after Kumeyaay attorneys changed their plea for the bones, seeking university recognition of cultural affiliation.

SOURCE: CLEANTECH



Italian laboratory escapes quake damage

The Gran Sasso National Laboratory, a particle-physics research centre 15 kilometres northeast of L'Aquila in central Italy, has survived without damage the earthquake that devastated the region on 6 April, although experiments have been suspended.

The laboratory, 10 kilometres east of the quake's epicentre, is a large underground facility built deep inside the Gran Sasso mountain. Its surface structures will be used to shelter some of those left homeless by the quake, which measured 6.3 on the Richter scale and killed at least 179 people.

US AIDS programme 'essential and expensive'

Between 2004 and 2007, the US President's Emergency Plan for AIDS Relief (PEPFAR) cut deaths from AIDS by about 10% in 12 African countries, at a cost of \$2,700 per life saved. So say researchers who published an independent analysis of the programme this week (E. Bendavid and J. Bhattacharya *Ann. Int. Med.* 150, 60520-117; 2009).

Costs for airborne telescope spiral upwards

An airborne observatory developed by the United States and Germany is running 10 years behind schedule, has more than tripled in budget, and continues to have cost-control problems, according to an independent NASA audit.



T. TSCHIDA/NASA

The Stratospheric Observatory for Infrared Astronomy (SOFIA) boasts a 2.5-metre-diameter telescope that peers out of a hole cut into the side of a 30-year-old Boeing 747 aeroplane (pictured). The partners in the project are NASA and the German Aerospace Center, or DLR.

In 1997, NASA estimated that SOFIA could start limited scientific operations by 2001 for \$265 million. It now says it will cost \$840 million to reach a similar point in 2011.

The 27 March audit from the NASA inspector general's office adds that SOFIA's management still cannot accurately assess the observatory's long-term costs. SOFIA's current schedule is under review, a NASA spokesman says.

PEPFAR has pumped \$15 billion into aid-recipient countries since 2004, and in 2008 was authorized to spend a further \$48 billion over five more years (see *Nature* 457, 254-256; 2009). It did not reduce the number of people living with HIV, nor the proportion of the population with the

disease, note Eran Bendavid and Jayanta Bhattacharya of Stanford University in California.

The researchers, who call the programme "essential and expensive", say they hope that their work will spur PEPFAR to evaluate the effectiveness of its spending.



C. ALBERTSON

BIOLOGY'S NEXT TOP MODEL?

From Antarctic icefish to Galapagos finches, there are some interesting characters at the fringes of developmental biology. **Brendan Maher** explores a world of alternative model organisms.

Debate wears on as to how, exactly, it happened. Some say it could have been a global cooling event brought on by falling greenhouse-gas levels. Others argue that it was the drifting continents, which opened up Drake Passage and kick-started frigid, circumpolar currents. Whatever the reason, to the fish that lived on the Antarctic shelf about 34 million years ago, all that mattered was that it was getting cold, very cold.

As the water temperatures plunged by about 5 °C to below zero over the next few million years, most fish became extinct or moved on to warmer climes. But one group, the Notothenioidei, remained. Thanks to some extraordinary evolutionary innovations, these bottom-dwellers radiated, speciated and ultimately dominated. Crucial proteins shifted shape so they could work at cold temperatures, and a digestive enzyme fragment took on a new role as anti-freeze. Because colder waters hold more dissolved oxygen, red blood cells became dispensable, and the 16 species of the Channichthyidae family no longer make them at all. These are the icefish of the Antarctic: clear blooded, up to almost a metre long and with eerie, crocodilian features.

To John Postlethwait, though, the icefish are “beautiful”. It’s not just their haunting looks that captivated Postlethwait, a developmental biologist at the University of Oregon, Eugene. It’s what they might do for the study of osteoporosis. A quirk of their evolution, he says, may make icefish a valuable model animal for discovering genetic controls on bone density.

For decades, developmental biology has been dominated by an established A-list of models including the mouse (*Mus musculus*), fruitfly (*Drosophila melanogaster*), nematode (*Caenorhabditis elegans*), zebrafish (*Danio rerio*), African clawed frog (*Xenopus laevis*), chicken (*Gallus gallus*) and mustard weed (*Arabidopsis thaliana*). It has been rare for

scientists’ fancies to stray beyond these supermodels. The ease with which the animals can be bred, their small size, fast generation times and the slew of laboratory tools with which to manipulate them make them irresistibly appealing. According to the Thompson Reuters Web of Science, more than 50,000 publications in 2008 mentioned mice, and around 6,000 featured *Drosophila*.

Icefish, on the other hand, appeared in about 20. Yet just as in advertising — where hand and foot models ply their modest trades on the basis of singular features rather than overall glamour — there is a place in science for models that have a specialist role. And the demand for them could grow as new tools make them easier to use. In November 2008, 23 alternative models, including fruit bats, comb jellies, wandering spiders and blind Mexican cave fish were featured in the first volume of *Emerging Model Organisms*, a laboratory manual from Cold Spring Harbor Laboratory Press in New York. (Icefish, whose larva is pictured above, haven’t yet made the cut.)

Alternative models present considerable obstacles: they are often difficult to collect and maintain, and genetic and genomic tools have to be custom-built. “You end up having to start from square one,” says Marianne Bronner-Fraser, a biologist at California Institute of Technology in Pasadena and current president of the Society for Developmental Biology based in Bethesda, Maryland. On the other hand, barriers to working with these organisms are less than they were, thanks to rapid, cheap genome sequencing and advances in other techniques for genetic manipulation. “The demarcation of what makes a good model is beginning to be blurred,” says Craig Albertson from Syracuse University in New York who studies craniofacial development in African cichlids and, with Postlethwait, has begun work on icefish. As the field of evolutionary development or ‘evo-devo’ continues

“You end up having to start from square one.”

— Marianne Bronner-Fraser

to captivate biologists, ever stranger critters may find themselves the subject of attention.

Icefish and their ilk are what Albertson and his colleagues call an “evolutionary mutant model” — one in which evolutionary processes have produced characteristics that imitate human disease¹ (see ‘The making of a model’, overleaf). Researchers can compare the genomes of closely related populations or species to find out how they changed as their bones demineralized, their eyesight deteriorated or another peculiarity arose. By doing so they may reveal the genes or genetic elements that are involved in parallel human processes, such as osteoporosis, blindness or even obesity. Russell Turner, who directs the bone-research laboratory at Oregon State University in Corvallis, says that “evolutionary mutant models have enormous potential”. But, he adds, this kind of work is “going to tell us more about how we got to where we are than help us find something that we can make use of for therapy, at least over the short run”.

For osteoporosis, the gold standard preclinical model is an ovariectomized rat, which has mammalian physiology and bone loss analogous to that of postmenopausal women. But although the rat is very useful, the story of how it got to be that way is not. The icefish, on the other hand, has a tale to tell. As competitors in the freezing Antarctic waters disappeared millions of years ago, some icefish began to explore niches above the sea floor, something for which they needed buoyancy. They had long ago lost their swim bladders, the air sacs that perform this function in many fish — and structures rarely re-evolve. Instead, their dense skeletons began to demineralize and soften, even to the point that one can see the outlines of their brains through their translucent skulls. Thus, several species of icefish, in addition to living happily with extreme anaemia, have essentially acquired adaptive osteoporosis.

Cold introductions

Postlethwait was introduced to icefish during a talk in 2004 by William Detrich, a marine biologist at Northeastern University in Boston, Massachusetts. Detrich studies their unusual blood development in part to understand human blood diseases such as anaemia. He has been collecting icefish for more than 25 years now, and has fished out a bevy of genes necessary for red-blood-cell development.

When the two met again in February 2007, at the 2nd Strategic Conference of Zebrafish Investigators in Asilomar, California, they, Albertson and Pamela Yelick, who studies tooth development at Tufts University in Boston, laid out a plan to investigate the underlying cause of bone loss in icefish. It would be a physical as well as an intellectual challenge: they would have to acquire their specimens during Antarctica’s winter when the fish are gravid. But the team suspected that the naturally occurring mutations that have led to adaptive bone loss over the past 34 million years, could teach them something important

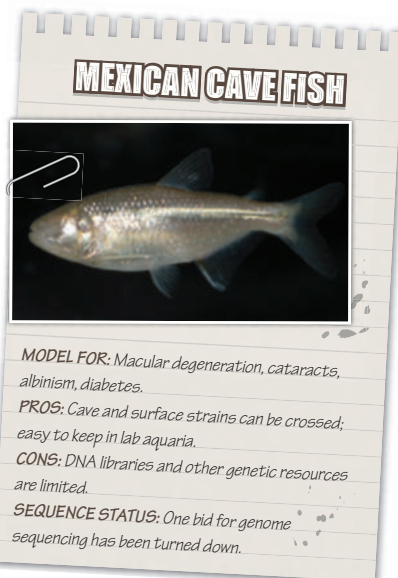


Blind cave fish, top, can be bred with sighted surface fish to explore forms of blindness.

about osteopenia and osteoporosis. Their US\$2.48-million proposal to the National Institute on Aging was accepted on the first try. John Williams, the programme officer on the grant, says that there has been ongoing discussion about bringing new models into the field of ageing, and this seemed to fit the bill. “Postlethwait’s work gets neatly into that and with a very well designed study,” he says.

Postlethwait and the other investigators reason that human and icefish bone loss may have evolved in similar ways. Although strong teeth and bones are necessary early in human life, the pressure to maintain these amenities wanes in later years. For the icefish expanding into niches above the sea bed, the need for strong, heavy bones also lessened. Thus conserved programs involved in bone formation and maintenance may shut off through similar mechanisms, but earlier in the development of the fish than in humans. “You can use these slow evolutionary changes to study changes that might occur in a human in a lifetime,” says Yelick.

The collaborators have begun by comparing patterns of gene expression between developing icefish embryos and those of a closely related but dense-boned notothenioid species. They have already found delays in the expression of genes involved in bone mineralization. Postlethwait suspects that further work will uncover mutations that regulate the timing at which these bone genes act. As many of the genes are crucial for development, he says “you can’t destroy the gene. But you can destroy the regulatory elements that cause a gene to be expressed in a specific tissue at a specific time.” If they do identify potentially important genetic elements, the group will turn to model organisms that are easier to work with to test their function by amplifying or knocking them out. Three-spined sticklebacks (*Gasterosteus aculeatus*), for example, are closely related to the icefish but they have a fully sequenced genome and tools available for genetic tinkering. Alas, recent research has suggested that regulatory




sequences are less likely than the genes they control to be conserved across evolutionary time, potentially challenging the researchers' ability to translate the results to humans. "We need to do the work to see," says Postlethwait, "with the constant honest realization that an icefish does not ride a bicycle."

Neither does the blind Mexican cave fish (*Astyanax mexicanus*) — but that hasn't stopped a small group of researchers from looking at them for hints about human conditions. These cave fish, deprived for more than a million years of light and the trophic abundances it brings, have evolved a slew of 'troglomorphic' traits: they are pale, eyeless and have a keen sense of smell and a slow, efficient metabolism. The 29 populations in limestone caves scattered around Mexico can interbreed both with each other and with sighted *Astyanax* populations from the surface. This sets up opportunities to understand the nature of the cave fish's peculiar qualities because researchers can cross together different cave and surface fish in order to track down the genes inherited alongside its oddities.

Sight to the blind

Last year, Richard Borowsky, a biologist at New York University, and his collaborators showed that breeding together blind cave fish from two different populations can produce a brood in which about 40% of offspring can see². The results suggest that the parental fish have lost their eyesight through mutations in different developmental pathways, and that two sets of incomplete eye-making instructions can, when combined, make up enough of a readable manual to build a working eye. William Jeffery, an *Astyanax* researcher at the University of Maryland in College Park, says that cave fish may help provide clues about human forms of blindness such as macular degeneration and cataracts. "The cave-fish lens is one of the first things to decay in the embryo, leading to the

ANTARCTIC ICEFISH



MODEL FOR: Anaemias, blood disorders, osteoporosis, lipid storage disorders.
PROS: Many comparable species with wide phenotypic variability.
CONS: Must be kept at Antarctic temperatures.
SEQUENCE STATUS: Nothing yet. Researchers want to sequence the blackfin icefish and a related species.


loss of the eye," says Jeffery. One of the genes implicated is *αA crystallin*, a factor in the lens that prevents apoptosis. It has limited expression during cave-fish development and causes cataracts when mutated in zebrafish³.

Why cave fish lost their eyesight isn't clear. Some have hypothesized that the energetic cost of eye development and maintenance is so high that selection pressure in the dark environment quickly acts against it. Alternatively, eye loss could simply have arisen through neutral changes in each population that became fixed by genetic drift. Or it could be an inadvertent result of another adaptive change. Still, several populations have converged on this phenotype. Contrast that to albinism, which has happened in almost the same way in various cave-fish population, via a mutation to the *OCA2* gene⁴. This gene makes a protein crucial to development of pigmented 'melanocytes' and happens to be the most commonly mutated gene in human albinism. "It may be simply that this gene is a frequent target of mutation in all organisms," Jeffery says.

In addition to living without light, cave fish have evolved to live without much of the bounty that sunlight produces, extracting nutrients from waterborne organisms that slip

TURTLES

MODEL FOR: Rare connective-tissue disorder fibrodysplasia ossificans progressiva.
PROS: Unusual developmental program in which soft tissues turn to bone.
CONS: Opaque eggs make development difficult to visualize.
SEQUENCE STATUS: Nothing yet.



through the cracks into their limestone caves, or living off the organic matter deposited by overhead bats. Both Borowsky and Jeffery have been studying how the cave-fish metabolism has adapted to the extremely low nutrient level. As it turns out, says Jeffery, they're fatter and more resistant to starvation than their surface-dwelling populations, and Jeffery thinks there could be some parallels to humans. "We're trying to study it genetically. It would seem that this could be a very good model for obesity," Jeffery says. According to some theories, humans are also evolutionarily adapted to survival with little nutrition and this could explain why they easily become obese when food is abundant. Borowsky says his studies, which include an effort to build gene maps for various blind fish populations, have uncovered a variant for the growth hormone GH1 and he is currently sequencing the gene in more populations. Borowsky says of his cave-fish research. "It's certainly not going to cure blindness tomorrow or diabetes, but it's really relevant." Although Borowsky and other cave-fish researchers have attempted to drum up the interest of a high powered sequencing laboratory to sequence *Astyanax* populations, they've so far been unsuccessful.

Arkhat Abzhanov, at Harvard University's department of organismic and evolutionary biology, is another researcher whose move to obscure models has forced him to build his own genetic resources. Abzhanov had worked with fruit-flies and chickens in his studies of *HOX* genes, which are involved in establishing the animal body plan. But to understand how these genes work in an evolutionary context, he turned to Darwin's finches. The vast phenotypic diversity of the Galapagos finch populations that Charles Darwin marvelled at includes a variety of beak shapes that seem



Swordtails reproducibly develop melanoma in hybrid crosses.

W. DETRICH

R. NUSSBAUMER/NATUREPL.COM

J. BURTON/NATUREPL.COM

The making of a model

Some features can make an outlandish organism more suitable as a model for human disease:

Rapid evolution

Organisms that have undergone rapid adaptive radiation are likely to have a lot of related species that researchers can cross together to find the genes responsible for unusual traits.

Many differences

A wide divergence of physical characteristics

(phenotypes) offers greater opportunity to study 'quantitative traits', characteristics that vary in degree. For example, if every species has a different number of stripes, it will be easier to discern the genetic controls for stripe number.

A history

Organisms with a well understood evolutionary backstory will more easily offer clues as to how traits developed over time.

Convergence

Different species or populations in which the same trait — such as blindness — has evolved independently essentially count as replicates of the original natural experiment.

A good pedigree

Rapid development to sexual maturity, small adult size, easy availability and the ability to alter and track genes, all make organisms better for experimentation. **B.M.**

custom built for the food source where a given finch lives: thick heavy bills for cracking seeds, or more elongate bills for probing cactus fruit.

By building microarrays for the different species of finch and comparing their gene expression, Abzhanov has been able to get a picture of the genes that are differently regulated in their embryos. He found, for instance, that higher expression of calmodulin, a protein that mediates calcium signalling, is associated with longer beaks. He went back to chickens and used established experimental methods to boost calmodulin signalling in the beaks of embryos. The manipulated chickens recapitulated the finches' elongated beaks⁵.

Better safe than sorry?

Abzhanov is also working with African seedcrackers, *Pyrenestes ostrinus*, another bird with an assortment of beak shapes. He is currently applying to the National Institute of Dental and Craniofacial Research in Bethesda, Maryland, for a grant to explore whether comparisons of these birds can identify genes and regulatory pathways that sometimes go awry in human craniofacial development, resulting in conditions such as cleft palate. "They're interested because this is a story of naturally occurring variants which genetically change the integration of craniofacial components," says a hopeful Abzhanov.

Not everyone finds funding agencies receptive though. Bronner-Fraser says that some of her best postdocs are interested in alternative models, but "a lot of times they come and realize that it might be difficult to get jobs and money and they might branch out to more traditional models".

Working with alternative models also requires passion and patience. Abzhanov

can't order the animals he needs online. He must go on lengthy field trips to the Galapagos Islands, taking great care not to disrupt their breeding and placing mock eggs for every egg he takes from a nest. Postlethwait and Detrich arguably had it harder, spending weeks in Antarctica in the middle of its sunless winter, trawling for notothenioids. Postlethwait was able to bring back developing embryos, but he found that maintaining the fish in captivity is extremely difficult. "You can have a freezer at minus 20 and you can have a fridge at plus 4. But the temperatures in between, especially temps at around 0 are very hard to maintain," Postlethwait says. Many of the embryos hatched after about six or seven months, he says, when they should take nine.

For many researchers, the adventure is part of the attraction. "I think that the people who work on the non-traditional models are often people who want to get out of the lab and into the real world," says developmental biologist Scott Gilbert at Swarthmore College, Pennsylvania. Gilbert, who works on shell development in red-eared terrapins, says they're a "horrible system to use if one wants reproducibility or to have research material at any given day". But he persists because turtles naturally turn soft tissues into bone and so hold broader lessons for these types of transition from one cell type to another.

Gilbert says he is taking cues from human biology to inform his studies on turtle development.

Research on fibrodysplasia ossificans progressiva (FOP) — a rare and devastating human genetic disorder in which normal muscle tissue turns into bone — has revealed some of the key proteins involved in the turtle shell development program that he studies. Frederick Kaplan, an orthopaedic surgeon at the University of Pennsylvania, Philadelphia, had discovered mutations in patients with FOP affecting the expression of bone morphogenetic protein. Similar programs seem to direct extension of bony plates from turtle ribs in forming the shell. "I think we're benefiting in a way from his work more than he is from ours," says Gilbert.

When it comes to the Antarctic icefish, it is unclear who, if anyone, will benefit: the researchers trying to lift them out of frozen obscurity, or the people with osteoporosis who could share some part of their biology with these fish.

For Yelick though, who has worked with mouse, zebrafish and human cells prior to her work on icefish, expanding the menagerie is invigorating. "Getting these interactions between evolutionary biologists, molecular biologists, stem-cell biologists and tissue engineers, it's just a really exciting time to be working in this field."

Brendan Maher is Nature's Research Highlights editor.

1. Albertson, R. C., Cresko, W., Detrich, H. W. & Postlethwait, J. H. *Trends Genet.* **25**, 74–81 (2008).
2. Borowsky, R. *Curr. Biol.* **18**, R23–R24 (2008).
3. Goishi, K. et al. *Development* **133**, 2585–2593 (2006).
4. Protas, M. E. et al. *Nature Genet.* **38**, 107–111 (2006).
5. Abzhanov, A. et al. *Nature* **442**, 563–567 (2006).

DARWIN'S FINCHES

MODEL FOR: Craniofacial development disorders.

PROS: Literature on ecology, adaptation, beak morphology and function.

CONS: Cannot be taken from the Galapagos Islands.

SEQUENCE STATUS: Consortium of researchers has convinced the pharmaceutical firm Roche to sequence several species as a 'birthday present' to Darwin.



SWORDTAILS

MODEL FOR: Melanoma

PROS: Simple aquarium fish with genetic maps and cell lines.

CONS: No transgenic technologies.

SEQUENCE STATUS: Sequencing under way.





Feast and famine

While researchers in Greece starve for government support, biomedicine is thriving at a lavish new centre in Athens, finds **Alison Abbott**.

Athens' newest research institute, the Bioacademy, is a grandiose structure of exquisite marble and sandstone that blends modern and classical styles. Its colonnaded wings enclose a triangular courtyard, which features a shimmering pool that mirrors the activity of the 400 scientists within. Athena, goddess of wisdom, would probably feel as much at home here today as she did in the nearby Parthenon, built to honour her in the fifth century BC.

Elsewhere in Greece, though, Athena might feel a little lost. The country has one of the lowest levels of national research funding in the European Union (EU) and the government has not held a competition for grants in five years.

That contrast makes the Bioacademy (pictured) all the more remarkable. Established by the Biomedical Research Foundation of the Academy of Athens, the Bioacademy opened for business in 2004, and has already recruited 50 group leaders and around 350 postdocs and doctoral students. Together, they have published more than 100 papers in strong journals. The Bioacademy coordinates two major EU biology infrastructure projects and has brought in more than €16 million (US\$21 mil-

lion) in competitive grant money, mostly from international sources. When a planned new wing is completed, it will be one of the largest centres for translational medicine in Europe.

The entire credit for the Bioacademy's existence is attributed to one man: Gregorios Skalkelas, an 82-year-old surgeon who founded the first organ-transplant centre in Greece. Through political skill and force of personality, he made the €40-million building a reality. The Bioacademy's rapid scientific success, says Achilleas Mitsos, former head of the European Commission's research directorate, illustrates "the contradictions in the Greek scientific landscape, where the level of science is generally low but you'll find extraordinary pockets of excellence everywhere".

Greece is a relatively poor country where science is not a priority. In 2002, when the EU voiced its intention to raise its average research spending to 3% of its gross domestic product (GDP) within a decade, Greece was the lowest spender on research of the then 15 member states. It is the only one of those states to have actually reduced investment since that time — from 0.64% of GDP then to 0.57% in 2006. Many of the 12 states that have since joined the EU,

mostly from the poor eastern bloc, spend much more. The Czech Republic, for example, devotes 1.54% of its GDP to science (see chart).

As a result, Greek researchers depend on EU funding more than scientists elsewhere do. Without a national research council that gives out grants, small pots of money for competitive research tended to pop out of various ministries at irregular intervals, but now even these opportunities seem to have dried up.

Budget woes

Scientists get by mostly on grants from the EU's Framework research programmes, in which Greek investigators do exceptionally well. Until 2006, Greece received the highest proportion of Framework money per researcher than any other EU country. Now it is second to Slovenia. Its relegation could be because Greece does less well in the large integrated projects that the Framework programmes now favour. "Or it may be in part because of the running down of science in Greece," says George Thireos, who until last month headed another of Greece's top research institutions — the Institute of Molecular Biology & Biotechnology (IMBB) in Heraklion, Crete.

T. STAVRAKIS/AP

EU dependence doesn't come for free — national governments are expected to match what the EU provides through its Framework and structural funds. But the Greek government says it will be able to give at most a 14% top-up this year, leaving institutes in the middle of multi-year projects with scorching debts. For example, the IMBB recently won EU money to develop a €1-million proteomics suite. The grant covered three-fifths of the costs, but then, halfway through the acquisition, the government contribution shrank. "I don't know where we are going to find the money," says Thireos. "This is a very serious problem for Greek scientists."

Thireos is now transferring to the Bioacademy — which has proved an irresistible magnet for many — to head up a new systems-biology centre. He says that Skalkeas "has realized a true vision — the Bioacademy will allow Greece to attract back good scientists working abroad". The Bioacademy has already lured back many researchers, including two from Columbia University in New York — molecular biologist Dimitris Thanos, who heads the centre of basic research, and Argiris Efstratiadis who will direct a planned cancer centre.

A man of uncommon political influence, Skalkeas has always thought big. He ventured into experimental and translational medicine decades before it became fashionable. In the 1960s, he set up a laboratory for experimental surgery at the University of Athens, which has since trained more than 200 research students. "But even back then I thought that if one day I ever had the opportunity, I'd like to do something bigger for medical science," he says.

That opportunity came with his election to the prestigious Academy of Athens in 1989. Within two years he had created the Biomedical Research Foundation under the academy's umbrella, and set about lobbying politicians to cough up money for it in order to build an internationally competitive medical research centre — the Bioacademy. "I'm old and honest, and I have an ability to persuade," says Skalkeas. And his regal charm — he is one of those gentlemen who will kiss, rather than shake, the hands of ladies — no doubt also helped his quest to draw blood from what seemed to be stone.

Lots of blood, in fact. The Bioacademy's 25,000-square-metre main building has state-of-the-art equipment, for applications ranging from brain imaging to simulation surgery. It is not only well appointed but also, many would argue, a model of how a modern research institution should be run. In a country where most scientists are hired as civil servants with jobs for life, only 14 of its 50 principal investigators are tenured. The rest are on tenure-track contracts.

Next year, construction will begin on a

20,000-square-metre additional wing for the Bioacademy, which will house a further 300 scientists and cost another €25 million in government funds. When completed, the Bioacademy will be Greece's biggest-ever injection of research money.

Is the Bioacademy, with its €14-million annual running costs, sustainable in such a research-parched general environment? Many believe so. Its unusual status as a part of the powerful Academy of Athens gives it considerable political protection. The national economy, though, is now falling through the floor.

Pockets of success

The Bioacademy has something in common with the relatively few other success stories in Greek science, says Fotis Kafatos, a molecular biologist from Imperial College London who heads the European Research Council. "There are a few institutes that have done well because they were established by strong people."

But those few pockets of success in Greek science do not have a multiplier effect, says Mitsos, who is now an economics professor at the University of the Aegean. Apart from some very local connections, centres such as the Bioacademy and the IMBB are isolated from most universities and do not catalyse excellence within them. "The problems start at the top," he says. "No government has ever had any real interest in research — there are no institutions like a research council, and no serious science planning."

Four years ago, the conservative government

of Kostas Karamanlis launched an attempt to create an efficient national science system. What particularly excited scientists was the government's intention to establish an agency like the US National Science Foundation, which would be able — finally — to offer competitive grants on a regular basis.

Filippos Tsalidis, head of the development ministry office for research and technology, consulted extensively with the academic community, and a law was passed last year. But the legislation turned out to be unworkable. It required a large number of administrative actions in a short time — something the government was not able to deliver. Tsalidis has unofficially told the directors of research institutes that the law needed some rewriting and that he had formed a committee to suggest changes. "Amateurish," says

Mitsos scornfully. The scientific community is bewildered and disappointed. "We are in the dark," says George Kollias, director of the Alexander Fleming Biomedical Sciences Research Center in Athens. Tsalidis declined to comment to *Nature*.

A few positive things have happened in Greek research policy of late, though. In 1995, the government's office of science and technology started to evaluate its research institutes every five years, using foreign reviewers. Since 2000, these evaluations have been linked to distribution of EU structural funds for research. And in 2005, the government passed a law requiring that universities be similarly evaluated. Although professors and students have put up enormous resistance, the evaluations began last year. Also, Greece joined the European Space Agency (ESA) in 2005. Although the nation's small community of astronomers and astrophysicists is still finding its feet among the big players in European space science, ESA membership has raised their aspirations.

Greece processes plenty of PhD students — more than 21,000 were registered in 2006–07 — but many go abroad when they graduate and then find it hard to justify coming back. The Bioacademy will help to stop that leakage of talent. But scientists in Greece say that the government must also create a systematic, balanced and appropriately funded national plan for science so that fewer researchers will be lost. They know that Athena would be happy to see the spirit of the great ancient Greek civilization rekindled.

Alison Abbott is Nature's senior European correspondent.



Gregorios Skalkeas created a bioacademy in Athens.



SOURCE: EUROPEAN COMMISSION

CORRESPONDENCE

The letters below respond to the Essay 'We cannot live by scepticism alone'
by Harry Collins (*Nature* **458**, 30–31; 2009).

Let's not reignite an unproductive controversy

SIR — Far from being dominated by scepticism about science, as Harry Collins claims, mainstream philosophy of science opposes the relativism that Collins decries. We are both philosophers of biology, a field that analyses key biological concepts such as species and genes, dissects theoretical debates in biology and examines emerging fields such as systems biology. This work often involves criticism of scientific positions. But if any of it is part of Collins's sceptical 'second wave' of science studies, Richard Dawkins is a bishop.

Collins dismisses philosophy of science as a 'first wave of science studies' largely coinciding with post-war confidence in science and superseded by the work of sociologists of knowledge like himself. In fact, mainstream philosophy of science — which was being developed before the Second World War by Rudolph Carnap, Carl Hempel, Karl Popper, Hans Reichenbach and others — remains a thriving discipline in most universities. It teaches students that science is neither the 'voice of a God' nor merely the view of one social group, just as Collins advocates.

The only contemporary 'philosopher' Collins mentions (though not by name) is Steve Fuller, whose statement to a US court that intelligent design is science Collins uses as evidence that post-modern scepticism pervades science studies. However, Fuller is a professor of sociology. All the philosophers of science who, like Fuller, were witnesses or advisers in the Dover Area School District case (see *Nature* **439**, 6–7; 2006) appeared for the other side, supporting evolution.

Working in an interdisciplinary

research centre alongside historians and sociologists of biology and medicine, we can assure Collins that post-modern science sceptics are thin on the ground. The 'science wars' of the 1990s were whipped up by a selective focus on the work of a very few scholars, many of whom did not work in the philosophy, history or sociology of science. Let us hope that Collins's remarks do not reignite this unproductive controversy.

John Dupré Economic and Social Research Council Centre for Genomics in Society (Egenis), University of Exeter, Byrne House, St German's Road, Exeter EX4 4PJ, UK
e-mail: j.a.dupre@exeter.ac.uk

Paul E. Griffiths Sydney Centre for the Foundations of Science, A14 University of Sydney, NSW 2006, Australia, and Egenis

What does applying 'scientific values' mean in reality?

SIR — Harry Collins calls for scientists to become 'moral leaders' and says that the 'values of science' can help us run our social and political lives. However, the argument raises at least two questions.

First, what does applying 'scientific values' mean in the real world, beyond observation, theorization, experimentation and 'open debate among those with experience'? If scientific values recognize plurality of perspective, freedom of expression and political negotiation beyond the alliances of the powerful, they would fit with the values of a liberal democracy. But the banner of 'scientific values' could equally be raised by an authoritarian technocracy, in which tacit and indigenous knowledge is marginalized. For example, some powerful people say that

authoritarianism is what we need to tackle climate change.

Second, Collins recognizes that science is fallible and its findings 'do not lead straight to political conclusions'. So where does such uncertainty leave policy-making? How do Collins's scientific values help us in tackling difficult issues such as climate change or genetically modified crops?

Classifying different types of expertise is a worthy start, but we are still left with two further problems. First, who decides what expertise is legitimate in different situations? Second, how do we translate such expertise into action? In the rough and tumble of political processes, there is frequently no clear judge. Custom and power relationships usually decide whose expertise is heard. Without a theoretically based and politically supported manifesto to address these problems, a call for scientific values to 'run our lives' risks giving too much power to certain forms of knowledge.

Mike Hulme, John Turnpenny School of Environmental Sciences, University of East Anglia, Norwich NR4 7TJ, UK
e-mail: m.hulme@uea.ac.uk

Dialogue between the disciplines is thriving

SIR — As an interdisciplinary group of scholars, committed to the social studies of science and engaged in a series of productive dialogues with colleagues in the life sciences, we were taken aback to be branded as "overly cynical" towards science by Harry Collins.

Contrary to Collins's view, hardly anyone in science studies rejects the values of science and expertise. We find it striking that he does not provide a single specific example of the scepticism he is talking about.

Collins does not adequately

credit the fruitful cooperation between scientists and social scientists that is a long-established reality in many universities and networks worldwide. (Last year's joint EU-US Science and Technology Studies conference in Rotterdam, the Netherlands, called 'Acting with Science, Technology and Medicine', is one example.)

In this sense, talk of a "third wave" that will be "resisted" by "post-modernists" is surprising. This is not how most sociologists think about the natural sciences: the field is already filled with scholars who are engaging scientists in conversation, collaboration and — yes — mutual critique, without resorting to the cliché version of post-modernism depicted by Collins. With backgrounds ranging from sociology to molecular biology, all of those signing this letter are committed to continuing and developing this dialogue.

Giovanni Franzetto on behalf of 16 co-authors* BIOS, London School of Economics, Houghton Street London WC2A 2AE, UK
e-mail: g.frazzetto@lse.ac.uk

*See supplementary information for full author list

Widen the channels of communication with society

SIR — After two abortive attempts, are social scientists finally beginning to get a grip on the meaning and value of science? Harry Collins says yes. But although he correctly identifies the need for science to take its proper place in informing good government, he seems to do so in spite of his misapprehensions about scientists and the scientific enterprise. In an Essay loaded with sweeping statements and

“Someone asked why beans cause flatulence, and I thought it would be fun to find out.” Harold McGee, page 707

cherry-picked data, he presents a caricature of science that I do not recognize.

Why do social scientists find science so difficult to fathom? In my experience, most working scientists have a much better appreciation of the power — and the limitations — of the scientific method than Collins is prepared to allow. Most have a robust understanding of Karl Popper’s idea of falsification, of the impact of experimental error and the need for reproducibility in generating convincing evidence for a new hypothesis. Crucially, most would never assume that their findings represent an impregnable truth, or anything other than a work in progress.

Where I might agree with Collins is that science still struggles to make its authentic voice heard on many important issues that affect society. In part, that is because some of these issues, such as climate change, are complex and attract the attention of powerful vested interests. But it is not clear what social scientists aim to contribute to solving this problem.

What is needed is a broader channel of communication between scientists and society, both directly and through the news media, so that the real nature of the scientific process and the value of its output are made more accessible to citizens and policy-makers.

This is already emerging, independently of the musings of social scientists. Much of the initiative is coming from scientists, teachers, bloggers and other science communicators, with the open-access movement providing an interesting new dimension.

Stephen Curry Blackett Laboratory, Imperial College, London SW7 2AZ, UK
e-mail: s.curry@imperial.ac.uk

Readers are welcome to comment at <http://tinyurl.com/anykw6>.



For anyone who ever said there’s no such thing as a poetic gene

SIR — Art encoded in living cells has a long and illustrious history (J. Vallverdú *Aesthetika* **2**, 2; 2006 and E. DaSilva *Electron. J. Biotechnol.* **7**, 4; 2004). For obvious reasons, the focus has been to decode naturally existing biological codes (proteins or DNA) in the context of art, instead of coding new art into a biological system.

As Christian Bök proposes in *Books & Arts* (‘Poetry in the genes’ *Nature* **458**, 35; 2009), the emergence of *de novo* gene-synthesis technology now makes the tools available to build poetry directly into coding genes.

In 2005, our organization made a gene encoding the first verse of the poem *Tomten* by Viktor Rydberg (50 words, or 800 base pairs). The verse was rewritten using the single-letter amino-acid code where O (no amino acid) was replaced by Q (glutamic acid) and spaces omitted. The protein sequence was backtranslated to DNA using the codon bias of reindeer (*Rangifer tarandus*). The gene was synthesized and cloned behind an *Escherichia coli* promoter in a pUC-derived

vector. The construct was then lyophilized on filter paper and sent out as a Christmas card (see <http://tinyurl.com/cxhy9a>). The nucleotide and protein sequence of *Tomten* is available in GenBank, accession number EU600200. To our knowledge, this is the first example of an organism that ‘recites’ poetry.

Claes Gustafsson DNA2.0 Inc., 1430 O’Brien Drive, Suite E, Menlo Park, California 94025, USA
e-mail: cgustafsson@dna20.com

Brain technologies raise unprecedented ethical challenges

SIR — We share Jens Clausen’s opinion, expressed in his Commentary ‘Man, machine and in between’ (*Nature* **457**, 1080–1081; 2009), that brain-machine interfaces promise many benefits and should be pursued. However, we do not agree that these technologies pose similar ethical challenges to those already addressed. Some consequences may be unprecedented.

Imagine if insights from the field of cortical prosthetics in human and non-human primates were combined with research on bodily self-consciousness in

humans. Signals recorded by multi-electrodes implanted in the motor cortex can already be used to control robotic arms and legs. Cognitive cortical prosthetics will allow the use of other cortical signals and regions for prosthesis control. Several research groups are investigating indications that the conscious experience of being in a body can be experimentally manipulated. The frontal and temporoparietal signals that seem to be involved encode fundamental aspects of the self, such as where humans experience themselves to be in space and which body they identify with (O. Blanke and T. Metzinger *Trends Cogn. Sci.* **13**, 7–13; 2009). If research on cortical prosthetics and on the bodily self were applied to humans using brain-controlled prosthetic devices, there might be no clear answer to Clausen’s question: which of them is responsible for involuntary acts?

It may sound like science fiction, but if human brain regions involved in bodily self-consciousness were to be monitored and manipulated online via a machine, then not only will the boundary between user and robot become unclear, but human identity may change, as such bodily signals are crucial for the self and the ‘I’ of conscious experience. Such consequences differ from those outlined by Clausen for deep brain stimulation and treatment with psychoactive drugs.

New links between cognitive neuroscience, engineering, brain-machine interfacing and medicine could lead to a generation of technologies that may not just blur the limits of human and machine, but fundamentally alter an individual’s sense of self. We should welcome the machine to the brain, but should proceed with caution, given that such an addition could change the criteria for self and identity.

Olaf Blanke, Jane E. Aspell Laboratory of Cognitive Neuroscience, Ecole Polytechnique Fédérale de Lausanne, Lausanne, Switzerland
e-mail: olaf.blanke@epfl.ch

BOOKS & ARTS



An early museum mural depicts Neanderthals as innovative and alert, unlike popular portrayals of 'apemen' at the time.

A clash of visual cultures

Nick Hopwood applauds an account of how US scientists used images to counter creationism and promote public understanding of evolution in the 1920s.

God — or Gorilla: Images of Evolution in the Jazz Age

by Constance Areson Clark

Johns Hopkins University Press: 2008.
312 pp. \$35, £23.50

Pictures, as *God — or Gorilla* reminds us, have been central to the public communication of evolutionary biology, and its enemies have prominently exploited their ambiguity. In 1925, when a Tennessee court tried John Thomas Scopes for teaching in a public school that “man has descended from a lower order of animals”, the address by prosecutor William Jennings Bryan peaked in his denunciation of a diagram. The picture, in a state-prescribed biology text, represented the relations of animal groups by circles of size corresponding to number of species: huge for insects and tiny for mammals. That “little ring” appalled Bryan, who later objected that “no circle is reserved for man alone”. “What,” he demanded to know, “shall we say of the intelligence, not to say religion, of those who ... put man with an immortal soul in the same circle with the wolf, the hyena, and the skunk?”

Historian Constance Clark helps uncover the larger processes that made the Scopes trial significant by investigating the role of

images in American scientists’ responses to the anti-evolutionism of the 1920s. The ‘jazz age’ of her title alludes to the culture wars in which traditionalists painted modernists as Bolsheviks, atheists, evolutionists — and jazz-lovers. There is little music here; the reference is to the practice of ‘jazzing up’ or enlivening science.

Clark’s theme is how ideas were condensed into symbols that were viewed in light of “the pictures in our heads”, as journalist Walter Lippmann called them, and added to our stock of images of the distant past. She engagingly explores the dissonances between changing ideas, images that were evocative but hard to control, and audiences’ divergent expectations. The book is not a detailed analysis of the practicalities of producing and reproducing pictures, or making science news. Rather, it reconstructs the attempts of influential evolutionists to get their messages across in a world of unruly images, competing voices and fragile authority.

The 1920s were riven by conflicts about the status and limits of science. Evolution was particularly awkward for biologists to defend. Although many researchers accepted that

humans and other organisms evolved, they were deeply divided about the mechanisms, and most kept their heads down. Clark focuses on the palaeontologist Henry Fairfield Osborn, president of New York’s American Museum of Natural History, which at that time received two million visitors a year. The museum’s educational mission and the media preference for established figures gave the conservative Osborn a platform for dated and increasingly controversial views. When evolution came under attack, he and a few like-minded senior scientists announced that it was compatible with their own Protestant religion, and gave “a sublime conception of God”. This theistic evolutionism repelled secular scientists and

fundamentalist Christians alike, but was often presented as the scientific consensus. Scopes’s legal team drew on a large literature reconciling science and religion. Osborn became isolated only after his distaste for simian origins led him to put so much distance between humans and apes that many saw him as selling out.

The museum led the production of textbook figures, charts, lantern slides and plaster



Palaeontologist Henry Osborn saw a place for God in evolution.

casts. Effective visuals embodied theories, even hypotheses. Clark shows how tree diagrams and image series communicated understandings of descent, but accusations of guessing pushed Osborn to pretend they illustrated unvarnished facts. He commissioned murals and book covers that ennobled cave-painting Cro-Magnon man (as pictured, left), but well-known sequences confirmed the connection to brutish apemen more strongly than he could deny. Cartoons played on images of the Scopes 'monkey trial', and people joked about missing links.

God — or Gorilla hints at a larger clash of visual cultures between modernists and fundamentalists: Neanderthals versus Adam and Eve,

church frescoes depicting ascent from protozoa against a 'picturable God'. That would be a great topic for further research, which would need to pay religious icons more attention, but this highly readable book is valuable as it stands. It is also timely. The 1920s shaped pictures of evolution, and of evolutionary debate, that are still in our heads. As biologists work with illustrators to communicate science, and creationists attack textbook icons, it is helpful to reflect on the struggles of that decisive decade. ■

Nick Hopwood is in the Department of History and Philosophy of Science, University of Cambridge, Cambridge CB2 3RH, UK. e-mail: ndh12@cam.ac.uk

Drawing from Darwin

Endless Forms: Charles Darwin, Natural Science and the Visual Arts

Yale Center for British Art, New Haven, Connecticut, USA

Until 3 May 2009

Fitzwilliam Museum, Cambridge, UK

From 16 June until 4 October 2009



Darwin200

How many geneticists today spend their free time reading about aesthetics? How many painters keep abreast of the latest developments in geology? I would wager precious

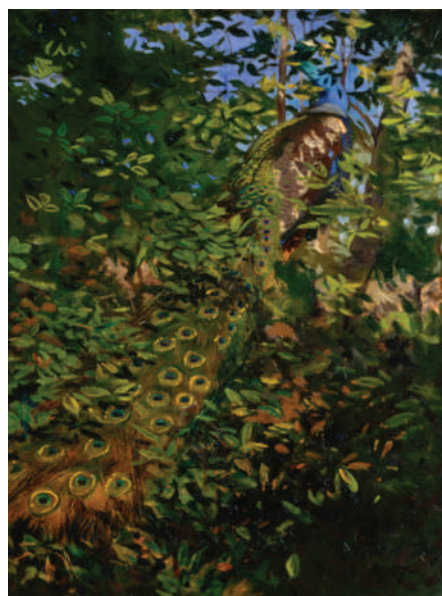
few. But things were different in the nineteenth century: artists shaped the way scientists saw nature, and thought deeply about how science changed the nature of art.

The exhibition *Endless Forms* explores Charles Darwin's influence on the artists of his day, and shows how paintings and photographs helped to shape Darwin's understanding of nature. Some 200 works are displayed in this collaboration between the Yale Center for British Art in New Haven, Connecticut, where the exhibition is located until May, and the Fitzwilliam Museum in Cambridge, UK, where it moves in June.

The exhibit does a good job of showing how differently people saw the world at the dawn of the nineteenth century. Nature was replete with signs of divine design. A painting of Noah's flood was considered historical art. Yet Darwin was able to learn a great deal from art of this time, whether he was studying illustrations of geological formations or marvelling at the paintings of French-American naturalist John James Audubon, who Darwin met as a teenager.

As Darwin developed as a scientist, he made

some modest art of his own. On his journeys in South America, he painted the rock strata of the Andes in watercolour. On his return to the United Kingdom, he began to scribble odd little tree diagrams in his notebooks — a visual expression of his great epiphany that species are related through common descent. Darwin worked closely with artists to illustrate his books. This may surprise readers of *On the Origin of Species* — a book with a single illustration showing the branching of species. But his other books were lavishly illustrated. The exhibition includes a gorgeous fold-out picture of a fossilized sloth skull from *The Zoology of the Voyage of H.M.S. Beagle*, along with engravings of elegant orchids, birds with luxurious



Not all artists agreed with Charles Darwin's theory that peacocks use their bright tail to attract a mate.

plumage and other creatures from later books.

Darwin was at the cutting edge of visualization. His 1872 work *The Expression of the Emotions in Man and Animals* was one of the first books ever to be illustrated with photographs — including pictures of faces distorted by electric currents, produced by the work of French physician Guillaume Duchenne. *Endless Forms* includes Darwin's personal copies of these photographs, which are disturbingly rich in detail.

Darwin did not use art simply to illustrate his ideas, but to investigate them. In Duchenne's pictures he saw evidence that human expressions of surprise or fear were reflexes triggered by electrical activity, in the same way that a dog is made to snarl. He corresponded with painters of animals, recognizing their deep knowledge of expressions on non-human faces. Indeed, the very notion of beauty was something Darwin wanted to explain: the beauty of orchids actually masked a complex contrivance for getting pollen onto insects; the beauty of an Argus pheasant's feathers was the result of sexual selection.

Artists paid close attention to Darwin. They modelled faces after the ones in his illustrations. They replaced sentimental scenes of nature with bleaker portraits of the struggle for survival. The US artist Abbott Handerson Thayer used his art to explore the subtleties of animal camouflage. One of his most famous paintings, *Peacock in the Woods* (1907; pictured), is a rebuke to Darwin; Thayer refused to believe that brightly coloured feathers were a conspicuous display for attracting a mate, so he showed a peacock almost completely hidden in a dappled forest.

Endless Forms captivates the eye while getting the science right. It deserves great credit for not shying away from difficult subjects: some wrongly took it as justification to elevate whites over other races, cloaking their freak-show voyeurism in the guise of anthropology. Not all of the ties to Darwin in the exhibition are convincing. Some beautiful paintings by impressionists are included, but the links are tenuous — Paul Cézanne was friends with a Darwinian archaeologist, for example, and Claude Monet was careful about painting rock formations accurately.

The exhibition presents evidence that undermines the case for Darwin's universal influence. Even before Darwin published *On the Origin of Species* in 1859, people were seeing nature and the history of life in new ways. They were fascinated by the massive dinosaur reconstructions at London's Crystal Palace in 1854, for example. By the end of the nineteenth century, the world looked very different, but it was not Darwin alone who helped change the way we see. ■

Carl Zimmer is author of *Evolution: The Triumph of an Idea*.

e-mail: carl@carlzimmer.com

Shaking the tree of life

Perspectives in Animal Phylogeny and Evolution

by Alessandro Minelli

Oxford University Press: 2008.
336 pp. \$70, £34.95

Reading *Perspectives in Animal Phylogeny and Evolution* is like visiting a Michelin-starred restaurant where you are served an appetizer of a plate of chips, followed by a refined main course that, to your surprise, is accompanied by the chef's apologies for its distinctive flavour. You might save your appetite for the main dish by sampling the chips sparingly, or transfer them to a doggy bag for later consumption. I recommend a similar strategy for reading this book.

Alessandro Minelli's starter consists of six introductory chapters that sketch out the field of animal phylogenetics, the study of the evolutionary genealogy of animals. The material provides context for our quest to understand animal evolution, which is explored in the last three chapters. A shorter starter, however, would have left more room for the genuine insights that come later.

Minelli manages reasonably well the difficult task of capturing the ever-shifting structure of the phylogenetic froth that bubbles up continually in the literature. Aware of the short lives of many hypotheses, Minelli to his credit avoids some obvious 'Nonsensozoa' clades and limits his selection to well-supported phylogenetic groupings, such as Ecdysozoa (including arthropods and nematodes) and Lophotrochozoa (including phyla such as molluscs and segmented worms).

Although Minelli claims to discuss alternative and conflicting phylogenetic hypotheses, he lists them with few critical remarks. He includes some that are without merit, such as the Vermizoa hypothesis, in which nemertean and annelid worms were thought to belong to sister taxa because of a misunderstanding of the structure of their blood vessels. Such dead or dying bits of phylogenetic shrubbery might have been pruned. Readers would have benefited from more thorough

discussions in the light of recent molecular and morphological data.

One shouldn't judge a Michelin-star chef too harshly for his chips, however, and the main course is vintage Minelli. The final sections on the evolution of animal body plans contain many arresting insights that arise out of his distinctive evolutionary perspective and encyclopaedic knowledge of the zoological literature. Even though he introduces these chapters apologetically as expressing his "personal and sometimes idiosyncratic views", it is this that makes them so inspiring.



Even the tiniest mite can reveal clues about body patterning and evolution.

Many recent insights into animal evolution are the results of painstaking research on a handful of model organisms. Minelli emphasizes the need to integrate information about the morphology, development and evolution of less studied, non-model organisms. For example, he discusses how the study of miniaturized animals can reveal clues

"The book is a celebration of the intellectual puzzles posed by the wonderful diversity of animals."

about the body's patterning mechanisms. Comparing the symmetry of skin structures in two miniaturized chelicerates, a mite and a tiny spider, Minelli surmises that the irregular asymmetry of the spider indicates that its evolutionary origin is more recent, and that there has been insufficient time for it to evolve a regular pattern. The book is full of such brief teasers to provoke further research.

Minelli's observations have great value, irrespective of the lack of a consensus phylogeny of the animal kingdom. He takes a refreshingly

critical look at traditional biological concepts, such as larval stages, sexual reproduction and even development. Although developmental processes can be seen as intermediary steps on the way to an adult organism, this realization does not necessarily help us to understand their evolutionary origin. Instead, he urges us to consider developmental processes and steps as the outcome of a competitive process of developmental modules, such as cells. In this way, he attempts to understand the origin of novelties such as gametes, programmed cell death and larval set-aside cells from which an adult organism develops.

Not all of Minelli's ideas will be embraced. His antipathy to thinking about organisms in terms of hierarchical organization seems, in part, to be the result of his viewing hierarchies as rigid and immutable structures rather than as useful descriptions. Nevertheless, his perspectives are worth pondering.

Minelli also scrutinizes relationships between concepts that are traditionally placed in separate categories, such as sexual reproduction resulting in embryogenesis, asexual development and regeneration. He convincingly argues that it takes more than mapping these features onto a phylogeny to understand their evolution: we should also take into account past selection pressures and environmental conditions that prevailed during their origin. Moreover, we should consider biological processes that may indicate a closer relationship between features that seem to be phylogenetically distinct, such as sexual and asexual reproduction. This integrative approach aims to produce synthetic evolutionary scenarios.

The book does not merely list facts about animal evolution. It is a celebration of the intellectual puzzles posed by the wonderful diversity of animals, an effective spur for further exploration and debate of the mysterious but unmistakable signs of unity hidden beneath this diversity. No serious student of animal evolution can afford to miss this book. Minelli gives it a distinctive flavour eminently suited to repeated sampling, with or without a glass of wine at hand. ■

Ronald Jenner is a researcher in the Department of Zoology, Natural History Museum, Cromwell Road, London SW7 5BD, UK.
e-mail: r.jenner@nhm.ac.uk

S. GSCHMEISSNER/SPL

Q&A: The molecular master chef

Twenty-five years ago this week, food writer **Harold McGee** published a *Nature* paper on the science of whipping egg whites in copper bowls. Here he explains how he first developed an interest in science and cooking.

Why were you drawn to the science of cooking?

As an undergraduate I went to the California Institute of Technology planning to study astronomy, but I ended up doing literature. When it proved difficult to get a tenure-track position, I thought of recouping my interest in science by writing about it. Around this time, Stephen Hawking was writing about black holes and Lewis Thomas about medicine — no one was covering the science of everyday life. Several of my friends were getting together at weekends to cook, so that subject suggested itself. Someone asked me why beans cause flatulence, and I thought it would be fun to find out.

What sparked your 1984 paper in *Nature*?

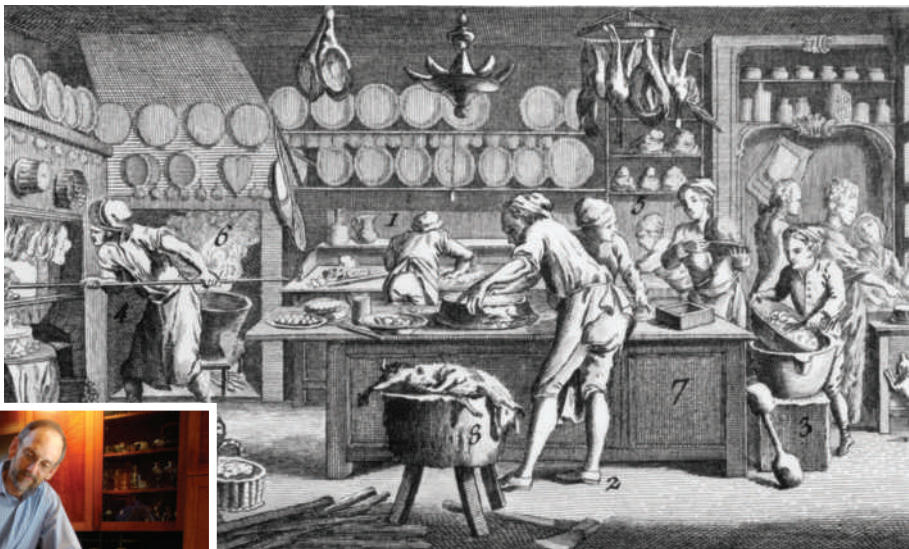
I was looking for illustrations for my book *On Food and Cooking* and found a picture of a pastry kitchen in an eighteenth-century French encyclopaedia, in which a boy was using a copper bowl to whip egg whites. I thought that if that idea had been around for centuries I should look at it. My wife had just started teaching at Stanford University in California, and her colleague at the Carnegie Institution near Stanford had a spectrophotometer, so we decided to experiment. We found a link between how the functional behaviour of egg whites changes when a protein in the egg whites, ovotransferrin, absorbs copper from the surface of the bowl (see *Nature* 308, 667–668; 1984).

How did the editors respond to it?

They were generally positive and showed no signs that there was anything out of the ordinary. I remember someone said the science looked sound although the subject was fluffy.

What inspired you to write *On Food and Cooking*?

There was a vast body of information about the science of food and food manufacturing, but not much application of it to cooking. So I waded into that literature to translate



The techniques of eighteenth-century French chefs inspired Harold McGee (left) to study why copper bowls are best for beating egg whites.



it for the average cook. My initial thought was to write a question-

and-answer book, focusing on the practical side of cooking. Before I'd even finished a chapter I was approached by a publisher. I told him about the myth that searing meat seals in the juices, and he said: "That is as interesting as how to cook or not cook a piece of meat." That changed my perspective, and I tried to write a portrait of the various ingredients.

At the time I was writing for the reader who enjoys eating and some cooking, and I thought the cookery profession didn't need a basic book like this. But I was disabused of that idea when the book came out. Students at culinary institutions told me they asked their teachers, "Why do it this way?" and the teachers replied, "Don't ask questions, this is the way it's done, just do it." I think there has been a huge change within the profession — chefs are now much more interested in innovation.

What are you working on now?

I'm just finishing the book I intended to write in the first place: a practical book that's going to be short; a kitchen manual. Then I have a longer-term project about taste and smell and flavour, subjects I've been interested

in since the 1970s. Back then, no one really understood how those sensations developed, either the molecules in food responsible or the human mechanisms for detecting them and processing the information.

And what do you like to cook?

My mother is part east Indian, so when I was growing up in Chicago we had curries. You could smell it streets away when I was walking home from school with my friends. They thought the smell was appalling but those same smells made my stomach rumble. I love the long, slow process of putting together all those spices, onions, fresh ginger and garlic and so on into a really complex sauce. It turns out that Mexican food is based on many of the same principles. Those are my two favourites.

Interview by **Daniel Cressey**, a reporter for *Nature*.

Corrections

Meg Urry's book review 'Myth of the missing mothers' (*Nature* 458, 150–151; 2009) incorrectly referred to two contributors as the daughters of editor Emily Monosson. They are the daughters of Anne Douglass, a scientist at NASA's Goddard Space Flight Center in Greenbelt, Maryland.

Mark Buchanan's book review 'Bringing clarity to complexity' (*Nature* 458, 411; 2009) incorrectly referred to "the late Jim Crutchfield", who is still very much alive.

Our sincere apologies to all concerned.

DRUG DISCOVERY

Fresh target for cancer therapy

Raymond J. Deshaies

The Byzantine system for degrading proteins inside cells is already the target of a successful anticancer drug. A compound that inhibits another part of this system also shows promise in models of cancer in mice.

Drug discovery is hard. Even harder is drug discovery aimed at biological systems that haven't previously been tested as therapeutic targets. The extraordinary challenge is brought home with sobering clarity by numbers: in 2008, only one new compound was approved by the US Food and Drug Administration (FDA) for treating cancer. In the same year, the US pharmaceutical industry alone spent about \$65 billion in the pursuit of new medicines¹, much of which went towards anticancer research — so the apparently slow progress in discovering new cancer medicines is certainly not due to lack of investment.

The identification of proteins that are 'druggable', and of molecules that inhibit them, are therefore unusual events that generate considerable excitement. On page 732 of this issue, Soucy *et al.*² report just such a finding. They have discovered a compound that inhibits the never-before-targeted NEDD8-activating enzyme (NAE), and show that this compound suppresses the growth of human lung-tumour tissue transplanted into mice.

In the early 1980s, it was found that protein degradation in cells involves a mechanism by which the small protein ubiquitin becomes covalently attached to the target protein, thereby generating a signal that is recognized by a large, protein-degrading enzyme complex called the proteasome³. The attachment process is mediated by a cascade of enzymes. Ubiquitin-activating enzyme (E1) primes ubiquitin for attachment to the protein target by adding an AMP molecule to ubiquitin's carboxy terminus. The activated ubiquitin is transferred to a ubiquitin-conjugating enzyme (E2) and then covalently grafted onto the target protein by a ubiquitin ligase enzyme (E3).

This curious mechanism was soon shown to control a broad range of processes, ranging from cell division to the turnover of damaged proteins. Twenty-five years on, we now know that the ubiquitin-proteasome system (UPS) is, as its name implies, a ubiquitous regulator of cell biology: in humans, the E3 family alone potentially consists of more than 650 enzymes. The extent of ubiquitin's impact on the regulation of proteins is rivalled only by the other big hitter of covalent modifications, phosphorylation.

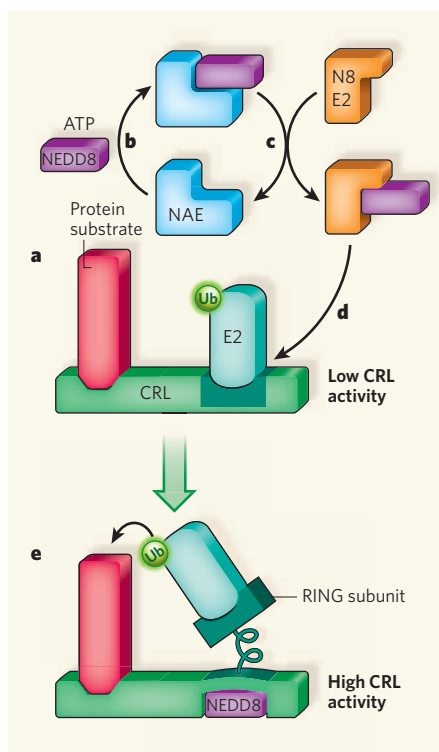


Figure 1 | Activation of CRL enzymes by the NEDD8 protein. When the ubiquitin (Ub) protein is covalently attached to other proteins, it often marks them for degradation. **a**, CRL enzymes mediate the final stage of ubiquitylation, in which Ub is transferred from an E2 enzyme to the protein substrate targeted for degradation. In the absence of NEDD8 (a ubiquitin-like protein), CRL activity is low. **b**, NEDD8 activation of CRLs begins when NEDD8 reacts with ATP and binds to the NEDD8-activating enzyme (NAE). **c, d**, NEDD8 is transferred to the NEDD8-conjugating enzyme (N8 E2), and then to the CRL. **e**, The attachment of NEDD8 to the CRL causes the CRL's RING subunit to spring up like a jack-in-the-box. This activates the CRL by bringing the Ub-E2 complex close to the target protein.

The complexity and biological importance of the UPS fuelled speculation about its potential as a target for drug discovery. Proof that it is indeed a worthy target was provided in 2003, when the FDA granted Millennium

Pharmaceuticals approval to market a proteasome inhibitor, bortezomib, to treat relapsed refractory multiple myeloma⁴ (a cancer of immune cells called plasma cells). The drug arose from pioneering research on proteasome inhibitors^{5,6} and was the first new compound approved for treating multiple myeloma since the 1970s. Bortezomib was first synthesized within just seven years of the discovery of the proteasome itself, and gained FDA approval in near-record time (about 8 years; once synthesized, most compounds take about 15 years to gain FDA approval). It thus serves as a remarkable testament to the way in which basic research can drive rapid advances in molecular medicine.

Bortezomib's target isn't very substrate-specific — it degrades all ubiquitin-tagged proteins that are destined for elimination. Such lack of substrate specificity is generally regarded as a disadvantage for drug discovery, as it can cause unwanted side effects. Despite this, bortezomib is a great success, both clinically and commercially: in 2009 it is expected to achieve worldwide sales of \$US1 billion. This impressive performance has fanned interest in the potential of drugs that target substrate-specific factors of the UPS, such as the E3 enzymes. But the details of how these enzymes work are poorly defined, and so there is great uncertainty about how to target them and whether such efforts will be rewarded by the development of a successful drug.

Soucy *et al.*² (another team from Millennium) now report a clever way around these problems. They realized that, instead of targeting E3 enzymes directly, it might be possible to inhibit other enzymes that activate them. One such enzyme is NAE, which is required to activate E3 enzymes known as cullin-RING ubiquitin ligases (CRLs)⁷. Human cells potentially express more than 350 CRLs. The cullin subunit forms a scaffold on which CRLs assemble, and is reversibly switched on and off when the ubiquitin-like protein NEDD8 is attached and removed.

As is the case for the ubiquitylation of proteins, the attachment of NEDD8 to cullins relies on the activity of a dedicated set of E1, E2 and E3 enzymes^{8,9} (Fig. 1). In the first step of

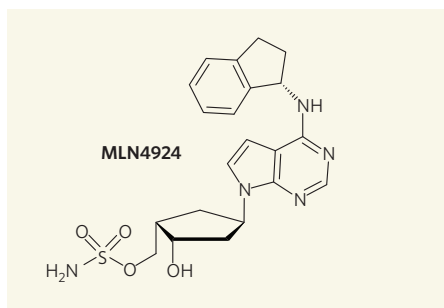


Figure 2 | Structure of an NAE inhibitor. Soucy *et al.*² have discovered MLN4924, an inhibitor of CRL activity that blocks the first step of NEDD8 activation.

'neddylation', NAE catalyses the reaction of NEDD8 with ATP (a fuel molecule). The active site of NAE that catalyses this process has been well defined by enzymological studies and X-ray crystallography¹⁰, providing invaluable information on targeting the enzyme for drug discovery. Reasoning that this active site might be a prime target for small, drug-like molecules, Soucy *et al.* carried out a high-throughput screen of a chemical library for NAE inhibitors. This identified an AMP analogue as a good starting point for a medicinal-chemistry programme, from which the authors eventually obtained MLN4924 (Fig. 2) as a highly potent and selective inhibitor of NAE.

With MLN4924 in hand, Soucy *et al.*² set out to characterize the dynamics of neddylation–deneddylation cycles and the consequences of abrupt inactivation of NAE. They found that CRLs account for a substantial fraction (about 20%) of all proteasome-dependent protein degradation. More startling was their finding that the NEDD8 cycle is extraordinarily fast — MLN4924 induces nearly complete loss of neddylated cullins within five minutes in cells grown in culture. The consequent inactivation of CRLs leads to a large build-up of CRL substrates, as well as over-replication of and damage to DNA. These results demonstrate that MLN4924 will be an awesome tool for cell-biological investigations on the functions of CRLs and their regulation by NEDD8.

Soucy *et al.* took their studies a remarkable step further by asking two key questions. Can neddylation be inhibited so as to cause accumulation of CRL substrates in human tumours that have been transplanted into mice? And if so, does this affect the growth of the tumours? They had good reason to expect such effects, because they had observed that MLN4924 induces cell suicide in proliferating cancer cells *in vitro*, possibly as a result of the deregulation of DNA synthesis. Happily, the answer to both questions is a resounding 'yes'. Most impressively, the authors report nearly complete regression of transplanted human lung-tumour tissue in MLN4924-treated mice, with no obvious side effects. It remains unclear, however, why a drug that inactivates so many different

CRLs (presumably also those in healthy cells) should kill only cancer cells.

These are exciting findings², but it is prudent to remember that many promising drug candidates have been shown to cure cancer in mice, only to fail spectacularly in humans. Although MLN4924 is sufficiently promising that Millennium is conducting clinical trials in humans, it remains to be seen whether it will become the second marketed drug that deliberately targets components of the ubiquitin system.

What is clear is that research on the UPS — and more specifically, on CRLs and the NEDD8 pathway — has led to a thorough description of neddylation, the identification of NEDD8's cullin targets, and an exploration of the effects of neddylation on the structure and function of CRLs^{11,12}, all in the short span of about 10 years. This has culminated in the discovery of an exciting drug candidate², currently in clinical trials as an anticancer therapy. And it is worth remembering that NAE genes were first uncovered in the mustard weed *Arabidopsis* in a screen for mutants resistant to the plant hormone auxin¹³. Perhaps the seeds

of the next breakthrough in cancer therapy will also sprout from some unlikely place. ■

Raymond J. Deshaies is in the Division of Biology and the Howard Hughes Medical Institute, California Institute of Technology, 1200 East California Boulevard, Pasadena, California 91125, USA.
e-mail: deshaies@its.caltech.edu

1. *The Biopharmaceutical Sector's Impact on the U.S. Economy: Analysis at the National, State, and Local Levels* www.archstoneconsulting.com/biopharmapdf/report.pdf (2009).
2. Soucy, T. A. *et al.* *Nature* **459**, 732–736 (2009).
3. Pickart, C. M. *Cell* **116**, 181–190 (2004).
4. Kane, R. C., Bross, P. F., Farrell, A. T. & Pazdur, R. *Oncologist* **8**, 508–513 (2003).
5. Rock, K. L. *et al.* *Cell* **78**, 761–771 (1994).
6. Adams, J. *et al.* *Bioorg. Med. Chem. Lett.* **8**, 333–338 (1998).
7. Petroski, M. D. & Deshaies, R. J. *Nature Rev. Mol. Cell Biol.* **6**, 9–20 (2005).
8. Lammer, D. *et al.* *Genes Dev.* **12**, 914–926 (1998).
9. Liakopoulos, D., Doenges, G., Matuschewski, K. & Jentsch, S. *EMBO J.* **17**, 2208–2214 (1998).
10. Walden, H., Podgorski, M. S. & Schulman, B. A. *Nature* **422**, 330–334 (2003).
11. Saha, A. & Deshaies, R. J. *Mol. Cell* **32**, 21–31 (2008).
12. Duda, D. M. *et al.* *Cell* **134**, 995–1006 (2008).
13. Leysner, H. M. *et al.* *Nature* **364**, 161–164 (1993).

ASTROPHYSICS

Hidden Universe uncovered

Ian Smail

An experiment flying on a balloon at the edge of the atmosphere offers the deepest far-infrared view of the sky yet achieved, revealing previously unidentified, dust-obscured, star-forming galaxies in the early Universe.

To the human eye, the night sky is a canopy of stars. With the aid of a small telescope it is possible to see our nearest Galactic neighbours, and using sensitive charge-coupled detectors and the world's largest optical telescopes we can go beyond this and peer into the farthest reaches of the Universe. However, even the most sensitive of these visible-light surveys miss much of the light emitted by galaxies over the history of the Universe. This missing light comes from the youngest stars, which are still cocooned in their natal dust clouds. Dust clouds absorb starlight and re-emit it at far-infrared wavelengths. Surveys of the sky in the far-infrared and the longer-wavelength submillimetre wavebands are thus essential if we are to obtain a complete picture of the star-formation history of galaxies, and hence to identify more precisely the epoch at which galaxies such as our own formed.

On page 737 of this issue, Devlin and colleagues¹ present results from an experiment that identifies for the first time the sources of the bulk of this far-infrared and submillimetre emission in the Universe: a population of dust-obscured, star-forming galaxies seen in the first 5 billion years after the Big Bang. The implication of these observations

is that the active growth phase of most galaxies that are seen today is well behind them — they are declining into their equivalent of middle age.

For more than a decade, astronomers have known that the birth of many of the stars that formed in young galaxies in the early Universe is hidden from direct view by dust and finally emerges at far-infrared wavelengths. Because of the subsequent expansion of the Universe, this far-infrared radiation is redshifted (its wavelength is stretched to longer wavelengths), and appears in the submillimetre waveband today. Unfortunately, Earth's atmosphere is relatively opaque to submillimetre wavelengths. Hence, to identify these young, dust-obscured galaxies, astronomers need to get their experiments above the atmosphere, either by sending them into space or by flying them at high altitude.

As its name suggests, the Balloon-borne Large-Aperture Submillimetre Telescope (BLAST) uses a high-altitude balloon to fly a telescope with a 2-metre mirror and a sensitive submillimetre detector at altitudes of up to 40 kilometres to undertake surveys of the cosmos (Fig. 1). Devlin *et al.*¹ report the results of BLAST's most recent flight, an 11-day voyage



M. HALPERN

Figure 1 | Ready to launch. The BLAST (Balloon-borne Large-Aperture Submillimeter Telescope) is prepared for lift-off from Antarctica. BLAST's observations¹ indicate that most of the far-infrared cosmic radiation comes from previously undetected galaxies that formed stars at impressive rates during the first 5 billion years after the Big Bang.

from McMurdo Station in Antarctica in late 2006. This highly successful flight provided our first representative maps of the extragalactic sky at wavelengths of 250, 350 and 500 micrometres, identifying hundreds of individual emission sources.

The sources detected by BLAST are likely to range from relatively nearby galaxies whose star formation has been enhanced by minor disturbances, such as mergers with small galaxies; through massive, gas-rich disk galaxies, which are either gravitationally disturbed by interactions with other galaxies or become inherently unstable and collapse in a burst of star formation; to the most extreme and most distant events, 'cosmic collisions'. These collisions represent the mergers of two (or more) 10^{32} -kilogram galaxies that plough into each other at relative velocities of a million kilometres per hour. The resulting impact triggers a burst of star formation that consumes all the gas in the system and that at its peak has a luminosity 1,000 times that of the Milky Way, equivalent to 10^{13} Suns. These bursts are capable of forming all the stars in our Galaxy in less than 100 million years — an instant in astronomical terms — and they are the most powerful Galactic-scale events known.

The mix of these different populations is reflected in the way the number of sources changes as a function of their brightness, or flux — the number counts — in the BLAST maps. If the population being observed was dominated by nearby low-luminosity, star-forming galaxies, the number counts would depend on flux (S) as $S^{-2.5}$, the Euclidean model. Number counts that rise more steeply at fainter fluxes than the Euclidean model predicts would mean a larger contribution from the more distant and luminous, merger-triggered starbursts —

galaxies forming stars at extremely high rates.

The number counts in the BLAST maps are steeper than the Euclidean model (see Fig. 2 on page 738), showing that most sources are likely to be distant starbursts seen at a time when the Universe was 5 billion years old. Moreover, the counts are steeper in the submillimetre than in the far-infrared waveband, demonstrating that these starbursts are an increasingly important galaxy population in the submillimetre waveband. Devlin *et al.*¹ confirm this trend by looking at how submillimetre emission from the whole population of galaxies changes with their distances from Earth.

The authors¹ show that the most distant starburst galaxies contribute an increasing fraction of the total flux detected in their maps as one moves to longer wavelengths. This conclusion is consistent with earlier ground-based observations at wavelengths around 1,000 micrometres (to which the atmosphere is transparent), where almost all of the sources detected are extremely luminous and very distant starbursts², potentially representing the formation of massive galaxies in a single burst of star formation. After their youthful phase of activity, these galaxies are expected to evolve more sedately. As seen today, their light will be dominated by older, redder stars and their characteristics will match those of the more massive galaxies in the local Universe.

Studies of these extreme galaxy-forming events in the early Universe will be aided by three major advances due over the next year or so. First, the submillimetre camera on BLAST is actually a copy of one to be launched on the ESA/NASA Herschel Space Observatory³ later this year. The larger, 3.5-metre-diameter mirror on Herschel and the even darker skies in space mean that Herschel should be able to

see beyond the galaxy population identified by BLAST. Herschel will map larger areas of sky, and hence identify many thousands of submillimetre galaxies, compared with the 450 sources seen by BLAST. This advance should greatly improve the statistics of the analysis and allow more detailed studies of individual classes of submillimetre sources.

Second, the development of large-format detectors working at submillimetre wavelengths (the first example of which is the new SCUBA-2 submillimetre camera⁴ mounted on the James Clerk Maxwell Telescope) will facilitate surveys of even more distant and luminous galaxies. Such surveys are needed if we are to understand the physics involved in the youngest phases of formation of galaxies such as our own.

Finally, the commissioning of the first phase of the Atacama Large Millimeter Array (ALMA)⁵ will provide a 100-fold improvement in both the spatial resolution and the sensitivity of submillimetre maps. Such observations will allow astronomers to study the distribution of gas and star formation within these early galaxies, which in turn will help to identify the physical process that triggers these ultraluminous bursts of star formation and their role in the formation of the galaxies we see in the Universe today. ■

Ian Smail is at the Institute for Computational Cosmology, Durham University, Durham DH1 3LE, UK.
e-mail: ian.smail@durham.ac.uk

1. Devlin, M. J. *et al.* *Nature* **458**, 737–739 (2009).
2. Chapman, S. C. *et al.* *Nature* **422**, 695–698 (2003).
3. Herschel Space Observatory <http://sci.esa.int/science-e/www/area/index.cfm?fareaid=16>
4. SCUBA-2 www.roe.ac.uk/ukatc/projects/scubatwo/index.html
5. ALMA www.eso.org/sci/facilities/alma

CANCER

When restriction is good

Anne Brunet

Dietary restriction can prolong life and delay the onset of cancer. Suppressing the signalling pathway that is mediated by the hormone insulin might be crucial for the anticancer effects of reduced caloric intake.

It is well established that dietary restriction, which involves limiting nutrient intake below normal levels but without reaching malnutrition, extends lifespan in most, if not all, species — probably including humans¹. This amazing benefit is likely to be due to the evolutionary advantage of keeping alive under suboptimal nutrient availability, and postponing reproduction until food is plentiful. On the basis of this evolutionary hypothesis, dietary restriction should prolong not only lifespan, but also youthfulness. Indeed, in both rodents and humans, limiting caloric intake delays many age-associated traits and diseases, including cognitive deterioration and cancer^{2,3}. But dietary restriction does not affect all types of cancer similarly⁴, raising questions about the generality of its effects and its mode of action in cancer. Writing in this issue, Kalaany and Sabatini⁵ (page 725) address these questions in both human tumour cells and animal models of human cancer.

The authors find that, when human-tumour cell lines are implanted into mice, some lines cannot expand if the animals' caloric intake is reduced by 40% for a period of 3 weeks. Intriguingly, the cell lines that were resistant to the antitumour benefits of this nutrient restriction carried mutations that led to the constitutive (continuous) activation of the signalling pathway mediated by the hormone insulin. Specifically, these cell lines had mutations that activated the enzyme PI3K, a key component of the insulin signalling pathway, or inactivated PTEN phosphatase, an enzyme that counteracts PI3K action. So it seems that, to exert its anticancer benefits, limited dietary intake must reduce insulin-mediated signalling.

To investigate whether reducing the activity of the insulin-PI3K pathway was indeed required for mediating the effects of dietary restriction, Kalaany and Sabatini next studied the consequences of short-term limitations in food intake on mice that had been genetically engineered to develop tumours with either a constitutively active PI3K pathway or constitutive activation of other oncogenic signalling pathways. Strikingly, only tumours with an active PI3K pathway were resistant to dietary restriction. What's more, activating this pathway was both necessary and sufficient for tumour resistance to reduced food intake. Finally, the FOXO proteins, which are major downstream targets of the PI3K signalling pathway and affect gene transcription, seem to execute the effects of dietary restriction, as

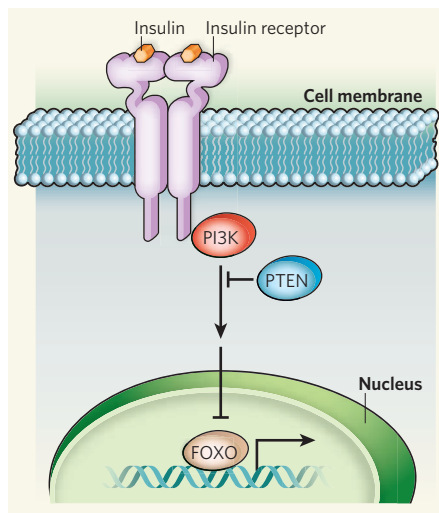


Figure 1 | Dietary restriction, insulin-mediated signalling, and cancer. Activation of cell-surface receptors by insulin triggers a signalling cascade in the cell that is mediated by the enzyme PI3K and subsequently by FOXO transcription factors. Kalaany and Sabatini⁵ find that dietary restriction reduces the activity of this pathway in some tumour cells, thereby enhancing cell death and reducing tumour size. However, tumours in which this pathway is constitutively active — owing to mutations in PI3K or in the PTEN enzyme, which normally counteracts PI3K — are resistant to the beneficial effects of dietary restriction.

FOXO transcription factors were inactivated in the tumours resistant to reduced nutrient intake (Fig. 1).

In search of a cellular mechanism to explain the effect of dietary restriction on tumours, Kalaany and Sabatini found that, in these tumour cells, there was an increase in programmed cell death (apoptosis). Further studies on how dietary restriction reduces tumour growth *in vivo* will be needed to explain whether it acts solely on the tumour itself, on the tumour microenvironment, or on both. Indeed, reduced food intake could affect other cellular processes that contribute to tumour size. For instance, it might inhibit cell proliferation; it could trigger autophagy, a 'self-eating' cellular process that would help to recycle nutrients and ward off cancer by eliminating damaged proteins or organelles; or it might help to reduce the growth of new blood vessels in tumours — a process known as angiogenesis — thus affecting the tumour microenvironment rather than the tumour cells.

It would be informative to compare Kalaany

and Sabatini's data⁵ with previous observations on the mechanisms of dietary-restriction-induced longevity and tumour suppression in other species⁶. Studies in yeast and worms have revealed various signalling pathways that mediate the effects of reduced food intake on longevity — including those involving the Sir2 family of deacetylase enzymes^{7,8}, the FOXA/*pha-4* (ref. 9) and NRF2/*skn-1* (ref. 10) transcription factors, and the AMPK (ref. 11), TOR (ref. 12) and Rheb (ref. 13) signalling molecules. Curiously, the insulin-PI3K-FOXO pathway was not essential for the effect of dietary restriction on longevity in most, although not all^{11,13}, of the studies. So how can these findings be reconciled with those of Kalaany and Sabatini?

There could be several explanations. First, compared with invertebrates, mammals may be more dependent on normal insulin signalling to extract maximum benefit from dietary restriction in relation to longevity and tumour resistance. Indeed, mutation of the growth-hormone receptor, which affects the production of insulin-like growth factor, interferes with dietary-restriction-induced longevity in mice¹⁴. Second, reduced insulin-mediated signalling resulting from a decrease in food intake may be even more important for fighting off cancer than for extending lifespan. In mice, for example, NRF2/*skn-1* mediates the effects of dietary restriction on cancer but not on longevity¹⁵. Third, the methods that researchers use to restrict dietary intake in invertebrates may expose pathways other than that mediated by insulin. Reduced food intake probably engages several pathways that cooperate to prolong lifespan and prevent cancer. Understanding how these pathways regulate longevity and age-dependent traits will be crucial for harnessing the full benefits of nutrient restriction.

It is worth noting that Kalaany and Sabatini implemented reduced food intake for a short period (3 weeks), whereas it is known that longer restriction regimens (several months to years) are needed to extend lifespan¹. It would be informative to know whether longer dietary-restriction regimens can still suppress tumours, or if tumours recur after a while. Could responsive tumours become resistant to the beneficial effects of dietary restriction with time, just as they acquire resistance to chemotherapy? This, in turn, raises the possibility that downregulation of insulin-mediated signalling through reduced food intake may only initiate the anticancer benefits; other pathways might need to be activated to maintain its suppressive effects on tumours. Finally, in mammals and other species, different dietary-restriction regimens can all extend lifespan. It would be interesting to test whether different regimens could also reduce PI3K-dependent cancer expansion, as only some regimens might be realistically applicable to humans — for instance, feeding every other day rather than a 40% restriction every day.

As for cancer prevention and anticancer therapies, simply decreasing food intake might

help to delay the onset of cancer. Moreover, involvement of the insulin-mediated pathway indicates that drugs that ameliorate insulin resistance in type 2 diabetes might be beneficial in preventing cancer, even in non-diabetic patients. One could also envisage using dietary restriction as a possible therapy in some specific cancers, and to predict which tumours would be vulnerable to such treatment on the basis of their mutation profiles, in particular in the genes encoding PTEN and PI3K. Limited food intake, together with a PI3K-pathway inhibitor, might have synergistic effects on cancer regression in tumours that have mutations in *PI3K* and/or *PTEN* genes. In addition, depriving tumours of nutrients locally by means of

anti-angiogenic drugs, which would interfere with the tumour's blood supply, may be yet another way to apply the beneficial effects of dietary restriction. In general, developing such additional strategies to mimic restriction could be particularly useful, because — as we all know — restricting food intake is notoriously difficult to implement in humans, and may even be psychologically damaging. ■

Anne Brunet is in the Department of Genetics, Stanford University, Stanford, California 94305, USA.

e-mail: anne.brunet@stanford.edu

1. Masoro, E. J. *Mech. Ageing Dev.* **126**, 913–922 (2005).
2. Witte, A. V., Fobker, M., Gellner, R., Knecht, S. & Flöel, A. *Proc. Natl Acad. Sci. USA* **106**, 1255–1260 (2009).

3. Hursting, S. D., Lavigne, J. A., Berrigan, D., Perkins, S. N. & Barrett, J. C. *Annu. Rev. Med.* **54**, 131–152 (2003).
4. Weindruch, R. & Walford, R. L. *Science* **215**, 1415–1418 (1982).
5. Kalaany, N. Y. & Sabatini, D. M. *Nature* **458**, 725–731 (2009).
6. Mair, W. & Dillin, A. *Annu. Rev. Biochem.* **77**, 727–754 (2008).
7. Lin, S. J., Defossez, P. A. & Guarente, L. *Science* **289**, 2126–2128 (2000).
8. Anderson, R. M., Bitterman, K. J., Wood, J. G., Medvedik, O. & Sinclair, D. A. *Nature* **423**, 181–185 (2003).
9. Panowski, S. H., Wolff, S., Aguilaniu, H., Durieux, J. & Dillin, A. *Nature* **447**, 550–555 (2007).
10. Bishop, N. A. & Guarente, L. *Nature* **447**, 545–549 (2007).
11. Greer, E. L. *et al. Curr. Biol.* **17**, 1646–1656 (2007).
12. Kaerberlein, M. *et al. Science* **310**, 1193–1196 (2005).
13. Honjoh, S., Yamamoto, T., Uno, M. & Nishida, E. *Nature* **457**, 726–730 (2009).
14. Bonkowski, M. S., Rocha, J. S., Masternak, M. M., Al Regaiey, K. A. & Bartke, A. *Proc. Natl Acad. Sci. USA* **103**, 7901–7905 (2006).
15. Pearson, K. J. *et al. Proc. Natl Acad. Sci. USA* **105**, 2325–2330 (2008).

BIOGEOCHEMISTRY

Less nickel for more oxygen

Mak A. Saito

The availability (or lack) of oceanic trace elements is providing fresh lines of explanation for turning points in Earth's history — the Great Oxidation Event being one such momentous occasion.

About 2.4 billion years ago, the oxygen content of Earth's atmosphere increased in what is called the Great Oxidation Event (GOE). This marked the beginning of the most significant series of chemical changes Earth has ever experienced, setting the stage for oxidative weathering of the continents, successive changes in ocean chemistry, and the eventual rise of multicellular life.

Yet the sequence of events leading up to the GOE is not well understood. Most researchers agree that the evolution of oxygenic photosynthesis within a group called the cyanobacteria was the source of the molecular oxygen that caused the GOE¹. But the timing of the rise of these bacteria is uncertain^{2,3}, and there may have been a period of inertia — due, for example, to chemical reactions with methane that consumed oxygen⁴ — that prevented a swift increase in atmospheric oxygen. It remains a matter of debate how these two phenomena might have induced the GOE: an early rise of cyanobacteria and slow crumbling of chemical resistance^{3,4}; or a late rise of cyanobacteria leading to rapid initiation of the GOE⁵.

On page 750 of this issue⁶, Konhauser *et al.* report evidence for an alternative driving mechanism of the GOE, one that would have decreased microbial methane production in the oceans and paved the way for increased oxygen abundances. The authors find significant decreases in the nickel-to-iron ratios in ancient rocks, known as banded iron formations, that provide records of element concentrations in the oceans (Fig. 1). They estimate that a major decrease in the oceanic inventory of nickel must have occurred around 2.7 billion

years ago. This, they conclude, led to a cascade of events in which methanogens, with their gluttonous appetite for nickel to feed three nickel-containing metalloenzymes, would have become starved of the element and so have produced much less methane. With the decrease in chemical inertia associated with methane⁴, the stage was set for cyanobacterial oxygen to accumulate, leading to the GOE. Moreover, although Konhauser *et al.* don't go into detail, the decline in atmospheric methane, a powerful greenhouse gas, is believed to help account for the initiation of a planetary-scale glaciation known as Snowball Earth that



Figure 1 | Record site. This is a view of Dales Gorge, northwest Australia, one of the banded iron formations sampled by Konhauser *et al.*⁶

is thought to have begun between 2.3 billion and 2.2 billion years ago^{4,5}.

The idea that significant changes in seawater trace-metal abundance have occurred during Earth's history is becoming popular^{7,8}. For example, it is thought that iron and cobalt were abundant in ancient oceans, whereas zinc and copper were probably extremely scarce owing to precipitation with sulphides⁸. When the oceans became oxygenated, it is likely that this scheme was reversed, with iron and cobalt becoming scarce through oxidation and precipitation as oxyhydroxides, and zinc and copper becoming much more abundant upon the oxidation of sulphide to sulphate in sea water. These predictions of broad changes in ocean chemistry are mirrored by the physiological and genomic traits of archaea and bacteria, relative to those of the later-evolving eukaryotes^{8,9}.

Nickel has largely been left out of this intriguing story. On the evidence of chemical modelling⁸, it seems that nickel was not as strongly affected by the variations in sulphide and oxygen during Earth's history. But such a conclusion does not take into account the possible involvement of external factors. Konhauser *et al.* show how such a factor might have come into play, with the cooling of Earth's mantle resulting in decreased eruption of nickel-rich rocks and causing an estimated 50% fall in the oceanic nickel inventory.

Konhauser and colleagues' thinking⁶ may come as a surprise to those familiar with the chemistry of the modern oceans. Trace metals — as their name suggests — are extraordinarily scarce in sea water. In vast regions of the modern oceans, photosynthesis is limited by low iron availability, with iron concentrations often being less than 0.05 nanomoles per litre¹⁰. Yet, of the trace metals required by life, nickel is one of the more abundant in sea water, with surface water concentrations of 1–2 nanomoles per litre¹¹. In this modern context, the idea of a nickel famine seems odd. But the nickel requirements of methanogens are reported⁶ to be in the hundreds of nanomoles per litre, suggesting that methanogens cannot live in the modern oceans and are perhaps relegated to

I. PATERSON/ALAMY

sedimentary, coastal and freshwater environments, where nickel is more abundant.

By connecting changes in mantle temperature to nickel fluxes and methanogens, Konhauser and colleagues' study is particularly satisfying. Instead of relying on the uncertain timing of the rise of cyanobacteria to explain the GOE, that event can instead be tied to a specific mechanism recorded in the banded iron formations. In addition, this 'nickel famine' mechanism is consistent with evidence¹² of 'whiffs of oxygen' that occurred more than 50 million years before the GOE. But I cannot help but wonder whether there is a reason — such as the slow chemical kinetics of nickel ions — why methanogens could not evolve a high-affinity nickel-uptake mechanism similar to those that exist for the uptake of iron, zinc and cobalt^{13–15}.

Finally, there is another context in which the research of Konhauser *et al.* is set — the exciting endeavour of trying to understand how the elemental cycles (of nickel, carbon, iron, nitrogen and so on) have 'co-evolved' with microbial life. Many of the changes in element cycling were probably caused by the rise and fall of specific microbial metabolisms, while also strongly affecting the trajectory and composition of life on Earth. Life and the cycling of elements have both been changing throughout Earth's history, often influencing each other profoundly along the way. One of the sobering realizations of studies such as this is that, although natural selection provides a clear, single positive-feedback mechanism for the continuation of life, elemental cycles are instead influenced by an aggregate of mechanisms, including biological evolution, chemical reactions, changes in ocean circulation and geological events. If, as Konhauser *et al.* suggest, a single geological change can starve a major oceanic microbial community, and thereby change the trajectory of life on Earth, it suggests that there is a fragility to Earth's elemental cycles that we are only beginning to uncover. ■

Mak A. Saito is at the Woods Hole Oceanographic Institution, Woods Hole, Massachusetts 02543, USA.
e-mail: msaito@whoi.edu

1. Canfield, D. E. *Annu. Rev. Earth Planet. Sci.* **33**, 1–36 (2005).
2. Rasmussen, B., Fletcher, I. R., Brocks, J. J. & Kilburn, M. R. *Nature* **455**, 1101–1104 (2008).
3. Brocks, J. J., Logan, G. A., Buick, R. & Summons, R. E. *Science* **285**, 1033–1036 (1999).
4. Claire, M. W., Catling, D. C. & Zahnle, K. J. *Geobiology* **4**, 239–269 (2006).
5. Kopp, R. E., Kirschvink, J. L., Hilburn, I. A. & Nash, C. Z. *Proc. Natl Acad. Sci. USA* **102**, 11131–11136 (2005).
6. Konhauser, K. O. *et al.* *Nature* **458**, 750–753 (2009).
7. Anbar, A. D. & Knoll, A. H. *Science* **297**, 1137–1142 (2002).
8. Saito, M. A., Sigman, D. M. & Morel, F. M. M. *Inorganica Chim. Acta* **356**, 308–318 (2003).
9. Dupont, C. L., Yang, S., Palenik, B. & Bourne, P. E. *Proc. Natl Acad. Sci. USA* **103**, 17822–17827 (2006).
10. Martin, J. H. & Fitzwater, S. E. *Nature* **331**, 341–343 (1988).
11. Bruland, K. W. *Earth Planet. Sci. Lett.* **47**, 176–198 (1980).
12. Anbar, A. D. *et al.* *Science* **317**, 1903–1906 (2007).
13. Maldonado, M. T. & Price, N. M. *J. Phycol.* **37**, 298–310 (2001).
14. Sunda, W. G. & Huntsman, S. A. *Limnol. Oceanogr.* **43**, 1055–1064 (1998).
15. Saito, M. A., Moffett, J. W., Chisholm, S. W. & Waterbury, J. B. *Limnol. Oceanogr.* **47**, 1629–1636 (2002).

STEM CELLS

Low-risk reprogramming

Martin F. Pera

New techniques circumvent a roadblock to the production of embryonic-stem-cell-like lines from adult tissue. Such reprogrammed cell lines should be much safer to use for therapy.

Shinya Yamanaka's amazing discovery¹ that cells from differentiated tissues can be reprogrammed into induced pluripotent stem (iPS) cells — cells that can potentially differentiate into any cell type — has transformed research in stem-cell biology and regenerative medicine. The breakthrough provided both a deft approach to the production of patient-specific stem-cell lines with which to study disease, and a practical means of developing large banks of stem-cell lines suitable for tissue matching in transplantation therapy. But the original protocols for producing iPS cells relied on the integration of foreign 'reprogramming' genes into the host-cell genome, a process associated with risks including mutation, dysregulation of native gene expression, and the development of cancers after iPS-cell transplantation. Four studies^{2–5}, including two in this issue^{2,3}, now show that iPS cells can be produced without any permanent modification to the host-cell genome.

The first-generation iPS cells were produced from culture-grown mouse and human somatic (non-germ) cells, most often skin fibroblasts^{1,6,7}. The protocol involved the introduction into the host cell of reprogramming genes crucial for the establishment or maintenance of the pluripotent state using various lentiviral or retroviral constructs as vectors. The constructs integrated into the host genome at multiple sites.

Although in most cases the foreign genes eventually became inactive in the iPS cell lines, this was not always the case. Moreover, even if expression of the transcription factors that the genes encoded was stopped, the integrated foreign DNA remained in the host genome. This could, in principle, disrupt host genes, alter gene expression at nearby genomic loci or, if subsequently reactivated in the differentiated cells, result in these cells becoming cancerous. Indeed, chimaeric mice generated from normal cells and some iPS cell lines developed tumours⁸. Work with viral vectors that integrate into the host genome also left open the daunting possibility that integration and genetic modification of the host cell per se might be required for reprogramming.

Subsequently, several groups showed that, depending on the host cell type, reprogramming can be achieved using fewer foreign genes. But the goal of completely eliminating the need for genomic integration of foreign sequences remained a priority.

Given the intense activity in the field of

reprogramming, many groups pursued solutions to this particular obstacle. Two groups^{4,5} report using non-integrating adenoviral vectors or plasmids to achieve transient expression of reprogramming factors without disturbing the host genome. But such an approach presents two immediate problems: the requirement for prolonged expression of the pluripotency factors to achieve reprogramming, and the difficulty of repeatedly delivering the full complement of factors using a different vector for each one.

To address the first problem, the authors^{4,5} used hepatocytes — which, compared with other cell types, are more amenable to both reprogramming and infection with adenoviruses — and introduced the genes into the cells repeatedly over a period of days. The second problem was solved in one study⁵ by borrowing a clever trick from the foot-and-mouth virus. By inserting a virally derived oligopeptide sequence called 2A as a spacer between four reprogramming genes, the researchers made a multiprotein expression vector.

The key feature of the 2A sequence is its ability to undergo self-splicing and be removed from a peptide undergoing translation, possibly through a mechanism in which the ribosome skips over one codon without forming a peptide bond, thus allowing the production of several peptides from one transcript. Using this approach, several reprogramming genes can be introduced and efficiently expressed using a single adenoviral or plasmid construct.

Both groups obtained mouse iPS cells that express cell-surface markers and genes characteristic of embryonic stem cells, and that could undergo differentiation *in vitro*. *In vivo*, these cell lines contributed to teratomas (benign tumours containing cells from various differentiated tissues) in chimaeric mice, although their ability to form germ cells was not assessed. The main drawback of this approach was its relative inefficiency: at least 100-fold fewer iPS colonies were obtained than with the retroviral or lentiviral vectors. Given that the production of iPS cells from human cells is generally less efficient than from mice, it is questionable how practical it would be to use these methods^{4,5} for human cells. But the studies established one point clearly — viral integration is not necessary for reprogramming.

Two other elegant studies^{2,3} provide an alternative, more efficient, strategy that involves virus-free integration of reprogramming genes, followed by their removal. Woltjen



50 YEARS AGO

The Eddington Memorial Lectures have come to occupy a special place in the scheme of things, because they enable men of distinction to illuminate some particular facet of the working of that great mind. In his recent lecture entitled "Science, Philosophy and Religion" ... Sir Russell Brain shows how the analysis of man, science and revelation, man and mechanization, perception and knowledge fit into the main stream of Eddington's thought ... If one lesson emerges clearly from pondering upon Eddington's philosophy, it is that a new concept will be needed to enable us to explain total behaviour in a way which transcends individual components. This is well said for biological systems, but it ... is becoming essential for inanimate phases, too, as witness the present discontents with 'classical' quantum theory. Ratiocination will try its hardest, though maybe these regions form part of the unseen world to which, as Eddington says, the human spirit must turn.

From *Nature* 11 April 1959.

100 YEARS AGO

An article is contributed by Dr. H. Marzell to *Naturwissenschaftliche Wochenschrift* (March 14) on the subject of plants which have been popularly endowed with magic qualities. The chief of these is undoubtedly the mandrake, *Mandragora officinalis*, the cultivation of which dates back to very ancient times, and spread from the East to various European countries ... Another plant, known as "moly" ($\mu\omicron\lambda\upsilon$), frequently mentioned in the classics, because it was given to Ulysses to protect him from the wiles of Circe, is generally regarded as a species of *Allium*. Reference is also made to an old English cantation, "The Song of the Nine Herbs," and to the superstition connected with "fern seeds," i.e. fern spores, which are supposed to render the bearer invisible.

From *Nature* 8 April 1909.

et al. (page 766)² and Kaji *et al.* (page 771)³ combined powerful technologies, developed independently, to overcome many of the difficulties others encountered in attempting virus-free reprogramming. These groups also made use of the virally derived 2A-peptide sequence⁵ to create multi-protein expression vectors incorporating all of the reprogramming genes. Instead of retroviruses or plasmids, however, they used the *piggyBac* transposon/transposase gene-delivery system. This vector can easily integrate into the genome. But more importantly, the integrated DNA can also be removed from the genome — through transient expression of the transposase enzyme — in a highly efficient and seamless fashion, leaving no trace of the integration in the genome of the iPS cells. The use of the 2A peptide is crucial, not just because it allows delivery of all of the required reprogramming genes in a single construct, but also because it makes complete excision of the foreign constructs much easier. What's more, the efficiency of this approach^{2,3} is much higher than that of transient transduction of cells using adenoviral vectors^{4,5}.

Kaji *et al.*³ also generated chimaeric mice using their iPS cells and found that these cells contributed to tissues derived from all three embryonic germ layers. The researchers do not mention, however, whether the animals could give rise to iPS-cell-derived offspring — the gold-standard test of pluripotency in mice. Moreover, they did not extensively characterize the human iPS cells, although these cells did have the expected features of pluripotent stem cells.

Together, these studies²⁻⁵ remove a major barrier to the generation of iPS cell lines that are safe for clinical use, showing beyond doubt that transient expression of reprogramming factors in somatic cells is sufficient to reset their gene expression to the pluripotent state. The

piggyBac technology, in particular, will find broader use for transiently introducing genes — such as those encoding 'reporter' proteins or master regulatory transcription factors — into embryonic stem cells and subsequently removing them. It could, in addition, be applied to the reprogramming of one differentiated cell type into another, such as the reprogramming of pancreatic exocrine cells into insulin-producing islet cells⁹, rather than reverting a cell back to an embryonic-like state.

It remains to be seen whether alternative reprogramming methods currently under development — such as reprogramming by simply exposing differentiated cells to small molecules, either alone or in combination with gene introduction — will prove more efficient than the techniques described so far. And crucial questions about the equivalency of human iPS cells to embryonic-stem-cell lines remain: do these cell lines have the same developmental capacity as embryonic stem cells, and will they prove to be stable genetically and epigenetically? Rapid progress in this exciting field hints that the answers to these questions will soon become clear. ■

Martin F. Pera is at the Eli and Edythe Broad Center for Regenerative Medicine and Stem Cell Research, Keck School of Medicine, University of Southern California, Los Angeles, California 90089, USA.

e-mail: martin.pera@keck.usc.edu

1. Takahashi, K. & Yamanaka, S. *Cell* **126**, 663–676 (2006).
2. Wolftjen, K. *et al.* *Nature* **458**, 766–770 (2009).
3. Kaji, K. *et al.* *Nature* **458**, 771–775 (2009).
4. Stadtfeld, M., Nagaya, M., Utikal, J., Weir, G. & Hochedlinger, K. *Science* **322**, 945–949 (2008).
5. Okita, K., Nakagawa, M., Hyenjong, H., Ichisaka, T. & Yamanaka, S. *Science* **322**, 949–953 (2008).
6. Takahashi, K. *et al.* *Cell* **131**, 861–872 (2007).
7. Yu, J. *et al.* *Science* **318**, 1917–1920 (2007).
8. Okita, K., Ichisaka, T. & Yamanaka, S. *Nature* **448**, 313–317 (2007).
9. Zhou, Q. & Melton, D. A. *Cell Stem Cell* **3**, 382–388 (2008).

PHYSICAL CHEMISTRY

How to improve your image

Michael J. Therien

The technique of second harmonic generation microscopy is used to obtain pictures of living systems, but the dyes required provide only modest imaging contrast per molecule. The latest dyes give a much better picture.

Optical imaging experiments have provided a wealth of structural, functional and mechanistic insights into biological processes, and at every level of organization: from the sub-cellular to the cellular, at the tissue level, and even in whole animals. Some of these investigations rely on multi-photon techniques, in which a fluorescent signal is generated from a dye by the near-simultaneous absorption of two or more photons. Writing in the *Journal of the American Chemical Society*, Reeve *et al.*¹

describe a new family of dyes that produce dramatic signal enhancements in a two-photon technique known as second harmonic generation (SHG) microscopy. The dyes could dramatically improve the scope of the technique for biological imaging — especially in studies of membranes.

Two-photon microscopy²⁻⁴, of which SHG microscopy is an example, has revolutionized the biological sciences by enabling non-invasive, high-resolution imaging of

living samples in real time. Perhaps the most commonly used variant is two-photon-excited fluorescence (TPEF) microscopy, in which a pair of low-energy photons is absorbed by an emissive probe molecule that would normally absorb a single photon at half the wavelength (twice the energy) of the low-energy photons. The resulting electronically excited dye relaxes to a fluorescent state that can be observed. By using low-energy (near-infrared, NIR) photons to generate fluorescence, rather than higher-energy (visible-light) photons, light-induced degradation of biological samples is minimized.

In contrast to TPEF imaging, the dye molecules in SHG microscopy do not absorb photons. Instead, they scatter light at exactly half the wavelength of the incoming radiation. As no real excited states are produced, phototoxic damage to biological samples can in principle be eliminated. Like TPEF imaging, SHG microscopy is

based on a nonlinear optical process in which the observed signal scales with the square of the intensity of the incident light; this relationship provides excellent spatial resolution. But whereas the light produced in SHG microscopy is always half the wavelength of the irradiating laser, that produced in TPEF imaging is determined by the spectral breadth of the dye's fluorescence emission band.

Both methods require pulsed-laser excitation, which provides the necessary peak intensity of light for these experiments, typically at NIR wavelengths. This is a particularly useful optical window for studying biological systems, because biological media do not absorb NIR light well, which reduces background noise in the images obtained. Furthermore, because light scattering diminishes with increasing wavelength, NIR light penetrates tissue more effectively than either ultraviolet or visible light.

To obtain high sensitivity and resolution in SHG microscopy, hyperpolarizable probes are required — dye molecules that have electron-density distributions that can be highly distorted under the influence of an optical field. Reeve and colleagues' probes¹ are based on previously reported 'porphyrin' dyes⁵ (Fig. 1a). Porphyrins provided a good template from which the authors could work, because such compounds have been shown to fluoresce intensely on absorbing low-energy photons⁶, and to be particularly good at absorbing pairs of photons^{7,8} — properties that are crucial for linear and nonlinear optical imaging applications.

When the porphyrin is attached to electron-

donating and electron-accepting groups by carbon-carbon triple bonds (C≡C), the electron density of its delocalized electrons can be hyperpolarized in an optical field. The C≡C bonds are particularly important in the design of imaging agents for biological applications, because porphyrin compounds featuring this bonding motif exhibit desirable nonlinear optical properties and exceptional hyperpolarizabilities^{5,9}, as well as strong NIR fluorescence^{6,8}. Yet another reason for the interest in porphyrins is that they are ubiquitous components

directed radiation that depends on the distribution and orientation of dipoles in the dye molecules. Accordingly, SHG microscopy can in many instances provide structural information that can't be obtained by TPEF imaging^{2,3}.

SHG microscopy has been used in such diverse applications as probing cell-cell interactions, scrutinizing cellular morphology and even recording waves of electrochemical activity (action potentials) in neurons in real time^{2-4,10}. But thus far, the method has relied on dyes that have only modest hyperpolarizabilities. Reeve

and colleagues' compounds¹ are a big improvement, but the authors have another trick up their sleeves that could further enhance imaging contrast per molecule of dye. Porphyrins readily bind dipositive metal ions. When the authors' dyes bind to certain such ions, such as copper ions (Cu²⁺), the resulting complex is non-fluorescent. If

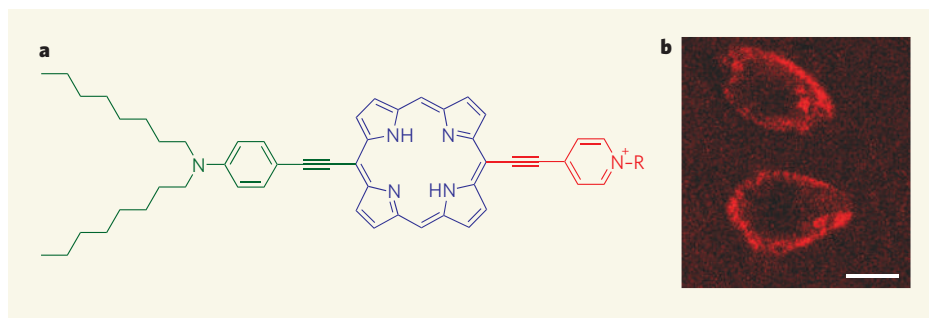


Figure 1 | Another way to dye. **a**, Reeve *et al.*¹ report improved fluorescent dyes for second harmonic generation (SHG) imaging. The molecular structure of the dyes consists of a porphyrin core (blue), to which an electron-donating group (green) and an electron-accepting group (red) are attached. R represents a methyl group, or a hydrocarbon chain to which a polar group is attached. **b**, The authors used their dyes to obtain SHG images of SK-OV-3 cancer cells. (Scale bar, 10 μm . Image reproduced from ref. 1.)

of the proteins involved in electron migration (cytochromes), oxygen transport (haemoglobin) and oxygen storage (myoglobin). Probes such as those described by Reeve *et al.*¹ might therefore exhibit the biocompatibility and biodegradability required for *in vivo* imaging applications.

Will SHG microscopy supplant TPEF as the standard microscopic method for biological imaging? To answer this question, it should be noted that SHG measurements require hyperpolarizable dyes to be ordered in an asymmetric fashion — a 'noncentrosymmetric' arrangement, for those in the know — over macroscopic dimensions. Reeve *et al.*¹ incorporated structural elements into their dyes (long hydrocarbon chains on the electron-donating portion of the molecules) that ensure asymmetric ordering of the molecules within biological membranes. This enabled the authors to generate SHG micrographs of SK-OV-3 cancer cells¹ (Fig. 1b). But TPEF imaging does not require asymmetric ordering of dyes to generate signals, and will thus always remain a more general two-photon microscopy method.

On the other hand, TPEF imaging is an incoherent process that entails light absorption and, in general, subsequent omnidirectional emission. This combination of processes often causes valuable information to be lost about how dye molecules interact with their local biological environment. In contrast, SHG microscopy is a coherent phenomenon that maintains phase information about the incident radiation. The scattered light observed in SHG imaging therefore consists of highly

these non-fluorescent complexes are used for SHG microscopy, the experimental set-up can be tuned to exploit an effect known as resonance enhancement. This increases the hyperpolarizability of the molecules^{5,9}, thus providing even more sensitive probes for SHG microscopy.

Reeve and colleagues' compounds are the first of a new generation of SHG imaging dyes that will undoubtedly enable multi-photon imaging at higher contrasts and resolution than was previously possible. Because the electron-donating and electron-accepting groups can be readily changed, an enormous range of dyes can be made and optimized for various applications. This, in turn, will provide new tools for visualizing cellular and subcellular events in living tissue. ■

Michael J. Therien is in the Department of Chemistry, Duke University, Durham, North Carolina 27708, USA.
e-mail: michael.therien@duke.edu

1. Reeve, J. E. *et al.* *J. Am. Chem. Soc.* **131**, 2758–2759 (2009).
2. Zipfel, W. R., Williams, R. M. & Webb, W. W. *Nature Biotech.* **21**, 1369–1377 (2003).
3. Moreaux, L., Sandre, O., Blanchard-Desce, M. & Mertz, J. *Optics Lett.* **25**, 320–322 (2000).
4. Campagnola, P. J. *et al.* *Biophys. J.* **81**, 493–508 (2002).
5. LeCours, S. M., Guan, H.-W., DiMaggio, S. G., Wang, C. H. & Therien, M. J. *J. Am. Chem. Soc.* **118**, 1497–1503 (1996).
6. Ghoroghchian, P. P. *et al.* *Proc. Natl Acad. Sci. USA* **102**, 2922–2927 (2005).
7. Drobizhev, M. *et al.* *J. Am. Chem. Soc.* **126**, 15352–15353 (2004).
8. Duncan, T. V., Susumu, K., Sinks, L. E. & Therien, M. J. *J. Am. Chem. Soc.* **128**, 9000–9001 (2006).
9. Uyeda, H. T. *et al.* *J. Am. Chem. Soc.* **124**, 13806–13813 (2002).
10. Sacconi, L., Dombeck, D. A. & Webb, W. W. *Proc. Natl Acad. Sci. USA* **103**, 3124–3129 (2006).

OBITUARY

Hidesaburo Hanafusa (1929–2009)

Inspiration and innovation in molecular cancer research.

Much of the molecular basis of cancer was revealed by research done during the last 40 years of the twentieth century, radically changing both diagnosis and treatment. One of the most influential and prolific contributors to this era was Hidesaburo Hanafusa, who died on 15 March at the age of 79. In the 1960s and early 1970s, Hanafusa's investigations of RNA 'tumour viruses' established that the cancer-causing genes of these retroviruses, now called oncogenes, have counterparts in normal animal and human cells. Then, during the 1980s and 1990s, work from his group on retroviral oncogenes provided insights into how cellular genes that normally regulate intracellular signalling go awry in cancer cells.

Born and educated in Japan, Hanafusa came to the United States in 1961 to work in Harry Rubin's laboratory at the University of California, Berkeley. The ability to quantitatively study the viral transformation of normal cells into cancer cells using the 'focus assay' had just been developed there by Howard Temin. While in Rubin's lab, Hanafusa published papers that laid the foundation for the 'oncogene hypothesis' of cancer.

Rubin and another postdoctoral fellow in the lab, Peter Vogt, had discovered that preparations of Rous sarcoma virus — RSV, first discovered in a chicken sarcoma by Peyton Rous in 1911 — contained another virus, which they called Rous-associated virus (RAV). Rubin suggested that Hanafusa try to isolate pure RSV and, in doing so, Hanafusa discovered that RSV was 'defective' — meaning that it lacked the genetic components necessary to replicate itself, but was able to transform normal cells into cancer cells. Hanafusa and Rubin isolated transformed cells infected with RSV that did not produce infectious virus. RAV was a 'helper' virus that provided the viral genes needed for replication. In return, the cancer-causing RSV promoted host-cell proliferation, aiding RAV in the production of the components needed for virus replication. This explained why the two viruses propagated together. That the non-transforming RAV could replicate without RSV, and that RSV could transform cells without RAV, implied that RSV carried a gene (or genes) that was not required for viral replication but was responsible for cell transformation and tumour growth. This was the earliest clear indication of the existence of a transforming oncogene.

Hanafusa established his own lab with his wife Teruko — herself a noted virologist — at

the Public Health Research Institute of the City of New York in 1966, and in 1973 moved uptown to The Rockefeller University. By this time, the region in RSV responsible for transformation had been mapped, and the gene located in this region had come to be known as *src* — for sarcoma. Hanafusa's and also Vogt's continuing research provided a foundation for the well-known 1977 report from the Hanafusa lab demonstrating that a transformation-defective RSV mutant was able to recover the ability to transform from a host cell. The reconstituted virus had regained the *src* gene. This work closely followed the classic 1976 report from the laboratories of Michael Bishop and Harold Varmus demonstrating that viral *src* sequences are similar to sequences in uninfected cells. The recovery of an active transforming *src* (later shown to be mutated) from a host cell by a transformation-defective virus confirmed that the sequences responsible for viral oncogenesis are captured and mutated cellular genes. Hanafusa shared the 1982 Lasker award with Bishop and Varmus for this work.

Subsequent research in many other laboratories identified other mutated cellular genes that had been captured by transforming retroviruses, including the well-known *ras* oncogene. All of these studies substantiated the hypothesis that cancer-causing genes carried by transforming retroviruses are mutated, usually overactive, versions of normal cellular genes. In 1982, it was discovered that DNA isolated from human cancer cells could by itself induce transformation in mouse fibroblast cells in culture. The gene in this human DNA was a mutant form of a gene originally characterized as a retroviral oncogene — namely, *ras*.

In the 1980s, Hanafusa's research shifted to the structure and function of proteins encoded by viral oncogenes. By this time it had been discovered that the *src* gene product was a protein kinase — an enzyme that phosphorylates and so regulates other proteins — and that it was specific for the tyrosine amino acid. In 1982, Hanafusa's group published the sequence of the Fujinami sarcoma virus and its oncogene *fps*, which, like *src*, also encodes a tyrosine kinase. Sequencing of *fps* revealed similarities between *fps* and *src*. This point did not escape the notice of Tony Pawson, who identified regions in *fps* that were homologous to regions in *src* — most significantly, the now-famous *src*-homology domain SH2. The significance of this discovery became evident



THE ROCKEFELLER UNIV.

when Hanafusa's group revealed that the *crk* oncogene, carried by the CT10 transforming retrovirus, encoded a small protein that consisted only of SH2 and another domain with homology to *src* — the SH3 domain.

In the early 1990s, Hanafusa's group, along with Pawson and Bruce Mayer, a Hanafusa lab graduate working in David Baltimore's lab, went on to demonstrate that SH2 domains bind proteins in a manner that depends on tyrosine phosphorylation. This observation provided a molecular explanation for the protein-protein interactions induced in response to the phosphorylation of proteins on tyrosine. For this and all his previous work, Hanafusa received the 1993 General Motors Sloan award.

With the untimely death of Teruko, his life-long collaborator, in 1996, Hanafusa left Rockefeller in 1998 to become the director of the Osaka Bioscience Institute in Japan, where he continued to contribute to our understanding of oncogenesis while inspiring a new group of Japanese scientists. He retired from the institute in 2008.

Apart from his enduring contributions to an unprecedented era of cancer research, Hanafusa trained a host of graduate students and postdoctoral fellows, many of whom have had notable scientific careers of their own. Hidesaburo Hanafusa had much to be proud of during his long scientific career. But perhaps his most enduring legacy will be his inspiration and nurturing of a generation of scientists who revered him for his sagacity, and for his warmth and quiet support.

David A. Foster and James E. Darnell Jr

David A. Foster is in the Department of Biological Sciences, Hunter College of the City University of New York, 695 Park Avenue, New York, New York 10065, USA. James E. Darnell Jr is in the Laboratory of Molecular Cell Biology, The Rockefeller University, 1230 York Avenue, New York, New York 10065, USA. e-mails: foster@gencetr.hunter.cuny.edu; darnell@rockefeller.edu

The cancer genome

Michael R. Stratton^{1,2}, Peter J. Campbell^{1,3} & P. Andrew Futreal¹

All cancers arise as a result of changes that have occurred in the DNA sequence of the genomes of cancer cells. Over the past quarter of a century much has been learnt about these mutations and the abnormal genes that operate in human cancers. We are now, however, moving into an era in which it will be possible to obtain the complete DNA sequence of large numbers of cancer genomes. These studies will provide us with a detailed and comprehensive perspective on how individual cancers have developed.

Cancer is responsible for one in eight deaths worldwide¹. It encompasses more than 100 distinct diseases with diverse risk factors and epidemiology which originate from most of the cell types and organs of the human body and which are characterized by relatively unrestrained proliferation of cells that can invade beyond normal tissue boundaries and metastasize to distant organs.

Early insights into the central role of the genome in cancer development emerged in the late nineteenth and early twentieth centuries from studies by David von Hansemann² and Theodor Boveri³. Examining dividing cancer cells under the microscope, they observed the presence of bizarre chromosomal aberrations. This led to the proposal that cancers are abnormal clones of cells characterized by and caused by abnormalities of hereditary material. Following the discovery of DNA as the molecular substrate of inheritance⁴ and determination of its structure⁵, this speculation was supported by the demonstration that agents that damage DNA and generate mutations also cause cancer⁶. Subsequently, increasingly refined analyses of cancer cell chromosomes showed that specific and recurrent genomic abnormalities, such as the translocation between chromosomes 9 and 22 in chronic myeloid leukaemia (known as the 'Philadelphia' translocation^{7,8}), are associated with particular cancer types. Finally, it was demonstrated that introduction of total genomic DNA from human cancers into phenotypically normal NIH3T3 cells could convert them into cancer cells^{9,10}. Isolation of the specific DNA segment responsible for this transforming activity led to the identification of the first naturally occurring, human cancer-causing sequence change—the single base G > T substitution that causes a glycine to valine substitution in codon 12 of the *HRAS* gene^{11,12}. This seminal discovery in 1982 inaugurated an era of vigorous searching for the abnormal genes underlying the development of human cancer that continues today.

Here we review the principles of our current understanding of cancer genomes. We look forward to the explosion of information about cancer genomes that is imminent and the insights into the process of oncogenesis that this promises to generate.

Cancer is an evolutionary process

All cancers are thought to share a common pathogenesis. Each is the outcome of a process of Darwinian evolution occurring among cell populations within the microenvironments provided by the tissues of a multicellular organism. Analogous to Darwinian evolution occurring in the origins of species, cancer development is based on two constituent processes, the continuous acquisition of heritable genetic variation in individual cells by more-or-less random mutation and natural selection acting on the resultant phenotypic diversity. The selection

may weed out cells that have acquired deleterious mutations or it may foster cells carrying alterations that confer the capability to proliferate and survive more effectively than their neighbours. Within an adult human there are probably thousands of minor winners of this ongoing competition, most of which have limited abnormal growth potential and are invisible or manifest as common benign growths such as skin moles. Occasionally, however, a single cell acquires a set of sufficiently advantageous mutations that allows it to proliferate autonomously, invade tissues and metastasize.

The catalogue of somatic mutations in a cancer genome

Like all the cells that constitute the human body, a cancer cell is a direct descendant, through a lineage of mitotic cell divisions, of the fertilized egg from which the cancer patient developed and therefore carries a copy of its diploid genome (Fig. 1). However, the DNA sequence of a cancer cell genome, and indeed of most normal cell genomes, has acquired a set of differences from its progenitor fertilized egg. These are collectively termed somatic mutations to distinguish them from germline mutations that are inherited from parents and transmitted to offspring.

The somatic mutations in a cancer cell genome may encompass several distinct classes of DNA sequence change. These include substitutions of one base by another; insertions or deletions of small or large segments of DNA; rearrangements, in which DNA has been broken and then rejoined to a DNA segment from elsewhere in the genome; copy number increases from the two copies present in the normal diploid genome, sometimes to several hundred copies (known as gene amplification); and copy number reductions that may result in complete absence of a DNA sequence from the cancer genome (Fig. 2).

In addition, the cancer cell may have acquired, from exogenous sources, completely new DNA sequences, notably those of viruses such as human papilloma virus, Epstein Barr virus, hepatitis B virus, human T lymphotropic virus 1 and human herpes virus 8, each of which is known to contribute to the genesis of one or more type of cancer¹³.

Compared to the fertilized egg, the cancer genome will also have acquired epigenetic changes which alter chromatin structure and gene expression, and which manifest at DNA sequence level by changes in the methylation status of some cytosine residues. Epigenetic changes can be subject to the same Darwinian natural selection as genetic events, provided that there is epigenetic variation in the population of competing cells, that the epigenetic changes are stably heritable from the mother to the daughter cell and that they generate phenotypic effects for selection to act on.

Finally, it should not be forgotten that another genome is harboured within the cancer cell. The thousands of mitochondria present each carry a circular genome of approximately 17 kilobases. Somatic mutations in

¹Cancer Genome Project, Wellcome Trust Sanger Institute, Hinxton, Cambridge CB10 1SA, UK. ²Institute of Cancer Research, 15 Cotswold Road, Sutton, Surrey SM2 5NG, UK. ³Department of Haematology, University of Cambridge, Cambridge CB2 2XY, UK.

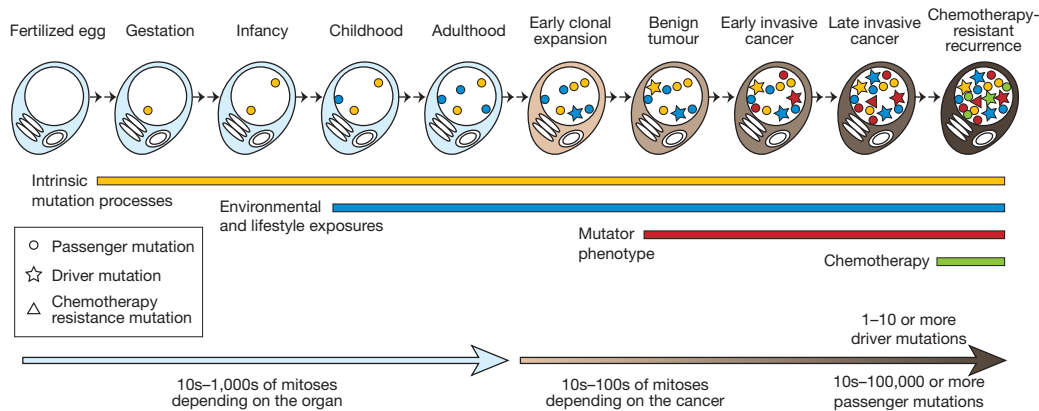


Figure 1 | The lineage of mitotic cell divisions from the fertilized egg to a single cell within a cancer showing the timing of the somatic mutations acquired by the cancer cell and the processes that contribute to them. Mutations may be acquired while the cell lineage is phenotypically normal, reflecting both the intrinsic mutations acquired during normal cell division and the effects of exogenous mutagens. During the development of the

cancer other processes, for example DNA repair defects, may contribute to the mutational burden. Passenger mutations do not have any effect on the cancer cell, but driver mutations will cause a clonal expansion. Relapse after chemotherapy can be associated with resistance mutations that often predate the initiation of treatment.

mitochondrial genomes have been reported in many human cancers, although their role in the development of the disease is not clear¹⁴.

Acquisition of somatic mutations in cancer genomes

The mutations found in a cancer cell genome have accumulated over the lifetime of the cancer patient. Some were acquired when ancestors of the cancer cell were biologically normal, showing no phenotypic characteristics of a cancer cell (Fig. 1). DNA in normal cells is continuously damaged by mutagens of both internal and external origins. Most of this damage is repaired. However, a small fraction may be converted into fixed mutations and DNA replication itself has a low intrinsic error rate. Our understanding of somatic mutation rates in normal human cells is still relatively rudimentary. However, it is likely that the mutation rates of each of the various structural classes of somatic mutation differ and that there are differences among cell types too. Mutation rates increase in the presence of substantial exogenous mutagenic exposures, for example tobacco smoke carcinogens,

naturally occurring chemicals such as aflatoxins, which are produced by fungi, or various forms of radiation including ultraviolet light. These exposures are associated with increased rates of lung, liver and skin cancer, respectively, and somatic mutations within such cancers often exhibit the distinctive mutational signatures known to be associated with the mutagen¹⁵. The rates of the different classes of somatic mutation are also increased in several rare inherited diseases, for example Fanconi anaemia, ataxia telangiectasia, mosaic variegated aneuploidy and xeroderma pigmentosum, each of which is also associated with increased risks of cancer^{16,17}.

The rest of the somatic mutations in a cancer cell genome have been acquired during the segment of the cell lineage in which predecessors of the cancer cell already show phenotypic evidence of neoplastic change (Fig. 1). Whether the somatic mutation rate is always higher during this part of the lineage is controversial^{18,19}. For some cancers this is clearly the case. For example, colorectal and endometrial cancers with defective DNA mismatch repair due to abnormalities in genes such as *MLH1* and *MSH2*, exhibit increased rates of acquisition of single nucleotide changes and small insertions/deletions at polynucleotide tracts²⁰. Other classes of such ‘mutator phenotypes’ may exist, for example leading to abnormalities in chromosome number or increased rates of genomic rearrangement, although these are generally less well characterized²⁰. The merit of an increased somatic mutation rate with respect to the development of cancer is that it increases the DNA sequence diversity on which selection can act. However, it has been suggested that the mutation rates of normal cells may be sufficient to account for the development of some cancers, without the requirement for a mutator phenotype^{18,19}.

The course of mutation acquisition need not be smooth and predecessors of the cancer cell may suddenly acquire a large number of mutations. This is sometimes termed ‘crisis’²¹, and can occur after attrition of the telomeres that normally cap the ends of chromosomes, with the cell having to substantially reorganize its genome to survive.

Although complex and potentially cryptic to decipher, the catalogue of somatic mutations present in a cancer cell therefore represents a cumulative archaeological record of all the mutational processes the cancer cell has experienced throughout the lifetime of the patient. It provides a rich, and predominantly unmined, source of information for cancer epidemiologists and biologists with which to interrogate the development of individual tumours.

Driver and passenger mutations

Each somatic mutation in a cancer cell genome, whatever its structural nature, may be classified according to its consequences for cancer development. ‘Driver’ mutations confer growth advantage on the cells

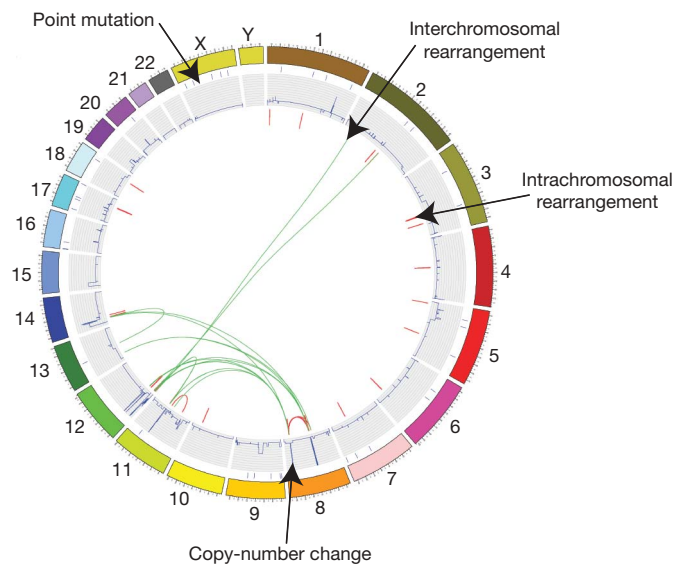


Figure 2 | Figurative depiction of the landscape of somatic mutations present in a single cancer genome. Part of catalogue of somatic mutations in the small-cell lung cancer cell line NCI-H2171. Individual chromosomes are depicted on the outer circle followed by concentric tracks for point mutation, copy number and rearrangement data relative to mapping position in the genome. Arrows indicate examples of the various types of somatic mutation present in this cancer genome.

carrying them and have been positively selected during the evolution of the cancer. They reside, by definition, in the subset of genes known as 'cancer genes'. The remainder of mutations are 'passengers' that do not confer growth advantage, but happened to be present in an ancestor of the cancer cell when it acquired one of its drivers (see Box 1).

The number of driver mutations, and hence the number of abnormal cancer genes, in an individual cancer is a central conceptual parameter of cancer development, but is not well established. It is highly likely that most cancers carry more than one driver and that the number varies between cancer types. On the basis of age–incidence statistics it has been suggested that common adult epithelial cancers such as breast, colorectal and prostate require 5–7 rate-limiting events, possibly equating to drivers, whereas cancers of the haematological system may require fewer²². These estimates are supported by experimental studies which show that engineering changes in the functions of at least five or

six genes in normal primary human cells is necessary to convert them into cancer cells²³. However, recent analyses of somatic mutation data from cancers indicate that the number of drivers might be much higher²⁴. Ultimately, direct estimates of the number of drivers in individual cancers will be provided by identifying all the cancer genes and systematically measuring the prevalence of mutations in them.

One important subclass of driver is a mutation that confers resistance to cancer therapy (Fig. 1). These are typically found in recurrences of cancers that have initially responded to treatment but that are now resistant. Resistance mutations often confer limited growth advantage on the cancer cell in the absence of therapy. Some seem to predate initiation of treatment, existing as passengers in minor subclones of the cancer cell population until the selective environment is changed by the initiation of therapy^{25,26}. The passenger is then converted into a driver and the resistant subclone preferentially expands, manifesting as the recurrence.

Box 1 | Driver and passenger mutations

All cancers arise as a result of somatically acquired changes in the DNA of cancer cells. That does not mean, however, that all the somatic abnormalities present in a cancer genome have been involved in development of the cancer. Indeed, it is likely that some have made no contribution at all. To embody this concept, the terms 'driver' and 'passenger' mutation have been coined.

A driver mutation is causally implicated in oncogenesis. It has conferred growth advantage on the cancer cell and has been positively selected in the microenvironment of the tissue in which the cancer arises. A driver mutation need not be required for maintenance of the final cancer (although it often is) but it must have been selected at some point along the lineage of cancer development shown in Fig. 1.

A passenger mutation has not been selected, has not conferred clonal growth advantage and has therefore not contributed to cancer development. Passenger mutations are found within cancer genomes because somatic mutations without functional consequences often occur during cell division. Thus, a cell that acquires a driver mutation will already have biologically inert somatic mutations within its genome. These will be carried along in the clonal expansion that follows and therefore will be present in all cells of the final cancer.

Some somatic mutations may actually impair cell survival. These will usually be subject to negative selection and hence be absent from the cancer genome. The traces of negative selection in cancer genomes are currently limited but it would be surprising if it was not operative.

A central goal of cancer genome analysis is the identification of cancer genes that, by definition, carry driver mutations. A key challenge will therefore be to distinguish driver from passenger mutations. The main strategy generally used exploits a number of structural signatures associated with mutations that are under positive selection. For example, driver mutations cluster in the subset of genes that are cancer genes whereas passenger mutations are more or less randomly distributed. This has been the approach adopted fruitfully in the past to identify most somatically mutated cancer genes in studies targeted at small regions of the genome.

Whole-genome sequencing, however, incorporating analysis of more than 20,000 protein-coding genes and unknown numbers of functional elements in intronic and intergenic DNA, presents a greater challenge, one rendered more daunting by the likelihood that passenger mutations in most cancer genomes substantially outnumber drivers. Because many cancer genes seem to contribute to cancer development in only a small fraction of tumours, large sample sets will have to be analysed to distinguish infrequently mutated cancer genes from genes with random clusters of passenger mutations. Furthermore, it is conceivable that some mutational processes are directed at specific genomic regions and thus generate clusters of passenger mutations that may be mistaken for drivers.

Therefore, all such signatures of positive selection need to be interpreted with caution. In practice, however, used in an informed and critical manner they will remain effective and reliable guides to the identification of cancer genes. Investigation of the biological consequences of putative driver mutations will often consolidate the evidence implicating them in oncogenesis and will provide insight into the subverted biological processes by which they contribute to cancer development.

The repertoire of somatically mutated cancer genes

The identification of driver mutations and the cancer genes that they alter has been a central aim of cancer research for more than a quarter of a century. It has been a remarkably successful endeavour, with at least 350 (1.6%) of the ~22,000 protein-coding genes in the human genome reported to show recurrent somatic mutations in cancer with strong evidence that these contribute to cancer development²⁷ (<http://www.sanger.ac.uk/genetics/CGP/Census/>). Most were identified by first establishing their physical location in the genome through low-resolution genome-wide screens, in particular cytogenetics for chromosomal translocations in leukaemias and lymphomas. A few were discovered using biological assays for transforming activity of whole cancer cell DNA and others through targeted mutational screens guided by biologically well-informed guesswork. Mutations in ~10% of these genes are also found in the germ line, where they confer an increased risk of developing cancer, and these were often initially identified by genetic linkage analysis of affected families. The size of the full repertoire of human cancer genes is a matter of speculation. However, studies in mice have suggested that more than 2,000 genes, when appropriately altered, may have the potential to contribute to cancer development²⁸.

The known cancer genes run the gamut of tissue specificities and mutation prevalences. Some, for example *TP53* and *KRAS*, are frequently mutated in diverse types of cancer whereas others are rare and/or restricted to one cancer type (<http://www.sanger.ac.uk/genetics/CGP/cosmic/>). In some cancer types, for example colorectal and pancreatic cancer, abnormalities in several known cancer genes are common. In contrast, in gastric cancer, relatively few mutations in known cancer genes have been reported.

Approximately 90% of the known somatically mutated cancer genes are dominantly acting, that is, mutation of just one allele is sufficient to contribute to cancer development. The mutation in such cases usually results in activation of the encoded protein. Ten per cent act in a recessive manner, requiring mutation of both alleles, and the mutations usually result in abrogation of protein function (these are sometimes known as tumour suppressor genes).

Patterns of mutation differ between dominant and recessive cancer genes. Recessive cancer genes are characterized by diverse mutation types, ranging from single base substitutions to whole gene deletions, which have the common outcome of abolishing the function of the encoded protein. In each dominantly acting cancer gene, however, the repertoire of cancer-causing somatic mutations is usually more constrained, both with respect to the type of mutation and its location in the gene. Missense amino acid changes (often restricted to certain key amino acids), in-frame insertions and deletions, and gene amplification are all common mutational mechanisms for activating dominantly acting cancer genes. Most, however, are activated through genomic rearrangement. This may join the sequences of two different genes to create a fusion gene or it may position the cancer gene adjacent to regulatory elements from elsewhere in the genome, resulting in abnormal expression patterns. Most of the known rearranged cancer

genes are operative in the relatively rare subset of cancers constituted by leukaemias, lymphomas and sarcomas. Recently, however, rearranged cancer fusion genes were discovered in more than half of prostate cancer cases²⁹ and in lung adenocarcinomas³⁰. Their late discovery probably reflects the difficulty of identifying them amidst the jumble of passenger rearrangements present in many cancer genomes and hints that there are many more rearranged cancer genes to be found in common cancers.

Much of what we know about the biological pathways and processes that are subverted in cancer has originated from experiments exploring the functions of cancer genes. Certain gene families, notably the protein kinases, feature particularly prominently among cancer genes. Furthermore, cancer genes cluster on certain signalling pathways. For example, in the classical MAPK/ERK pathway³¹ upstream mutations are found in cell-membrane-bound receptor tyrosine kinases such as *EGFR*, *ERBB2*, *FGFR1*, *FGFR2*, *FGFR3*, *PDGFRA* and *PDGFRB* and also in the downstream cytoplasmic components *NF1*, *PTPN11*, *HRAS*, *KRAS*, *NRAS* and *BRAF*. Recent exhaustive mutational analyses in gliomas have indicated that almost all cases have a mutation at one of the genes on these critical signalling pathways³².

For some cancers, classification and treatment protocols are now defined by the presence of abnormal cancer genes. Acute myeloid leukaemia, for example, is subclassified on the basis of the presence of abnormalities involving specific cancer genes³³. Each subtype has a characteristic gene expression profile, cellular morphology, clinical syndrome, prognosis and opportunity for targeted therapy. Moreover, because cancer cells are dependent on the abnormal proteins encoded by mutated cancer genes, they have become targets for the development of new cancer therapeutics. Flagships for this new generation of treatments include imatinib, an inhibitor of the proteins encoded by the *ABL* and *KIT* genes, which are mutated and activated, respectively, in chronic myeloid leukaemia³⁴ and gastrointestinal stromal tumours³⁵, and trastuzumab, an antibody directed against the protein encoded by *ERBB2* (also known as *HER2*), which is commonly amplified and overexpressed in breast cancer³⁶.

Early systematic sequencing of cancer genomes

Provision of the reference human genome sequence at the turn of the millennium offered new strategies and opportunities for surveying cancer genomes. Rather than depending on low-resolution maps, the highest possible resolution map, the DNA sequence itself, became available and has empowered investigation of cancer genomes in several ways. For example, much higher-resolution arrays have been developed, allowing finer mapping of copy number changes in cancer genomes leading to the identification of several new amplified cancer genes.

The availability of the human genome sequence has also raised the possibility that DNA sequencing itself could become the primary tool for exploration of cancer genomes. This has prompted several pilot experiments. So far, most have sequenced large numbers of PCR products to detect the base substitutions and small insertions and deletions (collectively termed 'point' mutations) present in the coding exons of protein-coding genes^{32,37–44}. Typically, such studies have covered several hundred megabases of cancer genome with designs ranging from hundreds of genes analysed in a few hundred cancers to most of the ~22,000 protein-coding genes in 10–20 examples of a particular cancer class.

Several insights have been provided by these screens. They have brought success in the identification of point-mutated cancer genes including *BRAF*⁴⁵, *PIK3CA*⁴⁶, *EGFR*⁴⁷, *HER2* (ref. 48), *JAK2* (ref. 49), *UTX* (ref. 50) and *IDH1* (ref. 41). Some of these were unique discoveries, whereas others were simultaneously discovered in targeted mutational screens. Some were previously known cancer genes, but the discovery of point mutations highlighted new mechanisms and cancer types in which they are operative. Some were surprising and highlight the virtue of systematic and comprehensive screens, for example the discovery of the enzyme isocitrate dehydrogenase (*IDH1*), which constitutes part of the Krebs cycle of oxidative phosphorylation, as a cancer gene mutated in glioma⁴¹. Because many are kinases that are activated by the

mutations found in cancer, they have prompted a wave of drug discovery to find inhibitors that may serve as anticancer therapeutics⁵¹, some of which are already in clinical trials.

Exposing the landscape of the cancer genome

Important insights into the general parameters and patterns of somatic mutation in cancer have also emerged from these early studies. It appears that most somatic point mutations in cancer genomes are passengers³⁹. Although this might have been predicted for mutations in intergenic and intronic DNA, it applies even in protein-coding exons. There is, however, statistical evidence in favour of many more driver mutations than can be accounted for by known cancer genes. These drivers appear to be distributed across a large number of genes, each of which is mutated infrequently, suggesting that the repertoire of somatically mutated human cancer genes is much larger than the ~350 currently catalogued^{39,44}. Conceivably, these infrequently mutated cancer genes confer less selective growth advantage on a clone of cancer cells than more commonly mutated cancer genes, but other explanations can also be invoked. Some analyses also indicate that there may be as many as 20 driver mutations in individual cancers, considerably more than the 5–7 previously predicted²⁴.

Understanding of the prevalence and types of somatic mutation in cancer genomes has been greatly fostered by these studies. Some cancer genomes carry >100,000 point mutations whereas others have fewer than 1,000. Some of this variation can be accounted for by previous heavy mutagenic exposures or the existence of known DNA repair defects. However, in a subset of breast cancers there are large numbers of C-to-G base substitutions, almost always occurring at cytosines that follow a thymine, for which there is no obvious explanation and for which unknown exposures and/or mutator phenotypes are presumably responsible^{42,43}.

The effects of chemotherapy on the cancer genome have also been revealed by systematic sequencing experiments. For example, gliomas that recur after treatment with the DNA alkylating agent temozolomide have been shown to carry huge numbers of mutations with a signature typical of such agents^{32,52,53}. The fact that the mutations could be detected at all indicates that these recurrences are clonal. Thus, these studies indicate that, although temozolomide only confers a short increased lifespan for the patient, almost all cells in a glioma respond and a single cell that is resistant to the chemotherapy proliferates to form the recurrence. Additional studies guided by these observations led to the identification of the underlying mutated resistance gene^{52,53}.

Beyond point mutations, some investigations have begun to explore the features of genomic rearrangements in common cancers, about which remarkably little is known. Early studies using conventional Sanger sequencing indicated that there is substantial complexity of rearrangement in these genomes^{54,55}. The recent advent of massively parallel, second-generation sequencing technologies has enabled more comprehensive genome-wide screens revealing that some cancer genomes carry hundreds of somatically acquired rearrangements, whereas others carry very few. Moreover, the distinctive patterns of rearrangement found indicate that currently uncharacterized mutational processes may be at work⁵⁶.

Sequencing of cancer genomes in the future

The large-scale, systematic sequencing studies conducted so far have been constrained by the relatively low throughput and high cost of sequencing. They have therefore generally been restricted to components of the cancer genome (for example, coding exons), to small numbers of cancer samples or to a subset of the mutational classes present. In principle, however, all the structural classes of somatic mutation can be detected genome-wide by randomly fragmenting the cancer genome and sequencing large numbers of fragments such that each base in the reference human genome is covered several times by a sequence generated from the cancer. With a high enough level of coverage, essentially a full catalogue of somatic mutations from an individual

cancer genome can be obtained, including all point mutations, rearrangements and copy number changes. Mutations in the accompanying mitochondrial genomes of the cancer will also be collected. With further adaptation this could be extended to include epigenetic alterations and could be applied to the transcriptomes of cancers to investigate the first phenotypic effects of all these changes. This catalogue will include all the driver mutations and hence all the cancer genes operating in that cancer, whether they are protein-coding genes, non-coding RNA genes or more cryptic functional elements of the genome. Indeed, if known or unknown DNA viruses have contributed to oncogenesis these will also be discovered. The catalogue will also include all the passenger mutations that incorporate the signatures of previous exposures, DNA repair defects and other mutational processes the cancer has experienced over the decades during which it was evolving.

Until recently, this was an unattainable fantasy. However, the arrival of second-generation sequencing technologies promises a new era for cancer genomics. These platforms currently generate billions of bases of DNA sequence per week, yields that are predicted to increase rapidly over the next couple of years (Fig. 3). Several proof-of-principle studies have recently been published applying these technologies to cancer samples. These have demonstrated that the current generation of massively parallel sequencing platforms can identify the full range of somatically acquired genetic alteration in cancer, including point mutations on a genome-wide basis⁵⁷, insertions and deletions⁵⁷, copy number changes⁵⁶ and genomic rearrangements⁵⁶, as well as characterizing the cancer cell transcriptome^{40,41}. Furthermore, these approaches have the potential to identify subclonal genetic diversity within the population of cancer cells⁵⁸, with particular relevance to the detection of subclones carrying drug-resistance mutations⁵⁹. Indeed, one high-coverage cancer genome sequence has recently been reported⁵⁷ and several others will emerge during the course of 2009.

Even with the remarkable technological advances in sequencing, however, the parameters of experiments to catalogue all somatically acquired variants in a cancer genome are sobering. To obtain a complete catalogue of somatic mutations from an individual human cancer may require 20-fold sequence coverage of the cancer genome, and possibly more. Somatic mutations then have to be distinguished from inherited DNA variants. Although most inherited variants that are common in human populations (>5% allele frequency) have been discovered and are registered in databases, there are myriad rare inherited single nucleotide polymorphisms and structural variants that are not. In most cancer genomes these rare germline variants far outnumber the somatic mutations present. Therefore, for the foreseeable future at least, a high-coverage sequence of the normal genome from the same individual as the cancer will be an inescapable extra

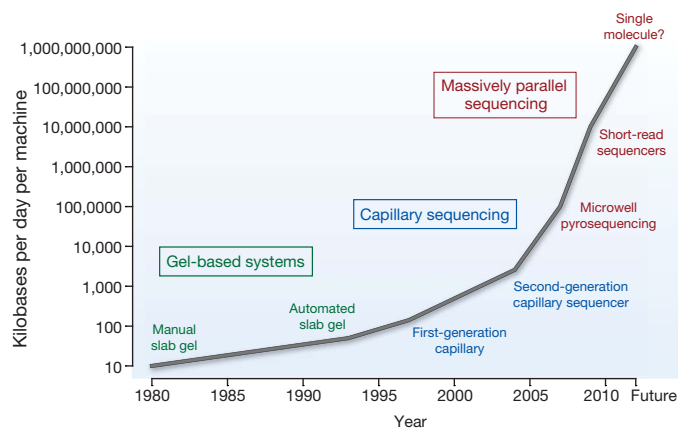


Figure 3 | Improvements in the rate of DNA sequencing over the past 30 years and into the future. From slab gels to capillary sequencing and second-generation sequencing technologies, there has been a more than a million-fold improvement in the rate of sequence generation over this time scale.

burden to allow identification of the somatic changes. Thus, more than 100,000,000,000 base pairs of DNA sequence will probably be required to identify the catalogue of somatic mutations in a single cancer genome.

Subsequently, it will be necessary to distinguish driver mutations from passengers (see Box 1). The power to distinguish clusters of driver mutations in cancer genes from chance clusters of randomly distributed passenger mutations will depend on how frequently a cancer gene is mutated and the prevalence of passenger mutations. To be confident of identifying a cancer gene that is mutated in ~5% of a particular type of cancer will require hundreds of cases to be sequenced. Each of the >100 cancer types will probably require similar sample sizes.

Coordinating the sequencing of cancer genomes

There is, therefore, much work to be done over the next few years. Ideally, it should be organized to maximize use of resources and harmonize the product. This is the mission of the International Cancer Genome Consortium (ICGC, see <http://www.icgc.org/home>). Building on the success of previous multinational, collaborative initiatives such as the Human Genome Project and the HapMap consortium, the aim of ICGC is to comprehensively characterize somatically acquired genetic events in at least fifty classes of cancer, including those with the highest global incidence and mortality, requiring high-coverage sequencing of 20,000 cancer genomes or more. The full catalogues of somatic mutation from each of these cancers will be integrated with expression and epigenetic profiles of the same cases and correlated with clinical features.

Projects under the ICGC imprimatur will adhere to predetermined standards and procedures for ethical approval, data release, intellectual property, sample quality, clinical annotation, data quality, data storage and sequencing completion. Most importantly, given the demanding nature of the task, the ICGC will coordinate studies to minimize duplication of effort and enable the most parsimonious deployment of resources.

The proposal to sequence large numbers of cancer genomes has generated controversy reminiscent of the debate before sequencing of the reference human genome almost 20 years ago. The experiments will be expensive and, to some extent, we cannot predict what will be found. However, the human genome is finite. Therefore, with further technological advances in DNA sequencing that are already in sight, this is a deliverable project that will comprehensively elucidate central questions relating to the nature of human cancer. The clinical and translational implications of such a body of work are profound. Beyond the identification of further potentially druggable cancer genes, a comprehensive catalogue of somatic mutations in carefully characterized clinical samples will generate new insights into the genetic patterns that underpin disease phenotype, prognosis, drug response and chemotherapy resistance. As the costs of sequencing whole cancer genomes drop towards US\$1,000, routine sequencing in a clinical, diagnostic setting will become feasible. Such data may drive individualized therapeutic decision-making through the ability to predict prognosis, to choose therapeutic regimens known to have efficacy for the particular genetic subtype of cancer, to sensitively monitor response to therapy and to identify rare subclones harbouring drug-resistance mutations before therapy is even initiated. Individualized therapeutics will require individualized diagnostics.

The discussion is therefore not about whether to do the experiment, but when and how. In a manner similar to the Human Genome Project we have to coordinate the work internationally to maximize use of resources and minimize duplication of effort to generate a resource of high quality so that we only have to do it once, empowering cancer research with a lasting legacy for the future.

Forward look

Approximately 100,000 somatic mutations from cancer genomes have been reported in the quarter of a century since the first somatic

mutation was found in *HRAS*. Over the next few years several hundred million more will be revealed by large-scale, complete sequencing of cancer genomes. These data will provide us with a fine-grained picture of the evolutionary processes that underlie our commonest genetic disease, providing new insights into the origins and new directions for the treatment of cancer.

1. Garcia, M. *et al.* *Global Cancer Facts and Figures 2007* (ACS, 2007).
2. von Hanseemann, D. Ueber asymmetrische Zelltheilung in epithel Krebsen und deren biologische Bedeutung. *Virchows Arch. Path. Anat.* **119**, 299 (1890).
3. Boveri, T. *Zur Frage der Entstehung Maligner Tumoren*. 1–64 (Gustav Fischer, 1914).
4. Avery, O. T., MacLeod, C. M. & McCarty, M. Studies on the chemical nature of the substance inducing transformation of Pneumococcal types: Induction of transformation by a desoxyribonucleic acid fraction isolated from *Pneumococcus* type III. *J. Exp. Med.* **79**, 137–158 (1944).
5. Watson, J. D. & Crick, F. H. Molecular structure of nucleic acids; a structure for deoxyribose nucleic acid. *Nature* **171**, 737–738 (1953).
6. Loeb, L. A. & Harris, C. C. Advances in chemical carcinogenesis: a historical review and prospective. *Cancer Res.* **68**, 6863–6872 (2008).
7. Nowell, P. & Hungerford, D. A minute chromosome in human granulocytic leukemia. *Science* **132**, 1497 (1960).
8. Rowley, J. A new consistent chromosomal abnormality in chronic myelogenous leukaemia identified by quinacrine fluorescence and Giemsa staining. *Nature* **243**, 290–293 (1973).
This is a pivotal paper describing the identification of the recurrent Philadelphia chromosome in chronic myeloid leukaemia.
9. Krontiris, T. G. & Cooper, G. M. Transforming activity of human tumor DNAs. *Proc. Natl Acad. Sci. USA* **78**, 1181–1184 (1981).
10. Shih, C., Padhy, L. C., Murray, M. & Weinberg, R. A. Transforming genes of carcinomas and neuroblastomas introduced into mouse fibroblasts. *Nature* **290**, 261–264 (1981).
11. Reddy, E. P., Reynolds, R. K., Santos, E. & Barbacid, M. A point mutation is responsible for the acquisition of transforming properties by the T24 human bladder carcinoma oncogene. *Nature* **300**, 149–152 (1982).
This paper and the next are seminal papers identifying the first somatic point mutation in a human cancer. These findings launched a new era of molecular cancer genetics research.
12. Tabin, C. J. *et al.* Mechanism of activation of a human oncogene. *Nature* **300**, 143–149 (1982).
13. Talbot, S. J. & Crawford, D. H. Viruses and tumours — an update. *Eur. J. Cancer* **40**, 1998–2005 (2004).
14. Chatterjee, A., Mambo, E. & Sidransky, D. Mitochondrial DNA mutations in human cancer. *Oncogene* **25**, 4663–4674 (2006).
15. Olivier, M., Hussain, S. P., Caron de Fromental, C., Hainaut, P. & Harris, C. C. TP53 mutation spectra and load: a tool for generating hypotheses on the etiology of cancer. *IARC Sci. Publ.* 247–270 (2004).
16. Kennedy, R. D. & D'Andrea, A. D. DNA repair pathways in clinical practice: lessons from pediatric cancer susceptibility syndromes. *J. Clin. Oncol.* **24**, 3799–3808 (2006).
17. Hanks, S. & Rahman, N. Aneuploidy-cancer predisposition syndromes: a new link between the mitotic spindle checkpoint and cancer. *Cell Cycle* **4**, 225–227 (2005).
18. Bodmer, W. & Loeb, L. A. Genetic instability is not a requirement for tumor development. *Cancer Res.* **68**, 3558–3561 (2008).
19. Loeb, L. A., Bielas, J. H., Beckman, R. A. & Bodmer, I. W. Cancers exhibit a mutator phenotype: clinical implications. *Cancer Res.* **68**, 3551–3557 (2008).
20. Lengauer, C., Kinzler, K. W. & Vogelstein, B. Genetic instabilities in human cancers. *Nature* **396**, 643–649 (1998).
21. Stewart, S. A. & Weinberg, R. A. Telomeres: cancer to human aging. *Annu. Rev. Cell Dev. Biol.* **22**, 531–557 (2006).
22. Miller, D. G. On the nature of susceptibility to cancer. The presidential address. *Cancer* **46**, 1307–1318 (1980).
23. Schinzel, A. C. & Hahn, W. C. Oncogenic transformation and experimental models of human cancer. *Front. Biosci.* **13**, 71–84 (2008).
24. Beerenwinkel, N. *et al.* Genetic progression and the waiting time to cancer. *PLoS Comput. Biol.* **3**, e225 (2007).
25. Roche-Lestienne, C. *et al.* Several types of mutations of the *Abl* gene can be found in chronic myeloid leukemia patients resistant to ST1571, and they can pre-exist to the onset of treatment. *Blood* **100**, 1014–1018 (2002).
26. Mullighan, C. G. *et al.* Genomic analysis of the clonal origins of relapsed acute lymphoblastic leukemia. *Science* **322**, 1377–1380 (2008).
27. Futreal, P. A. *et al.* A census of human cancer genes. *Nature Rev. Cancer* **4**, 177–183 (2004).
28. Touw, I. P. & Erkeland, S. J. Retroviral insertion mutagenesis in mice as a comparative oncogenomics tool to identify disease genes in human leukemia. *Mol. Ther.* **15**, 13–19 (2007).
29. Tomlins, S. A. *et al.* Recurrent fusion of *TMPRSS2* and *ETS* transcription factor genes in prostate cancer. *Science* **310**, 644–648 (2005).
This is an important paper that, in addition to identifying a major somatic genetic contributor to prostate cancer, proved that highly prevalent gene fusions can drive common adult solid tumours.
30. Soda, M. *et al.* Identification of the transforming *EML4-ALK* fusion gene in non-small-cell lung cancer. *Nature* **448**, 561–566 (2007).
31. Johnson, G. L. & Lapadat, R. Mitogen-activated protein kinase pathways mediated by ERK, JNK, and p38 protein kinases. *Science* **298**, 1911–1912 (2002).
32. The Cancer Genome Atlas Research Network. Comprehensive genomic characterization defines human glioblastoma genes and core pathways. *Nature* **455**, 1061–1068 (2008).
This is an important paper in a series of ever-larger studies designed to comprehensively screen cancer genomes for somatically mutated cancer genes.
33. Haferlach, T. Molecular genetic pathways as therapeutic targets in acute myeloid leukemia. *Hematology Am. Soc. Hematol. Educ. Prog.* **2008**, 400–411 (2008).
34. Druker, B. J. Translation of the Philadelphia chromosome into therapy for CML. *Blood* **112**, 4808–4817 (2008).
35. Sleijfer, S., Wiemer, E. & Verweij, J. Drug insight: gastrointestinal stromal tumors (GIST)—the solid tumor model for cancer-specific treatment. *Nature Clin. Pract. Oncol.* **5**, 102–111 (2008).
36. Mariani, G., Fasolo, A., De Benedictis, E. & Gianni, L. Trastuzumab as adjuvant systemic therapy for HER2-positive breast cancer. *Nature Clin. Pract. Oncol.* **6**, 93–104 (2009).
37. Bardelli, A. *et al.* Mutational analysis of the tyrosine kinome in colorectal cancers. *Science* **300**, 949 (2003).
38. Ding, L. *et al.* Somatic mutations affect key pathways in lung adenocarcinoma. *Nature* **455**, 1069–1075 (2008).
39. Greenman, C. *et al.* Patterns of somatic mutation in human cancer genomes. *Nature* **446**, 153–158 (2007).
This paper describes the heterogeneity of somatic mutation type and prevalence in human cancers, provides evidence for the concepts of passenger and driver mutations, and highlights the existence of many infrequently mutated cancer genes.
40. Jones, S. *et al.* Core signaling pathways in human pancreatic cancers revealed by global genomic analyses. *Science* **321**, 1801–1806 (2008).
41. Parsons, D. W. *et al.* An integrated genomic analysis of human glioblastoma multiforme. *Science* **321**, 1807–1812 (2008).
42. Sjoblom, T. *et al.* The consensus coding sequences of human breast and colorectal cancers. *Science* **314**, 268–274 (2006).
This is an important paper in a series of systematic large-scale screens of coding exons for point mutations in human cancer.
43. Stephens, P. *et al.* A screen of the complete protein kinase gene family identifies diverse patterns of somatic mutations in human breast cancer. *Nature Genet.* **37**, 590–592 (2005).
44. Wood, L. D. *et al.* The genomic landscapes of human breast and colorectal cancers. *Science* **318**, 1108–1113 (2007).
45. Davies, H. *et al.* Mutations of the *BRAF* gene in human cancer. *Nature* **417**, 949–954 (2002).
46. Samuels, Y. *et al.* High frequency of mutations of the *PIK3CA* gene in human cancers. *Science* **304**, 554 (2004).
47. Paez, J. G. *et al.* *EGFR* mutations in lung cancer: correlation with clinical response to gefitinib therapy. *Science* **304**, 1497–1500 (2004).
48. Stephens, P. *et al.* Lung cancer: intragenic *ERBB2* kinase mutations in tumours. *Nature* **431**, 525–526 (2004).
49. Levine, R. L. *et al.* Activating mutation in the tyrosine kinase *JAK2* in polycythemia vera, essential thrombocythemia, and myeloid metaplasia with myelofibrosis. *Cancer Cell* **7**, 387–397 (2005).
50. van Haften, G. *et al.* Somatic mutations of the histone H3K27 demethylase gene *UTX* in human cancer. *Nature Genet.* (in the press).
51. Sawyers, C. Targeted cancer therapy. *Nature* **432**, 294–297 (2004).
52. Hunter, C. *et al.* A hypermutation phenotype and somatic *MSH6* mutations in recurrent human malignant gliomas after alkylator chemotherapy. *Cancer Res.* **66**, 3987–3991 (2006).
53. Cahill, D. P. *et al.* Loss of the mismatch repair protein *MSH6* in human glioblastomas is associated with tumor progression during temozolomide treatment. *Clin. Cancer Res.* **13**, 2038–2045 (2007).
54. Bignell, G. R. *et al.* Architectures of somatic genomic rearrangement in human cancer amplicons at sequence-level resolution. *Genome Res.* **17**, 1296–1303 (2007).
55. Volik, S. *et al.* End-sequence profiling: sequence-based analysis of aberrant genomes. *Proc. Natl Acad. Sci. USA* **100**, 7696–7701 (2003).
56. Campbell, P. J. *et al.* Identification of somatically acquired rearrangements in cancer using genome-wide massively parallel paired-end sequencing. *Nature Genet.* **40**, 722–729 (2008).
57. Ley, T. J. *et al.* DNA sequencing of a cytogenetically normal acute myeloid leukaemia genome. *Nature* **456**, 66–72 (2008).
58. Campbell, P. J. *et al.* Subclonal phylogenetic structures in cancer revealed by ultra-deep sequencing. *Proc. Natl Acad. Sci. USA* **105**, 13081–13086 (2008).
59. Thomas, R. K. *et al.* Sensitive mutation detection in heterogeneous cancer specimens by massively parallel picoliter reactor sequencing. *Nature Med.* **12**, 852–855 (2006).

Acknowledgements We would like to thank N. Rahman for comments on the manuscript, G. Tang and B. Barrell for contributions to the figures and the Kay Kendall Leukaemia Fund and the Wellcome Trust for support.

Author Information Reprints and permissions information is available at www.nature.com/reprints. Correspondence and requests for materials should be addressed to M.R.S. (mrs@sanger.ac.uk).

Tumours with PI3K activation are resistant to dietary restriction

Nada Y. Kalaany^{1,2,3} & David M. Sabatini^{1,2,3,4}

Dietary restriction delays the incidence and decreases the growth of various types of tumours, but the mechanisms underlying the sensitivity of tumours to food restriction remain unknown. Here we show that certain human cancer cell lines, when grown as tumour xenografts in mice, are highly sensitive to the anti-growth effects of dietary restriction, whereas others are resistant. Cancer cells that form dietary-restriction-resistant tumours carry mutations that cause constitutive activation of the phosphatidylinositol-3-kinase (PI3K) pathway and in culture proliferate in the absence of insulin or insulin-like growth factor 1. Substitution of an activated mutant allele of PI3K with wild-type PI3K in otherwise isogenic cancer cells, or the restoration of PTEN expression in a *PTEN*-null cancer cell line, is sufficient to convert a dietary-restriction-resistant tumour into one that is dietary-restriction-sensitive. Dietary restriction does not affect a *PTEN*-null mouse model of prostate cancer, but it significantly decreases tumour burden in a mouse model of lung cancer lacking constitutive PI3K signalling. Thus, the PI3K pathway is an important determinant of the sensitivity of tumours to dietary restriction, and activating mutations in the pathway may influence the response of cancers to dietary restriction-mimetic therapies.

The life-prolonging anti-tumorigenic effects of dietary restriction (DR) were first described in the beginning of the twentieth century^{1–3}. To date, reports indicate that the incidence, as well as the growth rate, of various tumour types is reduced in laboratory rodents undergoing DR, the latter being achieved by a 10 to 50% decrease in caloric intake^{4–11}. Interestingly, the effects of DR are not uniform, with tumours from different tissues responding to restriction to different degrees, and a fraction of tumours originating in the same tissues being resistant to DR^{4,7,10–14}.

A consistent response of animals to dietary restriction is a reduction in the levels of circulating factors influencing cellular and organismal growth, notably insulin and insulin-like growth factor 1 (IGF1)^{8,11,12,15,16}. Despite the common systemic changes that accompany DR and its general anti-tumorigenic effects, the question of whether all tumours, under similar experimental conditions, respond equally to DR remains unanswered. Here we investigate the responsiveness of different types of human and mouse tumours to DR. We identify the activation status of the PI3K pathway as a molecular signature that largely predicts the sensitivity of a tumour to DR and show that by modulating PI3K activation we can convert a DR-resistant tumour into one that is DR-sensitive.

Differential sensitivities of tumour xenografts to DR

To investigate the responsiveness of different types of tumours to dietary restriction, we injected six established human cancer cell lines derived from the brain (U87-MG), colon (SW620), prostate (PC3) and breast (MDA-MB-231, MDA-MB-435, and MCF10DCIS.com¹⁷, hereafter described as MCF10DCIS) subcutaneously into NOD/SCID (non-obese diabetic, severe combined immunodeficient) mice. MDA-MB-231 and MCF10DCIS cells were also injected orthotopically into the mammary fat pads of the mice. Xenograft-bearing mice were then fed *ad libitum* a standard rodent diet for 3–4 days (20 days in the case of U87-MG and orthotopic MDA-MB-231), after which

they were subdivided into *ad libitum* fed or DR (dietary-restricted) groups for 2 to 3 weeks. All DR mice received daily meals amounting to 60% of the caloric intake of their *ad libitum* counterparts (that is, 40% DR), and underwent similar decreases in body weight (20–30%) at the end of the restriction period (Supplementary Fig. 1a, b). In contrast, the tumours formed showed differential sensitivities to DR and could be classified into two main categories: DR-sensitive tumours, which showed significant decreases in tumour volume (MDA-MB-435, MDA-MB-231 and SW620), and DR-resistant tumours, which grew to similar sizes in *ad libitum* and DR mice (PC3, U87-MG and MCF10DCIS) (Fig. 1a and Supplementary Fig. 1g). As with their subcutaneous counterparts, DR caused a significant reduction in the volume of orthotopically generated MDA-MB-231 tumour xenografts, whereas MCF10DCIS tumours were completely resistant to DR (Fig. 1b). Consistent with earlier reports^{15,16}, in response to DR all mice experienced notable decreases in plasma levels of insulin and IGF1 (Supplementary Fig. 1c–f). These findings suggest that factors other than systemic changes in the host underlie the differential sensitivities of the tumour xenografts to DR.

Constitutive PI3K signalling in DR-resistant tumours

Because the xenografted tumours responded differentially to DR despite similar decreases in insulin and IGF1 levels, we determined whether the six cancer cell lines studied have differential requirements for these factors for their growth in tissue culture. Indeed, in cell lines that form DR-sensitive tumours (MDA-MB-231, MDA-MB-435 and SW620) insulin or IGF1 caused a dose-dependent increase in cell numbers (Fig. 2a). In contrast, cell lines that generate DR-resistant tumours (MCF10DCIS, U87-MG and PC3) grew in culture in an insulin- and IGF1-independent fashion (Fig. 2b).

These results indicated that the cancer cell lines forming DR-resistant tumours have a deregulation in an insulin/IGF1-activated signalling pathway, with the PI3K/Akt pathway¹⁸ being an attractive

¹Whitehead Institute for Biomedical Research, Nine Cambridge Center, Cambridge, Massachusetts 02142, USA. ²Howard Hughes Medical Institute, Department of Biology, Massachusetts Institute of Technology, Cambridge, Massachusetts 02139, USA. ³Koch Institute for Integrative Cancer Research at MIT, 77 Massachusetts Avenue, Cambridge, Massachusetts 02139, USA. ⁴Broad Institute, Seven Cambridge Center, Cambridge, Massachusetts 02142, USA.

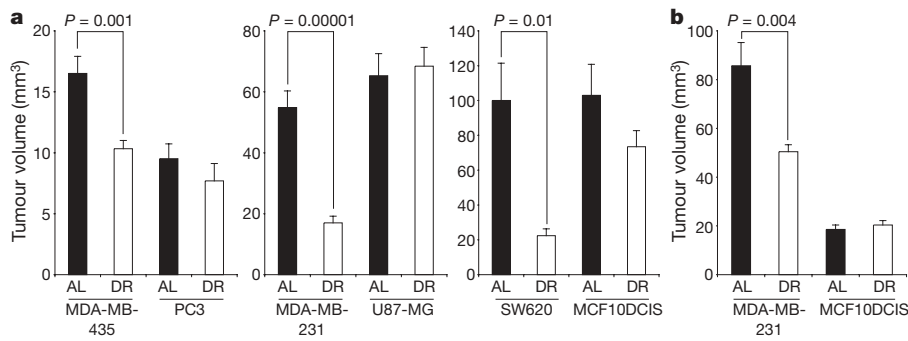


Figure 1 | Human tumour xenografts display differential sensitivities to dietary restriction. **a, b**, Volumes of six different subcutaneous (a) or two orthotopic human tumour xenografts (b) in NOD/SCID mice that were either *ad-libitum* fed (AL) or dietary restricted (DR) ($n = 6-12$ tumours). Data are means and s.e.m.; P values are indicated.

candidate. Acting through receptor tyrosine kinases, insulin and IGF1 recruit PI3K to the cell membrane¹⁹, where its activity, which is antagonized by the PTEN (phosphatase and tensin homologue deleted on chromosome 10) tumour suppressor, leads to the recruitment and

activation of Akt, a serine/threonine kinase. In turn, Akt phosphorylates and regulates several targets that enhance cellular growth and inhibit apoptosis. Consistent with a deregulation in PI3K signalling in cell lines that form DR-resistant tumours, serum withdrawal for 1 or

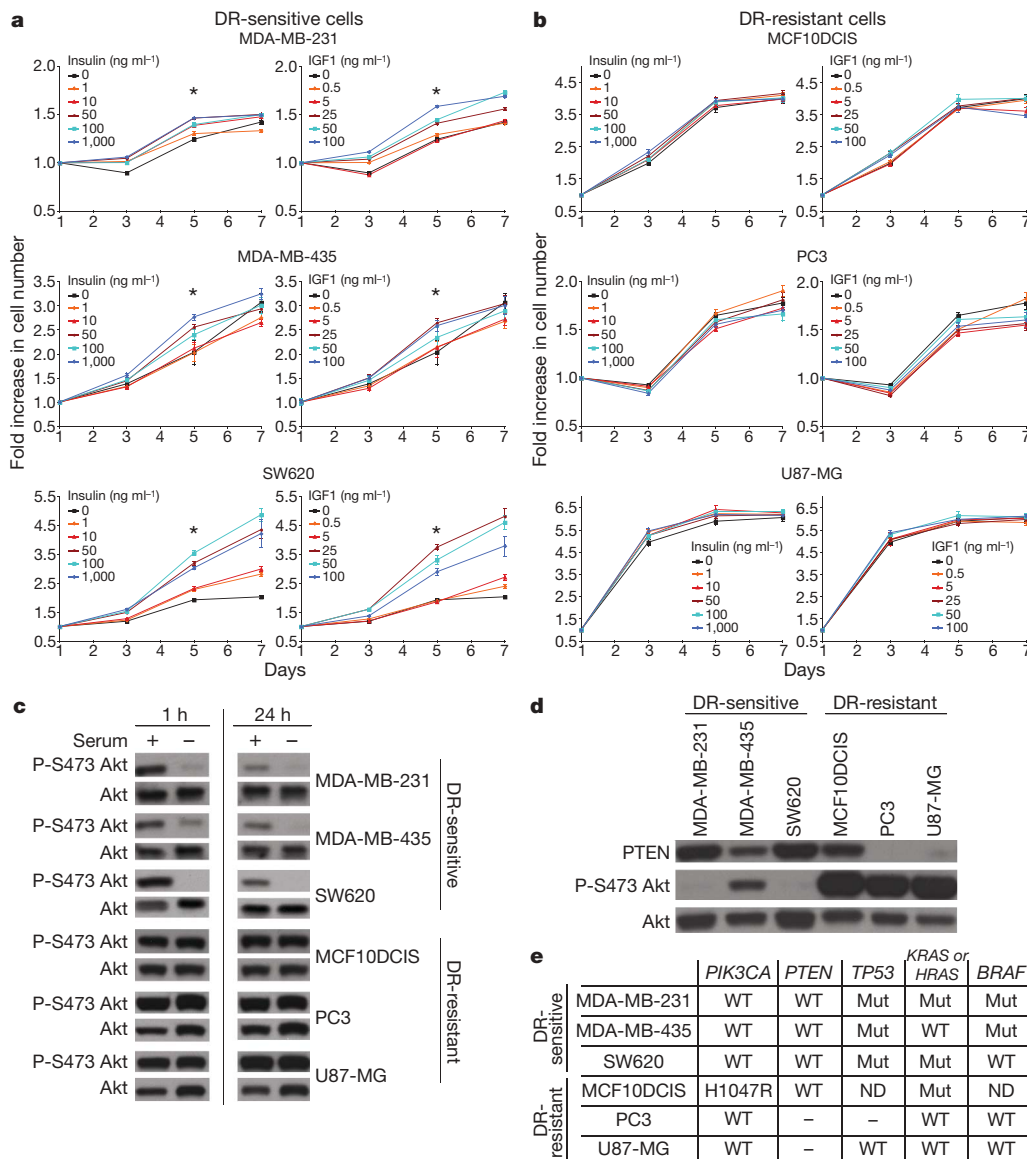


Figure 2 | Constitutive PI3K activation correlates with tumour resistance to DR. **a, b**, Proliferation curves of cancer cells that form DR-sensitive (a) and DR-resistant (b) tumours, cultured in the presence of increasing concentrations of insulin or IGF1 ($n = 6$). Data are means \pm s.e.m.; $*P \leq 0.001$ for differences between 0 and 1,000 ng ml^{-1} insulin, or between 0 and 100 ng ml^{-1} IGF1 at day 5. **c**, Phospho-S473 (P-S473) Akt and total Akt

levels in cells grown in the presence or absence of serum for 1 or 24 h. **d**, PTEN, phospho-S473 Akt and total Akt expression in the different cell lines. **e**, Sequencing results for *PIK3CA* hot-spot mutations, loss of or mutational status of *PTEN*, *TP53*, *KRAS*, *HRAS* and *BRAF* in all cell lines studied. Mut, mutant; ND, not determined; WT, wild-type. '-' indicates absence of the gene.

24 h did not affect Akt S473 phosphorylation, a marker of Akt activation, in MCF10DCIS, PC3 and U87-MG cells, but did in MDA-MB-231, MDA-MB-435 and SW620 cells (Fig. 2c).

Analysis of PTEN expression showed that PTEN loss could account for the serum-insensitive Akt activity²⁰ in PC3 and U87-MG, but not in MCF10DCIS cells (Fig. 2d). Activating mutations in the *PIK3CA* gene, which encodes the catalytic subunit of PI3K, also lead to constitutive Akt activity in cancer cells^{21–24}. By sequencing in all the cell lines exons 9 and 20 of *PIK3CA*—which can be the sites of the ‘hot-spot’ E545K and H1047R mutations^{21,25}, respectively—we found that the MCF10DCIS cells harbour a previously unknown H1047R mutation. None of the cell lines that form DR-sensitive tumours have lost PTEN function or carry PI3K activating mutations²⁶ (Fig. 2e). Furthermore, no other common oncogene-activating (for example, *HRAS*, *KRAS* or *BRAF*) or tumour suppressor-inactivating (for example, *TP53*) mutations correlated with tumour cell sensitivity to insulin/IGF1 *in vitro* or tumour sensitivity to DR *in vivo*²⁶ (Fig. 2e). Although PI3K can be directly activated by Ras²⁷ and this is necessary for the initiation of Ras-driven tumours²⁸, the MDA-MB-231 and SW620 cell lines carrying activated *KRAS* alleles form DR-sensitive tumours (Fig. 2e). These results indicate that tumour resistance to DR correlates with constitutive activation (for example, through *PIK3CA* mutations or PTEN loss), rather than with hyperactivation of the PI3K pathway.

DR increases apoptosis in DR-sensitive tumours

Although phospho-S473 Akt could not be detected in DR-sensitive tumours by immunohistochemistry, it was readily detectable in DR-resistant tumours and its levels did not decrease after DR (data not shown). Thus, to assay for changes in PI3K signalling in DR-sensitive tumours after restriction, we examined the FOXO1 transcription factor—a major downstream target of Akt that is selectively phosphorylated as a result of PI3K activation²¹. Phosphorylation of FOXO1 by Akt leads to its cytoplasmic sequestration and degradation so that a decrease in Akt signalling causes relocalization of FOXO1 to the nucleus, where it induces transcription of pro-apoptotic and anti-proliferative genes²⁹. In the DR-resistant tumours (PC3 and MCF10DCIS), FOXO1 was predominantly localized to the cytoplasm of tumour cells in both *ad libitum* and DR mice (Supplementary Fig. 2a, b). In contrast, DR caused a significant relocalization of FOXO1 from the cytoplasm to the nucleus in the cells of DR-sensitive tumours (MDA-MB-435, SW620 and MDA-MB-231) (Supplementary Fig. 2a, b), indicating that in these tumours DR inhibited PI3K signalling.

Suppression by DR of the growth of DR-sensitive tumours could be the result of enhanced cellular death, decreased cellular proliferation, or both. To distinguish between these possibilities, we measured the number of tumour cells that were proliferating or undergoing apoptosis by assaying for Ki67 staining and caspase 3 cleavage, respectively. Although DR tended to decrease the number of Ki67-positive cells in the DR-sensitive but not DR-resistant tumours, these effects did not reach statistical significance (data not shown). However, a common apoptotic response to DR was observed in all DR-sensitive, but not DR-resistant tumour xenografts (Supplementary Fig. 2c, d), correlating with the presence of nuclear FOXO1 in DR-sensitive tumours (Supplementary Fig. 2a, b). Indeed, whereas PC3 tumours maintained low levels of apoptosis under *ad libitum* or DR conditions, MDA-MB-435 tumours increased cellular apoptotic rates by 5.6-fold (from 7% to 39%; $P = 0.003$) and SW620 tumours showed massive DR-induced apoptosis, which occurred at the edges of tumours (21.3-fold increase, from 2% to 42.5%) and also at their centres (2.9-fold increase, from 30.7% to 88.8%) averaging to a 3.6-fold increase (from 18.4% to 65.6%; $P = 0.0003$) in whole tumours (Supplementary Fig. 2c). In orthotopic MCF10DCIS and MDA-MB-231 xenografted tumours, no obvious apoptosis was noted after 12 days of DR (data not shown). Nevertheless, when these tumours were collected only 2 days after restriction, a significant sixfold increase in

apoptosis was observed in the MDA-MB-231 (1.1 to 6.6%; $P = 0.05$) but not the MCF10DCIS tumours (Supplementary Fig. 2d), indicating that in MDA-MB-231 tumours, sensitivity to DR-induced apoptosis occurs at earlier stages of the tumorigenic process. Hence, these analyses show that decreased PI3K signalling in human tumour xenografts correlates with DR-induced apoptosis.

Conversion of a tumour from DR-resistance to DR-sensitivity

The correlation between tumour sensitivity to DR and the activation status of the PI3K pathway led us to consider that constitutive PI3K signalling in tumour cells is sufficient to decrease the sensitivity of tumours to DR. To begin testing this idea, we used two cell lines derived from the DLD-1 colorectal cancer cell line²¹. These cells are isogenic except that one carries a wild-type allele (DLD-WT) and the other has a constitutively active mutant allele (E545K; DLD-mut) of *PIK3CA*. Consistent with their genetic statuses, DLD-mut, but not DLD-WT cells, maintained high levels of phospho-S473 Akt after serum withdrawal for 1 or 24 h (Fig. 3a). The growth responses of the DLD-mut and the DLD-WT cells in culture to increasing concentrations of insulin or IGF1 (Fig. 3b, c) were reminiscent of those of the cancer lines that form DR-resistant and DR-sensitive tumours, respectively (Fig. 2).

In xenograft studies, the subcutaneous injection of 0.6×10^6 DLD-WT or 0.25×10^6 DLD-mut cells into NOD/SCID mice yielded tumours of approximately equal volume in 18 days (Fig. 3d). The application of a 14-day DR regimen to xenografted mice 4 days after tumour cell injection resulted in DLD-WT tumours that were 2.7-fold smaller in volume than those in *ad libitum* mice (Fig. 3d). Although DLD-mut tumours grew at a faster rate than DLD-WT tumours, they showed no significant decrease in tumour size after DR (Fig. 3d). There was a significant relocalization of FOXO1 from the cytoplasm to the nucleus in the DLD-WT tumour cells after DR (Fig. 4a). Conversely, FOXO1 remained cytoplasmic in DLD-mut cells regardless of restriction (Fig. 4a). Furthermore, DLD-WT but not DLD-mut tumours had a significant enhancement in caspase 3 cleavage (12.5-fold) after the 14-day DR period (Fig. 4c). Thus, the presence of a PI3K activating mutation in an otherwise DR-sensitive tumour cell line is sufficient to protect tumours formed by these cells from the anti-growth and pro-apoptotic effects of DR.

Because PTEN loss also leads to aberrant PI3K activation²⁰, we investigated the role of PTEN in determining tumour sensitivity to DR. We made use of a *PTEN*-null cell line (U87-MG) that was engineered to induce PTEN expression after the addition of doxycycline³⁰. In culture *in vitro*, doxycycline-induced PTEN expression caused a decrease in phospho-S473 Akt levels in these cells (Fig. 3e, left panel) and was sufficient to transform the serum-insensitive U87-MG cells (see Fig. 2c) into serum-sensitive cells that responded to serum withdrawal by decreasing levels of phospho-S473 Akt (Fig. 3e, right panel). In contrast to the *PTEN*-null U87-MG cells (Fig. 2b), *PTEN*-expressing U87-MG cells increased their net growth rates in response to increasing levels of insulin and IGF1 (Fig. 3f).

In vivo doxycycline administration induced PTEN expression in tumour xenografts formed from U87-MG cells (Supplementary Fig. 3a, b). As expected from restoring the expression of a tumour suppressor, the growth rate of U87-MG tumours decreased significantly in the presence of doxycycline, regardless of diet. Nevertheless, the re-expression of PTEN was sufficient to switch the response of U87-MG tumours from being resistant to DR (Figs 1a and 3g, left panel) to being DR-sensitive (Fig. 3g, right panel). After DR, the number of Ki67-positive cells tended to decrease (by 15%) in *PTEN*-expressing U87-MG tumours, but without reaching statistical significance (data not shown). In the absence of PTEN, FOXO1 was mostly sequestered in the cytoplasm of U87-MG tumour cells in *ad libitum* as well as DR mice (Fig. 4b). However, after DR of mice bearing *PTEN*-expressing U87-MG tumours, FOXO1 relocalized to the nucleus of tumour cells (Fig. 4b), and this correlated with enhanced apoptosis (Fig. 4d), consistent with results obtained for all DR-sensitive tumours

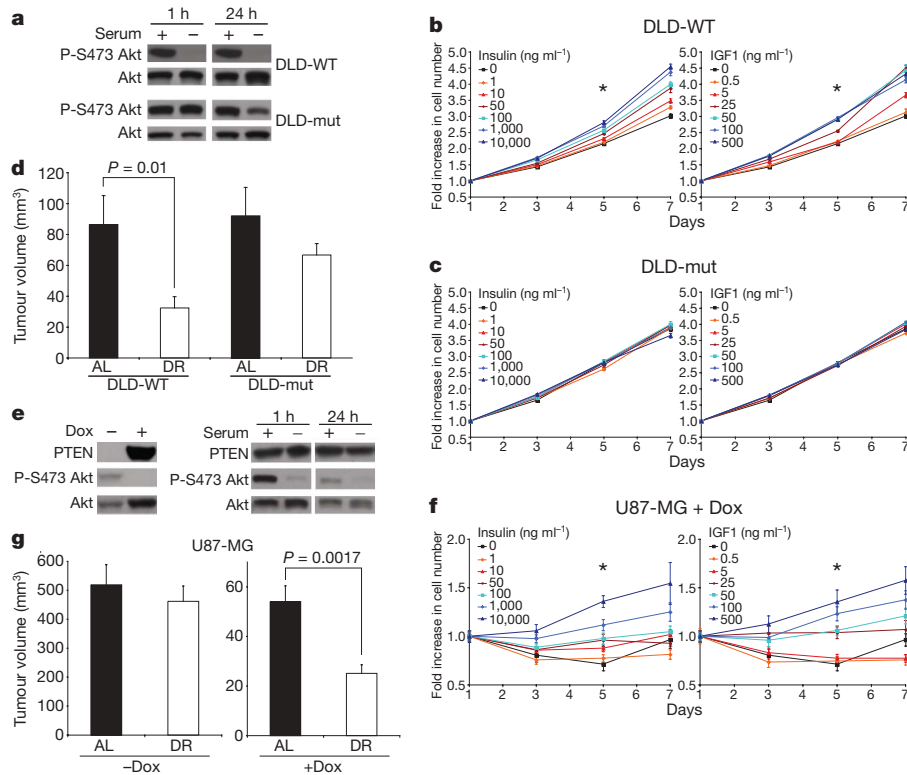


Figure 3 | PIK3CA activating mutations or PTEN loss suppress tumour sensitivity to DR. **a**, Phospho-S473 (P-S473) Akt and total Akt levels in DLD-WT and DLD-mut cells, in the presence or absence of serum for 1 or 24 h. **b, c**, Proliferation curves of DLD-WT, DLD-mut, and doxycycline (Dox)-treated ($1 \mu\text{g ml}^{-1}$) U87-MG cells in the presence of increasing concentrations of insulin or IGF1 ($n = 6$). $*P \leq 0.001$ as in Fig. 2a, b. **d**, Volumes of DLD-WT and DLD-mut tumours in AL or DR mice

($n = 7-10$). **e**, PTEN, phospho-S473 Akt and total Akt levels in U87-MG cells in the presence or absence of doxycycline (left panel), and in doxycycline-treated U87-MG cells in the presence or absence of serum for 1 h or 24 h (right panel). **g**, Volumes of U87-MG tumours in AL and DR mice administered drinking water with or without doxycycline ($n = 7-9$). Data represent means and s.e.m.

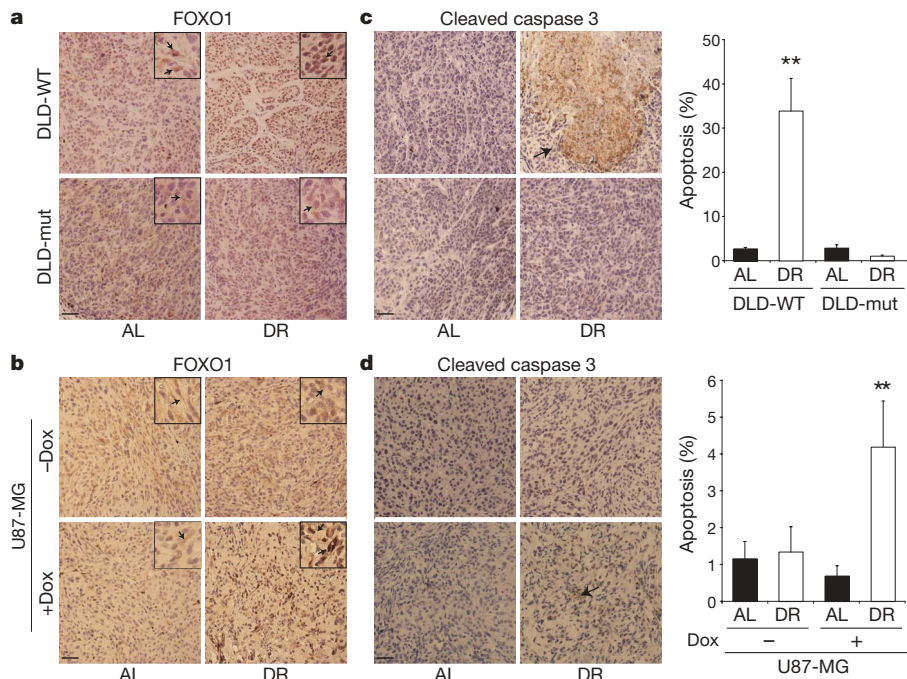


Figure 4 | Effects of modulation of PI3K signalling on the apoptotic response of tumours to DR. **a-d**, Immunohistochemical analyses of FOXO1 (**a, b**) and cleaved caspase 3 (**c, d**) in tumours formed by DLD-WT and DLD-mut cells and by the doxycycline (Dox)-inducible U87-MG cells in mice treated or non-treated with Dox. Graphs to the right of the images indicate the percentage of total cells that are positive for cleaved caspase 3. Data in

graphs are means and s.e.m., measured in nine images (1,000 nuclei counted per image) from three different tumours per group. $**P \leq 0.01$. All images were acquired at the same magnification; scale bars, $20 \mu\text{m}$. Framed insets in **a** and **b** are a 3.9-fold magnification of a representative area of the corresponding larger image. Arrows point to immunoreactivity for FOXO1 (**a, b**) or cleaved caspase 3 (**c, d**).

(Supplementary Fig. 2 and Fig. 4). Therefore, restoration of PTEN expression in a DR-resistant, *PTEN*-null cancer cell line is sufficient to convert it to a cell line that forms DR-sensitive tumour xenografts *in vivo*.

FOXO1 overexpression sensitizes tumours to DR

To investigate the effects of the FOXO factors on the response of tumours to DR, we overexpressed FOXO1 in SW620 cells (Supplementary Fig. 4a), and analysed the sensitivity to DR of the corresponding tumour xenografts compared to control tumours expressing green fluorescent protein (GFP). A cell line that forms DR-sensitive rather than DR-resistant tumours was used because FOXO1 function is unlikely to be regulated by DR in cancer cells in which Akt is constitutively active. FOXO1 overexpression in SW620 xenograft tumours slightly slowed tumour growth (30% decrease) in the *ad libitum* feeding condition, probably owing to aberrant entry of exogenous FOXO1 into the nucleus (Supplementary Fig. 4b). Notably, in tumours overexpressing FOXO1, DR caused a greater fold reduction in tumour volume (4.1-fold) than in tumours expressing GFP (2.3-fold) (Supplementary Fig. 4b). Immunohistochemical analyses showed that after DR, FOXO1 localized to the nucleus in FOXO1-overexpressing as well as control tumours (Supplementary Fig. 4c), particularly in areas that coincided with enhanced caspase 3 cleavage (Supplementary Fig. 4d). Under *ad libitum* conditions the number of apoptotic cells was slightly enhanced in FOXO1-overexpressing tumours compared to the control tumours. However, the

DR-induced apoptotic response increased to a greater extent after DR in FOXO1-overexpressing tumours than in control tumours (Supplementary Fig. 4d). No significant changes in proliferation were detected among the different tumours (data not shown). These findings are consistent with FOXO1 having a crucial role in the anti-tumour effects of DR, but do not preclude the involvement of other PI3K effectors, including other FOXO family members.

A murine *PTEN*-null prostate cancer is resistant to DR

We next examined the effects of DR in two engineered mouse models of cancer. The first model (*probasin-Cre; PTEN^{lox/lox}*—hereafter *Pb-Cre; PTEN^{L/L}*) is driven by *PTEN* loss in the prostate and recapitulates human prostate cancer progression³¹. The second (*KRAS^{LA2}; p53-lox-stop-lox/WT*—hereafter *KRAS^{LA2}; p53^{LSL/WT}*) is driven by *KRAS* activation as well as *p53* heterozygosity and leads to the development of lung adenocarcinoma^{32,33}. Compared to the *ad libitum* condition, DR significantly reduced the size of tumour nodules (42% decrease) in the lungs of 7-week-old *KRAS^{LA2}; p53^{LSL/WT}* mice (Fig. 5a). Although the lung tumours were of similar pathological grade under both the *ad libitum* feeding and dietary restriction (Fig. 5b), DR strongly decreased the number of proliferating tumour cells (fourfold; 12.5% to 3.1%; $P = 8 \times 10^{-8}$) without affecting the rates of apoptosis (Fig. 5c, d).

In the prostates of 11-week-old *Pb-Cre; PTEN^{L/L}* mice, DR did not have any detectable effect on the extent or histological appearance of the prostate intraepithelial neoplasia (Fig. 5e) or on the activation levels of Akt (Fig. 5f). Indeed, neither the proliferative nor the apoptotic

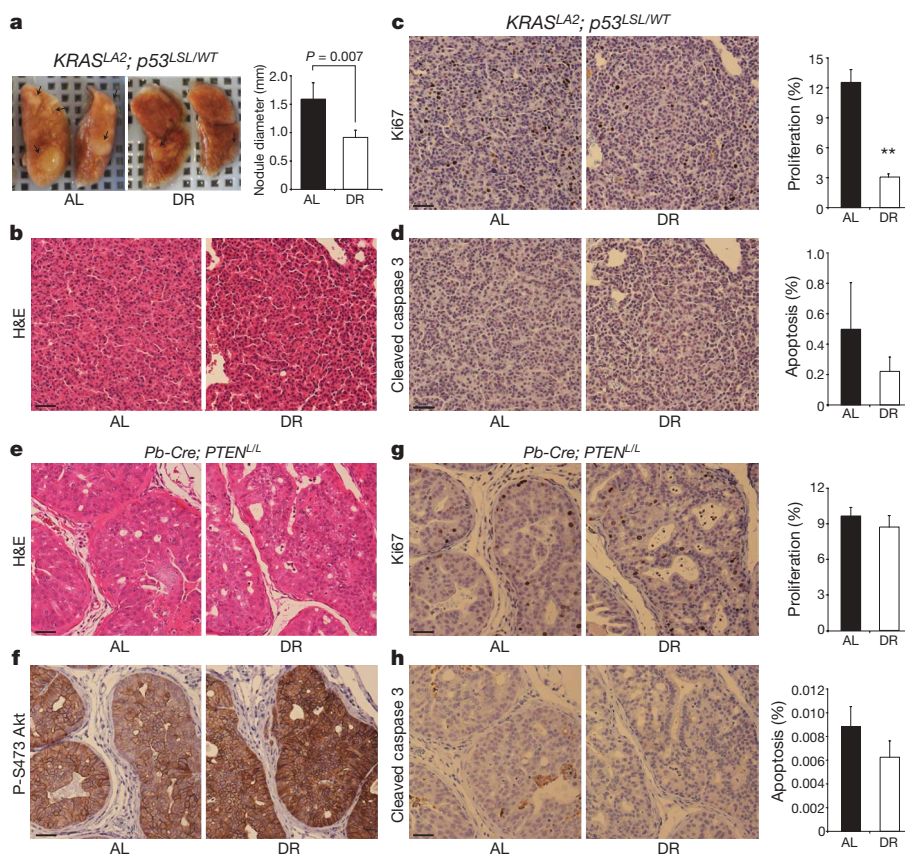


Figure 5 | A *KRAS* mouse model of lung cancer, but not a *PTEN*-null model of prostate cancer, is sensitive to DR. **a**, Representative images of lungs and average diameter of tumour nodules on the surface of the lungs (graph) of 7-week-old *KRAS^{LA2}; p53^{LSL/WT}* mice under AL or DR conditions ($n = 3$). **b–d**, H&E staining (**b**) and immunohistochemical analyses of Ki67 (**c**) and cleaved caspase 3 (**d**) in sections prepared from lungs in **a**. **e–h**, H&E staining (**e**) and immunohistochemical analyses of phospho-Akt S473 (**f**), Ki67 (**g**) and cleaved caspase 3 (**h**) in prostates of 11-week-old *Pb-Cre; PTEN^{L/L}*

mice under AL or DR conditions. Graphs to the right of images indicate the percentage of total cells that are positive for Ki67 (proliferation) or cleaved caspase 3 (apoptosis). Data are means and s.e.m. of the percentage of proliferating (**c, g**) or apoptotic cells (**d, h**) measured in ten images (1,000 nuclei counted per image) from two different tumours per group. All pictures were captured under the same magnification; scale bars, 20 μm . $**P = 8.3 \times 10^{-8}$.

indices of the prostate intraepithelial neoplasia were affected by DR (Fig. 5g, h). Similar results were obtained in the prostates of 7–8-week-old *Pb-Cre; PTEN^{L/L}* mice given the same DR regimen (data not shown). Thus, consistent with the human tumour xenograft studies, engineered mouse tumours without mutations that confer constitutive PI3K signalling seem to be DR-sensitive, whereas those with such mutations are DR-resistant.

Discussion

Dietary restriction has long been known to suppress tumour growth in laboratory rodents¹⁰. We find that genetic alterations in *PIK3CA* or *PTEN* can predict the response of tumours to DR, classifying them into DR-sensitive and DR-resistant tumours. Our results indicate that differential levels of PI3K activation in tumours contribute to their differential sensitivities to DR. It is important to note that we have studied the effects of relatively short-term DR on the growth of tumours at early stages of the tumorigenic process. Thus, at more advanced tumour stages, signalling pathways other than PI3K may have a central involvement in mediating the effects of DR.

It is interesting to consider which of the downstream effectors of PI3K may mediate the responses of tumours to DR that we have observed. Attractive candidates are the FOXO family of transcription factors that regulate proliferation and apoptosis. Reminiscent of the cell-type- and tissue-microenvironment-dependent effects of the FOXO factors on proliferation and apoptosis³⁴, we find that DR causes strong suppression of proliferation in the engineered mouse lung cancer model, while having a prominent pro-apoptotic effect in the human tumour xenograft models. After DR, FOXO moves from the cytoplasm to the nucleus only in the cells of DR-sensitive tumours and overexpression of FOXO sensitizes tumours to the anti-growth effects of DR. These results indicate an important role for the FOXO factors but do not exclude potential roles for other PI3K effectors. The activity of signalling molecules that interact at several levels with the PI3K pathway, such as mTOR, AMPK and SIRT1, probably fine-tune the sensitivities of tumours to DR (see Supplementary Discussion).

Our findings are consistent with the effects of dietary restriction on the growth of early tumours being the result of both systemic changes in the host and signalling events intrinsic to the tumour. These findings should allow for the prediction of the responsiveness of a specific tumour to DR, on the basis of a readily measurable molecular signature, namely the activation status of the PI3K pathway in the tumour cells.

METHODS SUMMARY

Cell lines were obtained from the Karmanos Cancer Institute (MCF10DCIS.com), B. Vogelstein (DLD-WT and DLD-mut), M. M. Georgescu (U87-MG) and the American Type Culture Collection (ATCC) (all others), and grown under conditions described by the providers. SW620 cell lines stably overexpressing human FOXO1 or GFP were generated by infection with lentiviruses expressing the corresponding complementary DNA. Cellular proliferation was measured using the XTT kit (Roche). For immunoblotting, protein lysates were probed with phospho-S473 Akt, Akt or PTEN antibodies (1:1,000, Cell Signaling Technologies). Immunohistochemical detection of PTEN, FOXO1 and cleaved caspase3 antibodies (1:100, Cell Signaling Technologies) was performed on paraffin-embedded, sliced tumour sections according to the manufacturer's protocols. The PI3K mutations E545K and H1047R were detected by sequencing two *PIK3CA* fragments amplified by RT-PCR from total RNA extracted from each cell line. All animal studies and procedures were approved by the MIT Institutional Animal Care and Use Committee. Mouse xenografts were generated by injecting tumour cells subcutaneously into male (female for breast cancer cell lines) or orthotopically in the fat pads of female NOD/SCID mice. Five-week-old *KRAS^{LΔ2}; p53^{LSL/WT}* mice, obtained from the Jackson laboratory^{32,33}, and 5- and 9-week-old *Pb-Cre; PTEN^{L/L}* (ref. 31) mice were used in the DR studies. DR was achieved by providing individually caged mice a daily portion of a chow diet fortified with vitamins and minerals amounting to 60% of the daily food intake of their *ad libitum* counterparts. Mice were euthanized at the beginning of the light cycle, after retro-orbital blood withdrawal. Tumours were collected, measured and either flash-frozen in liquid nitrogen or fixed in formalin. Plasma insulin and IGF1 levels were determined by ELISA (CrystalChem and Diagnostic Systems

Laboratories, respectively). Data are presented as means ± s.e.m., and significant *P* values (≤ 0.05) were obtained by performing non-paired, two-tailed Student's *t*-tests to compare two groups.

Full Methods and any associated references are available in the online version of the paper at www.nature.com/nature.

Received 16 July 2008; accepted 15 January 2009.

Published online 11 March 2009.

- Moreschi, C. Beziehung zwischen Ernährung und Tumorwachstum. *Zeitschrift f. Immunitätsforsch. Originale* **2**, 651–675 (1909).
- Rous, P. The influence of diet on transplanted and spontaneous tumors. *J. Exp. Med.* **20**, 351–413 (1914).
- McCay, C. M., Crowell, M. F. & Maynard, L. A. The effect of retarded growth upon the length of life span and upon the ultimate body size. *J. Nutr.* **10**, 63–79 (1935).
- Tannenbaum, A. & Silverstone, H. The influence of the degree of caloric restriction on the formation of skin tumors and hepatomas in mice. *Cancer Res.* **9**, 724–727 (1949).
- Tannenbaum, A. & Silverstone, H. Effect of limited food intake on survival of mice bearing spontaneous mammary carcinoma and on the incidence of lung metastases. *Cancer Res.* **13**, 532–536 (1953).
- Cheney, K. E. *et al.* Survival and disease patterns in C57BL/6J mice subjected to undernutrition. *Exp. Gerontol.* **15**, 237–258 (1980).
- Weindruch, R. & Walford, R. L. Dietary restriction in mice beginning at 1 year of age: effect on life-span and spontaneous cancer incidence. *Science* **215**, 1415–1418 (1982).
- Klurfeld, D. M., Welch, C. B., Davis, M. J. & Kritchevsky, D. Determination of degree of energy restriction necessary to reduce DMBA-induced mammary tumorigenesis in rats during the promotion phase. *J. Nutr.* **119**, 286–291 (1989).
- Zhu, Z., Haegle, A. D. & Thompson, H. J. Effect of caloric restriction on pre-malignant and malignant stages of mammary carcinogenesis. *Carcinogenesis* **18**, 1007–1012 (1997).
- Kritchevsky, D. Caloric restriction and cancer. *J. Nutr. Sci. Vitaminol. (Tokyo)* **47**, 13–19 (2001).
- Thompson, H. J., Zhu, Z. & Jiang, W. Dietary energy restriction in breast cancer prevention. *J. Mammary Gland Biol. Neoplasia* **8**, 133–142 (2003).
- Sell, C. Caloric restriction and insulin-like growth factors in aging and cancer. *Horm. Metab. Res.* **35**, 705–711 (2003).
- Cheney, K. E. *et al.* The effect of dietary restriction of varying duration on survival, tumor patterns, immune function, and body temperature in B10C3F1 female mice. *J. Gerontol.* **38**, 420–430 (1983).
- Pugh, T. D., Oberley, T. D. & Weindruch, R. Dietary intervention at middle age: caloric restriction but not dehydroepiandrosterone sulfate increases lifespan and lifetime cancer incidence in mice. *Cancer Res.* **59**, 1642–1648 (1999).
- Ruggeri, B. A., Klurfeld, D. M., Kritchevsky, D. & Furlanetto, R. W. Caloric restriction and 7,12-dimethylbenz(a)anthracene-induced mammary tumor growth in rats: alterations in circulating insulin, insulin-like growth factors I and II, and epidermal growth factor. *Cancer Res.* **49**, 4130–4134 (1989).
- Breese, C. R., Ingram, R. L. & Sonntag, W. E. Influence of age and long-term dietary restriction on plasma insulin-like growth factor-1 (IGF-1), IGF-1 gene expression, and IGF-1 binding proteins. *J. Gerontol.* **46**, B180–B187 (1991).
- Miller, F. R., Santner, S. J., Tait, L. & Dawson, P. J. MCF10DCIS.com xenograft model of human comedo ductal carcinoma *in situ*. *J. Natl. Cancer Inst.* **92**, 1185–1186 (2000).
- Manning, B. D. & Cantley, L. C. AKT/PKB signaling: navigating downstream. *Cell* **129**, 1261–1274 (2007).
- Engelman, J. A., Luo, J. & Cantley, L. C. The evolution of phosphatidylinositol 3-kinases as regulators of growth and metabolism. *Nature Rev. Genet.* **7**, 606–619 (2006).
- Salmena, L., Carracedo, A. & Pandolfi, P. P. Tenets of PTEN tumor suppression. *Cell* **133**, 403–414 (2008).
- Samuels, Y. *et al.* Mutant PIK3CA promotes cell growth and invasion of human cancer cells. *Cancer Cell* **7**, 561–573 (2005).
- Kang, S., Bader, A. G. & Vogt, P. K. Phosphatidylinositol 3-kinase mutations identified in human cancer are oncogenic. *Proc. Natl. Acad. Sci. USA* **102**, 802–807 (2005).
- Saal, H. H. *et al.* PIK3CA mutations correlate with hormone receptors, node metastasis, and ERBB2, and are mutually exclusive with PTEN loss in human breast carcinoma. *Cancer Res.* **65**, 2554–2559 (2005).
- Zhao, J. J. *et al.* The oncogenic properties of mutant p110 α and p110 β phosphatidylinositol 3-kinases in human mammary epithelial cells. *Proc. Natl. Acad. Sci. USA* **102**, 18443–18448 (2005).
- Samuels, Y. *et al.* High frequency of mutations of the *PIK3CA* gene in human cancers. *Science* **304**, 554 (2004).
- Cancer Cell Line Project. <www.sanger.ac.uk/genetics/CGP/CellLines/> (1992).
- Rodriguez-Viciana, P. *et al.* Phosphatidylinositol-3-OH kinase as a direct target of Ras. *Nature* **370**, 527–532 (1994).
- Gupta, S. *et al.* Binding of ras to phosphoinositide 3-kinase p110 α is required for ras-driven tumorigenesis in mice. *Cell* **129**, 957–968 (2007).
- Calnan, D. R. & Brunet, A. The FoxO code. *Oncogene* **27**, 2276–2288 (2008).

30. Radu, A., Neubauer, V., Akagi, T., Hanafusa, H. & Georgescu, M. M. PTEN induces cell cycle arrest by decreasing the level and nuclear localization of cyclin D1. *Mol. Cell. Biol.* **23**, 6139–6149 (2003).
31. Wang, S. *et al.* Prostate-specific deletion of the murine Pten tumor suppressor gene leads to metastatic prostate cancer. *Cancer Cell* **4**, 209–221 (2003).
32. Johnson, L. *et al.* Somatic activation of the *K-ras* oncogene causes early onset lung cancer in mice. *Nature* **410**, 1111–1116 (2001).
33. Ventura, A. *et al.* Restoration of p53 function leads to tumour regression *in vivo*. *Nature* **445**, 661–665 (2007).
34. Fu, Z. & Tindall, D. J. FOXOs, cancer and regulation of apoptosis. *Oncogene* **27**, 2312–2319 (2008).

Supplementary Information is linked to the online version of the paper at www.nature.com/nature.

Acknowledgements We thank B. Vogelstein for providing the isogenic DLD-1 cell lines and M. M. Georgescu for the doxycycline-inducible U87-MG cell line; T. Jacks for the *KRAS*^{LA2}; *p53*^{L^{SL}/WT} mice and H. Wu for the *Pb-Cre*; *PTEN*^{L/L} mice;

F. Reinhardt for assistance with animal experiments; R. Bronson for histological analysis; the Histology Facility at the Koch Institute for Integrative Cancer Research and the Histology Core Laboratory at MIT for assistance with sectioning and immunohistochemistry; the Imaging Platform at the Broad Institute for assistance with image analysis; R. Weinberg, D. Guertin, Y. Chudnovsky and Y. Sancak for critical reading of the manuscript; and members of the Sabatini and Weinberg laboratories for support and discussions. This research is supported by the Alexander and Margaret Stewart Trust Award, the David H. Koch Cancer Research Award and National Institutes of Health grants R01 AI04389 and R01 CA129105. D.M.S. is an investigator of the Howard Hughes Medical Institute.

Author Contributions D.M.S. and N.Y.K. conceived the project and designed the experiments. N.Y.K. performed the experiments. The manuscript was written by N.Y.K. and edited by D.M.S.

Author Information Reprints and permissions information is available at www.nature.com/reprints. Correspondence and requests for materials should be addressed to D.M.S. (sabatini@wi.mit.edu).

METHODS

Cell lines. MDA-MB-231, MDA-MB-435, PC3 and SW620 cell lines were obtained from the ATCC and cultured in DMEM supplemented with 10% FBS. SW620 cell lines stably overexpressing human FOXO1 or GFP were generated by infection with lentiviruses expressing the corresponding cDNA, and were selected for puromycin resistance ($2 \mu\text{g ml}^{-1}$) for 7 days before injection into mice. MCF10DCIS.com cell lines were from the Karmanos Cancer Institute and grown in DMEM/F12 with 5% horse serum. The isogenic cell lines DLD-WT and DLD-mut were from B. Vogelstein and cultured as described²¹. The doxycycline-inducible U87-MG cell lines were provided by M. M. Georgescu and maintained as described³⁰.

Proliferation assay. On day 0, cell lines were seeded in their appropriate media in four 96-well plates each, at a density of 3,000 (DLD-WT, DLD-mut and SW620), 5,000 (MCF10DCIS, PC3) or 7,500 (MDA-MB-231, MDA-MB-435 and U87-MG) cells per well, and all plates were incubated overnight. On day 1, three assay plates (for days 3, 5 and 7) of each cell line were washed once with DMEM in the absence of serum and their media were replaced with DMEM supplemented with 0.1% FBS only or with 0.1% FBS and 12 different concentrations of insulin (1, 10, 50, 100, 1,000 and 10,000 ng ml^{-1}) or IGF1 (0.5, 5, 25, 50, 100 and 500 ng ml^{-1}). Six wells per media condition were used in each plate. The fourth plate from each cell line was used as a baseline day 1 measurement of cell number without addition of the assay media. The cell proliferation kit II (XTT, Roche) was used to measure cell number on days 1, 3, 5 and 7 of the assay.

Immunoblotting. Cells were rinsed once in ice-cold PBS and collected in lysis buffer containing 50 mM HEPES, pH 7.4, 40 mM NaCl, 2 mM EDTA, 1.5 mM orthovanadate, 50 mM NaF, 10 mM pyrophosphate, 10 mM glycerophosphate, EDTA-free protease inhibitors (Roche) and 1% Triton X-100. Tumour tissues were homogenized in lysis buffer supplemented with 1% deoxycholate and 0.1% SDS. Proteins from total lysates were resolved by 8–12% SDS-PAGE, and analysed by immunoblotting as described³⁵ using antibodies for phospho-S473 Akt, Akt and PTEN (1:1,000, Cell Signaling Technology).

DNA sequencing. RNA was extracted and cDNA was prepared from all cell lines as previously described³⁶. Two fragments of the *PIK3CA* gene (NM_006218) were amplified by PCR that enclosed either the E545K (nucleotides 1573–1996) or the H1047R (nucleotides 3213–3466) PI3K hot-spot mutation²¹ using primer pairs PIK1-F/PIK3-R or PIK5-F/PIK2-R, respectively. PCR conditions were as follows: 95 °C for 3 min, 40 cycles of 94 °C for 30 s, 54 °C (PIK1-F/PIK3-R) or 53 °C (PIK5-F/PIK2-R) for 30 s, and 68 °C for 30 s (PIK1-F/PIK3-R) or 20 s (PIK5-F/PIK2-R), followed by a final cycle of 68 °C for 10 min. The amplified fragments from the PIK1-F/PIK3-R and PIK5-F/PIK2-R primer pairs were then purified and sequenced using PIK7-F and PIK2-R, respectively. The primers used were: PIK1-F, 5'-CTTAGAGTTGGAGTTTGGACTGG-3'; PIK2-R, 5'-CATGGATTGTGCAATTCCTATGC-3'; PIK3-R, 5'-ACCTCGAACCATAGGATCTGG-3'; PIK5-F, 5'-TTGCATACATTCGAAAGACC-3'; and PIK7-F, 5'-GATTGAAGAGCATGCCAATTG-3'.

Mouse studies. All animal studies and procedures were approved by the MIT Institutional Animal Care and Use Committee. Six- to eight-week-old NOD/SCID mice (from Jackson laboratory) were used for generating all xenografts, with females for breast cancer and males for all other cancer models. In subcutaneous xenografts, mice were injected at two sites in the dorsal region, under isoflurane anaesthesia with 100 μl per injection of tumour cell suspension in Hank's buffered salt solution (HBSS, Invitrogen) with 15% Matrigel. In orthotopic xenografts, mice were anaesthetized with 2,2,2-tribromoethanol, a ventral incision was made in the skin and 25 μl of cell suspension in HBSS with 33% Matrigel were injected into the fourth pair of inguinal fat pads. Matrigel used in

all experiments was phenol-red-free and growth-factor-reduced (BD Biosciences). Appropriate tumour cell numbers were injected depending on the tumour growth rates *in vivo*. For subcutaneous tumours xenografts: 0.25×10^6 cells for DLD-mut, 0.5×10^6 for PC3, 0.6×10^6 for DLD-WT, 1×10^6 for MCF10DCIS and SW620, 2×10^6 for MDA-MB-435 and U87-MG, and 2.5×10^6 for MDA-MB-231. For orthotopic xenografts: 0.1×10^6 cells for MCF10DCIS and 1×10^6 for MDA-MB-231.

Dietary restriction. For a period of 3–4 days (20 days for U87-MG and orthotopic MDA-MB-231 xenografts) after injection of tumour cells, all mice were fed an *ad libitum* irradiated rodent chow diet (Prolab RMH 3000, 5P00) providing 3.46 kcal g^{-1} physiological fuel value, 26% of which is from protein, 14% from fat and 60% from carbohydrates. All mice were then individually caged and subdivided into an *ad libitum* group and a 40% DR group. Weekly body weights and daily *ad libitum* food intake were recorded. Restricted mice received a daily afternoon meal of a DR diet that amounted to 60% of the daily food intake of their *ad libitum* counterparts. The DR diet has similar consistency to the *ad libitum* diet except that it is fortified with vitamins and minerals (LabDiet, 5B6V) so as to prevent deficiency in these nutrients in the restricted mice. For U87-MG xenografts, 0.2 mg ml^{-1} doxycycline was administered in the drinking water 3 days before food restriction and was then replenished three times a week throughout the experiment. DR was carried for 12–15 days (24 days for subcutaneous MCF10DCIS and MDA-MB-231).

Five-week-old *KRAS*^{LA2}; *p53*^{LSL/WT} mice (obtained from the Jackson laboratory)^{32,33} and 9-week-old as well as 5-week-old *Pb-Cre*; *PTEN*^{f/f} (ref. 31) mice of mixed background were used in the DR studies.

Necropsy and plasma analyses. Mice were euthanized at the beginning of the light cycle after retro-orbital blood withdrawal, and plasma was prepared as described³⁶. Plasma insulin and IGF1 were assayed using kits from CrystalChem and Diagnostic Systems Laboratories, respectively. Tumours were collected, their dimensions (termed *a*, *b* and *c*) were measured with a caliper and tumour volume was estimated according to the ellipsoid formula: $4/3 \times \pi \times (a/2 \times b/2 \times c/2)$ (ref. 37). Tumours were then either immediately frozen in liquid nitrogen or fixed in formalin for later processing.

Immunohistochemistry. Formalin-fixed tumours were embedded in paraffin and sections were immunostained according to the manufacturer's protocol using PTEN (1:100), FOXO1 (1:50) or cleaved caspase 3 (1:100) antibodies (Cell Signaling Technology). The latter staining was performed using an automated stainer in the Histology Core Laboratory at MIT. Quantification analysis was accomplished by measuring the ratios of cleaved caspase-3-stained cells (visual count) over haematoxylin-stained cells (automated count using CellProfiler program^{38,39}) in an average of nine pictures of three different tumours (1,000 nuclei per picture) for each particular xenograft/diet condition.

Statistical analysis. Data are presented as means and s.e.m. In comparing two groups, a two-tailed non-paired Student's *t*-test was performed, and $P \leq 0.05$ (unless otherwise stated) was considered significant.

- Kim, D. H. *et al.* mTOR interacts with raptor to form a nutrient-sensitive complex that signals to the cell growth machinery. *Cell* **110**, 163–175 (2002).
- Kalaany, N. Y. *et al.* LXRs regulate the balance between fat storage and oxidation. *Cell Metab.* **1**, 231–244 (2005).
- Wapnir, I. L., Wartenberg, D. E. & Greco, R. S. Three dimensional staging of breast cancer. *Breast Cancer Res. Treat.* **41**, 15–19 (1996).
- Carpenter, A. E. *et al.* CellProfiler: image analysis software for identifying and quantifying cell phenotypes. *Genome Biol.* **7**, R100 (2006).
- Lamprecht, M. R., Sabatini, D. M. & Carpenter, A. E. CellProfiler: free, versatile software for automated biological image analysis. *Biotechniques* **42**, 71–75 (2007).

ARTICLES

An inhibitor of NEDD8-activating enzyme as a new approach to treat cancer

Teresa A. Soucy¹, Peter G. Smith¹, Michael A. Milhollen¹, Allison J. Berger¹, James M. Gavin¹, Sharmila Adhikari¹, James E. Brownell¹, Kristine E. Burke¹, David P. Cardin¹, Stephen Critchley¹, Courtney A. Cullis¹, Amanda Doucette¹, James J. Garnsey¹, Jeffrey L. Gaulin¹, Rachel E. Gershman¹, Anna R. Lublinsky¹, Alice McDonald¹, Hirotake Mizutani¹, Usha Narayanan¹, Edward J. Olhava¹, Stephane Peluso¹, Mansoureh Rezaei¹, Michael D. Sintchak¹, Tina Talreja¹, Michael P. Thomas¹, Tary Traore¹, Stepan Vyskocil¹, Gabriel S. Weatherhead¹, Jie Yu¹, Julie Zhang¹, Lawrence R. Dick¹, Christopher F. Claiborne¹, Mark Rolfe¹, Joseph B. Bolen¹ & Steven P. Langston¹

The clinical development of an inhibitor of cellular proteasome function suggests that compounds targeting other components of the ubiquitin–proteasome system might prove useful for the treatment of human malignancies. NEDD8-activating enzyme (NAE) is an essential component of the NEDD8 conjugation pathway that controls the activity of the cullin-RING subtype of ubiquitin ligases, thereby regulating the turnover of a subset of proteins upstream of the proteasome. Substrates of cullin-RING ligases have important roles in cellular processes associated with cancer cell growth and survival pathways. Here we describe MLN4924, a potent and selective inhibitor of NAE. MLN4924 disrupts cullin-RING ligase-mediated protein turnover leading to apoptotic death in human tumour cells by a new mechanism of action, the deregulation of S-phase DNA synthesis. MLN4924 suppressed the growth of human tumour xenografts in mice at compound exposures that were well tolerated. Our data suggest that NAE inhibitors may hold promise for the treatment of cancer.

The ubiquitin–proteasome system (UPS) is responsible for the regulated degradation of intracellular proteins with important roles in a broad array of cellular functions¹. One drug which targets the UPS, the proteasome inhibitor bortezomib (Velcade), is approved for the treatment of patients with multiple myeloma or mantle cell lymphoma^{2,3}. The anti-cancer activity of bortezomib suggests that inhibitors of other enzymes that modulate UPS activity might lead to the development of new anti-cancer drugs with differentiated clinical use⁴.

Covalent linkage of the small protein modifier ubiquitin to a protein frequently acts to initiate a process that results in the degradation of the protein by the proteasome⁵. The ubiquitinylation pathway is executed by a series of three distinct enzymatic steps. Ubiquitin is first ‘activated’ by ubiquitin-activating enzyme (E1) in an ATP-dependent reaction⁶. In the second step, ubiquitin is transferred from the E1 to an ubiquitin-conjugating enzyme (E2). The E2 then collaborates with a ubiquitin ligase enzyme (E3) to conjugate the ubiquitin to the substrate protein targeted for degradation.

Although the ubiquitinylation pathway was the first such pathway to be discovered⁷, homologous pathways for protein conjugation by ubiquitin-like proteins (UBLs) have subsequently been identified⁸. One such conjugation pathway uses the ubiquitin-like protein NEDD8 (ref. 9). Similar to ubiquitin, NEDD8 is first activated by an E1 enzyme (NEDD8 activating enzyme (NAE; a heterodimer of NAE1 and UBA3 subunits)), transferred to an E2 enzyme (Ubc12, also known as UBE2M), and then conjugated to target substrates. The best characterized substrates of the NEDD8 pathway are the cullin family of proteins¹⁰. Cullin proteins function as a core scaffold for a subclass of ubiquitin E3 ligases, the cullin-RING ligases (CRLs)¹¹, and covalent modification of the cullin protein within the CRL by NEDD8 is required for holoenzyme ubiquitin ligase

activity^{12–14}. Recent work suggests that there are several mechanisms by which NEDD8 modification activates CRLs^{15,16}. Thus, one function of the NEDD8 pathway is to regulate the ubiquitinylation rate (and degradation kinetics) of the subset of proteins whose ubiquitinylation is dependent on CRLs.

Here we report the discovery of MLN4924, a small molecule inhibitor of NAE that is at present being evaluated in several phase I clinical trials. MLN4924 selectively inhibits NAE activity compared to the closely related ubiquitin-activating enzyme (UAE, also known as UBA1) and SUMO-activating enzyme (SAE; a heterodimer of SAE1 and UBA2 subunits), in purified enzyme and cellular assays. MLN4924 exhibits potent *in vitro* cytotoxic activity against a variety of human tumour-derived cell lines. Treatment of tumour cells with MLN4924 increases the abundance of known CRL substrates, but unlike proteasome inhibition by bortezomib, MLN4924 did not significantly inhibit bulk protein turnover. In the human cell lines studied, the mechanism of cell death seems to be a consequence of uncontrolled DNA synthesis in the S-phase of the cell cycle leading to DNA damage and induction of apoptosis. *In vivo*, MLN4924 demonstrates potent anti-tumour activity in mice bearing human tumour xenografts, at drug exposures that are well tolerated.

MLN4924 is a selective inhibitor of NAE

MLN4924 was discovered as a result of iterative medicinal chemistry efforts on N6-benzyl adenosine that was originally identified as an inhibitor of NAE via high throughput screening (see Supplementary Information for chemical characterization). As shown in Fig. 1a, MLN4924 is structurally related to adenosine 5′-monophosphate (AMP)—a tight binding product of the NAE reaction^{6,17}. The main differences between AMP and MLN4924 are: (1) in place of the adenine base, MLN4924 has a deazapurine base substituted with an

¹Discovery, Millennium Pharmaceuticals, Inc., 40 Landsdowne Street, Cambridge, Massachusetts 02139, USA.

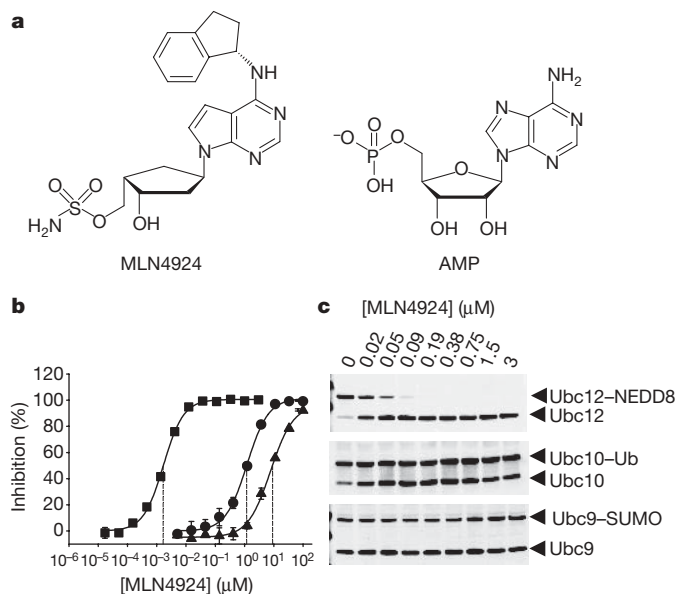


Figure 1 | MLN4924 is a potent and selective inhibitor of NEDD8-activating enzyme. **a**, Chemical structure of MLN4924 ((1*S*,2*S*,4*R*)-4-[(1*S*)-2,3-dihydro-1*H*-inden-1-ylamino]-7*H*-pyrrolo[2,3-*d*]pyrimidin-7-yl]-2-hydroxycyclopentyl)methyl sulphamate. The structure of AMP is shown for comparison. **b**, MLN4924 demonstrates potent and selective inhibition of NAE (squares) *in vitro* ($\text{IC}_{50} = 4.7 \pm 1.5 \text{ nM}$) compared to SAE (triangles) and UAE (circles) (IC_{50} values of $8.2 \pm 6.2 \mu\text{M}$ and $1.5 \pm 0.71 \mu\text{M}$, respectively). **c**, MLN4924 selectively inhibits NAE in cells. Inhibition of NAE, SAE and UAE in cells was assessed by immunoblot analysis of the Ubc12-NEDD8, Ubc9 (also known as UBE2I)-SUMO and Ubc10-Ub thioester levels respectively, in HCT-116 cell lysates.

aminoindane at N6; (2) in place of the ribose sugar, MLN4924 has a carbocycle and the equivalent of the 2'-hydroxyl group of AMP is absent; (3) in place of the phosphate, MLN4924 has a sulphamate; and (4) in contrast to the stereochemistry of AMP, the methylene sulphamate of MLN4924 is in a non-natural anti-relationship to the deazapurine. X-ray crystallography confirmed that MLN4924 bound in the nucleotide-binding site of NAE^{18,19} (J.E.B. *et al.*, manuscript in preparation).

MLN4924 is a potent inhibitor of NAE (half-maximal inhibitory concentration (IC_{50}) = $0.004 \mu\text{M}$), and is selective relative to the closely related enzymes UAE, SAE, UBA6 and ATG7 (IC_{50} = 1.5, 8.2, 1.8 and $>10 \mu\text{M}$, respectively) when evaluated in purified enzyme assays that monitor the formation of E2-UBL thioester reaction products (Fig. 1b and data not shown). The selectivity profile of MLN4924 for NAE was also evident in cell-based assays evaluating the levels of E2-UBL thioester products by immunoblotting (Fig. 1c). Molecules of this general class have been shown to inhibit transfer RNA synthetases²⁰. To rule out this possibility, MLN4924 was shown to have no effect in an assay monitoring the incorporation of [³⁵S]methionine into newly synthesized proteins (Supplementary Fig. 1). Furthermore, MLN4924 did not demonstrate detectable inhibition of other ATP-using enzymes (Supplementary Table 1).

NAE regulates a subset of UPS substrates

Polyubiquitinated proteins are normally degraded by cellular proteasomes, and inhibition of proteasome activity has been shown to substantially suppress bulk intracellular protein turnover²¹. In contrast, inhibition of the NAE pathway should only affect the degradation of proteins whose ubiquitinylation is mediated by CRLs. The effect of NAE inhibition on total intracellular protein turnover and proteasome-dependent protein turnover was examined by comparing the consequence of NAE inhibition and proteasome inhibition on the degradation of metabolically labelled proteins in cultured HCT-116 cells. MLN4924 and bortezomib were used at concentrations that

result in rapid and complete inhibition of detectable CRL and proteasome activity, respectively (Supplementary Fig. 2). As early as 15 min after treatment, bortezomib was found to inhibit protein turnover, whereas MLN4924 did not have a significant effect (Fig. 2, inset). Over longer exposure times, MLN4924 treatment inhibited overall protein turnover by $\approx 9\%$ ($P = 0.023$), and bortezomib treatment inhibited protein turnover by $\approx 50\%$ ($P < 0.001$) as estimated from the associated area under curve (AUC) values from 2–4 h. These observations suggest that in HCT-116 cells, approximately 20% of the proteasome-dependent degradation is mediated by CRL-ubiquitinylation.

NAE inhibition results in S-phase defects

NAE inhibition and subsequent decrease in the steady-state level of Ubc12-NEDD8 thioesters in cells treated with MLN4924 predicts that a corresponding decrease in the abundance of NEDD8-cullin conjugates should be observed. Moreover, inhibition of this pathway should also result in the diminished activity of CRLs leading to the accumulation of CRL-target proteins. Treatment of HCT-116 cells with MLN4924 for 24 h resulted in a dose-dependent decrease of Ubc12-NEDD8 thioester and NEDD8-cullin conjugates, with an $\text{IC}_{50} < 0.1 \mu\text{M}$ (Fig. 3a), resulting in a reciprocal increase in the abundance of the known CRL substrates CDT1 (refs 22–24), p27 (refs 14, 25) and NRF2 (also known as NFE2L2)²⁶, but not non-CRL substrates (Supplementary Fig. 3). In similar experiments, we have observed the accumulation of other CRL substrates including c-Jun²⁷, HIF1 α (ref. 28), cyclin E²⁹, CDC25A (ref. 30), EMI1 (also known as FBXO5)³¹ and phosphorylated I κ B α (refs 13, 32) (data not shown).

The observed accumulation of CRL substrates in MLN4924-treated HCT-116 cells is consistent with the idea that the abundance of most, if not all, CRL target proteins can be modulated by NAE inhibition. However, the cellular consequences of such inhibition could conceivably vary depending on numerous physiological parameters regulated by proteins under the control of different CRLs in different cell types. In HCT-116 cells, the most prominent phenotype observed was the disruption of S-phase regulation leading to cellular death (Fig. 3b).

In these experiments, HCT-116 cells were treated with $0.3 \mu\text{M}$ MLN4924, a concentration sufficient to decrease the steady-state level of NEDD8-cullin conjugates by $>80\%$ relative to untreated cells

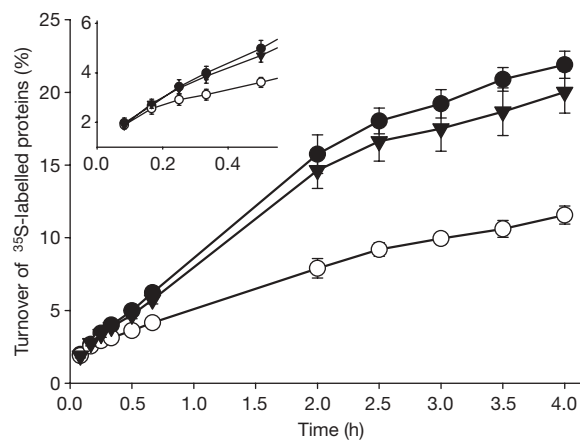


Figure 2 | NEDD8 pathway inhibition, in contrast to proteasome inhibition, minimally affects bulk intracellular protein turnover. The proteins in HCT-116 cells were metabolically labelled by culturing the cells for 20 min in the presence of [³⁵S]methionine. The cells were then chased with fresh media containing excess cold methionine and dimethylsulphoxide (DMSO) (filled circles), $3 \mu\text{M}$ MLN4924 (filled triangles) or $3 \mu\text{M}$ bortezomib (open circles). Protein degradation, measured by the appearance of radioactivity in the media over time, was determined as described in Methods. Inset, expanded view of early timepoints. Error bars show s.d.; $n = 6$.

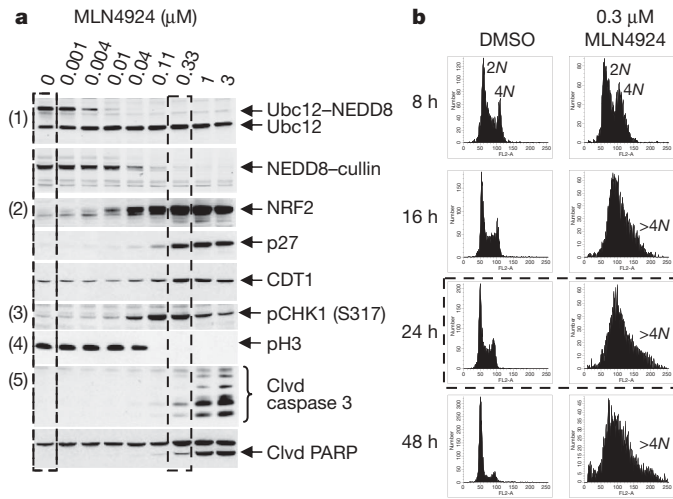


Figure 3 | Inhibition of the NEDD8 pathway in cells results in S-phase defects, DNA damage and apoptosis. **a**, HCT-116 cells were treated with MLN4924 for 24 h. Cell lysates were immunoblotted for (1) Ubc12–NEDD8 and NEDD8–cullin conjugate levels, (2) CRL substrates, NRF2, p27 and CDT1, (3) DNA damage marker, phosphorylated CHK1 (Ser 317), (4) mitotic marker pH3, and (5) apoptotic markers, cleaved (Clvd) caspase 3 and cleaved PARP. **b**, HCT-116 cells were treated with DMSO or 0.3 μM MLN4924 for 8, 16, 24 and 48 h. DNA profiles were analysed by flow cytometry. $>4N$ represents cells having greater than tetraploid DNA content.

(Fig. 3a, dashed outline), and the cell-cycle profiles were monitored by DNA content using flow cytometry. As early as 8 h after compound treatment, cells began to accumulate in S-phase (Fig. 3b). By 24 h, a significant fraction of cells contained $\geq 4N$ DNA content (Fig. 3b, dashed outline); however, the absence of detectable phosphohistone H3 (pH3) staining indicated that the cells were not transitioning into mitosis (Fig. 3a). By 48 h, an increase in the sub- $2N$ DNA content population was observed, consistent with cells undergoing apoptosis and further supported by the accumulation of cleaved caspase 3 and PARP (Fig. 3a).

The cell-cycle phenotype observed after MLN4924 treatment is similar to that of cells undergoing re-replication, a phenomenon in which several rounds of DNA synthesis are initiated in the absence of cycle progression. Although several mechanistic defects can result in such a phenotype, our finding that CDT1, a protein essential for ‘licensing’ origins of DNA replication^{33,34}, accumulated in MLN4924-treated cells (Fig. 3a) suggests that this substrate for CRL1^{SKP2} (refs 22–23, 35) and CRL4–DDB1^{CDT2} (refs 24, 36, 37) might represent an important mediator of MLN4924 activity. Forced expression of CDT1 in cells, or RNA interference (RNAi)-mediated ablation of the endogenous CDT1-inhibitor geminin, results in the DNA re-replication phenotype^{38–41}.

Re-replication is known to induce DNA damage and elicit cellular DNA damage signalling^{42,43}. We observed a MLN4924 concentration-dependent accumulation of phosphorylated CHK1 (at Ser 317; also known as CHEK1), indicative of DNA damage signal transduction through the ATM/ATR pathway⁴⁴. The levels of other DNA damage markers also increased in a similar manner (data not shown). Whether DNA damage signalling represents the primary event leading to the activation of apoptosis, or whether other alterations induced by inhibition of the NAE pathway can independently lead to cellular death will require further experimentation.

The observed phenotype is probably the result of specific effects of NAE inhibition by MLN4924, because ablation of NAE expression by short interfering RNA (siRNA) resulted in similar S-phase defects (Supplementary Fig. 4). Importantly, although NAE and proteasome inhibition induce apoptosis, the treatment of HCT-116 cells with proteasome inhibitors did not elicit re-replication or DNA damage

(data not shown). MLN4924 treatment of other human-tumour-derived cell lines, including Calu-6 (lung), SKOV-3 (ovarian), H460 (lung), DLD-1 (colon), CWR22 (prostate) and OCI-LY19 (lymphoma), also resulted in S-phase-defective phenotypes (data not shown). Different cells however, show variable sensitivity to the effects of MLN4924 treatment (Supplementary Table 2). The mechanism(s) underlying these differential sensitivities remains to be determined. Notably, the non-transformed MCF10A breast epithelial cells were more sensitive to MLN4924 when actively proliferating, consistent with the idea that cycling cells are more susceptible to NAE-inhibition-induced re-replication.

MLN4924 inhibits the NAE pathway *in vivo*

To assess the ability of MLN4924 to inhibit NAE *in vivo*, HCT-116 tumour-bearing mice received a single subcutaneous dose of 10, 30 or 60 mg kg^{-1} MLN4924, and tumours were excised at various time-points over the subsequent 24 h period. The pharmacodynamic effects of treatment were assessed in tumour lysates which were analysed for NEDD8–cullin, NRF2 and CDT1 protein levels (Fig. 4a–c). A single dose of MLN4924 resulted in a dose- and time-dependent decrease of NEDD8–cullin levels as early as 30 min after administration of compound (Fig. 4a), with maximal effect 1–2 h post-dose. A significant difference was observed between the 10 and 60 mg kg^{-1} response profiles ($P < 0.01$), although the 10 and 30 mg kg^{-1} ($P = 0.11$) and 30 and 60 mg kg^{-1} ($P = 0.24$) profiles were not significantly different from each other. A single dose of MLN4924 also led to a dose- and time-dependent increase in the steady state levels of NRF2 and CDT1 (Fig. 4b, c). For all dose levels, NRF2 protein levels peaked 2–4 h after administration of MLN4924 and started to decline by 4–8 h post-dose. The timing of CDT1 accumulation was slightly delayed compared to NRF2, peaking 4 h after MLN4924 administration (Fig. 4c). Evidence of DNA damage in the tumour was indicated by the increased levels of phosphorylated CHK1 (Ser 317) at 8 h after a single administration of 30 and 60 mg kg^{-1} MLN4924 (Fig. 4d). It should be noted that MLN4924 also decreased NEDD8–cullin levels in normal mouse tissue as illustrated in mouse bone marrow cells (Supplementary Fig. 5). These data suggest that MLN4924-mediated inhibition of

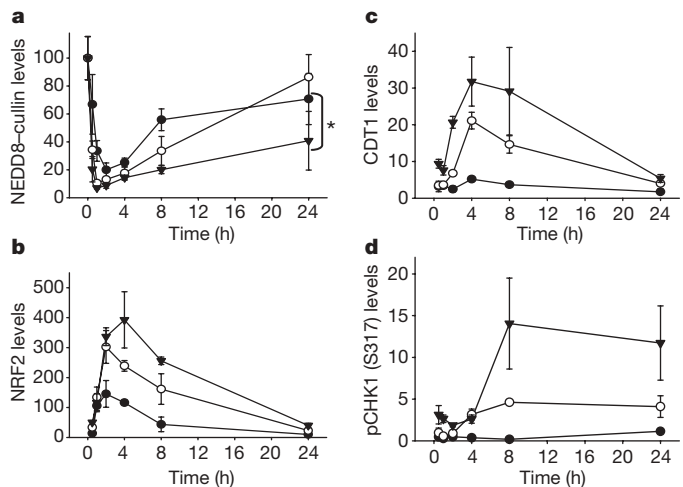


Figure 4 | MLN4924 inhibits the NEDD8 pathway resulting in DNA damage in human tumour xenografts. Mice bearing HCT-116 xenografts were administered a single subcutaneous dose of vehicle or MLN4924 at 10 mg kg^{-1} (filled circles), 30 mg kg^{-1} (open circles) or 60 mg kg^{-1} (filled triangles). Tumours were excised at the indicated times and NEDD8–cullin conjugate levels (**a**) and relative NRF2 protein levels (**b**) were measured in the tumour lysates (20 μg protein per lane) by quantitative immunoblot analysis. Units are arbitrary. **c**, **d**, CDT1 (**c**) and phosphorylated CHK1 (Ser 317) (**d**) levels were assessed by immunohistochemistry. Data are expressed as the percentage area of DAB stain. Error bars show s.d. $n = 3$; $*P < 0.01$.

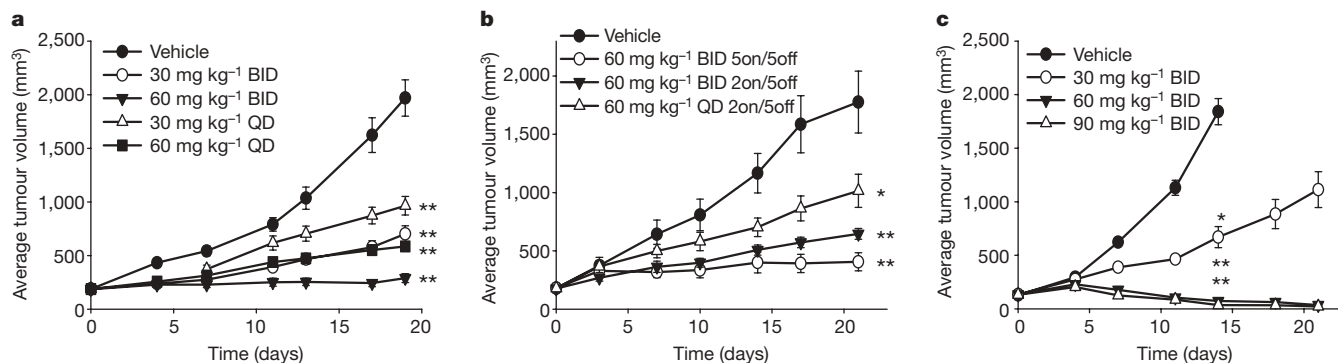


Figure 5 | MLN4924 produces tumour growth inhibition in human tumour xenografts. **a–c**, Nude mice bearing HCT-116 (**a**, **b**) or H522 (**c**) tumour xenografts were dosed by subcutaneous administration with either vehicle control or MLN4924 at the doses and schedules indicated. For example, 5on/

5off represents five days treatment followed by five days free of treatment, repeated for two cycles during the 21-day study. Mean tumour volumes \pm s.e.m. are shown. $n = 10$ mice per group; * $P < 0.01$, ** $P < 0.001$.

NAE in this *in vivo* tumour model results in pathway responses and cellular phenotypic effects compatible with those observed in cultured cells.

MLN4924 inhibits tumour xenograft growth

To evaluate the anti-tumour activity of MLN4924, we administered the compound to nude mice bearing subcutaneous human tumour cell xenografts and monitored tumour growth rate. MLN4924 was administered by subcutaneous injection once (QD) or twice (BID) daily to mice bearing HCT-116 xenografts, and inhibition of tumour growth (T/C, average treated tumour volume/average control tumour volume) was calculated on the last day of treatment (Fig. 5). MLN4924 administered on a BID schedule at 30 and 60 mg kg⁻¹ inhibited tumour growth with T/C values of 0.36 and 0.15, respectively ($P < 0.001$, Fig. 5a). Significant inhibition of tumour growth was also observed when MLN4924 was administered at 30 mg kg⁻¹ (T/C = 0.49, $P < 0.001$) and 60 mg kg⁻¹ (T/C = 0.3, $P < 0.001$) on a QD schedule. Notably, a total dose of 60 mg kg⁻¹ day⁻¹ gave comparable tumour growth inhibition whether it was delivered as 60 mg kg⁻¹ QD or 30 mg kg⁻¹ BID. Less frequent administration of MLN4924 was also found to be efficacious. MLN4924 was administered at 60 mg kg⁻¹ BID on two different daily dosing schedules; either three cycles of two-days treatment followed by five treatment-free days, or two cycles of five-days treatment followed by five treatment-free days (Fig. 5b). Statistically significant inhibition of tumour growth was observed with both of these schedules (T/C = 0.36, $P < 0.001$ and T/C = 0.23, $P < 0.001$, respectively). Furthermore, MLN4924 administered once daily at 60 mg kg⁻¹ for three cycles of two-days treatment followed by five treatment-free days, resulted in modest but significant tumour growth inhibition (T/C = 0.57, $P < 0.01$). All doses and schedules were well tolerated, with an average weight loss for all dose groups at the end of treatment of less than 10% (data not shown).

The anti-tumour activity of MLN4924 was also evaluated in mice bearing H522 lung tumour xenografts (Fig. 5c). Significant tumour growth inhibition was observed after continuous daily administration of MLN4924 at 30, 60 and 90 mg kg⁻¹ BID in this model with 10/10 regressions observed at the 60 and 90 mg kg⁻¹ doses (T/C at day 14 = 0.36, 0.04 and 0.02 respectively; $P < 0.001$). The anti-tumour activity of MLN4924 in the Calu-6 lung carcinoma xenograft is described in Supplementary Fig. 6. These results demonstrate that MLN4924 treatment inhibits the growth of human tumour xenografts in mice, and is efficacious when administered on various daily and less frequent schedules.

Conclusions

Here we have described the initial characterization of MLN4924, a small molecule inhibitor of NAE that represents a new approach to targeting the UPS for the treatment of cancer. MLN4924 completely

inhibits detectable NAE pathway function in cells, disrupting the turnover of CRL substrates, with important roles in cell-cycle progression and survival. Our results indicate that inhibition of the NAE pathway disrupts cancer cell protein homeostasis more selectively than the inhibition of proteasome activity, which may contribute to useful differences in clinical efficacy and safety profiles. Sustained NAE pathway inhibition was found to result in the activation of apoptosis as a consequence of cell-cycle-dependent DNA re-replication. This phenotype was presumably a result of the inability of the cell to degrade the CRL substrate CDT1, which has been shown to induce re-replication when overexpressed. Similar cell-cycle profiles were obtained when NAE levels were reduced by RNAi or when NAE activity was compromised in a temperature-sensitive mutant cell line^{45,46}.

In vivo, we demonstrated that MLN4924 suppressed the growth of human tumour xenografts at doses and schedules that were well tolerated. Analysis of tumours from treated animals confirmed inhibition of the NEDD8 pathway, suggesting that these pharmacodynamic markers may have use in monitoring NAE inhibition in patients treated with MLN4924. These preclinical findings have supported the transition of MLN4924 into clinical development.

METHODS SUMMARY

The full Methods provides information about all experimental procedures: (1) generation of protein reagents for *in vitro* assays; (2) detailed description of *in vitro* E1-activating enzyme assays; (3) description of assay to assess bulk protein turnover in cultured cells; (4) description of cell viability assay; (5) list of antibodies used for western blot analysis of cultured cells and tumour lysates; (6) cell-cycle analysis using flow cytometry; (7) details for conducting tumour xenograft efficacy experiments in mice; (8) details for conducting pharmacodynamic studies in tumour-xenograft-bearing mice; (9) description of instrumentation used for quantification of pharmacodynamic markers; (10) description of assay to evaluate protein synthesis inhibition in cells; and (11) procedure for isolation of bone marrow from mouse femurs.

Full Methods and any associated references are available in the online version of the paper at www.nature.com/nature.

Received 10 October 2008; accepted 2 February 2009.

- Hershko, A. The ubiquitin system for protein degradation and some of its roles in the control of the cell division cycle. *Cell Death Differ.* **12**, 1191–1197 (2005).
- Kane, R. C., Bross, P. F., Farrell, A. T. & Pazdur, R. VELCADE®: U.S. FDA Approval for the treatment of multiple myeloma progressing on prior therapy. *Oncologist* **8**, 508–513 (2003).
- Kane, R. C. *et al.* Bortezomib for the treatment of mantle cell lymphoma. *Clin. Cancer Res.* **13**, 5291–5294 (2007).
- Nalepa, G., Rolfe, M. & Harper, J. W. Drug discovery in the ubiquitin proteasome system. *Nature Rev. Drug Discov.* **5**, 596–613 (2006).
- Hershko, A. & Ciechanover, A. The ubiquitin system. *Annu. Rev. Biochem.* **67**, 425–479 (1998).
- Haas, A. L. & Rose, I. A. The mechanism of ubiquitin activating enzyme: A kinetic and equilibrium analysis. *J. Biol. Chem.* **257**, 10329–10337 (1982).

7. Wilkinson, K. D. The discovery of ubiquitin-dependent proteolysis. *Proc. Natl Acad. Sci. USA* **102**, 15280–15282 (2005).
8. Kerscher, O., Felberbaum, R. & Hochstrasser, M. Modification of proteins by ubiquitin and ubiquitin-like proteins. *Annu. Rev. Cell Dev. Biol.* **22**, 159–180 (2006).
9. Gong, L. & Yeh, E. T. Identification of the activating and conjugating enzymes of the NEDD8 conjugation pathway. *J. Biol. Chem.* **274**, 12036–12042 (1999).
10. Pan, Z. Q., Kentsis, A., Dias, D. C., Yamoah, K. & Wu, K. NEDD8 on Cullin: building an expressway to protein destruction. *Oncogene* **23**, 1985–1997 (2004).
11. Petroski, M. D. & Deshaies, R. J. Function and regulation of cullin-RING ubiquitin ligases. *Nature Rev. Mol. Cell Biol.* **6**, 9–20 (2005).
12. Chiba, T. & Tanaka, K. Cullin-based ubiquitin ligase and its control by NEDD8 conjugation system. *Curr. Protein Pept. Sci.* **5**, 177–184 (2004).
13. Read, M. A. *et al.* Structural insights into NEDD8 activation of SCF^{TRCP}-dependent ubiquitination of I κ B α . *Mol. Cell Biol.* **20**, 2326–2333 (2000).
14. Podust, V. N. *et al.* A Nedd8 conjugation pathway is essential for proteolytic targeting of p27^{KIP1} by ubiquitination. *Proc. Natl Acad. Sci. USA* **97**, 4579–4584 (2000).
15. Duda, D. M. *et al.* Structural insights into NEDD8 activation of cullin-RING ligases: conformational control of conjugation. *Cell* **134**, 995–1006 (2008).
16. Saha, A. & Deshaies, R. J. Multimodal activation of the ubiquitin ligase SCF by NEDD8 conjugation. *Mol. Cell* **32**, 21–31 (2008).
17. Bohnsack, R. N. & Haas, A. L. Conservation in the mechanism of NEDD8 activation by the human AppBp1-Uba3 heterodimer. *J. Biol. Chem.* **278**, 26823–26830 (2003).
18. Walden, H., Podgorski, M. S. & Schulman, B. A. Insights into the ubiquitin transfer cascade from the structure of the activating enzyme for NEDD8. *Nature* **422**, 330–334 (2003).
19. Walden, H. *et al.* The structure of the APPBP1-UBA3-NEDD8-ATP complex reveals the basis for selective ubiquitin-like protein activation by an E1. *Mol. Cell* **12**, 1427–1437 (2003).
20. Bloch, A. & Coutsogeorgopoulos, C. Inhibition of protein synthesis by 5'-sulfamoyladenine. *Biochemistry* **10**, 4394–4398 (1971).
21. Rock, K. L. *et al.* Inhibitors of the proteasome block the degradation of most cell proteins and the generation of peptides presented on MHC class I molecules. *Cell* **78**, 761–771 (1994).
22. Nishitani, H. *et al.* Two E3 ubiquitin ligases, SCF-Skp2 and DDB1-Cul4 target human Cdt1 for proteolysis. *EMBO J.* **25**, 1126–1136 (2006).
23. Kondo, T. *et al.* Rapid degradation of Cdt1 upon UV-induced DNA damage is mediated by SCF^{Skp2} complex. *J. Biol. Chem.* **279**, 27315–27319 (2004).
24. Hu, J., McCall, C. M., Ohta, T. & Xiong, Y. Targeted ubiquitination of CDT1 by the DDB1-CUL4A-ROC1 ligase in response to DNA damage. *Nature Cell Biol.* **6**, 1003–1009 (2004).
25. Carrano, A. C., Eytan, E., Hershko, A. & Pagano, M. SKP2 is required for ubiquitin-mediated degradation of the CDK inhibitor p27. *Nature Cell Biol.* **1**, 193–199 (1999).
26. Kobayashi, A. *et al.* Oxidative stress sensor Keap1 functions as an adaptor for Cul3-based E3 ligase to regulate proteasomal degradation of Nrf2. *Mol. Cell Biol.* **24**, 7130–7139 (2004).
27. Nateri, A. S., Riera-Sans, L., DaCosta, C. & Behrens, A. The ubiquitin ligase SCF^{Fbw7} antagonizes apoptotic JNK signaling. *Science* **303**, 1374–1378 (2004).
28. Kamura, T. *et al.* Activation of HIF1 α ubiquitination by a reconstituted von-Hippel-Lindau (VHL) tumor suppressor complex. *Proc. Natl Acad. Sci. USA* **97**, 10430–10435 (2000).
29. Ye, X. *et al.* Recognition of phosphodegron motifs in human cyclin E by the SCF^{Fbw7} ubiquitin ligase. *J. Biol. Chem.* **279**, 50110–50119 (2004).
30. Donzelli, M. *et al.* Dual mode of degradation of Cdc25A phosphatase. *EMBO J.* **21**, 4875–4884 (2002).
31. Margottin-Goguet, F. *et al.* Prophase destruction of Emi1 by the SCF^{TRCP/Slimb} ubiquitin ligase activates the anaphase promoting complex to allow progression beyond prometaphase. *Dev. Cell* **4**, 813–826 (2003).
32. Winston, J. T. *et al.* The SCF^{TRCP}-ubiquitin ligase complex associates specifically with phosphorylated destruction motifs in I κ B α and β -catenin and stimulates I κ B α ubiquitination *in vitro*. *Genes Dev.* **13**, 270–283 (1999).
33. Machida, Y. J., Hamlin, J. L. & Dutta, A. Right place, right time and only once: replication initiation in Metazoans. *Cell* **123**, 13–24 (2005).
34. Arias, E. E. & Walter, J. C. Replication-dependent destruction of Cdt1 limits DNA replication to a single round per cell cycle in *Xenopus* egg extracts. *Genes Dev.* **19**, 114–126 (2005).
35. Li, X., Zhao, Q., Liao, R., Sun, P. & Wu, X. The SCF^{Skp2} ubiquitin ligase complex interacts with the human replication licensing factor Cdt1 and regulates Cdt1 degradation. *J. Biol. Chem.* **278**, 30854–30858 (2003).
36. Lovejoy, C. A., Lock, K., Yenamandra, A. & Cortez, D. DDB1 maintains genome integrity through regulation of Cdt1. *Mol. Cell Biol.* **26**, 7977–7990 (2006).
37. Higa, L. A., Mihaylov, I. S., Banks, D. P., Zheng, J. & Zhang, H. Radiation-mediated proteolysis of Cdt1 by CUL4-ROC1 and CSN complexes constitutes a new checkpoint. *Nature Cell Biol.* **5**, 1008–1015 (2003).
38. Saxena, S. & Dutta, A. Geminin and p53: deterrents to rereplication in human cancer cells. *Cell Cycle* **2**, 283–286 (2003).
39. Melixietian, M. *et al.* Loss of Geminin induces rereplication in the presence of functional p53. *J. Cell Biol.* **165**, 473–482 (2004).
40. Vaziri, C. *et al.* A p53-dependent checkpoint pathway prevents rereplication. *Mol. Cell* **11**, 997–1008 (2003).
41. Kim, Y. & Kipreos, E. T. Cdt1 degradation to prevent DNA rereplication: conserved and non-conserved pathways. *Cell Div.* **2**, 18–27 (2007).
42. Archambault, V., Ikui, A. E., Drapkin, B. J. & Cross, F. R. Disruption of mechanisms that prevent rereplication triggers a DNA damage response. *Mol. Cell Biol.* **25**, 6707–6721 (2005).
43. Zhu, W., Chen, Y. & Dutta, A. Rereplication by depletion of geminin is seen regardless of p53 status and activates a G2/M checkpoint. *Mol. Cell Biol.* **24**, 7140–7150 (2004).
44. Lin, J. J. & Dutta, A. ATR pathway is the primary pathway for activating G2/M checkpoint induction after re-replication. *J. Biol. Chem.* **282**, 30357–30362 (2007).
45. Handeli, S. & Weintraub, H. The ts41 mutation in Chinese hamster cells leads to successive S phases in the absence of intervening G2, M and G1. *Cell* **71**, 599–611 (1992).
46. Chen, Y., McPhie, D. L., Hirschberg, J. & Neve, R. L. The amyloid precursor protein-binding protein APP-BP1 drives the cell cycle through the S-M checkpoint and causes apoptosis in neurons. *J. Biol. Chem.* **275**, 8929–8935 (2000).

Supplementary Information is linked to the online version of the paper at www.nature.com/nature.

Acknowledgements As this project progressed through the discovery phase, many scientists made significant contributions to its success. The authors would like to thank all past contributors to the NAE project including M. H. Foley, V. Chau, T. Gladysheva and S. Sadis. We would also like to thank D. Bowman for technical help with imaging assays, J. Blank for technical help with protein turnover assays and A. Burkhardt, P. Veiby, M. Manfredi and B. Hibner for support and guidance.

Author Contributions T.A.S., P.G.S., M.A.M., A.J.B. and J.M.G. participated in the planning, initiation, data generation and analysis of biological experiments and preparation of the manuscript. C.A.C., E.J.O., S.V., G.S.W., S.C., S.P. and S.P.L. participated in the planning, initiation, design and execution of chemical synthesis. S.A., D.P.C., A.D., H.M., M.R., J.L.G., R.E.G. and T.Talreja performed chemical synthesis; U.N. performed *in vitro* cell culture experiments; T.Traore and J.Z. performed *in vivo* anti-tumour activity and pharmacodynamic experiments; J.Y., J.J.G. and M.P.T. performed pharmacodynamic analysis experiments; A.R.L. evaluated compound potencies in cell-based assays; K.E.B. and A.M. performed immunohistochemical experiments; M.D.S. performed crystallography studies. L.R.D., J.E.B., C.F.C., M.R. and J.B.B. provided oversight of the project, reviewed and edited the manuscript.

Author Information MLN4924 will be provided once a standard Materials Transfer Agreement has been executed. Reprints and permissions information is available at www.nature.com/reprints. The authors declare competing financial interests: details accompany the full-text HTML version of the paper at www.nature.com/nature. Correspondence and requests for materials should be addressed to T.A.S. (teresa.soucy@mpi.com).

METHODS

Protein reagents. Baculoviruses were generated with the Bac-to-Bac Expression System (Invitrogen) for the following proteins. His-NAE (NAE1 and His-tagged UBA3) and His-SAE (SAE1 and His-tagged UBA2) complexes were generated by co-infection of Sf9 cells, His-tagged mouse UAE (also known as Uba1), His-UBA6 and His-ATG7 were generated by single infection of Sf9 cells. Ubc12, Ubc9, Ubc2 (also known as UBE2A) were expressed as amino-terminally glutathione *S*-transferase (GST)-tagged fusion proteins in *Escherichia coli*. Use1 (UBE2Z) and ATG3 were expressed as N-terminally His-tagged proteins in *E. coli*. NEDD8, SUMO1 and ubiquitin were expressed as N-terminally Flag-tagged fusion proteins in *E. coli*. Expressed proteins were purified by affinity (Ni-NTA agarose, Qiagen) or conventional chromatography.

***In vitro* E1-activating enzyme assays.** A time-resolved fluorescence energy transfer assay format was used to measure the *in vitro* activity of NAE. The enzymatic reaction, containing 50 μ l 50 mM HEPES, pH 7.5, 0.05% BSA, 5 mM MgCl₂, 20 μ M ATP, 250 μ M glutathione, 10 nM Ubc12-GST, 75 nM NEDD8-Flag and 0.3 nM recombinant human NAE enzyme, was incubated at 24 °C for 90 min in a 384-well plate, before termination with 25 μ l of stop/detection buffer (0.1 M HEPES, pH 7.5, 0.05% Tween20, 20 mM EDTA, 410 mM KF, 0.53 nM Europium-Cryptate-labelled monoclonal Flag-M2-specific antibody (CisBio International) and 8.125 μ g ml⁻¹ PHYCOLINK allophycocyanin (XL-APC)-labelled GST-specific antibody (Prozyme)). After incubation for 2 h at 24 °C, the plate was read on the LJI Analyst HT Multi-Mode instrument using a time-resolved fluorescence method. A similar assay protocol was used to measure other E1 enzymes.

Assay of bulk protein turnover. HCT-116 cells were plated into 12-well plates at 1×10^5 cells per well and incubated overnight. The medium was exchanged with methionine-free DMEM (Invitrogen) containing 10% dialysed FBS and 50 μ Ci per well of [³⁵S]methionine, and the cells were incubated for 20 min to label proteins undergoing synthesis. The cells were then washed three times with DMEM supplemented with 2 mM methionine. Fresh medium containing 10% FBS, 2 mM methionine and the test compounds as described in Fig. 2 were then added. At the specified time points, media (50 μ l) was collected and subjected to liquid scintillation counting. At the end of the time course, remaining media was removed and the cells were solubilized by adding of 1 ml 0.2 N NaOH and the extract was subjected to liquid scintillation counting. The percentage of protein turnover at each time point was calculated as [(total acid soluble counts in supernatant)/(total acid soluble counts in supernatant + total counts in solubilized cells)] $\times 100$.

Cell viability assay. Cell suspensions were seeded at 3,000–8,000 cells per well in 96-well culture plates and incubated overnight at 37 °C. Compounds were added to the cells in complete growth media and incubated for 72 h at 37 °C. Cell number was quantified using the ATPlite assay (PerkinElmer).

Western blot analysis of cultured cells. HCT-116 cells grown in 6-well cell-culture dishes were treated with 0.1% DMSO (control) or MLN4924 for 24 h. Whole cell extracts were prepared and analysed by immunoblotting. For analysis of the E2-UBL thioester levels, lysates were fractionated by non-reducing SDS-PAGE and immunoblotted with polyclonal antibodies to Ubc12 (generated by Millennium), Ubc9 (AG Scientific) and Ubc10 (Boston Biochem). For analysis of other proteins, lysates were fractionated by reducing SDS-PAGE and probed with primary antibodies as follows: mouse monoclonal antibodies to CDT1 (Millennium), p27 (BD Transduction), geminin (Abcam), ubiquitin, securin/PTTG and p53 (Santa Cruz) or rabbit polyclonal antibodies to NRF2, Cyclin B1 (Santa Cruz) and GADD34 (Proteintech Group, Inc.). Rabbit monoclonal antibodies to NEDD8 and phosphorylated CHK1 (Ser317) were generated

by Millennium in collaboration with Epitomics, Inc. using Ac-KEIEIDIEPTDKVERIKERVEE-amide and Ac-VKYSS(pS)QPEPRT-amide as immunogens, respectively. Antibodies to pH3, cleaved PARP and cleaved caspase 3 were from Cell Signaling Technologies. Secondary HRP-labelled antibodies to rabbit IgG or mouse IgG (Santa Cruz) were used as appropriate. Blots were developed with ECL reagent (Amersham). For Supplementary Fig. 2, the secondary antibody was Alexa-680-labelled antibody to rabbit/mouse IgG (Molecular Probes) and the blots were imaged using the Li-Cor Odyssey Infrared Imaging system.

Cell-cycle analysis. Logarithmically growing HCT-116 cells were incubated with either MLN4924 or DMSO for the times indicated. Collected cells were fixed in 70% ethanol and stored overnight at 4 °C. Fixed cells were centrifuged to remove ethanol, and the pellets were resuspended in propidium iodide and RNase A in PBS for 1 h on ice protected from light. Cell-cycle distributions were determined using flow cytometry (FACS Calibur, Becton Dickinson) and analysed using Winlist software (Verity).

Tumour xenograft efficacy experiments. Female athymic NCR mice (Charles River Laboratories) were used in all *in vivo* studies. All animals were housed and handled in accordance with the Guide for the Care and Use of Laboratory Animals. Mice were inoculated with 2×10^6 HCT-116 cells (or 30–40 mg H522 tumour fragments) subcutaneously in the right flank, and tumour growth was monitored with caliper measurements. When the mean tumour volume reached approximately 200 mm³, animals were dosed subcutaneously with vehicle (10% cyclodextrin) or MLN4924. Inhibition of tumour growth (T/C) was calculated on the last day of treatment.

Pharmacodynamic marker analysis. Mice bearing HCT-116 tumours of 300–500 mm³ were administered a single MLN4924 dose, and at the indicated times tumours were excised and extracts prepared. The relative levels of NEDD8-cullin and NRF2 were estimated by quantitative immunoblot analysis (Li-cor Odyssey system) using Alexa680-labelled anti-IgG (Molecular Probes) as the secondary antibody. The statistical difference between the groups for NEDD8-cullin inhibition was determined using the Kruskal–Wallis test. For the analysis of CDT1 and phosphorylated CHK1 (Ser317) levels in tumour sections, formalin-fixed, paraffin-embedded tumour sections were stained with the relevant antibodies, amplified with HRP-labelled secondary antibodies and detected with the ChromoMap DAB Kit (Ventana Medical Systems). Slides were counterstained with haematoxylin. Images were captured using an Eclipse E800 microscope (Nikon Instruments) and Retiga EXi colour digital camera (QImaging) and processed using Metamorph software (Molecular Devices). CDT1 and phosphorylated CHK1 levels are expressed as a function of the DAB signal area.

Isolation of bone marrow cells from mice. For bone marrow pharmacodynamic studies, naive NCr-Nude mice (Taconic Farms) were administered MLN4924, and at the indicated times leg bones were excised. Marrow was flushed from the bones with PBS, pelleted by centrifugation and flash frozen. Thawed marrow was lysed in M-PER buffer (Pierce) with protease inhibitors. NEDD8-cullin levels were measured by immunoblot analysis.

Assay of protein synthesis. HCT-116 cells were plated into 6-well plates at 5×10^5 cells per well and incubated overnight. Fresh media containing inhibitors and 10 μ Ci per well of [³⁵S]methionine was added and the cells were incubated for 2 h to label proteins undergoing synthesis. After washing with ice-cold PBS, RIPA lysis buffer (250 μ l) was added and the cells were lysed for 30 min on ice. The lysate was transferred to Eppendorf tubes containing 500 μ l 0.5 mg ml⁻¹ BSA/5 mM EDTA, to which 200 μ l 100% (v/v) trichloroacetic acid was added. Precipitated proteins were filtered through glass microfibre discs and subjected to liquid scintillation counting.

Over half of the far-infrared background light comes from galaxies at $z \geq 1.2$

Mark J. Devlin¹, Peter A. R. Ade², Itziar Aretxaga³, James J. Bock⁴, Edward L. Chapin⁵, Matthew Griffin², Joshua O. Gundersen⁶, Mark Halpern⁵, Peter C. Hargrave², David H. Hughes³, Jeff Klein¹, Gaalen Marsden⁵, Peter G. Martin^{7,8}, Philip Maukopf², Lorenzo Moncelsi², Calvin B. Netterfield^{8,9}, Henry Ngo⁵, Luca Olmi^{10,11}, Enzo Pascale², Guillaume Patanchon¹², Marie Rex¹, Douglas Scott⁵, Christopher Semisch¹, Nicholas Thomas⁶, Matthew D. P. Truch¹, Carole Tucker², Gregory S. Tucker¹³, Marco P. Viero⁸ & Donald V. Wiebe⁹

Submillimetre surveys during the past decade have discovered a population of luminous, high-redshift, dusty starburst galaxies^{1–8}. In the redshift range $1 \leq z \leq 4$, these massive submillimetre galaxies go through a phase characterized by optically obscured star formation at rates several hundred times that in the local Universe. Half of the starlight from this highly energetic process is absorbed and thermally re-radiated by clouds of dust at temperatures near 30 K with spectral energy distributions peaking at 100 μm in the rest frame⁹. At $1 \leq z \leq 4$, the peak is redshifted to wavelengths between 200 and 500 μm . The cumulative effect of these galaxies is to yield extragalactic optical and far-infrared backgrounds with approximately equal energy densities. Since the initial detection of the far-infrared background (FIRB)¹⁰, higher-resolution experiments have sought to decompose this integrated radiation into the contributions from individual galaxies. Here we report the results of an extragalactic survey at 250, 350 and 500 μm . Combining our results at 500 μm with those at 24 μm , we determine that all of the FIRB comes from individual galaxies, with galaxies at $z \geq 1.2$ accounting for 70% of it. As expected, at the longest wavelengths the signal is dominated by ultraluminous galaxies at $z > 1$.

The Balloon-borne Large-Aperture Submillimeter Telescope (BLAST) was designed as a precursor to the Spectral and Photometric Imaging Receiver (SPIRE) instrument^{11,12} on the European Space Agency's Herschel Space Observatory. BLAST samples the emission from galaxies at 250, 350 and 500 μm close to the peak of the FIRB. The multiwavelength observations of BLAST fill the wavelength gap between the Multiband Imaging Photometer on NASA's Spitzer satellite (MIPS; 24–160 μm) and the windows at 850 μm and 1.2 mm accessible from the ground, providing a more complete understanding of galaxy evolution at this formative epoch.

The BLAST cosmological survey of the Great Observatories Origins Deep Survey¹³ (GOODS-South) region combines a wide-area map of 8.7 square degrees with a deeper, confusion-limited map of 0.8 square degrees. These nested surveys, which are the focus of this paper, are hereafter known as the BGS-Wide and BGS-Deep observations, respectively. The depth of the BGS-Deep map was chosen to produce maps that have high signal-to-noise ratios and in which the fluctuations are dominated by pixel-to-pixel fluctuations in signals from galaxies rather than detector noise. The BLAST map (Fig. 1) overlaps

some of the deepest multiwavelength data that exist in a cosmological survey, including radio, infrared, optical (Hubble Ultra Deep Field) and X-ray (Extended Chandra Deep Field-South) surveys^{13,14}. The

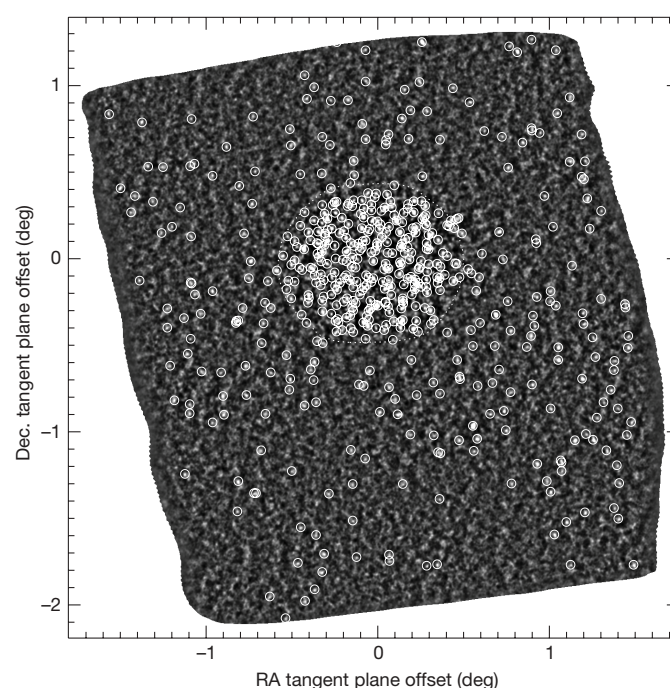


Figure 1 | Map showing the signal-to-noise ratio combination of all three BLAST bands for the entire BLAST GOODS-South observation. The circles show the locations of the ~ 500 sources extracted from the map that are detected with a signal-to-noise ratio > 5 . The 0.8-square-degree BGS-Deep region, centred at right ascension (RA) 3 h 32 min 28 s, declination (dec.) $-27^\circ 48' 30.00''$ was mapped to 1σ depths of 11, 9 and 6 mJy at 250, 350 and 500 μm , respectively, and contains 253 sources. It is visible as the region of high density in detected sources in the map. The 8.7-square-degree BGS-Wide field was mapped to 1σ depths of 36, 31 and 20 mJy at 250, 350 and 500 μm , respectively, and contains 261 sources. A more detailed description of the map making is provided in Supplementary Information.

¹Department of Physics & Astronomy, University of Pennsylvania, 209 South 33rd Street, Philadelphia, Pennsylvania 19104, USA. ²School of Physics & Astronomy, Cardiff University, 5 The Parade, Cardiff CF24 3AA, UK. ³Instituto Nacional de Astrofísica Óptica y Electrónica, Aptdo. Postal 51 y 72000 Puebla, Mexico. ⁴Jet Propulsion Laboratory, Pasadena, California 91109-8099, USA. ⁵Department of Physics & Astronomy, University of British Columbia, 6224 Agricultural Road, Vancouver, British Columbia V6T 1Z1, Canada. ⁶Department of Physics, University of Miami, 1320 Campo Sano Drive, Coral Gables, Florida 33146, USA. ⁷Canadian Institute for Theoretical Astrophysics, University of Toronto, 60 St George Street, Toronto, Ontario M5S 3H8, Canada. ⁸Department of Astronomy & Astrophysics, University of Toronto, 50 St George Street, Toronto, Ontario M5S 3H4, Canada. ⁹Department of Physics, University of Toronto, 60 St George Street, Toronto, Ontario M5S 1A7, Canada. ¹⁰University of Puerto Rico, Rio Piedras Campus, Physics Department, Box 23343, UPR Station 00931, Puerto Rico. ¹¹INAF – Osservatorio Astrofisico di Arcetri, Largo E. Fermi 5, I-50125 Firenze, Italy. ¹²Université Paris Diderot, Laboratoire APC, 10 rue Alice Domon et Léonie Duquet, 75205 Paris, France. ¹³Department of Physics, Brown University, 182 Hope Street, Providence, Rhode Island 02912, USA.

BGS-Wide map was designed to match the coverage area and sensitivity of the near-infrared and mid-infrared Spitzer Wide-area Infrared Extragalactic survey¹⁵. By considering both of the data sets together, we derive a catalogue of sources that covers a large dynamic range, (a factor of 50 in flux density) with sufficient sensitivity to resolve the FIRB into individual galaxies. The area is large enough that the source counts are minimally affected by clustering. The BLAST survey contains approximately 500 sources with significant ($>5\sigma$) detections.

The brightness distribution, or number counts, of submillimetre sources probes the luminosity function in relation to redshift and can be used to constrain models for the formation and evolution of dusty, star-forming galaxies. Models that simultaneously fit the entire range of existing data (24–850 μm) include at least two distinct galaxy populations with different spectral energy distributions and evolutionary histories^{16,17}. The BLAST data uniquely bridge these wavelengths across the energetic peak in the FIRB, and provide new strong constraints on the details of the evolution of these populations.

The number counts cannot be obtained directly from the distribution of detected sources in the BLAST catalogues because of several well-known biases. (1) The steep decrease in the counts with increasing flux density results in an Eddington bias whereby many more faint sources are boosted, rather than diminished in brightness, by noise fluctuations¹⁸. (2) The completeness of the survey falls off steeply at the faint end of the catalogue. (3) Multiple faint sources blend into brighter sources owing to a high surface density of the weakest sources and the 30–60'' resolution of the BLAST experiment. Rather than attempting to correct our source list for each of these effects, we estimate the counts from the distribution of pixel brightnesses in the entire map. This $P(D)$ analysis¹⁹ implicitly handles all of the effects mentioned above, yet uses more of the information available to us than just the brightest pixels of the extracted point sources in our catalogues.

Figure 2 shows the BLAST number counts with the results from experiments spanning 24–850 μm , for comparison. The BLAST counts are consistent with a single power law at low flux density. We can place limits on the shape of the number counts at the faint end by comparison with the FIRB. Using the naive model that the power law continues down to some limiting flux S_0 , with no sources fainter than S_0 , we find that the inferred integrated surface brightness equals the FIRB when $S_0 = 7.0 \pm 1.3$, 7.2 ± 1.7 and 4.6 ± 1.2 mJy at 250, 350 and 500 μm , respectively. A break in the counts, to a shallower slope, must occur at flux densities higher than the above limits to ensure that the integrated signal from the BLAST surveys is consistent with the amplitude of the FIRB. The increased sensitivity and higher resolution of SPIRE¹¹ should enable deeper surveys to detect the location of this spectral break.

BLAST is insensitive to individual sources significantly fainter than the 'confusion limit', which is conventionally defined as the flux at which sources reach a surface density of one object per 40 beams¹⁹. The confusion limits for BLAST and estimates of those for SPIRE based on the BLAST number counts are given in Table 1. We note that, through the $P(D)$ analysis, BLAST is sensitive to the number counts well below the confusion limit.

A stacking analysis using known positions of sources selected at different wavelengths is a powerful tool to estimate the contribution of a class of objects to the background at the wavelength of a particular map. The average brightness of these objects is calculated as the mean flux density measured at all of the positions in the map, a procedure that detects signals well below the threshold in signal-to-noise ratio used to make the BLAST catalogue. The contribution to the background from any stacked population is the product of its mean flux density and its surface density. A more detailed description of this method is provided in Supplementary Information.

We stack the 24- μm Far-Infrared Deep Extragalactic Legacy (FIDEL) survey catalogue (M. E. Dickinson *et al.*, in preparation) against the BLAST maps. The FIDEL catalogue contains sources

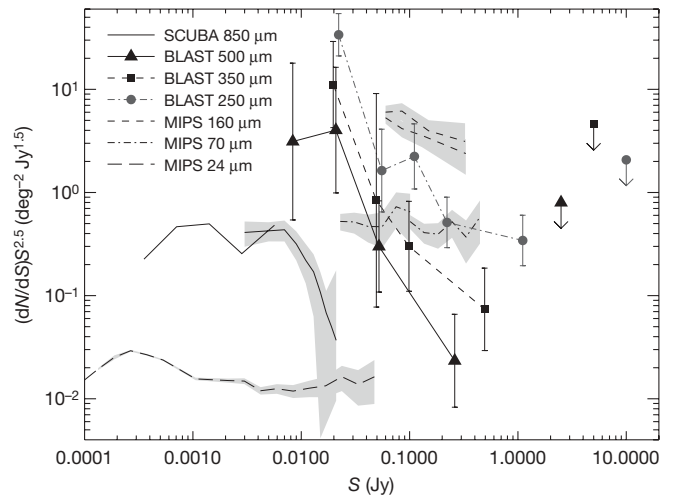


Figure 2 | The differential source counts at a variety of submillimetre and far-infrared wavelengths. If there is no evolution in number density or luminosity, we expect number counts to be Euclidean with $dN/dS \propto S^{-2.5}$. We have therefore multiplied the counts by $S^{2.5}$ so that a Euclidean slope would be horizontal. The BLAST 250, 350 and 500- μm counts (circles, squares and triangles) are measured by $P(D)$ analysis, as described in the text and Supplementary Information. Other data shown (lines only) are SCUBA 850- μm counts^{5,27} (solid lines); MIPS 160- μm counts²⁸ (short-dashed lines); MIPS 70- μm counts²⁸ (dash-dot lines); MIPS 24- μm counts²⁰ (long-dashed lines). The error bars are 1σ ; the shaded regions are 1σ error bands; the upper limits are 2σ . Nearby sources, such as the brighter sources measured at 24 μm , appear Euclidean. The counts at 850 μm are steep, which is an indication of strong evolution. A striking feature of the BLAST counts is that the slope steepens with increasing wavelength: this is the transition from the short-wavelength part of the FIRB dominated by local sources to the longer-wavelength regime dominated by distant starburst galaxies. There appears to be a break in the 500- μm counts at the low end. However, the large error bar in the last bin and the fact that adjacent bins are inherently anti-correlated make the result not very significant.

brighter than 13 mJy. The stacked flux values are given in Table 2. We include a ~ 7 –10% correction for completeness of the FIDEL catalogue based on extrapolation of 24- μm counts²⁰. From the results of these calculations, shown in Table 2, we conclude that the FIDEL sources produce 75–100% of the FIRB as measured using the Far-Infrared Absolute Spectrophotometer (FIRAS)²¹ on NASA's Cosmic Background Explorer.

Results similar to those from BLAST have been reported by stacking 24- μm Spitzer sources against the 70- μm and 160- μm maps²². Those data, recorded at wavelengths shorter than the peak intensity of the spectral energy distribution, are biased towards the low-redshift ($z \lesssim 1$) population that contributes to the FIRB. Surveys at 850 μm using the Submillimetre Common-User Bolometer Array (SCUBA) at the James Clerk Maxwell Telescope (Mauna Kea, Hawaii) sampled the higher-redshift contribution but resolved only 20–30% of the FIRB above the confusion limit⁵. Techniques using gravitational lensing to identify fainter sources below the confusion limits of ground-based submillimetre telescopes have been claimed to resolve a larger fraction

Table 1 | Source confusion limits determined by BLAST

Wavelength (μm)	BLAST r.m.s. flux density from sources (mJy)	BLAST confusion flux density (mJy)	SPIRE confusion flux density (mJy)
250	18	33 ± 4	22 ± 2
350	13	30 ± 7	22 ± 4
500	12	27 ± 4	18 ± 5

The fluctuations in the BLAST maps result from a combination of instrument noise and signals from sources. For each of the BLAST bands listed in the first column, the second column gives the residual map fluctuations from sources after subtracting instrument noise. The third and fourth columns give the formal confusion limits for BLAST and for SPIRE based on BLAST $P(D)$ analysis and the respective beam sizes. The confusion limit is the source brightness, S_{conf} , for which there is one source for every 40 beams. r.m.s., root mean squared.

Table 2 | The results of the 24- μm stacked flux

Wavelength (μm)	Stacked flux ($\text{nW m}^{-2} \text{sr}^{-1}$)	Corrected flux ($\text{nW m}^{-2} \text{sr}^{-1}$)	FIRB ($\text{nW m}^{-2} \text{sr}^{-1}$)
250	7.9 ± 0.5	8.5 ± 0.6	10.4 ± 2.3
350	4.5 ± 0.3	4.8 ± 0.3	5.4 ± 1.6
500	2.0 ± 0.2	2.2 ± 0.2	2.4 ± 0.6

For each of the BLAST bands in the first column, the second and third columns give the stacked and completeness-corrected fluxes, respectively. The fourth column is the expected flux determined by FIRAS²¹. The precision of the astrometry is 5". To verify the astrometry, the stacked flux was shown to drop off in all directions when the map is shifted with respect to the 24- μm catalogue. A similar stack was made against the 2-Ms Chandra Deep Field-South survey catalogue²⁵ which resolves $\sim 80\%$ of the soft and hard X-ray backgrounds²⁶. We find that these sources account for about 14% of the FIRB. Because active galactic nuclei account for 55% of the sources in the Chandra catalogue²⁵, we conclude that they only comprise 7% of the FIRB, although there may be a small contribution from Compton-thick active galactic nuclei that is missed.

of the FIRB²³. The wide spectral coverage of the BLAST data allows us to probe the Universe at both low redshift and high redshift. To demonstrate this, we use the Spitzer Infrared Array Camera (IRAC) colours to broadly divide the FIDEL catalogue into different populations to examine their relative contributions to the background at BLAST wavelengths. Using sources of known redshift in the GOODS Multiwavelength Southern Infrared Catalogue²⁴, we were able to define a simple cut in IRAC colours that effectively divides the catalogue into two galaxy populations above and below $z = 1.2$. At 250 μm , we find that there are approximately equal contributions to the background from sources above and below $z = 1.2$. We also note a systematic increase to 55% at 350 μm and 70% at 500 μm in the proportion of the background produced by sources at $z > 1.2$. These results are consistent with our expectation that objects in the longer-wavelength BLAST channels are dominated by the ultraluminous $z > 1$ galaxies discovered by SCUBA at 850 μm .

BLAST is the first instrument to make confusion-limited maps of the sky at wavelengths near the peak of the FIRB with enough sensitivity, sky coverage and angular resolution to identify a large number of sources, determine the detailed shape of the source counts and show that most of the FIRB comes from submillimetre sources already identified in deep 24- μm surveys. Combining these data with the results at 70 and 160 μm , we can account for essentially all of the FIRB with known galaxies. Combining the BLAST and future Herschel data at 250, 350 and 500 μm with spectroscopic and photometric redshifts will allow a determination of the optically obscured star-formation history of the Universe. These data will also provide catalogues of luminous submillimetre sources that will benefit from high-resolution imaging and spectroscopy from the Atacama Large Millimetre/submillimetre Array as we improve our understanding of galaxy formation and evolution in the high-redshift Universe.

Received 19 November 2008; accepted 9 February 2009.

1. Smail, I., Ivison, R. J. & Blain, A. W. A deep sub-millimetre survey of lensing clusters: a new window on galaxy formation and evolution. *Astrophys. J.* **490**, L5–L9 (1997).
2. Hughes, D. H. *et al.* High-redshift star formation in the Hubble Deep Field revealed by a submillimetre-wavelength survey. *Nature* **394**, 241–247 (1998).
3. Barger, A. J. *et al.* Submillimetre-wavelength detection of dusty star-forming galaxies at high redshift. *Nature* **394**, 248–251 (1998).
4. Greve, T. R. *et al.* A 1200- μm MAMBO survey of ELAIS2 and the Lockman Hole - I. Maps, sources and number counts. *Mon. Not. R. Astron. Soc.* **354**, 779–797 (2004).

5. Coppin, K. *et al.* The SCUBA Half-Degree Extragalactic Survey - II. Submillimetre maps, catalogue and number counts. *Mon. Not. R. Astron. Soc.* **372**, 1621–1652 (2006).
6. Eales, S. *et al.* The Canada-UK Deep Submillimetre Survey. IV. The survey of the 14 hour field. *Astron. J.* **120**, 2244–2268 (2000).
7. Borys, C., Chapman, S., Halpern, M. & Scott, D. The Hubble Deep Field North SCUBA Super-map - I. Submillimetre maps, sources and number counts. *Mon. Not. R. Astron. Soc.* **344**, 385–398 (2003).
8. Laurent, G. T. *et al.* The Bolocam Lockman Hole Millimeter-Wave Galaxy Survey: galaxy candidates and number counts. *Astrophys. J.* **623**, 742–762 (2005).
9. Coppin, K. *et al.* The SCUBA Half Degree Extragalactic Survey - VI. 350- μm mapping of submillimetre galaxies. *Mon. Not. R. Astron. Soc.* **384**, 1597–1610 (2008).
10. Puget, J.-L. *et al.* Tentative detection of a cosmic far-infrared background with COBE. *Astron. Astrophys.* **308**, L5–L8 (1996).
11. Griffin, M. *et al.* The Herschel-SPIRE instrument and its capabilities for extragalactic astronomy. *Adv. Space Res.* **40**, 612–619 (2007).
12. Pascale, E. *et al.* The Balloon-borne Large Aperture Submillimetre Telescope: BLAST. *Astrophys. J.* **681**, 400–414 (2008).
13. Giavalisco, M. *et al.* The Great Observatories Origins Deep Survey: initial results from optical and near-infrared imaging. *Astrophys. J.* **600**, L93–L98 (2004).
14. Lehmer, B. D. *et al.* The Extended Chandra Deep Field-South Survey: Chandra point-source catalogs. *Astrophys. J. Suppl. Ser.* **161**, 21–40 (2005).
15. Lonsdale, C. J. *et al.* SWIRE: The SIRTf Wide-Area Infrared Extragalactic Survey. *Publ. Astron. Soc. Pacif.* **115**, 897–927 (2003).
16. Lagache, G. *et al.* Polycyclic aromatic hydrocarbon contribution to the infrared output energy of the Universe at $z \approx 2$. *Astrophys. J. Suppl. Ser.* **154**, 112–117 (2004).
17. Rowan-Robinson, M. The star formation history of the Universe: an infrared perspective. *Astrophys. J.* **549**, 745–758 (2001).
18. Eddington, A. S. The correction of statistics for accidental error. *Mon. Not. R. Astron. Soc.* **100**, 354–361 (1940).
19. Condon, J. J. Confusion and flux-density error distributions. *Astrophys. J.* **188**, 279–286 (1974).
20. Papovich, C. *et al.* The 24 micron source counts in deep Spitzer Space Telescope surveys. *Astrophys. J. Suppl. Ser.* **154**, 70–74 (2004).
21. Fixsen, D. J., Dwek, E., Mather, J. C., Bennett, C. L. & Shafer, R. A. The spectrum of the extragalactic far-infrared background from the COBE FIRAS observations. *Astrophys. J.* **508**, 123–128 (1998).
22. Dole, H. *et al.* The cosmic infrared background resolved by Spitzer. Contributions of midinfrared galaxies to the far-infrared background. *Astron. Astrophys.* **451**, 417–429 (2006).
23. Knudsen, K. K., van der Werf, P. P. & Kneib, J.-P. Probing the submillimetre number counts at $f_{850\mu\text{m}} < 2 \text{ mJy}$. *Mon. Not. R. Astron. Soc.* **384**, 1611–1626 (2008).
24. Grazian, A. *et al.* The GOODS-MUSIC sample: a multicolour catalog of near-IR selected galaxies in the GOODS-South field. *Astron. Astrophys.* **449**, 951–968 (2006).
25. Luo, B. *et al.* The Chandra Deep Field-South Survey: 2 ms source catalogs. *Astrophys. J. Suppl. Ser.* **179**, 19–36 (2008).
26. Hickox, R. C. & Markevitch, M. Absolute measurement of the unresolved cosmic X-ray background in the 0.5–8 keV band with Chandra. *Astrophys. J.* **645**, 95–114 (2006).
27. Smail, I., Ivison, R. J., Blain, A. W. & Kneib, J.-P. The nature of faint submillimetre-selected galaxies. *Mon. Not. R. Astron. Soc.* **331**, 495–520 (2002).
28. Dole, H. *et al.* Far-infrared source counts at 70 and 160 microns in Spitzer deep surveys. *Astrophys. J. Suppl. Ser.* **154**, 87–92 (2004).

Supplementary Information is linked to the online version of the paper at www.nature.com/nature.

Acknowledgements We acknowledge the support of NASA, the US National Science Foundation Office of Polar Programs, the Canadian Space Agency, the Natural Sciences and Engineering Research Council of Canada and the UK Science and Technology Facilities Council. We are grateful to B. Magnelli for help with the FIDEL 24- μm data. This research was enabled by the WestGrid computing resources and the SIMBAD and NASA/IPAC databases. We thank the Columbia Scientific Balloon Facility, Ken Borek Air Ltd and the mountaineers of McMurdo Station for their work.

Author Information Reprints and permissions information is available at www.nature.com/reprints. Correspondence and requests for materials should be addressed to M.J.D. (devlin@physics.upenn.edu).

LETTERS

Interdimensional universality of dynamic interfaces

Kab-Jin Kim¹, Jae-Chul Lee^{1,2}, Sung-Min Ahn¹, Kang-Soo Lee¹, Chang-Won Lee³, Young Jin Cho³, Sunae Seo³, Kyung-Ho Shin², Sug-Bong Choe¹ & Hyun-Woo Lee⁴

Despite the complexity and diversity of nature, there exists universality in the form of critical scaling laws among various dissimilar systems and processes such as stock markets¹, earthquakes², crackling noise³, lung inflation⁴ and vortices in superconductors⁵. This universality is mainly independent of the microscopic details, depending only on the symmetry and dimension of the system. Exploring how universality is affected by the system dimensions is an important unresolved problem. Here we demonstrate experimentally that universality persists even at a dimensionality crossover in ferromagnetic nanowires. As the wire width decreases, the magnetic domain wall dynamics changes from elastic creep^{6–9} in two dimensions to a particle-like stochastic behaviour¹⁰ in one dimension. Applying finite-size scaling, we find that all our experimental data in one and two dimensions (including the crossover regime) collapse onto a single curve, signalling universality at the criticality transition. The crossover to the one-dimensional regime occurs at a few hundred nanometres, corresponding to the integration scale for modern nanodevices.

The universality manifests in the self-organized scale-invariant scaling behaviour of metastable states with huge degrees of freedom. This scaling behaviour is inevitably related to the system dimensions and so we wished to explore the scaling criticality for different dimensions and to clarify the interlinking between them. Much theoretical work has been devoted to clarifying universality classes in various dimensions^{11–15} but experimental evidence has been lacking for low-dimensional systems because signals from small specimens become harder to detect as the dimension reduces. Recently, however, two-dimensional (2D) systems have been successfully studied using magneto-optical Kerr effect (MOKE) microscopy on ferromagnetic thin films, manifesting the Barkhausen criticality¹⁶ and its tunability with temperature¹⁷. Another experimental test in two dimensions involves scaling criticality in the creep motion of a magnetic domain wall (DW) driven by a weak magnetic field^{6–9}. Excellent agreement is found with the theoretical formula^{6,7} predicting the collective DW motion. Starting from this well-established 2D creep criticality, here we demonstrate that the criticality in ferromagnetic nanowires exhibits universal transition behaviour from two dimensions to one as the wire width decreases. The transition threshold is revealed to be determined solely by the ratio between the wire width and the length of the DWs that move together. Below the transition threshold, the nanowires exhibit another distinct scaling behaviour of one-dimensional (1D) DW hopping criticality¹⁰.

Nanowires of various widths ranging from 4 μm to 150 nm were patterned by electron-beam lithography and ion milling onto a 5.0-nm Ta/2.5-nm Pt/0.3-nm Co₉₀Fe₁₀/1.0-nm Pt film with perpendicular magnetic anisotropy. The dynamic DW criticality was investigated by monitoring the DW propagation speed generated by a magnetic field. The nanowires were initially saturated under a sufficiently large magnetic field and then a reversed domain was formed by thermomagnetic

writing on the nanowires under a small reversed field. The DW arrival time after applying a magnetic field was then measured at a position 40 μm away from the initial DW position by means of MOKE detection. The arrival times observed spanned more than four orders of magnitude (10 ms to 1,000 s) while we varied the strength of the magnetic field.

We observed a distinct transition from the 2D creep criticality with decreasing wire width w . In two dimensions, the DW propagation speed V follows the form of the creep scaling criticality⁷ with respect to the applied magnetic field H according to $V(H) = V_0 \exp(-\alpha H^{-\mu})$. Here, V_0 is the characteristic speed and $\alpha (= U_C H_{\text{crit}}^\mu / k_B T)$ is a constant related to the scaling energy constant U_C , the critical magnetic field H_{crit} , and the thermal fluctuation energy $k_B T$. The scaling exponent μ is solely determined by the dimensionality of the system and the DW roughness. In 2D systems, it has been theoretically predicted⁷ and experimentally verified⁶ that μ equals 1/4. Figure 1 shows the plot of $\ln(V)$ versus $H^{-\mu}$ for nanowires of various widths. The linear dependence in Fig. 1a–c clearly demonstrates that wide wires ($w \geq 600$ nm) exhibit typical 2D creep behaviour. However, for wires narrower than 500 nm, the data begin to deviate from the 2D linear

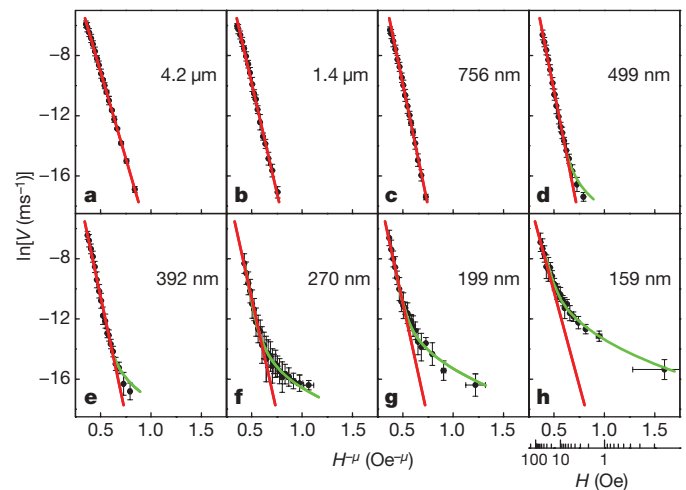


Figure 1 | Nonequilibrium criticality of DW speed along ferromagnetic nanowires. Data are shown for different wire widths: 4.2 μm (a), 1.4 μm (b), 756 nm (c), 499 nm (d), 392 nm (e), 270 nm (f), 199 nm (g) and 159 nm (h). The symbols show averaged values of ten repeated measurements for each H . The error bar (ordinate) is the standard deviation of the time measurements plus the maximum inaccuracy of initial DW positions. The error bar (abscissa) is ± 0.15 Oe corresponding to the inaccuracy of the H measurement. The scale bar beneath panel h shows the values of H . The red lines are the best fit to the 2D criticality ($\mu = 1/4$ is used) and the green lines are the best fit to the 1D criticality given by equation (1).

¹Center for Subwavelength Optics and School of Physics and Astronomy, Seoul National University, Seoul 151-742, Korea. ²Center for Spintronics Research, Korea Institute of Science and Technology, Seoul 136-791, Korea. ³Samsung Advanced Institute of Technology, Yongin 449-712, Korea. ⁴PCTP and Department of Physics, Pohang University of Science and Technology, Pohang, Kyungbuk 790-784, Korea.

behaviour and finally, completely distinct behaviour appears in Fig. 1f–h for $w \leq 300$ nm.

A standard scaling treatment is adopted to examine the crossover between these distinct scaling behaviours. All the data shown in Fig. 1 are replotted onto a single plot in Fig. 2a with scaling axes where the abscissa is $\alpha H^{-\mu}$ and the ordinate is $\ln(V/V_0)$. The values of α and V_0 are experimentally determined from the best fit for each wire (the red lines in Fig. 1). In Fig. 2a, all the data are collapsed onto a straight line with different thresholds for the upward deviations. The threshold values turn out to depend primarily on the ratio of the wire width to the collective DW length L_{col} . Here, L_{col} is the length of a DW segment that thermally jumps over the quenched disorder potential collectively and gives rise to the creep motion. According to ref. 6, $L_{col} = L_C [u_C \mu / 2\xi(\mu+1)]^{(2+\mu)/3} (H_{crit}/H)^{(2+\mu)/3}$ (Supplementary Information V), where the Larkin length $L_C = (\sigma \xi / M_S H_{crit})^{1/2}$ is the DW segment length ($<L_{col}$) above which effects of the disorder potential become dominant over the DW elasticity. Here σ is the DW energy density per unit area, M_S is the saturation magnetization, ξ is the correlation length of the disorder potential, and u_C is the roughness of the DW segment with length L_C . We note that L_{col} is proportional to a negative power of H and thus, for a sufficiently small field L_{col} becomes larger than the

wire width. When $L_{col} > w$, it is reasonable to expect that the collective DW segment length becomes w instead of L_{col} and the 2D criticality breaks down. Shorter collective segments experience a smaller energy barrier⁶, so this replacement of L_{col} by w boosts the DW speed and the scaling curve is consequently bent upward. The regime of the 2D criticality is therefore bounded by the ratio w/L_{col} , explaining why narrower wires exhibit larger deviation from the 2D criticality.

Strikingly, all the data collapse onto a universal crossover curve when w/L_{col} is chosen as the abscissa and $\ln(V_0/V)/\alpha H^{-\mu}$ as the ordinate (Fig. 2b). The values of L_{col} used in the plot are estimated by assuming⁶ $u_C \approx \xi \approx 10$ nm and $\sigma \approx 10$ mJ m⁻² and using the experimental values $M_S = 1.7$ T and $H_{crit} \approx H_p$. The Bloch wall energy density σ is estimated using the typical values of the magnetic anisotropy 5×10^5 J m⁻³ and the exchange constant 1.3×10^{-11} J m⁻¹. Here, H_p is the DW propagation field, as discussed below. The collapse onto a single curve is good evidence for the universality of the criticality transition and the existence of a finite-size scaling function with w/L_{col} as a single governing parameter. The criticality transition exhibits gradual, rather than abrupt, crossover behaviour from the 2D criticality to another universal criticality. We verify that a simple change of μ cannot explain this new criticality (Supplementary Information IV).

One-dimensional criticality successfully explains the new criticality. In a true 1D structure, the DW has zero dimension and should behave as a particle. In addition, there is no way of detouring around pinning sites and so the DW can propagate only by hopping over the pinning sites. Therefore, we adopt a 1D model¹⁰ that treats the DW as a particle stochastically hopping back-and-forth over a quenched disorder potential. The average DW speed at steady state under an applied field H is then given by $V(H) = (\langle \Delta x_n \rangle / \langle 1/W_n^+ \rangle) (1 - \langle W_{n+1}^- / W_n^+ \rangle)$, where W_n^\pm is the rate of jumping from a pinning site n to a neighbouring pinning site $n \pm 1$ per unit time and Δx_n is the distance between the sites n and $n+1$. The equation is generalized from the original theory¹⁰ by allowing the random distribution of not only W_n^\pm but also Δx_n . We verify that V involves only the decoupled separate averages of the two quantities. Here, $\langle \rangle$ denotes the average over all the sites n , because in general pinning sites are not identical. For the simplest case with all sites identical, the equation is simplified to $V = \Delta x (W^+ - W^-)$. We note that even when the DW is driven in one particular direction (say, $W^+ > W^-$), there exists a finite probability for a DW to hop in the reverse direction. Although this reverse motion is not important in the 2D regime, it turns out that it cannot be ignored in the 1D regime. In the thermally activated process, $W^\pm(H)$ becomes $f_0 \exp(-E_B^\pm(H)/k_B T)$ according to the Arrhenius law, where f_0 is the attempt frequency and E_B^\pm is the energy barrier. For small H , we use the Taylor expansion to obtain $E_B^\pm(H) = a_0^\pm + a_1^\pm H + \frac{1}{2} a_2^\pm H^2$, where $a_m^\pm = \partial^m E_B^\pm / \partial H^m |_{H=0}$. (Incidentally, the Taylor expansion is not allowed in the 2D regime because the energy barrier is singular at $H = 0$.) The inversion symmetry of the wire and magnetic field provides the symmetry relations $a_n^+ = (-1)^n a_n^-$ between the Taylor coefficients. The DW speed is then finally given to be:

$$V(H) = 2\Delta x f_0 \exp\left(-\frac{a_0^+ + \frac{1}{2} a_2^+ H^2}{k_B T}\right) \sinh\left(\frac{|a_1^+| H}{k_B T}\right) \quad (1)$$

The green lines in Figs 1 and 2 show the best fit to equation (1). This absolute theoretical conformity with all the experimental data provides strong evidence of the 1D criticality.

The Taylor coefficients in equation (1) have clear physical meanings in view of the conventional theory of thermally activated magnetization process^{18–20}. The zeroth-order coefficient a_0^\pm is closely related to the thermal stability of data storage with the retention time $\tau = f_0^{-1} \exp(a_0^\pm / k_B T)$. The first-order coefficient a_1^\pm corresponds to $\mp V_A M_S$. The activation volume V_A is the characteristic volume acting as a single particle during the magnetization process, which is

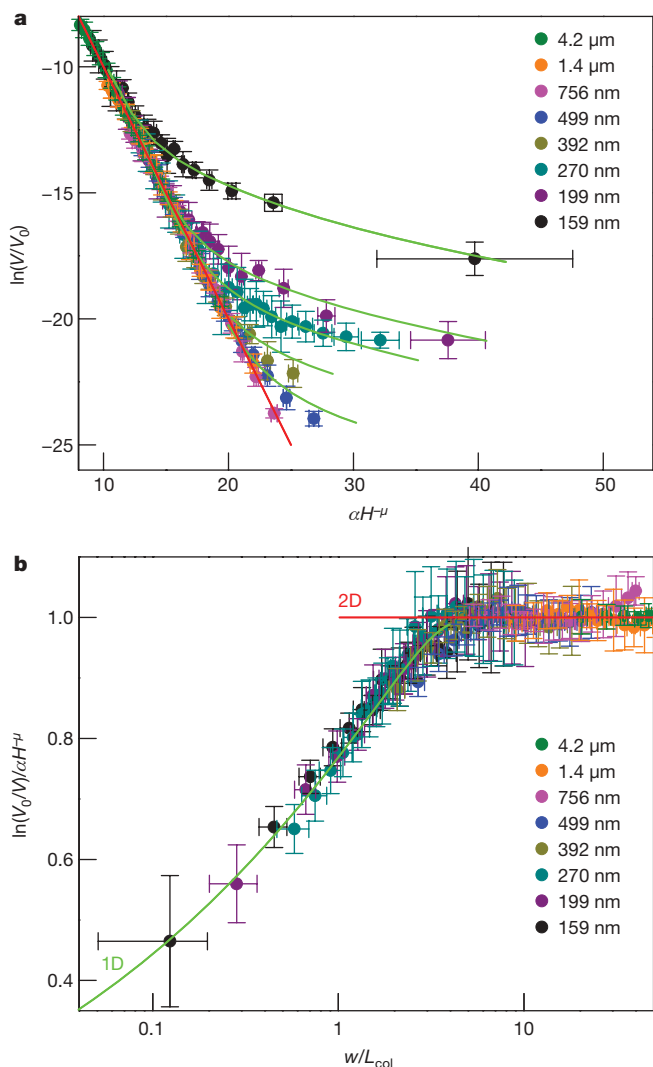


Figure 2 | Finite-size scaling and universal crossover behaviour of DW criticality. Scaled plots with $\ln(V/V_0)$ versus $\alpha H^{-\mu}$ (a) and $\ln(V_0/V)/\alpha H^{-\mu}$ versus w/L_{col} (b). In both panels, the symbols with different colours correspond to different wire widths as shown. The error bars are the same as those in Fig. 1. The red and green lines are the best fit to the 2D and 1D criticalities, respectively.

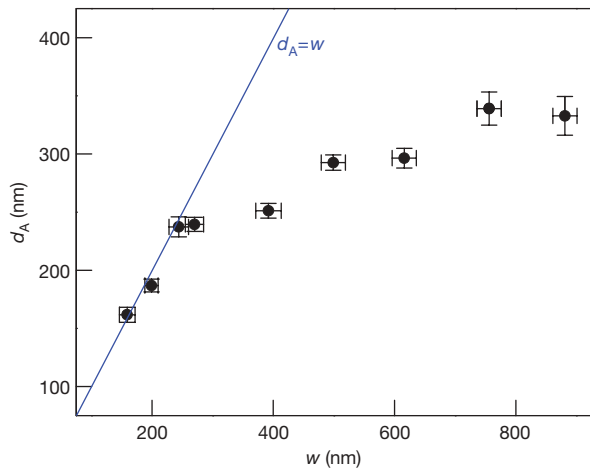


Figure 3 | Variation of activation diameter with respect to wire width. The symbols show the activation diameters d_A from the best fit to 1D criticality. The error bars correspond to the standard error in the χ -square fitting (ordinate) and the wire width variation (abscissa), respectively. The blue line guides the eye for $d_A = w$.

also related to the hopping distance Δx . The second-order coefficient a_2^\pm is seen in the uniaxial magnetic anisotropy model¹⁹ as $a_2^\pm = (a_1^\pm)^2 / 2a_0^\pm$. In this instance, the DW propagation field H_p can be defined as $H_p = |a_1^\pm / a_2^\pm|$, which is conceptually equivalent to the minimum field H_{crit} required to remove the energy barrier. Our experimental analysis reveals that the propagation field H_p exhibits $1/w$ dependence, which we ascribe to the influence of the wire edge roughness⁸, with a proportionality coefficient of 4.6 Oe μm and an intercept of 25.2 Oe (Supplementary Information VI).

The activation volume V_A provides a bound on the regime of the 1D criticality. Figure 3 shows the diameter d_A of the activation volume, that is, $V_A = \pi d_A^2 t_f / 4$, determined by the best fit to equation (1). Here, t_f denotes the film thickness. The figure clearly shows that there exist two distinct regimes of the wire width. For narrow wires, the activation diameter d_A equals the wire width w , as indicated by the blue line in Fig. 3, because the activation volume is extrinsically confined by the geometrical constriction²¹. A single activation volume then occupies the whole width of the wire and there remains only one possible DW motion: hopping over the activation volume along the wire as a 1D particle. On the other hand, for wide wires, the activation diameter is smaller than the wire width. For this case, the wire cross-section contains multiple activation volumes and the 1D particle picture breaks down. The crossover between the two regimes occurs at around 300 nm, in agreement with the transition between one and two dimensions as seen in Fig. 1. We therefore conclude that the activation volume in comparison with the wire width is another governing factor for dimensionality from the viewpoint of 1D criticality.

We report the experimental verification of new statistical scaling criticality in one dimension as well as the transitional behaviour from two dimensions to one. Universality exists at the criticality transition, manifesting gradual crossover behaviour between dimensions at about a few hundred nanometres. These results provide a step forward to a new scaling criticality for nanometre-sized physical structures, as yet much less examined, which are fundamental building blocks of emerging nanoscience and nanotechnologies.

METHODS SUMMARY

The scanning MOKE microscope is equipped with an objective lens (numerical aperture = 0.9) and a pulsed laser ($\lambda = 658 \text{ nm}$), which provides a 440-nm laser spot. The out-of-plane component of the magnetization state is monitored by detecting the polar MOKE signal. The laser intensity at the sample is kept lower than 45 μW to avoid possible heating damage. The temperature rise at the laser spot is estimated to be less than 1 K. The phase modulation technique is adopted with a lock-in amplifier, a photo-elastic modulator, and a low-noise photodiode

with $2 \times 10^6 \text{ V A}^{-1}$ signal gain. The signal voltage is collected by a data acquisition board at 250 kHz. A home-built electromagnet is used to generate a magnetic field of up to 200 Oe with the rising time less than 1 ms. A large magnetic field ($\sim 200 \text{ Oe}$) is first applied to saturate the nanowire and then a magnetic domain is initiated by thermomagnetic writing with a magnetic field pulse (25 Oe and 3 ms) and a laser pulse (5.6 mW and 1 s) focused on a local area of the nanowires. The DW is reproducibly formed with an accuracy of $\pm 1 \mu\text{m}$ ($\pm 2 \mu\text{m}$ for $w < 200 \text{ nm}$). Both the MOKE signal and the magnetic field trigger signal are simultaneously detected to precisely determine the DW arrival time. All the measurements are repeated ten times. The magnetic field H is swept from 0 to 200 Oe with increments of 0.1–0.5 Oe depending on the measurable DW speed range.

Received 30 October 2008; accepted 2 February 2009.

- Lux, T. & Marchesi, M. Scaling and criticality in a stochastic multi-agent model of a financial market. *Nature* **397**, 498–500 (1999).
- Carlson, J. M., Langer, J. S. & Shaw, B. E. Dynamics of earthquake faults. *Rev. Mod. Phys.* **66**, 657–670 (1994).
- Sethna, J. P., Dahmen, K. A. & Myers, C. R. Crackling noise. *Nature* **410**, 242–250 (2001).
- Suki, B., Barabási, A.-L., Hantos, Z., Peták, F. & Stanley, H. E. Avalanches and power-law behaviour in lung inflation. *Nature* **368**, 615–618 (1994).
- Blatter, G., Feigel'man, M. V., Geshkenbein, V. B., Larkin, A. I. & Vinokur, V. M. Vortices in high-temperature superconductors. *Rev. Mod. Phys.* **66**, 1125–1388 (1994).
- Lemerle, S. *et al.* Domain wall creep in an Ising ultrathin magnetic film. *Phys. Rev. Lett.* **80**, 849–852 (1998).
- Chauve, P., Giamarchi, T. & Le Doussal, P. Creep and depinning in disordered media. *Phys. Rev. B* **62**, 6241–6267 (2000).
- Cayssol, F., Ravelosona, D., Chappert, C., Ferré, J. & Jamet, J. P. Domain wall creep in magnetic wires. *Phys. Rev. Lett.* **92**, 107202 (2004).
- Metaxas, P. J. *et al.* Creep and flow regimes of magnetic domain-wall motion in ultrathin Pt/Co/Pt films with perpendicular anisotropy. *Phys. Rev. Lett.* **99**, 217208 (2007).
- Derrida, B. Velocity and diffusion constant of a periodic one-dimensional hopping model. *J. Stat. Phys.* **31**, 433–450 (1983).
- Bak, P., Tang, C. & Wiesenfeld, K. Self-organized criticality: an explanation of $1/f$ noise. *Phys. Rev. Lett.* **59**, 381–384 (1987).
- Fisher, D. S. Interface fluctuations in disordered systems: 5- ε expansion and failure of dimensional reduction. *Phys. Rev. Lett.* **56**, 1964–1967 (1986).
- Cizeau, P., Zapperi, S., Durin, G. & Stanley, H. E. Dynamics of a ferromagnetic domain wall and the Barkhausen effect. *Phys. Rev. Lett.* **79**, 4669–4672 (1997).
- Perković, O., Dahmen, K. & Sethna, J. P. Avalanches, Barkhausen noise, and plain old criticality. *Phys. Rev. Lett.* **75**, 4528–4531 (1995).
- Le Doussal, P. & Vinokur, V. M. Creep in one dimension and phenomenological theory of glass dynamics. *Physica C* **254**, 63–68 (1995).
- Kim, D.-H., Choe, S.-B. & Shin, S.-C. Direct observation of Barkhausen avalanche in Co thin films. *Phys. Rev. Lett.* **90**, 087203 (2003).
- Ryu, K.-S., Akinaga, H. & Shin, S.-C. Tunable scaling behaviour observed in Barkhausen criticality of a ferromagnetic film. *Nature Phys.* **3**, 547–550 (2007).
- Pommier, J. *et al.* Magnetic reversal in ultrathin ferromagnetic films with perpendicular anisotropy: domain observations. *Phys. Rev. Lett.* **65**, 2054–2057 (1990).
- Kirby, R. D., Shen, J. X., Hardy, R. J. & Sellmyer, D. J. Magnetization reversal in nanoscale magnetic films with perpendicular anisotropy. *Phys. Rev. B* **49**, 10810–10813 (1994).
- Choe, S.-B. & Shin, S.-C. Phase diagram of three contrasting magnetization reversal phases in uniaxial ferromagnetic thin films. *Appl. Phys. Lett.* **80**, 1791–1793 (2002).
- Skomski, R., Zeng, H., Zheng, M. & Sellmyer, D. J. Magnetic localization in transition-metal nanowires. *Phys. Rev. B* **62**, 3900–3904 (2000).

Supplementary Information is linked to the online version of the paper at www.nature.com/nature.

Acknowledgements This study was supported by KOSEF through the NRL programme (ROA-2007-000-20032-0). H.-W.L. was supported by KOSEF (R01-2007-000-20281-0, R11-2000-071). K.-J.K. was supported by the Seoul Science Fellowship and the Seoul R&BD programme. J.-C.L. was supported by KOSEF (R11-2008-095-01000-0). K.-H.S. was supported by the KIST Institutional Program and by the TND Frontier Project funded by MEST.

Author Contributions S.-B.C. planned and supervised the project; K.-J.K. designed and performed the experiments; C.-W.L., Y.J.C., and S.S. prepared sample films; J.-C.L. and K.-H.S. carried out patterning process; S.-M.A. and K.-S.L. characterized the films and nanostructures; K.-J.K., S.-B.C. and H.-W.L. performed theoretical analysis and wrote the manuscript.

Author Information Reprints and permissions information is available at www.nature.com/reprints. Correspondence and requests for materials should be addressed to S.-B.C. (sugbong@snu.ac.kr) or H.-W.L. (hwll@postech.ac.kr).

Enhancement of the Nernst effect by stripe order in a high- T_c superconductor

Olivier Cyr-Choinière^{1*}, R. Daou^{1*}, Francis Laliberté¹, David LeBoeuf¹, Nicolas Doiron-Leyraud¹, J. Chang¹, J.-Q. Yan^{2,†}, J.-G. Cheng², J.-S. Zhou², J. B. Goodenough², S. Pyon³, T. Takayama³, H. Takagi^{3,4}, Y. Tanaka^{5,3} & Louis Taillefer^{1,6}

The Nernst effect in metals is highly sensitive to two kinds of phase transition: superconductivity and density-wave order¹. The large, positive Nernst signal observed in hole-doped high- T_c superconductors² above their transition temperature (T_c) has so far been attributed to fluctuating superconductivity³. Here we report that in some of these materials the large Nernst signal is in fact the result of stripe order, a form of spin/charge modulation⁴ that causes a reconstruction of the Fermi surface⁵. In $\text{La}_{2-x}\text{Sr}_x\text{CuO}_4$ (LSCO) doped with Nd or Eu, the onset of stripe order causes the Nernst signal to change from being small and negative to being large and positive, as revealed either by lowering the hole concentration across the quantum critical point in Nd-doped LSCO (refs 6–8) or by lowering the temperature across the ordering temperature in Eu-doped LSCO (refs 9, 10). In the second case, two separate peaks are resolved, respectively associated with the onset of stripe order at high temperature and superconductivity near T_c .

The Nernst effect is the development of a transverse electric field E_y across the width (y axis) of a metallic sample when a temperature gradient $\partial T/\partial x$ is applied along its length (x axis) in the presence of a transverse magnetic field B (along the z axis). Two mechanisms can give rise to a Nernst signal, defined as $N = E_y/(\partial T/\partial x)$ (ref. 1). The first is superconducting fluctuations, of either phase or amplitude^{1,3}, which can only be positive¹. The second is due to mobile charge carriers, and produces a signal given by¹

$$N = -eL_0 T \frac{\partial}{\partial \varepsilon} \left(\frac{\sigma_{xy}}{\sigma_{xx}} \right) \Big|_{\varepsilon = \varepsilon_F} \quad (1)$$

where e is the elementary charge, $L_0 \equiv (\pi^2/3)(k_B/e)^2$ (k_B denoting the Boltzmann constant), T is the temperature, ε is the energy, ε_F is the Fermi energy, σ_{xy} is the (transverse) Hall conductivity and σ_{xx} is the (longitudinal) electrical conductivity. This quasiparticle Nernst signal can be either positive or negative.

Whereas in a single-band metal N is generally small, in a multiband metal it can be large¹, as indeed it is in semimetals, where the Nernst coefficient, $\nu \equiv N/B$, is typically very large^{1,11}. This implies that the quasiparticle Nernst coefficient should generically undergo a pronounced rise when the Fermi surface of a single-band metal is reconstructed into several pieces by the onset of some density-wave-like order. This is indeed what happens in metals like URu_2Si_2 (ref. 12) as they enter a semimetallic ordered state^{1,11}.

Evidence that the Fermi surface of high- T_c superconductors undergoes some reconstruction in the underdoped regime came

recently from the observation of low-frequency quantum oscillations in $\text{YBa}_2\text{Cu}_3\text{O}_y$ (ref. 13), which are thought to arise from orbits around a small, electron-like Fermi pocket¹⁴. Indeed, the standard mechanism for producing small electron pockets from a large, hole-like Fermi surface is the onset of some density-wave order that breaks translational symmetry^{5,15}. Within such a density-wave picture, the Nernst coefficient of a single-band metal such as LSCO would be expected to undergo a pronounced increase as the material is cooled below its ordering temperature. This is precisely what measurements of the Nernst effect in LSCO have revealed: ν is small (and negative) at high temperature and becomes large (and positive) at low temperature^{2,3}. However, this large rise in $\nu(T)$ with decreasing temperature has instead been attributed to a vortex contribution that grows with the approach of superconductivity³. Here we present two experiments which show that in some high- T_c superconductors the onset of ‘stripe order’—a form of spin/charge modulation—triggers a large enhancement of the Nernst signal, attributed to a change in the Fermi surface. The material used is LSCO with some of the La replaced with either Nd or Eu, a substitution that stabilizes stripe order^{7,9}.

In the first experiment, we switched stripe order on and off while keeping the superconductivity constant. This was achieved by measuring two samples of $\text{La}_{1.6-x}\text{Nd}_{0.4}\text{Sr}_x\text{CuO}_4$ (Nd-LSCO) with comparable transition temperatures (~ 20 K) but values of hole concentration on either side of the critical doping, p^* , where stripe order sets in^{6–9}, namely $p = 0.20$ and $p = 0.24$. The Nernst coefficient of this pair of samples is plotted in Fig. 1 as a function of temperature, along with the in-plane resistivity, ρ_{xx} , and the Hall coefficient, $R_H \approx \rho_{xy}/B$. In the sample with $p = 0.24$, all coefficients were monotonic and featureless, whereas in the sample with $p = 0.20$, they all showed a pronounced and simultaneous rise.

For $p = 0.24$, the fact that $R_H(T \rightarrow 0) = 1/e(1 + p)$ shows that the Fermi surface remains a single large hole cylinder as $T \rightarrow 0$ (ref. 6). In this case, ν is field independent above T_c (Supplementary Fig. 1) and remains small and negative as $T \rightarrow 0$, in agreement with previous data from a non-superconducting LSCO sample with $p = x = 0.26$ (ref. 3). This demonstrates that the onset of superconductivity has, by itself, little impact on ν . By dramatic contrast, for $p = 0.20$, $\nu(T)$ increases rapidly below 40 K to become large and positive, until it vanishes when superconductivity sets in. That the upturn in $\nu(T)$ tracks the upturn in $\rho(T)$ provides a second, independent, piece of evidence that the increase in $\nu(T)$ is not caused by incipient superconductivity.

The parallel rise observed in all three coefficients displayed in Fig. 1 demonstrates that the onset of a large positive Nernst coefficient is due to an enhancement of the quasiparticle contribution rooted in a

¹Département de Physique and RQMP, Université de Sherbrooke, Sherbrooke, Québec J1K 2R1, Canada. ²Texas Materials Institute, University of Texas at Austin, Austin, Texas 78712, USA. ³Department of Advanced Materials, University of Tokyo, Kashiwa 277-8561, Japan. ⁴RIKEN (The Institute of Physical and Chemical Research), Wako 351-0198, Japan. ⁵RIKEN SPring8 Center, Hyogo 679-5148, Japan. ⁶Canadian Institute for Advanced Research, Toronto, Ontario M5G 1Z8, Canada. [†]Present address: Ames Laboratory, Ames, Iowa 50011, USA.

*These authors contributed equally to this work.

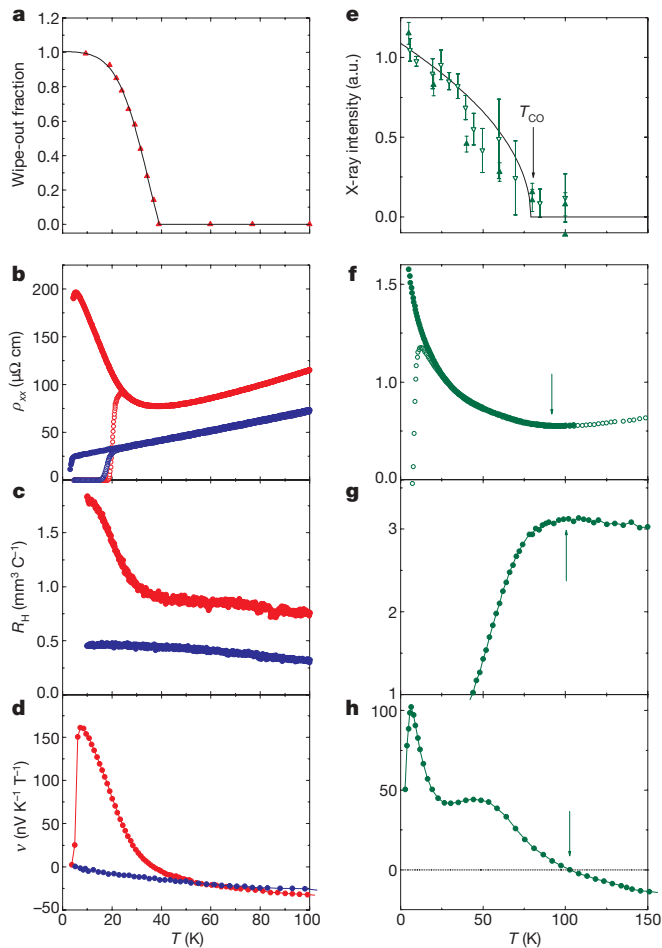


Figure 1 | Transport coefficients and stripe order in Nd-LSCO and Eu-LSCO. **a**, Charge stripe ordering in Nd-LSCO with $p = 0.20$, as measured by the loss of intensity in nuclear quadrupole resonance (NQR; from ref. 9). At dopings $p = 0.12$ and $p = 0.15$, where both X-ray diffraction and NQR were measured on Nd-LSCO, the lost (or ‘wipe-out’) fraction of the NQR intensity present at 100 K tracks the increase in the intensity of superlattice peaks detected with X-rays⁹. For $p = 0.20$, the onset of charge order occurs at $T_{CO} = 40 \pm 6$ K (ref. 9). **b–d**, Transport coefficients in two samples of Nd-LSCO, respectively with $p = 0.20$ (red) and $p = 0.24$ (blue): in-plane electrical resistivity, ρ_{xx} , in magnetic fields $B = 0$ (open symbols) and 15 T (filled symbols) (**b**; from ref. 6); Hall coefficient, R_H , for $B = 15$ T (**c**; from ref. 6); Nernst coefficient, ν , for $B = 10$ T (**d**; this work). In both samples, $T_c \approx 20$ K in zero field (see **b**). We note how for $p = 0.20$ all coefficients show a pronounced and simultaneous upturn starting at a temperature that coincides with the onset of charge order; this is strong evidence of Fermi surface reconstruction by stripe order being the cause of the large, positive Nernst signal. By contrast, for $p = 0.24$, $\nu(T)$ remains small and negative, unaffected by the onset of superconductivity. **e**, Charge stripe ordering in Eu-LSCO with $p = 0.125$ measured by diffraction using hard (filled symbols; this work) and soft (open symbols; ref. 10) X-rays. Error bars on filled symbols represent the standard error in the height of the Gaussian in a Gaussian-plus-background fit to the momentum scan at each temperature. Error bars on open symbols are from ref. 10. The onset of charge order is identified by both to be $T_{CO} = 80 \pm 10$ K. **a.u.**, arbitrary units. **f–h**, Transport coefficients measured on a sample of Eu-LSCO with $p = 0.125$: in-plane electrical resistivity, ρ_{xx} , in magnetic fields $B = 0$ (open symbols) and 15 T (filled symbols) (**f**); Hall coefficient, R_H , for $B = 10$ T (**g**); Nernst coefficient, ν , for $B = 10$ T (**h**). The onset of charge order is seen to coincide with anomalies in transport (marked by arrows): the minimum in $\rho(T)$, the decrease in $R_H(T)$ and the sign change in $\nu(T)$, all at ~ 100 K. As for Nd-LSCO with $p = 0.20$, this again argues for a Fermi surface reconstruction caused by stripe order.

modification of the Fermi surface⁶. In Fig. 1a, we reproduce the NQR wipe-out fraction measured on Nd-LSCO with $x = 0.20$ (ref. 7). The precipitous loss of NQR intensity below 40 K is caused by the onset of

stripe order⁷ (see also ref. 9). The crucial fact that the upturn in all coefficients matches with this onset strongly suggests that stripe order is the cause of the Fermi surface reconstruction⁵.

In a second experiment, we investigated the more underdoped regime in $\text{La}_{1.8-x}\text{Eu}_{0.2}\text{Sr}_x\text{CuO}_4$ (Eu-LSCO). In Fig. 1e, we show X-ray diffraction data on Eu-LSCO with $p = 0.125$. The intensity of scattering at the incommensurate stripe wavevector is seen to vanish at $T_{CO} = 80 \pm 10$ K. In Fig. 1f–h, we show transport data taken from one sample with $p = 0.125$. It is clear that the pronounced changes in $\rho(T)$, $R_H(T)$ and $\nu(T)$ all coincide with the onset of stripe order, as in Nd-LSCO with $p = 0.20$. We note that stripe ordering for $p = 0.125$ now causes $R_H(T)$ to decrease below T_{CO} , by contrast with the increase seen for $p = 0.20$. This evolution in the behaviour of $R_H(T)$ is consistent with calculations¹⁶ based on a theory of the Fermi surface reconstruction by stripe order¹⁷.

In Supplementary Fig. 2, we define T_v , the onset of the upturn in $\nu(T)$, whose doping dependence is plotted in the inset of Fig. 2. Because of the wide separation between $T_v \approx 140$ K and $T_c \approx 10$ K in Eu-LSCO with $p = 0.125$, we see that $\nu(T)$ consists of two separate peaks. The evolution of this two-peak structure with doping is shown in Fig. 2. The low-temperature peak, which is due to superconducting fluctuations, is suppressed by a magnetic field, whereas the high-temperature peak, which is due to quasiparticles, is not (Supplementary Figs 3 and 4). A similar situation prevails in the electron-doped copper oxide $\text{Pr}_{2-x}\text{Ce}_x\text{CuO}_4$, for which the Nernst signal separates clearly into a quasiparticle peak at high temperature and a superconducting peak near T_c (ref. 18). In that case, Fermi surface reconstruction is attributed to antiferromagnetic order^{18,19}. A comparison between Eu-LSCO and LSCO shows that the onset of the increase in $\nu(T)$ occurs at very similar values of T_v in both materials (Supplementary Figs 3 and 5), suggesting a common mechanism of Fermi surface reconstruction.

To conclude, we have resolved two contributions to the Nernst signal in the hole-doped copper oxide LSCO doped with Nd or Eu: one at low temperature, caused by superconducting fluctuations, and the other at high temperature, caused by a change in the Fermi surface.

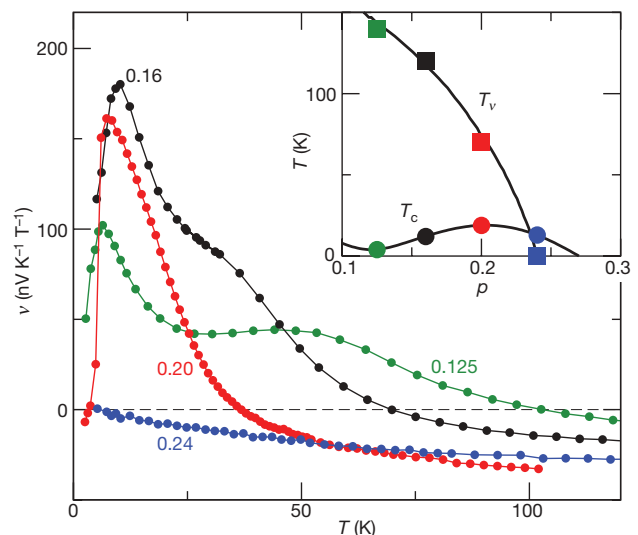


Figure 2 | Doping evolution of the Nernst coefficient and T_v . Temperature dependence of the Nernst coefficient, $\nu(T)$, for different dopings in Eu-LSCO (green, $p = 0.125$; black, $p = 0.16$) and Nd-LSCO (red, $p = 0.20$; blue, $p = 0.24$) for $B = 10$ T. This shows the doping evolution of the two contributions to $\nu(T)$, respectively from superconducting fluctuations at low temperature and quasiparticles on a reconstructed Fermi surface at high temperature. The gradual convergence of the two peaks in $\nu(T)$ is a consequence of the fact that T_v , which marks the onset of the high-temperature peak (Supplementary Fig. 2), and T_c , which controls the location of the low-temperature peak, come together as they approach p^* , the quantum critical point for the onset of stripe order⁶ (see inset).

In this case, the change in Fermi surface is clearly caused by the onset of stripe order at T_{CO} (ref. 6). The fact that $v(T)$ starts to rise at $T_v \approx 2T_{CO}$ suggests that stripe fluctuations are sufficient to cause $v(T)$ to increase⁵. It will be interesting to investigate whether the same mechanism is also involved in other hole-doped high- T_c superconductors.

Received 14 November 2008; accepted 23 February 2009.

- Behnia, K. The Nernst effect and the boundaries of the Fermi liquid picture. *J. Phys. Condens. Matter* **21**, 113101 (2009).
- Xu, Z. A. *et al.* Vortex-like excitations and the onset of superconducting phase fluctuation in underdoped $\text{La}_{2-x}\text{Sr}_x\text{CuO}_4$. *Nature* **406**, 486–488 (2000).
- Wang, Y., Li, P. & Ong, N. P. Nernst effect in high- T_c superconductors. *Phys. Rev. B* **73**, 024510 (2006).
- Tranquada, J. M. *et al.* Evidence for stripe correlations of spins and holes in copper oxide superconductors. *Nature* **375**, 561–563 (1995).
- Taillefer, L. Fermi-surface reconstruction in high- T_c superconductors. *J. Phys. Condens. Matter* (in the press); preprint at (<http://arXiv.org/abs/0901.2313>) (2009).
- Daou, R. *et al.* Linear temperature dependence of the resistivity and change in Fermi surface at the pseudogap critical point of a high- T_c superconductor. *Nature Phys.* **5**, 31–34 (2009).
- Ichikawa, N. *et al.* Local magnetic order vs superconductivity in a layered cuprate. *Phys. Rev. Lett.* **85**, 1738–1741 (2000).
- Daou, R. *et al.* Thermopower across the pseudogap critical point of $\text{La}_{1.6-x}\text{Nd}_{0.4}\text{Sr}_x\text{CuO}_4$: evidence of a quantum critical point in a hole-doped high- T_c superconductor. Preprint at (<http://arXiv.org/abs/0810.4280>) (2008).
- Hunt, A. W. *et al.* Glassy slowing of stripe modulation in $(\text{La},\text{Eu},\text{Nd})_{2-x}(\text{Sr},\text{Ba})_x\text{CuO}_4$: a ^{63}Cu and ^{139}La NQR study down to 350 mK. *Phys. Rev. B* **64**, 134525 (2001).
- Fink, J. *et al.* Charge order in $\text{La}_{1.8-x}\text{Eu}_{0.2}\text{Sr}_x\text{CuO}_4$ studied by resonant soft X-ray diffraction. Preprint at (<http://arXiv.org/abs/0805.4352>) (2008).
- Behnia, K., Méasson, M.-A. & Kopelevich, Y. Nernst effect in semi-metals: the effective mass and the figure of merit. *Phys. Rev. Lett.* **98**, 076603 (2007).
- Bel, R. *et al.* Thermoelectricity of URu_2Si_2 : giant Nernst effect in the hidden-order state. *Phys. Rev. B* **70**, 220501 (2004).
- Doiron-Leyraud, N. *et al.* Quantum oscillations and the Fermi surface in an underdoped high- T_c superconductor. *Nature* **447**, 565–568 (2007).
- LeBoeuf, D. *et al.* Electron pockets in the Fermi surface of hole-doped high- T_c superconductors. *Nature* **450**, 533–536 (2007).
- Chakravarty, S. From complexity to simplicity. *Science* **319**, 735–736 (2008).
- Lin, J. & Millis, A. J. Theory of low-temperature Hall effect in stripe-ordered cuprates. *Phys. Rev. B* **78**, 115108 (2008).
- Millis, A. J. & Norman, M. R. Antiphase stripe order as the origin of electron pockets observed in 1/8-hole-doped cuprates. *Phys. Rev. B* **76**, 220503 (2007).
- Li, P. & Greene, R. L. Normal-state Nernst effect in electron-doped $\text{Pr}_{2-x}\text{Ce}_x\text{CuO}_4$: superconducting fluctuations and two-band transport. *Phys. Rev. B* **76**, 174512 (2007).
- Hackl, A. & Sachdev, S. Nernst effect in the electron-doped cuprates. Preprint at (<http://arXiv.org/abs/0901.2348>) (2009).

Supplementary Information is linked to the online version of the paper at www.nature.com/nature.

Acknowledgements We thank K. Behnia, S. Sachdev and A.-M. S. Tremblay for discussions, and J. Corbin for his assistance with the experiments. J.C. is supported by a Fellowship from the Swiss National Science Foundation. J.-S.Z. and J.B.G. were supported by a US National Science Foundation grant. H.T. acknowledges MEXT Japan for a Grant-in-Aid for Scientific Research. L.T. acknowledges support from the Canadian Institute for Advanced Research and funding from the National Science and Engineering Research Council of Canada, the Fonds Québécois de la Recherche sur la Nature et les Technologies and a Canada Research Chair.

Author Information Reprints and permissions information is available at www.nature.com/reprints. Correspondence and requests for materials should be addressed to L.T. (louis.taillefer@physique.usherbrooke.ca).

LETTERS

Low-temperature oxidation of CO catalysed by Co₃O₄ nanorods

Xiaowei Xie^{1*}, Yong Li^{1*}, Zhi-Quan Liu², Masatake Haruta^{3,4} & Wenjie Shen¹

Low-temperature oxidation of CO, perhaps the most extensively studied reaction in the history of heterogeneous catalysis, is becoming increasingly important in the context of cleaning air and lowering automotive emissions^{1,2}. Hopcalite catalysts (mixtures of manganese and copper oxides) were originally developed for purifying air in submarines, but they are not especially active at ambient temperatures and are also deactivated by the presence of moisture^{3,4}. Noble metal catalysts, on the other hand, are water tolerant but usually require temperatures above 100 °C for efficient operation^{5,6}. Gold exhibits high activity at low temperatures and superior stability under moisture, but only when deposited in nanoparticulate form on base transition-metal oxides^{7–9}. The development of active and stable catalysts without noble metals for low-temperature CO oxidation under an ambient atmosphere remains a significant challenge. Here we report that tricobalt tetraoxide nanorods not only catalyse CO oxidation at temperatures as low as –77 °C but also remain stable in a moist stream of normal feed gas. High-resolution transmission electron microscopy demonstrates that the Co₃O₄ nanorods predominantly expose their {110} planes, favouring the presence of active Co³⁺ species at the surface. Kinetic analyses reveal that the turnover frequency associated with individual Co³⁺ sites on the nanorods is similar to that of the conventional nanoparticles of this material, indicating that the significantly higher reaction rate that we have obtained with a nanorod morphology is probably due to the surface richness of active Co³⁺ sites. These results show the importance of morphology control in the preparation of base transition-metal oxides as highly efficient oxidation catalysts.

Among the metal oxides, tricobalt tetraoxide is the most active for CO oxidation^{10,11}, but is severely deactivated by trace amounts of moisture (about 3–10 parts per million, p.p.m.) that are usually present in the feed gas. In fact, under dry conditions with a moisture content below 1 p.p.m., which can be obtained by passing the reaction gas through molecular-sieve traps cooled to dry-ice temperature, Co₃O₄ is intrinsically active for CO oxidation^{12,13} even below a temperature of –54 °C. However, in normal feed gas, most of the active sites of Co₃O₄ are covered by H₂O so the adsorption of CO and oxygen is appreciably hindered. Alumina-supported Co₃O₄ was reported to give 50% CO conversion at –63 °C for a normal feed gas, but the CO conversion was obtained with a transient method¹⁴ not at steady state. Here we show that Co₃O₄ nanorods can be steadily active for CO oxidation at a temperature as low as –77 °C, giving 100% CO conversion, and are quite stable even under a stream of normal feed gas containing moisture.

Nanorod-shaped Co₃O₄ was prepared by the calcination of a cobalt hydroxide carbonate precursor obtained by the precipitation of cobalt acetate with sodium carbonate in ethylene glycol. When cobalt acetate was mixed with ethylene glycol at 160 °C, the –OCH₂–CH₂O– chain

was tightly bound with the cobalt cations. The addition of aqueous sodium carbonate solution resulted in the formation of a solid cobalt hydroxide carbonate incorporating ethylene glycol, having a nanorod-shaped structure with a diameter of 10–20 nm and a length of 200–300 nm (Supplementary Fig. S1). Subsequent calcination of this precursor at 450 °C in air caused a spontaneous transformation of the morphology, forming Co₃O₄ nanorods with diameters of 5–15 nm and lengths of 200–300 nm.

Figure 1a shows a typical low-magnification transmission electron microscopy (TEM) image of the synthesized Co₃O₄, in which a batch of nanorods is developed from a cluster core, forming a coral-like morphology. Most of the nanorods have straight sides and regular ends, as shown in Fig. 1b, an enlarged TEM image. We examined the crystallographic nature of the individual Co₃O₄ nanorod using high-resolution TEM (HRTEM) observations. Figure 1c is a section of a Co₃O₄ nanorod in the [1–10] orientation, showing the growth direction as [110] and the flat side parallel to (001). These (001) side planes were also observed in the [100] orientation (Fig. 1d), which was constructed from {022} planes with a spacing of 0.286 nm. When the nanorod was tilted to the [001] zone axis (Fig. 1e), we clearly observed the two orthogonal sets of the {220} lattice. The flat top is the (110) atomic plane and the side plane is (1–10). Figure 1f shows the cross-section viewed near the [110] orientation, exhibiting a rectangular shape with the long edges parallel to (001) and the short edges parallel to (1–10). Taking all these TEM images into account, the real shape of the nanorod can be approximately reconstructed, as shown in Fig. 1g, in which the axial direction is [110]. The Co₃O₄ nanorod has two {001} flat planes, two {1–10} side planes and two {110} end planes. In other words, the Co₃O₄ nanorod mainly grows along the [110] direction and preferentially exposes the {110} plane, the surface area of which is estimated to be 41% of the total surface area.

The Co₃O₄ nanorods were tested for CO oxidation at –77 °C under a reaction stream with a gas composition of 1.0 vol.% CO/2.5 vol.% O₂/He. They showed 100% CO conversion to CO₂ during the initial 6 h; the CO conversion then tended to decrease, but only down to 80% after 12 h (Fig. 2). This catalytic performance is quite promising in terms of activity and stability when compared with the metal oxides reported thus far^{12–17}, and is even superior to supported gold nanoparticles⁷. Because Co₃O₄ is very sensitive to the presence of moisture in normal feed gas^{12,13}, we then measured the catalytic activity of the nanorods under dry conditions. Surprisingly, the CO conversion was almost the same (100%) as in the normal feed gas during the initial 6 h and there was only a slight improvement in stability during the subsequent operation (Fig. 2), suggesting that the Co₃O₄ nanorods are not very sensitive to the presence of moisture. The measured reaction rates of CO oxidation at –77 °C were $3.91 \times 10^{-6} \text{ mol g}^{-1} \text{ s}^{-1}$ for normal feed gas and $5.88 \times 10^{-6} \text{ mol g}^{-1} \text{ s}^{-1}$ under dry conditions. This indicates

¹State Key Laboratory of Catalysis, Dalian Institute of Chemical Physics, Chinese Academy of Sciences, Dalian 116023, China. ²Shenyang National Laboratory for Materials Science, Institute of Metal Research, Chinese Academy of Sciences, Shenyang 110016, China. ³Department of Applied Chemistry, Graduate School of Urban Environmental Sciences, Tokyo Metropolitan University, 1-1 Minami-osawa, Hachioji 192-0397, Tokyo, Japan. ⁴Japan Science and Technology Agency, CREST, 4-1-8 Hon-Cho, Kawaguchi 332-0012, Saitama, Japan. *These authors contributed equally to this work.

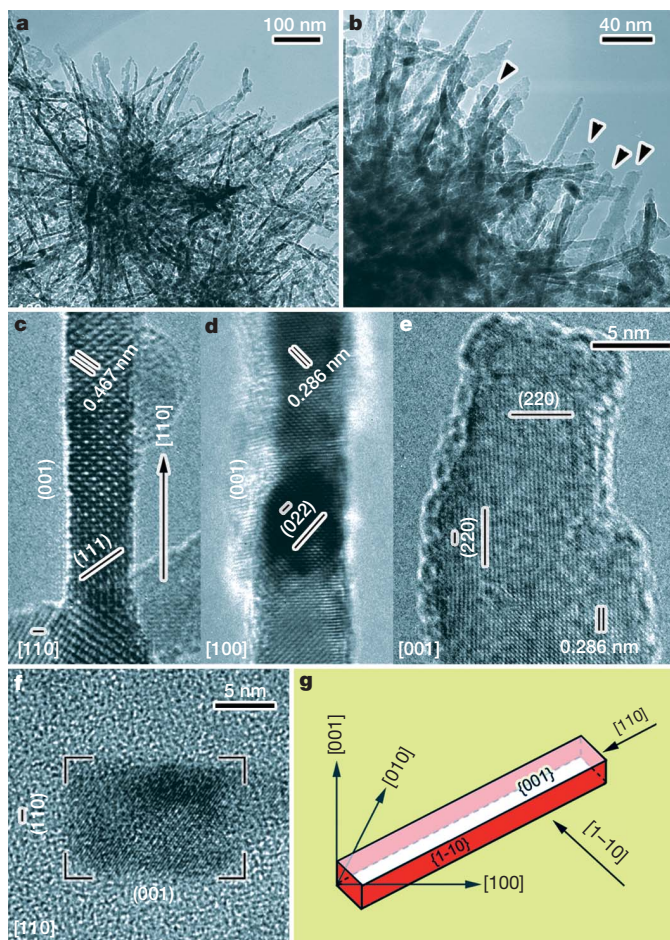


Figure 1 | TEM images of Co_3O_4 nanorods. **a, b**, Low and high magnifications, where the arrowheads indicate the straight sides and regular ends of the nanorods. **c–f**, HRTEM images viewed along the $[1-10]$ (**c**), $[100]$ (**d**), $[001]$ (**e**) and near $[110]$ (**f**) orientations. **g**, Shape of the nanorod, where red represents the catalytically active planes. Note, $[uvw]$ is an index of a specified crystal axis and (hkl) is an index of a specified crystal plane, while $\{hkl\}$ indicates a set of group crystal planes with the same atomic configuration.

that the removal of moisture does result in a higher reaction rate, but not significantly so when compared with the previous observations for the conventionally prepared Co_3O_4 nanoparticles^{12,13}.

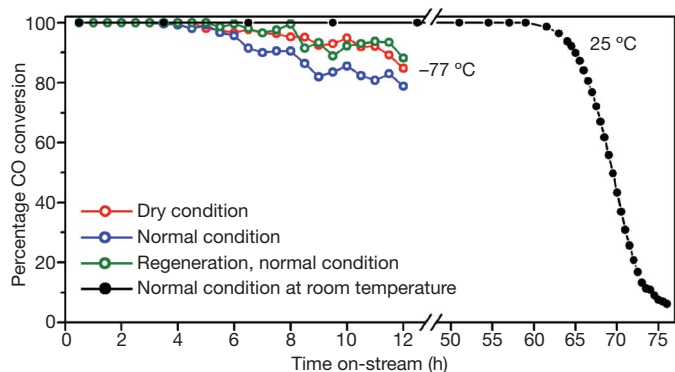


Figure 2 | Effects of moisture content, regeneration and temperature on the oxidation of CO over Co_3O_4 nanorods. CO oxidation with a feed gas of 1.0 vol.% CO/2.5 vol.% O_2 /He under normal (moisture 3–10 p.p.m., blue symbols) and dry (moisture <1 p.p.m., red symbols) conditions at -77°C . The used sample was regenerated with a 20 vol.% O_2 /He mixture at 450°C for 30 min and then tested for CO oxidation under normal conditions (green symbols) at -77°C . CO oxidation at 25°C (black symbols) was tested with the normal feed gas.

Co_3O_4 has a spinel structure containing Co^{3+} in an octahedral coordination and Co^{2+} in a tetrahedral coordination. The former is regarded as the active site for CO oxidation, whereas the latter is almost inactive^{18–20}. The redox cycle connecting the two stages is largely responsible for the successful CO oxidation. As shown in Fig. 3a, oxygen anions form a distorted face-centred cubic sublattice, in which Co^{2+} cations occupy one-eighth of the tetrahedral interstices and Co^{3+} cations occupy half of the octahedral interstices. The close-packed planes are $\{001\}$, $\{111\}$ and $\{110\}$, and their surface atomic configurations are illustrated in Fig. 3b–d. Clearly, the $\{001\}$ and $\{111\}$ planes contain only Co^{2+} cations, while the $\{110\}$ plane is composed mainly of Co^{3+} cations. In fact, surface differential diffraction studies have proved that the Co^{3+} cations are present solely on the $\{110\}$ plane^{21,22}. Therefore, it is most likely that CO oxidation on the Co_3O_4 nanorods follows the reaction pathway shown in Fig. 3e. The CO molecule interacts preferably with the surface Co^{3+} cation, which is the only favourable site for CO adsorption, as confirmed both theoretically²³ and experimentally^{13,24}. The oxidation of the adsorbed CO then occurs by abstracting the surface

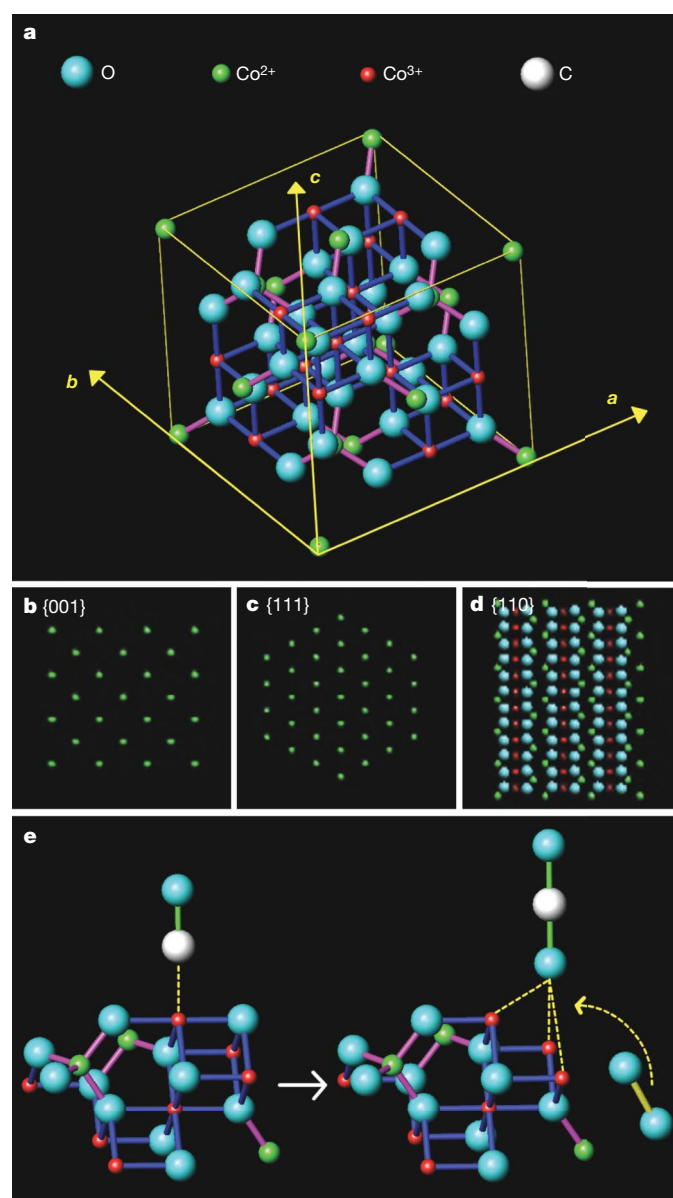


Figure 3 | Possible reaction pathway for CO oxidation on Co_3O_4 nanorod. **a**, Spinel structure of Co_3O_4 crystal. **b–d**, The surface atomic configurations in the $\{001\}$ (**b**), $\{111\}$ (**c**), and $\{110\}$ (**d**) planes. **e**, A ball-and-stick model for CO adsorption and oxidation on the active Co^{3+} site.

oxygen that might be coordinated with three Co^{3+} cations. Finally, the partially reduced cobalt site, which might be a Co^{2+} cation with a neighbouring oxygen vacancy, is re-oxidized by a gas-phase oxygen molecule to the active Co^{3+} site. The Co_3O_4 nanorod exposes four surface {110} planes that are rich in Co^{3+} sites, so we would expect it to exhibit a much higher activity for CO oxidation than the conventional nanoparticle, which exposes mainly the {001} and {111} planes (Supplementary Fig. S2), which contain only inactive Co^{2+} sites^{13,18}.

The reaction orders of CO and O_2 over the Co_3O_4 nanorods were 0.12 and 0.28 (Fig. 4a), respectively, suggesting that the surfaces of the nanorods are almost saturated with CO and O_2 , leading to very weak dependencies of the reaction rate on the gas-phase CO and O_2 concentrations. When the reaction temperature is far below room temperature, the rate of adsorption of reactant can usually exceed the rate of surface reaction. The abundant Co^{3+} cations on the {110} plane provides sufficient sites for CO adsorption, which occurs readily. The reaction between the adsorbed CO and the nearby oxygen species to form CO_2 seems to be the rate-determining step because the ensuing regeneration of the active oxygen site with a gas-phase oxygen molecule takes place rapidly through interactions with the partially reduced cobalt cations^{23,24}. As a result, CO oxidation could occur far below room temperature as long as both reactants are simultaneously present on the active surface.

The apparent activation energy of CO oxidation over the Co_3O_4 nanorods was 22 kJ mol^{-1} , which is almost the same as that of the Co_3O_4 nanoparticles (Fig. 4b). This implies that the active site for CO oxidation in both cases is identical and is Co^{3+} . Turnover frequencies estimated on the basis of the Co^{3+} site are essentially similar for the nanorods and the nanoparticles (Supplementary Table S1). The pre-exponential factor for the Co_3O_4 nanorods is $8.0 \times 10^{24} \text{ molecules g}^{-1} \text{ s}^{-1}$, whereas the corresponding value for the Co_3O_4 nanoparticles is only $5.7 \times 10^{23} \text{ molecules g}^{-1} \text{ s}^{-1}$. This strongly indicates that the difference in the reaction rate is due solely to the variation in the number of active sites and that the significantly higher reaction rate of the nanorods can be ascribed to the richness in active Co^{3+} sites on the surfaces through preferentially exposing the reactive {110} planes.

To identify the reason for the gradual deactivation of the Co_3O_4 nanorods during the course of the reaction at -77°C with the normal feed gas, a deactivated sample was treated with a 20 vol.% O_2/He mixture at 450°C , through which the deposited carbonates and/or bicarbonates and $\text{H}_2\text{O}/\text{OH}^-$ species are completely desorbed as water and CO_2 (Supplementary Fig. S3). When exposed to the reaction gas again at -77°C , the regenerated sample exhibited fully recovered and even better activity for CO oxidation (Fig. 2). Hence, the loss in activity

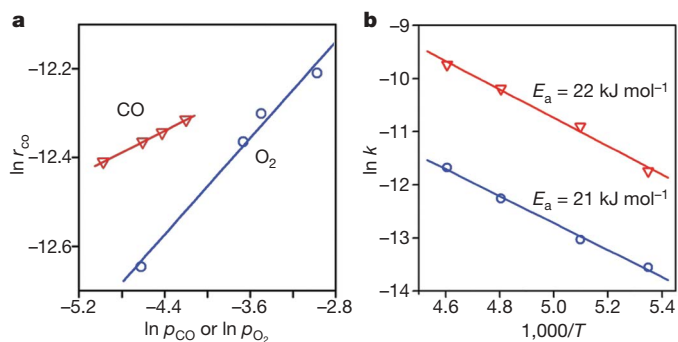


Figure 4 | Reaction kinetics of CO oxidation. **a**, Reaction rates (r_{CO}) as a function of CO or O_2 concentration over Co_3O_4 nanorods: (triangle symbols) CO and (circle symbols) O_2 . The reaction rates were measured at -77°C and the concentrations of CO and O_2 were in the ranges of 0.5–1.2 vol.% and 1.0–5.1 vol.%, respectively. p_{CO} , p_{O_2} , partial pressures. **b**, Arrhenius plots for the reaction rate constants (activation energies, E_a) on Co_3O_4 nanorods (triangle symbols) and nanoparticles (circle symbols) in the temperature (T) range of -86 to -56°C with a feed gas of 1.0 vol.% CO/2.5 vol.% O_2/He .

during CO oxidation can be ascribed to the accumulation of carbonates and/or bicarbonates and $\text{H}_2\text{O}/\text{OH}^-$ species on the surfaces of the nanorods, which gradually hinder the adsorption of CO and oxygen.

The Co_3O_4 nanorods were further tested for CO oxidation in the normal feed gas at temperatures close to those of practical applications. The reaction at room temperature gave 100% CO conversion for about 65 h owing to the limited accumulation of carbonates and $\text{H}_2\text{O}/\text{OH}^-$ species (Fig. 2). Subsequent regenerations of up to ten cycles showed that the Co_3O_4 nanorods gradually stabilized their high activity with 100% CO conversion for about 60 h, clearly indicating that the Co_3O_4 nanorods can easily catalyse CO oxidation at ambient temperature with sustainable durability.

The Co_3O_4 nanorods were also examined for the oxidation of CO and propane in feed streams containing large amounts of H_2O and CO_2 (Supplementary Fig. S4), similar to automotive exhaust gas composition²⁵. The conversion of CO was 100% at 200°C under stoichiometric conditions and in the presence of water. The coexistence of H_2O , CO_2 and C_3H_8 in the feed gas marginally lowered the conversion of CO (to $\sim 96\%$) at 200°C , suggesting that CO oxidation takes place preferentially over propane oxidation. The lower CO conversion ($\sim 40\%$) at 150°C might be caused by the deposition of carbonates, which tends to occur at such a low temperature and with less O_2 present. When a stoichiometric amount of O_2 for the combustion of both CO and propane was present in the feed stream, the conversion of CO reached 100% at 200°C , but only a trace amount of propane was oxidized to CO_2 and H_2O . The conversion of propane to CO_2 and H_2O reached 100% at 350°C , demonstrating that the oxidation ability of the Co_3O_4 nanorods for propane is at least comparable to that of Pt and Pd catalysts^{2,26}. This observation is in accord with the general understanding that CO is preferentially oxidized at low temperatures, whereas as the temperature is increased propane is gradually oxidized^{2,25}.

TEM observations of the samples used for the above catalytic tests proved that the nanorod-shaped structure is still well maintained (Supplementary Fig. S5), confirming the high thermal stability of the Co_3O_4 nanorods even in the presence of large amounts of H_2O and CO_2 . Hence, the Co_3O_4 nanorods presented here not only display high activities for the oxidation of CO and propane in the automotive exhaust at low temperatures but also meet the most essential requirement: thermal stability under practical conditions.

In conclusion, we have demonstrated that morphological control of Co_3O_4 is very rewarding: the nanorods not only exhibit surprisingly high catalytic activity for CO oxidation at temperatures as low as -77°C but are also sufficiently stable in feed gases containing large amounts of H_2O and CO_2 at 200 – 400°C . This fundamental understanding shows that morphological control of base transition-metal oxides allows preferential exposure of catalytically active sites, and will most probably be applicable in the development of the next generation of highly efficient oxidation catalysts.

METHODS SUMMARY

Co_3O_4 nanorods. 4.98 g of cobalt acetate tetrahydrate was dissolved in 60 ml of ethylene glycol and the mixture was gradually heated to 160°C . 200 ml of aqueous 0.2 M Na_2CO_3 solution was then added and the slurry was further aged for 1 h under vigorous stirring and a continuous flow of nitrogen. After filtration and being washed with water, the solid obtained was dried at 50°C overnight under vacuum and calcined at 450°C for 4 h in air.

Structural analysis. TEM images of the samples were recorded on a Philips Tecanai F 30 G² microscope. The specimen was prepared by ultrasonically suspending the Co_3O_4 powder in ethanol. A drop of the suspension was deposited on a carbon-enhanced copper grid and dried in air.

Catalytic evaluation. The CO oxidation reaction was performed in a continuous-flow fixed-bed quartz reactor under atmospheric pressure. 200 mg (40–60 mesh) sample was loaded and pre-treated with a 20 vol.% O_2/He mixture (50 ml min^{-1}) at 450°C for 30 min. After cooling to -77°C , a 1.0 vol.% $\text{CO}/2.5 \text{ vol.}\% \text{ O}_2/\text{He}$ mixture (50 ml min^{-1}) was introduced. Dry conditions were obtained by passing the feed gas through a molecular-sieve trap cooled to dry-ice temperature. Kinetic measurements were conducted at -86 to -56°C with feed streams of 0.5–1.2 vol.% CO and 1.0–5.1 vol.% O_2 balanced with He, and the CO conversions were adjusted

to below 15% by varying the hourly gas space velocity to calculate the reaction rates under differential reactor conditions. The amounts of CO, CO₂ and O₂ in the inlet and outlet streams were measured by an on-line gas chromatograph.

Received 9 December 2007; accepted 16 February 2009.

- Shelief, M. & McCabe, R. W. Twenty-five years after introduction of automotive catalysts: what next? *Catal. Today* **62**, 35–50 (2000).
- Twigg, M. V. Progress and future challenges in controlling automotive exhaust gas emissions. *Appl. Catal. B* **70**, 2–15 (2007).
- Merrill, D. R. & Scalione, C. C. The catalytic oxidation of carbon monoxide at ordinary temperatures. *J. Am. Chem. Soc.* **43**, 1982–2002 (1921).
- Yoon, C. & Cocke, D. L. The design and preparation of planar models of oxidation catalysts: I. Hopcalite. *J. Catal.* **113**, 267–280 (1988).
- Trimm, D. L. & Onsan, Z. I. Onboard fuel conversion for hydrogen-fuel-cell-driven vehicles. *Catal. Rev. Sci. Eng.* **43**, 31–84 (2001).
- Oh, S. H. & Hoflund, G. B. Low-temperature catalytic carbon monoxide oxidation over hydrous and anhydrous palladium oxide powders. *J. Catal.* **245**, 35–44 (2007).
- Date, M., Okumura, M., Tsubota, S. & Haruta, M. Vital role of moisture in the catalytic activity of supported gold nanoparticles. *Angew. Chem. Int. Edn Engl.* **43**, 2129–2132 (2004).
- Haruta, M., Kobayashi, T., Sano, H. & Yamada, N. Novel gold catalysts for the oxidation of carbon monoxide at a temperature far below 0 °C. *Chem. Lett.* **16**, 405–408 (1987).
- Haruta, M. *et al.* Low-temperature oxidation of CO over gold supported on TiO₂, α-Fe₂O₃ and Co₃O₄. *J. Catal.* **144**, 175–192 (1993).
- Yao, Y. Y. The oxidation of hydrocarbons and CO over metal oxides. III. Co₃O₄. *J. Catal.* **33**, 108–122 (1974).
- Perti, D. & Kabel, R. L. Kinetics of CO oxidation over Co₃O₄/Al₂O₃. *AIChE J.* **31**, 1420–1440 (1985).
- Cunningham, D. A. H., Kobayashi, T., Kamijo, N. & Haruta, M. Influence of dry operating conditions: observation of oscillations and low temperature CO oxidation over Co₃O₄ and Au/Co₃O₄ catalysts. *Catal. Lett.* **25**, 257–264 (1994).
- Grillo, F., Natile, M. M. & Glisenti, A. Low-temperature oxidation of carbon monoxide: the influence of water and oxygen on the reactivity of a Co₃O₄ powder surface. *Appl. Catal. B* **48**, 267–274 (2004).
- Thormählen, P., Skoglundh, M., Fridell, E. & Andersson, B. Low-temperature CO oxidation over platinum and cobalt oxide catalysts. *J. Catal.* **188**, 300–310 (1999).
- Saalfrank, J. W. & Maier, W. F. Directed evolution of noble-metal-free catalysts for the oxidation of CO at room temperature. *Angew. Chem. Int. Edn Engl.* **43**, 2028–2031 (2004).
- Fortunato, G., Oswald, H. R. & Reller, A. Spinel-oxide catalysts for low temperature CO oxidation generated by use of an ultrasonic aerosol pyrolysis process. *J. Mater. Chem.* **11**, 905–911 (2001).
- Szegedi, Á., Hegedüs, M., Margitfalvi, J. L. & Kiricsi, I. Low-temperature CO oxidation over iron-containing MCM-41 catalysts. *Chem. Commun.* 1441–1443 (2005).
- Petitto, S. C., Marsh, E. M., Carson, G. A. & Langell, M. A. Cobalt oxide surface chemistry: the interaction of CoO (100), Co₃O₄ (110) and Co₃O₄ (111) with oxygen and water. *J. Mol. Catal. A* **281**, 49–58 (2008).
- Jansson, J. *et al.* On the catalytic activity of Co₃O₄ in low-temperature CO oxidation. *J. Catal.* **211**, 387–397 (2002).
- Omata, K., Takada, T., Kasahara, S. & Yamada, M. Active site of substituted cobalt spinel oxide for selective oxidation of CO/H₂. Part II. *Appl. Catal. A* **146**, 255–267 (1996).
- Beaufils, J. P. & Barbaux, Y. Study of adsorption on powders by surface differential diffraction measurements. Argon on Co₃O₄. *J. Appl. Cryst.* **15**, 301–307 (1982).
- Ziólkowski, J. & Barbaux, Y. Identification of sites active in oxidation of butene-1 to butadiene and CO₂ on Co₃O₄ in terms of the crystallochemical model of solid surfaces. *J. Mol. Catal.* **67**, 199–215 (1991).
- Broqvist, P., Panas, I. & Persson, H. A. DFT study on CO oxidation over Co₃O₄. *J. Catal.* **210**, 198–206 (2002).
- Jansson, J. Low-temperature CO oxidation over Co₃O₄/Al₂O₃. *J. Catal.* **194**, 55–60 (2000).
- Heck, R. M. & Farrauto, R. J. Automobile exhaust catalysts. *Appl. Catal. A* **221**, 443–457 (2001).
- Sharma, S., Hegde, M. S., Das, R. N. & Pandey, M. Hydrocarbon oxidation and three-way catalytic activity on a single step directly coated cordierite monolith: High catalytic activity of Ce_{0.98}Pd_{0.02}O_{2–δ}. *Appl. Catal. A* **337**, 130–137 (2008).

Supplementary Information is linked to the online version of the paper at www.nature.com/nature.

Acknowledgements We thank C. Li, L. Lin and X. Bao of the Dalian Institute of Chemical Physics, Chinese Academy of Sciences, for their encouragement and discussions. We also acknowledge financial supports for this research work from the National Natural Science Foundation of China and the National Basic Research Program of China.

Author Contributions X.X. and Y.L. performed the synthesis of Co₃O₄ nanorods/nanoparticles and the catalytic tests. Z.-Q.L. conducted the transmission electron microscopy observations and structural analysis. M.H. and W.S. designed the study, analysed the data and wrote the paper. All authors discussed the results and commented on the manuscript.

Author Information Reprints and permissions information is available at www.nature.com/reprints. Correspondence and requests for materials should be addressed to W.S. (shen98@dicp.ac.cn).

LETTERS

Oceanic nickel depletion and a methanogen famine before the Great Oxidation Event

Kurt O. Konhauser¹, Ernesto Pecoits¹, Stefan V. Lalonde¹, Dominic Papineau², Euan G. Nisbet³, Mark E. Barley⁴, Nicholas T. Arndt⁵, Kevin Zahnle⁶ & Balz S. Kamber⁷

It has been suggested that a decrease in atmospheric methane levels triggered the progressive rise of atmospheric oxygen, the so-called Great Oxidation Event, about 2.4 Gyr ago¹. Oxidative weathering of terrestrial sulphides, increased oceanic sulphate, and the ecological success of sulphate-reducing microorganisms over methanogens has been proposed as a possible cause for the methane collapse¹, but this explanation is difficult to reconcile with the rock record^{2,3}. Banded iron formations preserve a history of Precambrian oceanic elemental abundance and can provide insights into our understanding of early microbial life and its influence on the evolution of the Earth system^{4,5}. Here we report a decline in the molar nickel to iron ratio recorded in banded iron formations about 2.7 Gyr ago, which we attribute to a reduced flux of nickel to the oceans, a consequence of cooling upper-mantle temperatures and decreased eruption of nickel-rich ultramafic rocks at the time. We measured nickel partition coefficients between simulated Precambrian sea water and diverse iron hydroxides, and subsequently determined that dissolved nickel concentrations may have reached ~400 nM throughout much of the

Archaean eon, but dropped below ~200 nM by 2.5 Gyr ago and to modern day values⁶ (~9 nM) by ~550 Myr ago. Nickel is a key metal cofactor in several enzymes of methanogens⁷ and we propose that its decline would have stifled their activity in the ancient oceans and disrupted the supply of biogenic methane. A decline in biogenic methane production therefore could have occurred before increasing environmental oxygenation and not necessarily be related to it. The enzymatic reliance of methanogens on a diminishing supply of volcanic nickel links mantle evolution to the redox state of the atmosphere.

Did a nickel famine at the end of the Archaean cause catastrophic collapse of atmospheric methane and thereby facilitate the rise of atmospheric oxygen? At the heart of our hypothesis is the distinct topography in molar Ni/Fe ratios preserved in banded iron formations (BIF) over time (Fig. 1; see also Supplementary Figs 1–3, Supplementary Tables 1, 2). An expanded trace element database for BIF that includes more than 1,200 bulk and grain-by-grain (haematite, magnetite) measurements shows a trend in BIF Ni/Fe ratios that can be defined by two broad stages. Stage 1, which spans

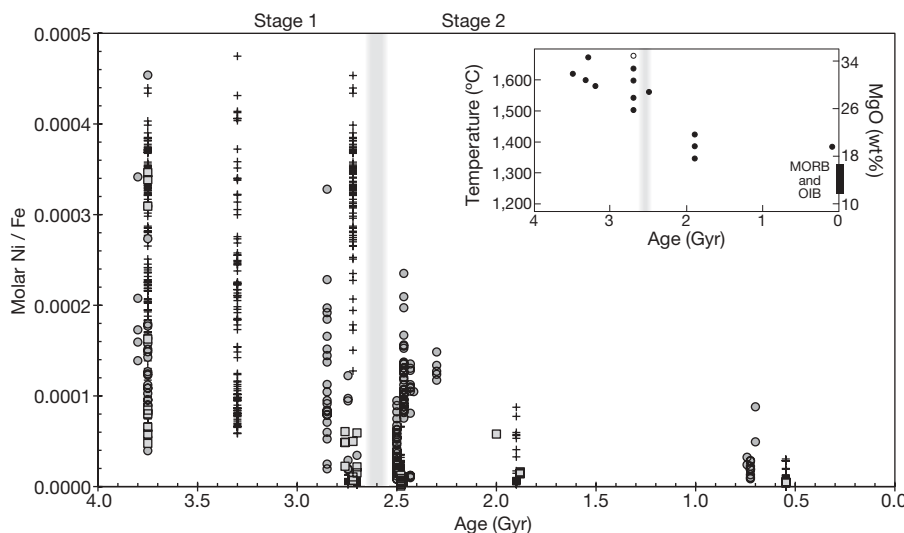


Figure 1 | Ni/Fe mole ratios for BIF versus age, and properties of parental komatiite liquids. The figure contains 1,214 measurements, including literature data (circles) and our new bulk (squares) and grain-by-grain laser ablation analyses (crosses). Two stages are identified based on maximal Ni/Fe ratios, with the transition period indicated by a grey bar. Inset, maximum MgO contents inferred for the parental komatiite liquids¹⁹, and

the probable eruption temperatures, plotted (filled circles) as a function of age. Eruption temperatures T were calculated using the relation $T = 1,000 + 20\text{MgO}$ (where T is in °C, and MgO in wt%; ref. 18), assuming essentially anhydrous magmas. Open circle, recent data by Berry *et al.*¹³. MORB, mid-ocean-ridge basalts; OIB, oceanic island basalt.

¹Department of Earth and Atmospheric Sciences, University of Alberta, Edmonton T6G 2E3, Canada. ²Geophysical Laboratory, Carnegie Institution of Washington, 5251 Broad Branch Road NW, Washington DC 20015, USA. ³Department of Earth Sciences, Royal Holloway University of London, Egham, Surrey TW20 0EX, UK. ⁴School of Earth and Environment, University of Western Australia, 35 Stirling Highway, Crawley, Western Australia 6009, Australia. ⁵Laboratoire de Géodynamique des Chaînes Alpines, Maison de Géosciences, Université Joseph Fourier, 1381 rue de la piscine, Grenoble 38041, France. ⁶NASA Ames Research Center, MS 245-3, Moffett Field, California 94035, USA. ⁷Department of Earth Sciences, Laurentian University, Sudbury, Ontario P3E 2C6, Canada.

from the oldest BIF (~3.8–3.7 Gyr) to those as young as 2.7 Gyr, shows a uniform maximum molar Ni/Fe ratio ($\sim 4.5 \times 10^{-4}$). Stage 2, which we demarcate at around 2.5 Gyr ago (the Archaean-Proterozoic boundary), shows strikingly lower maximal Ni/Fe ratios (below 2.2×10^{-4}). The boundary between stages 1 and 2, although at present not well constrained owing to gaps in the BIF record, marks a significant and irreversible decline in oceanic Ni concentrations: stage 1 values are never reached again. Stage 2 is characterized by a further steady decline in maximum Ni/Fe ratios, a trend that persists for the remainder of the Palaeoproterozoic BIF record. It is possible that a third stage exists, post-dating a resurgence in BIF deposition between 0.75 and 0.55 Gyr ago, but the scarcity of Neoproterozoic BIF trace element data precludes any further conclusion at present.

The transition from stage 1 to stage 2 is unlikely to have been driven by changes in Ni sinks, which appear to be relatively insensitive to evolving major element and redox conditions from Archaean-Palaeoproterozoic ferrous iron seas, through Mesoproterozoic sulphidic seas, to the onset of oxygenated bottom waters in the Neoproterozoic (ref. 8; their Fig. 4). Moreover, Fe^{2+} and Ni^{2+} show similar behaviour with increasing sulphide concentrations, indicating that the presence of sulphide will not lead to chemical fractionation between the two metals (ref. 8; their Fig. 2). In this regard, sulphide is not a major sink for Ni except for some magmatic sulphides (ref. 9, and references therein), and unlike Cu-Zn-Au, which are abundant in Precambrian volcanogenic massive sulphide deposits¹⁰, there are no accumulations that would indicate sequestration of Ni into the sea floor of a sulphidic ocean¹¹. The trends in our data also appear independent of oxidative mechanism or depositional environment. The prominent decline in molar Ni/Fe ratio is recorded in pre-Great Oxidation Event BIF (Supplementary Fig. 3) that appear to have been deposited in waters of greater than 200 m depth¹². During stage 2, so-called granular iron formations of the circum-Ungava belt of North America (for example, the 1.88 Gyr Gunflint Formation) formed in shallow-water, high-energy environments¹², yet they show no discernable difference in Ni/Fe ratios from deep-water stage 2 BIF (for example, the 0.55 Gyr Yermal Formation).

In contrast, Ni supply probably changed significantly with time. First, a hotter Archaean mantle¹³ produced abundant Ni-rich komatiite and olivine-rich basalt in oceanic crust, plateaus, and perhaps on land^{14,15}. Second, Archaean tholeiites, which made up most of the oceanic crust, were richer in Ni than their modern counterparts¹⁶. Third, a major peak in preserved komatiite abundance occurred during the most intense period of mantle plume magmatism and continental crustal growth in Earth's history, between 2.72 and 2.66 Gyr ago^{14,17}, after which their abundance decreased rapidly

(see Supplementary Fig. 4, Supplementary Table 3). All of the above factors are related to the extent of mantle source melting and temperature¹⁸, whose evolution can be reconstructed from the composition of mafic magmas (Fig. 1 inset)¹⁹. The hotter Archaean mantle produced more Ni-rich ultramafic rocks, resulting in a much greater supply of Ni than any time thereafter, a fact reflected in the similarity between the lava eruption temperature versus age curve and the molar Ni/Fe ratio of BIF. Nickel preserved in BIF was almost certainly supplied in dissolved form, as opposed to particulate material (that is, volcanic ash or clastic sediment). Supporting this are low concentrations of lithophile elements in BIF samples selected for this study (see Methods). Furthermore, the Cr/Ni ratios in Archaean BIF are lower than in Archaean basalts, komatiites and shales (Supplementary Fig. 5) which implies Ni mobilization during chemical weathering and hydrothermal alteration of Ni-bearing minerals and preferential supply of Ni (over Cr) to the ocean. Correspondingly, chemical analysis of Archaean basalt-derived palaeosols show accumulation of Cr and loss of Ni in their weathering profiles (see arrow, Supplementary Fig. 5).

The chemical archive preserved in BIF can be exploited using the predictable nature of adsorption reactions occurring at the surface of the authigenic hydrous ferric oxides (HFO) that would have originally precipitated from, and equilibrated with, contemporaneous seawater (see Supplementary Discussion). In natural systems, where trace element sequestration by HFO results from a continuum of adsorption and co-precipitation reactions, lumped-process distribution coefficient models can be used to relate the concentration of an element in the precipitate to the dissolved concentration present at the time of precipitation. In fact, this predictive aspect of HFO sorption reactions has been used to better understand the BIF record with respect to limitations on Precambrian primary productivity that may have arisen via HFO sequestration of bio-essential nutrients^{4,5}.

Nickel partition coefficients were determined for HFO precipitated in the presence of dissolved silica (Fig. 2). Assumptions made in our experiments and extrapolation include an ocean pH of 7–8, ionic strength ~ 0.5 M, seawater Si/Fe molar ratios of $\sim 12/1$ (as per ref. 5), and minimal remobilization of Ni during post-depositional diagenesis and/or metamorphism (see Supplementary Discussion). The experimentally determined partition coefficients allow a first-order estimation of the evolution of seawater Ni concentration from the solid-phase BIF data presented in this study. Figure 2 displays approximately linear relationships between dissolved Ni and the Ni/Fe ratio in the various HFOs examined, consistent with dissolved Ni concentrations well below those approaching site saturation for these particles. Different amounts of dissolved silica, which was added to the experiments to simulate waters at saturation with respect to cristobalite (0.67 mM) or amorphous silica (2.20 mM), had a pronounced effect on HFO reactivity (see Methods for the rationale of these silica concentrations). As Fe(III) hydrolyses and precipitates at circum-neutral pH, dissolved silica is incorporated into the particles, altering their surface properties, and also directly out-competing other dissolved ions for adsorption sites⁷. Using the Si-rich particles as the best proxy for particle composition in the Archaean, extrapolated dissolved Ni concentrations (Fig. 3) suggest that BIF record a drastic reduction in dissolved Ni, from values as high as ~ 400 nM to values no greater than 200 nM during the transition from stage 1 to stage 2; stage 2 shows a gradual decline to < 50 nM by 0.7 Gyr ago, with modern ocean values reached some time after 0.55 Gyr ago. Although it is difficult to quantify the uncertainty in our extrapolation from HFO sorption experiments to the ancient oceans, we feel that this approach is the best currently available for estimating palaeo-ocean Ni concentration. Moreover, we have deliberately taken a conservative approach, as any Ni loss that might have occurred during post-depositional alteration of HFO would lead to an underestimate of oceanic Ni concentrations.

Our finding of nickel-rich Archaean oceans has immediate implications for microbial life that requires it as a trace element. It has been previously suggested that nickel-containing enzymes are remnants from

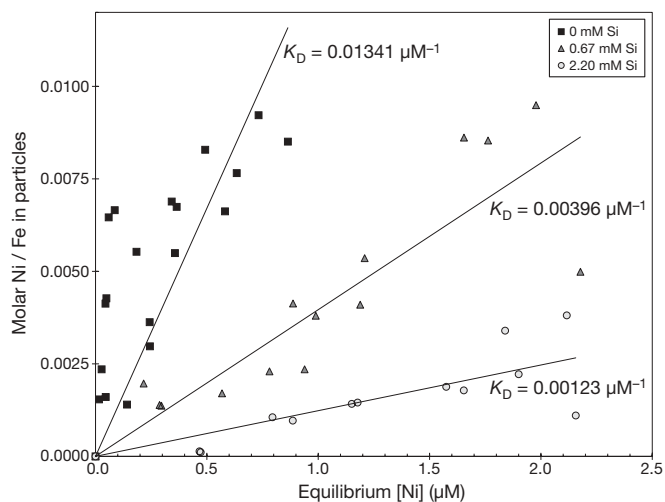


Figure 2 | Experimentally determined distribution coefficients for dissolved Ni. The K_D values were obtained during Ni co-precipitation with HFO, and in the presence of various concentrations of silica, as per ref. 5.

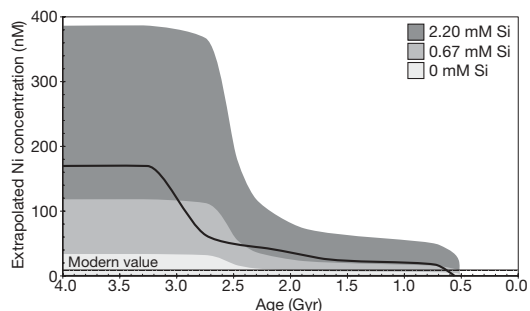


Figure 3 | Maximum dissolved Ni concentrations in sea water through time. Values were extrapolated from solid-phase BIF Ni/Fe data using experimentally determined Ni distribution coefficients. The three shaded areas represent maximum aqueous Ni concentrations at dissolved silica concentrations of 2.20 mM (dark grey), 0.67 mM (medium grey) and 0 mM (light grey). The solid black line represents the average dissolved Ni value from time-averaged Ni/Fe ratios as calculated in Supplementary Fig. 3. The modern mean oceanic Ni concentration (9 nM; ref. 6) is plotted as a line.

an early period in microbial evolution when nickel was abundant²⁰. Specifically, methanogens require Ni for the synthesis of three different [NiFe]-hydrogenases, carbon monoxide dehydrogenase, acetyl-CoA synthase/decarboxylase, and methyl-coenzyme M reductase (MCR), the latter being the catalyst of the final methane-forming step⁷. These nickel enzymes are present in high concentrations, with MCR accounting for approximately 10% of methanogen cytoplasmic proteins. Crucially, although methanogens may continue to grow in the absence of Ni (although some have reported cell autolysis when Ni is absent)²¹, the synthesis of co-factor F₄₃₀, the numbers of methanogen cells, and methane production all depend strongly on dissolved Ni availability. For example, co-factor F₄₃₀ content on a per-cell basis increases with Ni concentrations over a 75–2,500 nM range²², whereas methanogen cell numbers are strongly Ni-limited at concentrations below 100 nM (ref. 23). Similarly, it has been demonstrated²⁴ that methane production in continuous culture decreased progressively when Ni concentrations were reduced from 8,500 nM to 250 nM, the lowest concentration examined by these authors. Not surprisingly, the addition of Ni has been shown to increase the production of methane from mineral-poor peat samples, waste-water treatment facilities, and sewage sludge (for example, ref. 25). To put this into perspective, our data indicate that methanogenesis in the bulk oceans would have been Ni-stimulated throughout stage 1, and especially sensitive to plummeting Ni concentrations over the stage 1 to stage 2 transition, after which it remained in a state of strong Ni-limitation to the present day. Interestingly, methanogens do not appear to have abandoned their overall Ni dependency in the face of this famine (although some can produce nickel-free hydrogenases; see ref. 26 for review), perhaps because the biochemical re-tooling of so many energy-yielding metalloenzymes that are central to their metabolism was an obstacle too great to overcome. Cyanobacteria appear to have coped with changing metal availability over time by evolving metal-specific ligands (for example, ref. 8), but recent studies with methanogens have shown that they do not appear to produce Ni-specific ligands²⁷. This may be due to (1) the relatively high solubility of Ni under both oxic and anoxic conditions⁸, (2) the potentially high cost of ligand production²⁷, and (3) a lack of strong competition for Ni with other microorganisms. The fact that nickel concentrations in modern ocean surface waters are not as depleted as other bioactive metals²⁸ may indicate that the microbes that need it most can no longer access it due to the presence of oxygen.

Compounding this Ni famine would be waning fluxes of H₂ (their preferred reductant) with decreasing serpentinization of the sea floor (that is, $2\text{Mg}_{1.8}\text{Fe}_{0.2}\text{SiO}_4 + 2.933\text{H}_2\text{O} \rightarrow \text{Mg}_{2.7}\text{Fe}_{0.3}\text{Si}_2\text{O}_5(\text{OH})_4 + 0.9\text{Mg}(\text{OH})_2 + 0.033\text{Fe}_3\text{O}_4 + 0.033\text{H}_2$) accompanying the decrease in production of olivine-rich oceanic crust at the end of the 2.7-Gyr mantle plume event and the concomitant growth and stabilization of continental cratons^{14,17}. It has been argued²⁹ that the shift from

predominantly submarine volcanism to more subaerial volcanism further decreased abiotic H₂ fluxes because the latter yield more oxidized gases (H₂O, CO₂ and SO₂). In either case, a loss of H₂ would probably have contributed to a declining biogenic methane supply³⁰.

A drop in atmospheric methane around 2.4 Gyr ago has been invoked as the most parsimonious explanation for the onset of major Palaeoproterozoic glaciations, the ensuing demise of sulphur isotope mass-independent fractionation, and the progressive rise of atmospheric oxygen¹. The authors of ref. 1 hypothesized that the biogenic methane flux would have waned owing to increasing competition between methanogens and sulphate-reducing microorganisms before 2.4 Gyr ago. Moreover, anaerobic oxidation of methane, a nickel-dependent process involving *Archaea* that appear to possess a variant of MCR that operates in reverse³¹, would further have reduced methane escape with increasing sulphate concentrations at that time³². However, it is not until after the Great Oxidation Event that evidence in the rock record exists for pervasive oxidative weathering of terrestrial sulphides, a large oceanic sulphate pool, and the onset of widespread ocean euxinia (for example, refs 2, 3). We provide an alternative hypothesis, suggesting that the demise in large-scale methanogenesis occurred before, and was not necessarily related to, increasing environmental oxygenation. Our model provides a clear directionality in the evolution of the Earth's system, whereby a cooler mantle following the 2.7 Gyr event led to associated chemical changes in volcanism and trace element abundances in the oceans, triggering a decline in global methanogenesis, and ultimately facilitating the transition from anoxic to oxic atmospheric conditions some 2.4 Gyr ago. Thereafter, increased O₂ would have led to a larger oceanic sulphate pool, the end result being the marginalization of methanogens to anoxic and sulphate-poor niches, as is the case today.

METHODS SUMMARY

Ni and Fe contents representing 29 BIF were amassed from previously published bulk analyses ($n = 306$) as well as new analyses on both bulk ($n = 38$) and grain-by-grain (haematite and magnetite only; $n = 870$) scales. BIF samples were selected for low concentrations of Al (<1%) and incompatible elements (Ti, Zr, Th, Hf and Sc <20 p.p.m.) to avoid potential contamination from detrital components. Major elements were measured by electron microprobe (JOEL 8900), while trace element analyses were performed using a Perkin Elmer Elan6000 quadrupole ICP-MS (inductively coupled plasma mass spectrometer) operating in either solution mode for heated HF+HNO₃ whole-rock digests or using a New Wave Research UP213 laser ablation system (20–60 μm spot size) for grain-by-grain analysis of haematite and magnetite. Ni partitioning experiments were performed at ~23 °C in 0.5 M NaNO₃ to which 0.179 mM Fe (as ferrous ammonium sulphate hexahydrate) and various amounts of dissolved silica (0, 0.67 and 2.20 mM SiO₂, added as sodium silicate nonahydrate) were added. After an oxidation and equilibration period of 30 min, samples were filtered to 0.2 μm and analysed for Ni by quadrupole ICP-MS.

Full Methods and any associated references are available in the online version of the paper at www.nature.com/nature.

Received 27 August 2008; accepted 26 January 2009.

- Zahnle, K. J., Claire, M. W. & Catling, D. C. The loss of mass-independent fractionation of sulfur due to a Paleoproterozoic collapse of atmospheric methane. *Geobiology* 4, 271–283 (2006).
- Papineau, D., Mojzsis, S. J. & Schmitt, A. K. Multiple sulfur isotopes from Paleoproterozoic Huronian interglacial sediments and the rise of atmospheric oxygen. *Earth Planet. Sci. Lett.* 255, 188–212 (2007).
- Scott, C. et al. Tracing the stepwise oxygenation of the Proterozoic ocean. *Nature* 452, 456–459 (2008).
- Bjerrum, C. J. & Canfield, D. E. Ocean productivity before about 1.9 Gyr limited by phosphorus adsorption onto iron oxides. *Nature* 417, 159–162 (2002).
- Konhauser, K. O., Lalonde, S. V., Arnskov, L. & Holland, H. D. Was there really an Archean phosphate crisis? *Science* 315, 1234 (2007).
- Drever, J. I. *The Geochemistry of Natural Waters* 2nd edn (Prentice Hall, 1988).
- Jaun, B. & Thauer, R. K. in *Metal Ions in Life Sciences* Vol. 2, *Nickel and its Surprising Impact in Nature* (eds Sigel, A., Sigel, H. & Sigel, R. K. O.) 323–356 (Wiley & Sons, 2007).
- Saito, M. A., Sigman, D. M. & Morel, F. M. M. The bioinorganic chemistry of the ancient ocean: the co-evolution of cyanobacterial metal requirements and biogeochemical cycles at the Archean-Proterozoic boundary? *Inorg. Chim. Acta* 356, 308–318 (2003).

9. Öztürk, M. Trends of trace metal (Mn, Fe, Co, Ni, Cu, Zn, Cd and Pb) distributions at the oxic-anoxic interface and in sulfidic water of the Drammensfjord. *Mar. Chem.* **48**, 329–342 (1995).
10. Hannington, M. D., Santaguida, F., Kjarsgaard, I. M. & Cathles, L. M. Regional-scale hydrothermal alteration in the Central Blake River Group, western Abitibi subprovince, Canada: implications for VMS prospectivity. *Mineralium Deposita* **38**, 393–422 (2003).
11. Keays, R. R. The role of komatiitic and picritic magmatism and S-saturation in the formation of ore deposits. *Lithos* **34**, 1–18 (1995).
12. Trendall, A. F. in *Precambrian Sedimentary Environments: A Modern Approach to Ancient Depositional Systems* (eds Altermann, W. & Corcoran, P. L.) 33–66 (Special Publication 33, International Association of Sedimentologists, 2002).
13. Berry, A. J., Danyushevsky, L. V., O'Neill, H. C., Newville, M. & Sutton, S. R. Oxidation state of iron in komatiite melt inclusions indicates hot Archaean mantle. *Nature* **455**, 960–963 (2008).
14. Barley, M. E., Krapež, B., Groves, D. I. & Kerrich, R. The Late Archaean bonanza: metallogenic and environmental consequences of the interaction between mantle plumes, lithospheric tectonics and global cyclicity. *Precamb. Res.* **91**, 65–90 (1998).
15. Kamber, B. S., Whitehouse, M. J., Bolhar, R. & Moorbath, S. Volcanic resurfacing and the early terrestrial crust: zircon U-Pb and REE constraints from the Isua Greenstone Belt, southern West Greenland. *Earth Planet. Sci. Lett.* **240**, 276–290 (2005).
16. Arndt, N. T. High Ni in Archean tholeiites. *Tectonophysics* **187**, 411–420 (1991).
17. Barley, M. E., Bekker, A. & Krapež, B. Late Archean to early Paleoproterozoic global tectonics, environmental change and the rise of atmospheric oxygen. *Earth Planet. Sci. Lett.* **238**, 156–171 (2005).
18. Nisbet, E. G. in *Komatiites* (eds Arndt, N.T. & Nisbet, E.G.) 501–520 (George Allen and Unwin, 1982).
19. Arndt, N. T., Barnes, S. J. & Leshner, C. M. *Komatiite* (Cambridge University Press, 2008).
20. da Silva, J. J. R. F. & Williams, R. J. P. *The Biological Chemistry of the Elements: The Inorganic Chemistry of Life* (Oxford University Press, 1991).
21. Jarrell, K. F., Colvin, J. R. & Sprott, G. D. Spontaneous protoplast formation in *Methanobacterium bryantii*. *J. Bacteriol.* **149**, 346–353 (1982).
22. Diekert, G., Weber, B. & Thauer, R. K. Nickel dependence of factor F₄₃₀ content in *Methanobacterium thermoautotrophicum*. *Arch. Microbiol.* **127**, 273–278 (1980).
23. Schönheit, P., Moll, J. & Thauer, R. K. Nickel, cobalt, and molybdenum requirement for growth of *Methanobacterium thermoautotrophicum*. *Arch. Microbiol.* **123**, 105–107 (1979).
24. Kida, K. *et al.* Influence of Ni²⁺ and Co²⁺ on methanogenic activity and the amounts of coenzymes involved in methanogenesis. *J. Biosci. Bioeng.* **91**, 590–595 (2001).
25. Basiliako, N. & Yavitt, J. B. Influence of Ni, Co, Fe, and Na additions on methane production in *Sphagnum*-dominated Northern American peatland. *Biogeochemistry* **52**, 133–153 (2001).
26. Shima, S. & Thauer, R. K. A third type of hydrogenase catalysing H₂ activation. *Chem. Rec.* **7**, 37–46 (2007).
27. Hausrath, E. M., Liermann, L. J., House, C. H., Ferry, J. G. & Brantley, S. L. The effect of methanogen growth on mineral substrates: will Ni markers of methanogen-based communities be detectable in the rock record? *Geobiology* **5**, 49–61 (2007).
28. Saito, M. A., Moffett, J. W. & DiTullio, G. R. Cobalt and nickel in the Peru upwelling region: a major flux of labile cobalt utilized as a micronutrient. *Glob. Biogeochem. Cycles* **18**, GB4030 (2004).
29. Kump, L. R. & Barley, M. E. Increased subaerial volcanism and the rise of atmospheric oxygen 2.5 billion years ago. *Nature* **448**, 1033–1036 (2007).
30. Kharecha, P., Kasting, J. & Siefert, J. A coupled atmosphere-ecosystem model of the early Archean Earth. *Geobiology* **3**, 53–76 (2005).
31. Krüger, M. *et al.* A conspicuous nickel protein in microbial mats that oxidize methane anaerobically. *Nature* **426**, 878–881 (2003).
32. Catling, D. C., Claire, M. W. & Zahnle, K. J. Anaerobic methanotrophy and the rise of atmospheric oxygen. *Phil. Trans. R. Soc. A* **365**, 1867–1888 (2007).

Supplementary Information is linked to the online version of the paper at www.nature.com/nature.

Acknowledgements We thank M. Labbe for sample preparation, G. Chen and A. Simonetti for assistance with LA-ICP-MS analyses in the Radiogenic Isotope Facility at the University of Alberta, and S. Matveev for assistance with electron microprobe analyses. Field assistance by W. Mueller is acknowledged for Hunter Mine Group samples. Samples from the Loch Maree Group were provided by A. Wright. Funding was provided by the Natural Science and Engineering Research Council of Canada (NSERC) to K.O.K., the Canada Research Chairs Program to B.S.K., the Australian Research Council (ARC) to M.E.B., and NASA Exobiology and Evolutionary Biology Program individually to D.P. and K.Z. This manuscript was improved by discussions with R. Buick, J. Kasting and M. Leshner, and reviews by R. Frei and M. Saito.

Author Contributions BIF samples were provided by K.O.K., E.P., B.S.K. and D.P. E.P. performed LA-ICP-MS and electron microprobe analysis and S.V.L. conducted sorption experiments. K.O.K., S.V.L., E.P. and B.S.K. produced the manuscript with significant contributions from all co-authors. Specifically, insights into komatiites were provided by E.G.N., N.T.A. and M.E.B.; early Earth tectonics by M.E.B. and B.S.K.; and GOE and methanogens by D.P. and K.Z.

Author Information Reprints and permissions information is available at www.nature.com/reprints. Correspondence and requests for materials should be addressed to K.O.K. (kurtk@ualberta.ca).

METHODS

Sample selection. High abundances of Ni have been recorded in several Archaean clastic sedimentary rocks, and have generally been explained by the presence of an ultramafic dominated crustal source (for example, refs 33, 34). Average compositions of post-Archaean clastic sedimentary rocks define a progressive decrease in Ni concentrations through time, which is clearly related to a compositional change in the upper continental crust³⁵. Even though this decrease parallels the trend recorded in BIF, both in time and Ni/Fe concentration, reliable authigenic trace metal contents can be compromised by contamination with siliciclastic or volcanic inputs. Therefore, our interpretation of the Ni signal in BIF as a genuine reflection of palaeoseawater required a pre-selection of BIF samples with minimal detrital influence based on chemical composition (as below).

One method commonly used to differentiate detritally sourced components versus authigenic precipitation is through measurement of incompatible, immobile elements such as Al, Ti, Zr, Th, Hf, and Sc (ref. 36). Thus, data presented in Supplementary Tables 1 and 2 were selected according to the following criteria: (1) <1 wt% Al, (2) low concentrations (<20 p.p.m.) of Ti, Zr, Th, Hf and Sc, and (3) on the basis of lack of co-variations of Zr versus Y/Ho; Y/Ho versus Ce/Ce*; and Th versus La/La* (for example, refs 37, 38). Furthermore, samples noted or reported to contain sulphides were avoided, to minimize the influence of post-depositional hydrothermal activity on our data set. Through the use of these filters, we are confident that our BIF samples reflect precipitation from sea water. **Ni analyses in BIF.** Data are presented in Supplementary Tables 1 and 2. Selected BIF samples for geochemical analyses include both drill core and hand samples from fresh exposures. Oxidized surfaces, veins and samples with pyrite were avoided to minimize the effects of weathering and post-depositional overprinting.

For bulk trace element analyses, samples were cut into slabs and broken into small chips (<5 mm) without metal contact. Subsequently, between 20 and 150 g of the material was powdered in an automated agate mill. Crushed rock powders (<100 mesh) were completely dissolved with heated HF+HNO₃ and analysed using a Perkin Elmer Elan6000 Quad-ICP-MS (quadrupole inductively coupled plasma mass spectrometer). Accuracy and precision of the analytical protocol were verified with the use of well-established international whole rock standards (for example, BE-N Basalt, CRPG Nancy; see http://research.eas.ualberta.ca/rif/quad_icp_ms.html).

In situ trace element analyses were performed on haematite and magnetite grains using a quadrupole ICP-MS coupled to a laser ablation system (spot size 20–60 µm in diameter). Haematite was chosen as proxy for the original precipitates as it probably formed from dehydration of hydrous ferric oxide (HFO) precursors, and it provides a means of direct comparison between BIF samples of significantly different bulk composition. As magnetite is generally regarded as a secondary iron oxide phase formed by partial reduction of HFO or haematite, we used it to assess post-depositional Ni/Fe disturbances. In this regard, no significant differences between the two iron oxide minerals were observed.

Optimization of ICP-MS instrument parameters (RF power 1,200 W, peak hopping acquisition, 50 ms dwell time) were achieved by ablating either the NIST SRM 610 (~500 p.p.m.) or NIST SRM 612 (~50 p.p.m.) international glass standards. For quantitative trace element determinations, the NIST 610 (for 20 µm spot size) and 612 (for 60 µm spot size) standards and BIF samples were ablated using identical conditions with spot sizes of either 20 µm or 60 µm, 5 Hz repetition rate and energy density of ~13 J cm⁻². Quantitative results were obtained via the calibration of relative element sensitivities against the NIST 610 and 612 standards, while Fe values from electron microprobe analyses (JOEL 8900, University of Alberta) were used as internal standards. Data reduction and

concentration determinations were obtained using the GLITTER (XP version, New Wave Research) laser ablation software. Repeated analysis ($n = 10$) of the NIST 612 using a 60 µm spot size yielded relative standard deviations of between 5 and 15% (2σ level) and detection limits between 0.2 (for example, Cu) and 3 p.p.m. (for example, Cr) for most elements (except for P ~13 p.p.m., Fe ~20 p.p.m. and Ca ~165 p.p.m.). All new BIF measurements reported here were performed in the Radiogenic Isotope Facility at the Department of Earth and Atmospheric Sciences, University of Alberta.

Statistical treatment of the data are outlined in Supplementary Table 2, and graphically presented in Supplementary Figs 1, 2 and 3. Ni values were normalized on a molar ratio basis to total Fe for all bulk and laser-ablation analyses because (1) the similar Ni/Fe values observed between individual haematite and magnetite grains indicates that we cannot exclude Fe(II)-containing phases as significant sources of Ni, and (2) many of the published bulk analyses do not discriminate between Fe(II) and Fe(III).

Ni partitioning experiments. Concentrated ferrous iron stock solutions (0.1074 M) were freshly prepared at pH ~3 from ferrous ammonium sulphate hexahydrate and diluted to 0.179 mM in pH 7 receiving solutions consisting of 0.5 M NaNO₃ and various amounts of silica (0, 0.67 mM and 2.20 mM, added as sodium metasilicate nonahydrate) and dissolved nickel (0–4,000 nM). These dissolved silica concentrations were chosen to span conditions ranging from as high as amorphous silica saturation (2.20 mM), to cristobalite saturation (0.67 mM), and to modern oceans largely stripped of dissolved silica, in order to explore the effects of dissolved silica on Ni partitioning to iron oxides through time. The oceans were at least saturated with cristobalite, and probably amorphous silica, before 1.8 Gyr ago³⁹, only to achieve modern values in the Phanerozoic (<0.10 mM)⁴⁰ with the advent of silica-secreting eukaryotes.

Dissolved nickel was sourced from a 1,000 p.p.m. Ni commercial ICP-MS standard (in 2% HNO₃, SPEX CertiPrep). All experiments were performed at ~23 °C in acid-washed glassware with continuous mixing. The pH values of all experiments were monitored continuously and maintained at pH 7 by the addition of dilute HCl or NaOH. After an Fe(II) oxidation and equilibration period of 30 min, samples were filtered through 0.2 µm nylon in-line syringe filters, acidified with trace-metal grade HNO₃, and analysed within one week for Ni, as well as for Fe (to confirm complete oxidation and precipitation), by ICP-MS (Perkin Elmer Elan6000) at the University of Alberta.

33. McLennan, S. M., Taylor, S. R. & Eriksson, K. A. Geochemistry of Archean shales from Pilbara Supergroup, Western Australia. *Geochim. Cosmochim. Acta* **47**, 1211–1222 (1983).
34. Taylor, S. R. & McLennan, S. M. *The Continental Crust: Its Composition and Evolution* (Blackwell, 1985).
35. Condie, K. C. Chemical composition and evolution of the upper continental crust: contrasting results from surface samples and shales. *J. Chem. Geol.* **104**, 1–37 (1993).
36. Chester, R. *Marine Geochemistry* (Blackwell, 2000).
37. McLennan, S. M. in *Geochemistry and Mineralogy of Rare Earth Elements* (eds Lipin, B. R. & McKay, G. A.) 169–200 (Mineral Society of America, 1989).
38. Kamber, B. S. & Webb, G. E. The geochemistry of late Archaean microbial carbonate: implications for ocean chemistry and continental erosion history. *Geochim. Cosmochim. Acta* **65**, 2509–2525 (2001).
39. Maliva, R. G., Knoll, A. H. & Simonson, B. M. Secular change in the Precambrian silica cycle: insights from chert petrology. *Geol. Soc. Am. Bull.* **117**, 835–845 (2005).
40. Tréguer, P. *et al.* The silica balance in the world ocean: a reestimate. *Science* **268**, 375–379 (1995).

LETTERS

Phylogenetic biome conservatism on a global scale

Michael D. Crisp¹, Mary T. K. Arroyo², Lyn G. Cook³, Maria A. Gandolfo⁴, Gregory J. Jordan⁵, Matt S. McGlone⁶, Peter H. Weston⁷, Mark Westoby⁸, Peter Wilf⁹ & H. Peter Linder¹⁰

How and why organisms are distributed as they are has long intrigued evolutionary biologists^{1–4}. The tendency for species to retain their ancestral ecology has been demonstrated in distributions on local and regional scales^{5–7}, but the extent of ecological conservatism over tens of millions of years and across continents has not been assessed^{8–13}. Here we show that biome stasis at speciation has outweighed biome shifts by a ratio of more than 25:1, by inferring ancestral biomes for an ecologically diverse sample of more than 11,000 plant species from around the Southern Hemisphere. Stasis was also prevalent in transoceanic colonizations. Availability of a suitable biome could have substantially influenced which lineages establish on more than one landmass, in addition to the influence of the rarity of the dispersal events themselves. Conversely, the taxonomic composition of biomes has probably been strongly influenced by the rarity of species' transitions between biomes. This study has implications for the future because if clades have inherently limited capacity to shift biomes¹³, then their evolutionary potential could be strongly compromised by biome contraction as climate changes.

In recent years, the extent to which species retain ancestral ecological traits and environmental distributions ('niche conservatism') has been debated^{11,13–15}. Whether ecology is evolutionarily labile or conserved appears to be scale dependent, but most of the evidence for conservatism has come from studies at smaller (community-level) scales^{5–7,12}. Large-scale ecological conservatism is not well studied but there is evidence that ecological tolerances (for example as reflected in latitudinal range) are relatively conserved in lineages over long periods of macro-evolutionary time^{8–11}. This leads to the prediction that lineages might rarely colonize new biomes¹¹; however, the frequency of transitions has not been estimated¹³.

Biomes are broad vegetation types defined by climate, life-form and ecophysiology¹⁶ and, hence, are useful units for investigating the large-scale pattern of ecological conservatism. Biome conservatism might be a major determinant of the global distribution of biodiversity, such as the latitudinal gradient, which could have arisen because relatively few ancestrally tropical taxa were able to colonize temperate biomes¹⁷. Global comparisons across multiple lineages are needed to investigate the generality of conservatism and how much it has influenced the assembly of biomes¹⁸. Here we quantify the frequency of biome changes using a large sample of plant phylogenies distributed across multiple biomes and landmasses.

The widely separated landmasses in the Southern Hemisphere provide an outstanding opportunity to assess the relative frequency of phylogenetic biome conservatism on a broad scale and over long time periods (tens of millions of years). First, each southern continent contains a rich array of biomes among which taxa could have moved. Second, many taxa are spread across the southern landmasses and are

largely restricted to that region, defining a biogeographically meaningful study area^{2,4}. Although some of these transoceanic disjunctions are likely vicariant remnants of once-continuous distributions on Gondwana^{2,4,19}, many more are probably the result of long-distance colonization^{20,21}. Third, the oceanic gaps in the Southern Hemisphere are so wide that disjunct sister taxa are likely to have remained effectively separate in their new biomes, without ongoing gene flow confounding comparisons of their subsequent evolution. Last, the number of plant phylogenies that are dated and well sampled at species level for the Southern Hemisphere has grown to a statistically meaningful size.

We assembled a data set comprising 11,064 species of vascular plants in 45 taxa from extratropical Africa, Madagascar, Australia–New Guinea, New Caledonia, New Zealand and South America, equivalent to an estimated 15% of the total flora of these regions. We reconstructed ancestral distributions and, by dating divergences, inferred which disjunctions were likely to be the result of long-distance dispersal and establishment (colonization) across oceans. Each plant species was assigned to one or more of seven biomes (wet forest, sclerophyll, alpine, bog, temperate grassland, savannah and arid) and transitions among biomes were recorded.

We found strong support for the hypothesis of phylogenetic biome conservatism because biome shifts were rare, being associated with only 396 (3.6%) of the approximately 11,000 evolutionary divergences. Of these shifts, 356 occurred within landmasses (Fig. 1) and 40 were linked to transoceanic colonizations (Fig. 2 and Table 1). Investigating taxa individually, we found a consistent pattern in which closely related species were more ecologically similar than would be expected by chance (Supplementary Results), irrespective of whether the taxa have been considered Gondwanan relics (for example *Araucariaceae*, *Casuarinaceae*, *Nothofagus*^{19,22}) or otherwise (for example eucalypts, grasses and some legume tribes^{23,24}).

Most transoceanic colonizations involved no change of biome (sign test: $n = 226$; biome shifts, 40; $P = 0.00001$). Moreover, a bias towards biome stasis in colonizations was consistent across all landmass pairs, in both directions (Fig. 2; Wilcoxon matched-pairs signed-rank test: $n = 30$, $z = -3.552$, $P = 0.00019$). Similarly, the bias towards stasis in colonizations was consistent among biomes (Table 1), whether comparing source biomes (Wilcoxon matched-pairs signed-rank test: $n = 7$, $z = -2.113$, $P = 0.017$) or destination biomes ($n = 7$, $z = -2.197$, $P = 0.014$). We suggest that constraint on biome shifts following colonization from one landmass to another is a consequence of the dynamics of colonization. The frequency at which propagules of a species have crossed the southern oceans is likely to be extremely small. For successful colonization, immigrant propagules must germinate and establish reproductively successful populations. Establishment should be easier in a biome to which the species is pre-adapted, that is, one approximately equivalent to its

¹School of Botany and Zoology, The Australian National University, Canberra, Australian Capital Territory 0200, Australia. ²Institute of Ecology and Biodiversity, University of Chile, Casilla 653, Santiago, Chile. ³School of Integrative Biology, The University of Queensland, Brisbane, Queensland 4072, Australia. ⁴L. H. Bailey Hortorium, Department of Plant Biology, Cornell University, Ithaca, New York 14853, USA. ⁵School of Plant Science, University of Tasmania, Private Bag 55, Hobart, Tasmania 7001, Australia. ⁶Landcare Research, PO Box 40, Lincoln 7640, New Zealand. ⁷National Herbarium of New South Wales, Mrs Macquaries Road, Sydney, New South Wales 2000, Australia. ⁸Department of Biological Sciences, Macquarie University, Sydney, New South Wales 2109, Australia. ⁹Department of Geosciences, Pennsylvania State University, University Park, Pennsylvania 16802, USA. ¹⁰Institute of Systematic Botany, University of Zurich, Zurich 8008, Switzerland.

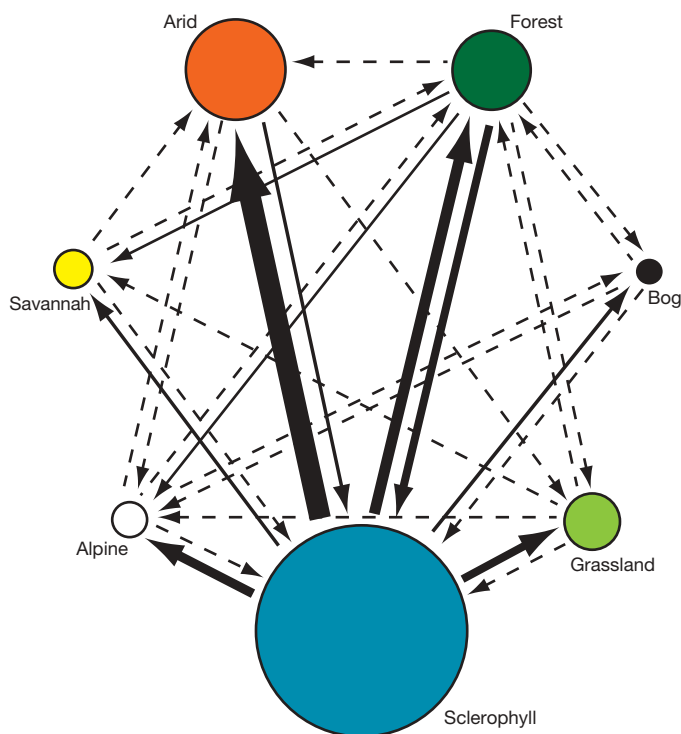


Figure 1 | Biome shifts within landmasses. Shifts occurred with only 356 of 10,800 speciation events within landmasses. Number of species sampled within each biome is proportional to the area of each circle: sclerophyll, 7,250; arid, 1,683; wet forest, 1,005; temperate grassland, 504; savannah, 242; montane, 186; bog, 84. Arrow thickness is proportional to the number of transitions in each direction, ranging from 6 to 95 events; dashed lines indicate 1–5 events and lack of an arrow indicates that there was no event.

source biome²⁵. An interesting parallel is the niche conservatism observed in many invasive species that are introduced by humans and usually establish in the same biomes as in their regions of origin^{26,27}.

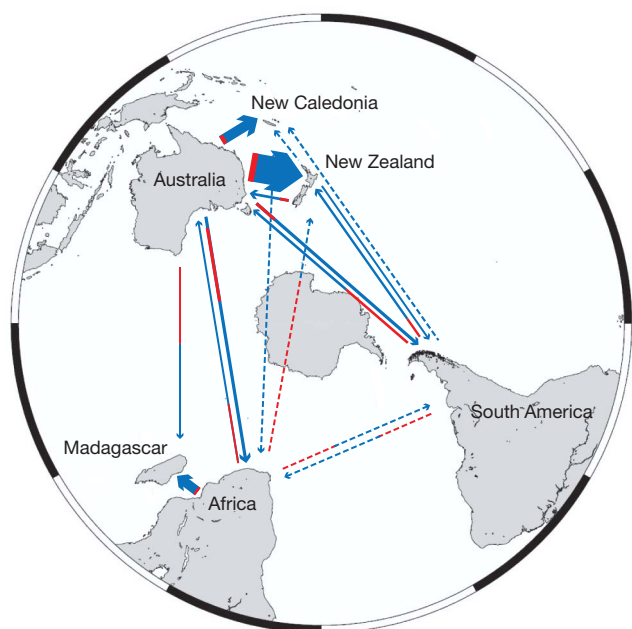


Figure 2 | Biome conservatism in transoceanic plant colonizations around the Southern Hemisphere. Proportion of colonizations into the same (blue) or a different (red) biome are shown along each arrow. Arrow thickness is proportional to the number of colonizations, ranging from 4 to 107 events; dashed lines indicate fewer than 4 events. Four ambiguous colonizations are not shown.

Table 1 | Biome transitions coincident with transoceanic colonizations

Destination	Source							Total
	Arid	Bog	Forest	Grassland	Sclerophyll	Alpine	Savannah	
Arid	2							
Bog		13.3			3.3			3.3
Forest			50.8		10			10
Grassland				21.7	5.3	1		6.3
Sclerophyll	1	0.3	3.5	2.7	87		1	8.5
Alpine			1	2	7	12		10
Savannah			1		0.5			1.5
Total	1	0.3	5.5	4.7	26.1	1	1	39.6

The number of biome transitions is shown for each biome in terms of source (columns) and sink (rows). Bold numbers along the diagonal show colonizations with no change of biome. Totals are for transitions only, that is, excluding values along the diagonal. Non-integer values result from fractional weighting of ambiguous reconstructions. For clarity, zeroes are left blank.

The frequency of transitions between biomes within continents varied markedly among biome pairs (Fig. 1). This variation is consistent with biome conservatism, given that biomes differ in their ecological similarity. For example, the sclerophyll and arid biomes in both Australia and Africa are characterized by extensive areas of oligotrophic soils and differ mainly in degree of moisture deficit²⁸. We recorded more transitions between sclerophyll and arid biomes than between any other pair, even after correcting for differential species richness of biomes (Supplementary Tables 1 and 2). Conversely, there were no transitions between strongly contrasting biome pairs, such as arid and bog, savannah and bog, and savannah and alpine (Fig. 2).

There has been directional bias in transitions among biomes, with the sclerophyll biome being a net source and the arid, alpine and grassland biomes being net sinks (Fig. 1 and Supplementary Tables 1 and 2). Consistent with this, the arid, alpine and grassland biomes expanded considerably during the last 25 Myr, whereas the forest and sclerophyll biomes were predominant in older fossil floras^{3,16,22,23}. The most frequent destination of transitions was the arid biome, which expanded mainly after 15 Myr ago^{3,16,22}. Nearly all of the dated shifts into the arid biome occurred after this time.

From our broad sample of taxa across continents and biomes of the temperate Southern Hemisphere, we can confidently conclude that phylogenetic biome conservatism has been prevalent during the radiation of plant lineages, both within continents and in transoceanic colonizations. The great majority of pairs of sister species (>96%) occurred in the same biome as their most recent shared ancestor. Such conservatism is probably accepted in the popular imagination for iconic Gondwanan plants such as Araucariaceae, Casuarinaceae and *Nothofagus*, but we have found it also characterized clades within the eucalypts, grasses and legumes that have diversified greatly during the last 20 Myr. Their evolutionary success might have resulted not from adaptation to new biomes but from expansion of their biome as climate changed. Thus, our results have implications for the better understanding of biological invasions and the survival of species under global climate change.

METHODS SUMMARY

A large data set was assembled comprising 45 molecular phylogenies of vascular plants occurring in seven biomes across all major Southern Hemisphere landmasses except Antarctica.

Ancestral landmasses and biomes were reconstructed at nodes, and transitions inferred, using parsimony optimization. By dating transoceanic divergences using fossils and relaxed molecular clocks, transoceanic colonizations were distinguished from vicariance events.

The extent of biome conservatism was assessed for 226 transoceanic colonizations using a sign test with the null expectation that biomes within each landmass were colonized in proportion to their areas. Whether clades tend to remain in their ancestral biomes was tested in 13 individual phylogenies using Monte Carlo randomizations of the tips. Whether biome conservatism was consistent between all 30 pairwise combinations of landmasses was tested using a Wilcoxon matched-pairs signed-rank test.

Within landmasses, directional bias in transitions among biomes was assessed using a binomial test, with a correction for species richness effects.

Full Methods and any associated references are available in the online version of the paper at www.nature.com/nature.

Received 19 August 2008; accepted 12 January 2009.

Published online 15 February 2009.

- Darwin, C. Does sea-water kill seeds? *Garden. Chron.* **21**, 356–357 (1855).
- Raven, P. H. & Axelrod, D. I. Angiosperm biogeography and past continental movements. *Ann. MO Bot. Gard.* **61**, 539–673 (1974).
- Hallam, A. *An Outline of Phanerozoic Biogeography* (Oxford Univ. Press, 1994).
- Humphries, C. J. & Parenti, L. *Cladistic Biogeography* (Oxford Univ. Press, 1999).
- Losos, J. B. *et al.* Niche lability in the evolution of a Caribbean lizard community. *Nature* **424**, 542–545 (2003).
- Ackerly, D. D., Schwilk, D. W. & Webb, C. O. Niche evolution and adaptive radiation: testing the order of trait divergence. *Ecology* **87**, S50–S61 (2006).
- Silvertown, J. *et al.* Absence of phylogenetic signal in the niche structure of meadow plant communities. *Proc. R. Soc. Lond. B* **273**, 39–44 (2006).
- Prinzinger, A., Durka, W., Klotz, S. & Brandl, R. The niche of higher plants: evidence for phylogenetic conservatism. *Proc. R. Soc. Lond. B* **268**, 2383–2389 (2001).
- Svenning, J. C. Deterministic Plio-Pleistocene extinctions in the European cool-temperate tree flora. *Ecol. Lett.* **6**, 646–653 (2003).
- Qian, H. & Ricklefs, R. E. Geographical distribution and ecological conservatism of disjunct genera of vascular plants in eastern Asia and eastern North America. *J. Ecol.* **92**, 253–265 (2004).
- Wiens, J. J. & Graham, C. H. Niche conservatism: integrating evolution, ecology, and conservation biology. *Annu. Rev. Ecol. Syst.* **36**, 519–539 (2005).
- Ricklefs, R. E. History and diversity: explorations at the intersection of ecology and evolution. *Am. Nat.* **170** (suppl.), 56–70 (2007).
- Losos, J. B. Phylogenetic niche conservatism, phylogenetic signal and the relationship between phylogenetic relatedness and ecological similarity among species. *Ecol. Lett.* **11**, 995–1003 (2008).
- Peterson, A. T., Soberon, J. & Sanchez-Cordero, V. Conservatism of ecological niches in evolutionary time. *Science* **285**, 1265–1267 (1999).
- Pearman, P. B., Guisan, A., Broennimann, O. & Randin, C. F. Niche dynamics in space and time. *Trends Ecol. Evol.* **23**, 149–158 (2008).
- Woodward, F. I., Lomas, M. R. & Kelly, C. K. Global climate and the distribution of plant biomes. *Phil. Trans. R. Soc. Lond. B* **359**, 1465–1476 (2004).
- Wiens, J. J. & Donoghue, M. J. Historical biogeography, ecology and species richness. *Trends Ecol. Evol.* **19**, 639–644 (2004).
- Crisp, M. D. Biome assembly: what we know and what we need to know. *J. Biogeogr.* **33**, 1332–1333 (2006).
- Linder, H. P. & Crisp, M. D. *Nothofagus* and Pacific biogeography. *Cladistics* **11**, 5–32 (1995).
- Sanmartin, I. & Ronquist, F. Southern Hemisphere biogeography inferred by event-based models: plant versus animal patterns. *Syst. Biol.* **53**, 216–243 (2004).
- de Queiroz, A. The resurrection of oceanic dispersal in historical biogeography. *Trends Ecol. Evol.* **20**, 68–73 (2005).
- Hill, R. S. Origins of the southeastern Australian vegetation. *Phil. Trans. R. Soc. Lond. B* **359**, 1537–1549 (2004).
- Stromberg, C. A. E. Decoupled taxonomic radiation and ecological expansion of open-habitat grasses in the Cenozoic of North America. *Proc. Natl Acad. Sci. USA* **102**, 11980–11984 (2005).
- Crisp, M., Cook, L. G. & Steane, D. A. Radiation of the Australian flora: what can comparisons of molecular phylogenies across multiple taxa tell us about the evolution of diversity in present-day communities? *Phil. Trans. R. Soc. Lond. B* **359**, 1551–1571 (2004).
- Alsos, I. G. *et al.* Frequent long-distance plant colonization in the changing Arctic. *Science* **316**, 1606–1609 (2007).
- Thuiller, W. *et al.* Niche-based modelling as a tool for predicting the risk of alien plant invasions at a global scale. *Glob. Change Biol.* **11**, 2234–2250 (2005).
- Peterson, A. T. Predicting the geography of species' invasions via ecological niche modeling. *Q. Rev. Biol.* **78**, 419–433 (2003).
- Orians, G. H. & Milewski, A. V. Ecology of Australia: the effects of nutrient-poor soils and intense fires. *Biol. Rev. Camb. Phil. Soc.* **82**, 393–423 (2007).

Supplementary Information is linked to the online version of the paper at www.nature.com/nature.

Acknowledgements We thank the Australian Research Council-New Zealand Research Network for Vegetation Function for facilitating this collaboration. Participation by M.A.G. and P.W. was supported in part by a grant from the US National Science Foundation.

Author Contributions All authors participated in two workshops where the phylogenetic and biome data were initially compiled. All authors participated in analysis and interpretation at the workshops and subsequently by email. M.W. designed and facilitated the study. M.A.G., G.J.J. and P.W. provided palaeobotanical dates. M.D.C. drafted the paper in collaboration with H.P.L., and provided supplementary statistical analyses during review.

Author Information Reprints and permissions information is available at www.nature.com/reprints. Correspondence and requests for materials should be addressed to M.D.C. (mike.crisp@anu.edu.au).

METHODS

Data and sampling. Molecular phylogenies of vascular plants were sampled representing 11,064 species in 45 taxa from extratropical Africa, Madagascar, Australia–New Guinea, New Caledonia, New Zealand and South America, equivalent to an estimated 15% of the total flora of these regions. Seven biomes (wet forest, sclerophyll, alpine, bog, temperate grassland, savannah and arid) were recognized. Landmasses and biomes are defined below.

We aimed to include all monophyletic vascular plant taxa (Supplementary Table 4) satisfying the following conditions: (1) they have adequately sampled molecular phylogenies; (2) there is a plausible source for dating of significant nodes; (3) they are centred in the Southern Hemisphere temperate and subtropical regions (more or less south of latitude 23° S). We excluded taxa occurring mainly in the tropics but included some primarily temperate taxa with northern outliers, usually in higher elevation habitats, such as the central African mountains and New Guinea highlands.

We considered the following areas.

(1) South America: excludes the equatorial areas and the northern and north-central Andes.

(2) New Zealand: includes Chatham and associated islands.

(3) Australia: includes Tasmania and New Guinea but not Timor.

(4) Southern Africa: includes the areas in the Cape Provinces (Northern, Western and Eastern) south of the Orange River.

(5) New Caledonia and (6) Madagascar: both of these islands extend into the tropics but have a small upland temperate flora element.

(7) Rest of the world: several of the sampled taxa included clades occurring north of the limit of 23° S set above. Inferred transitions in both directions between these and the defined southern temperate areas were noted but excluded from our analysis (but see notes above on montane outliers).

We considered the following biomes.

(1) Wet forest: closed canopy of trees, typically in high-precipitation climate.

(2) Sclerophyll woodland or heathland: most species are sclerophyll shrubs; either on low-nutrient soils or in Mediterranean climate or both. Local types include fynbos (Africa); eucalypt-dominated woodland and open forest, kwongan, wallum and *Triodia*-dominated 'hummock-grasslands' (Australia); chaparral (America); and maquis (New Caledonia). However, this biome excludes true grasslands and rainforests with scattered emergent eucalypts.

(3) Savannah: most species are graminoids or forbs, with variable presence of trees and shrubs; dominant grasses always C4; climate monsoonal (summer rain, dry winter).

(4) Temperate grassland: most species are grasses or forbs, with variable presence of trees and shrubs; grasses can be either C3 or C4; climate has cold winters, otherwise various but not arid. Can include ruderal and grassy riparian patches.

(5) Arid: mean annual rainfall <300 mm, to <400 mm in subtropics; includes semi-arid under European definitions; graminoid cover sparse in comparison with grasslands, if present at all; variable mixture of forbs, shrubs and trees.

(6) Alpine or tundra: above treeline, cover comprises graminoids, forbs and shrubs.

(7) Bog: permanently saturated peaty soil normally lacking surface water; not including seasonally flooded ground (swamps, floodplains) or riparian habitat, which we include in the wider biome within which they are embedded, such as sclerophyll or forest.

Species of other azonal habitats (cliffs, riverbeds, coastal strands, aquatics) were few in our data set and were included in the biome in which they are embedded.

We are aware that, as climate changed through the Cenozoic era, biomes fluctuated in size and changed in taxonomic composition, and that some were more stable than others^{22,29,30}. Despite these changes, the defining characteristics of the biomes, which are reflected in the physiological and morphological adaptations of species to the biome, have been maintained from the late Eocene epoch to the present^{22,29,30}.

Scoring and optimization. Terminal taxa (species) in the phylogenies were scored for occurrence in the biomes and landmasses. The few widely distributed species, that is, those occurring in more than one landmass or biome, were scored as polymorphic. Parsimony optimization was used to infer both ancestral biome and area of occurrence at internal nodes of the phylogenies, either by hand or using MESQUITE³¹.

In cases of ambiguous reconstructions at a node, all equally parsimonious alternatives were scored as fractions of a single state transition at that node. For example, if a shift from bog to alpine, or the reverse, were equally parsimonious at a node, each was scored with a weight of 0.5. Each polymorphism was counted as a single transition within the terminal species. For 'soft' polytomies in the phylogenies (reflecting uncertain or conflicting resolution³¹), all alternative resolutions

of the tree were treated as equally likely. This created ambiguity where a transition was inferred at a polytomy and the alternative transitions were weighted as above.

Apart from parsimony, maximum-likelihood and Bayesian methods are available for inferring ancestral traits³², but these do not necessarily perform better with biogeographical data³³ and their use was not practicable given the size of our meta-data set. Moreover, these methods require branch length estimates and monomorphic terminals, requirements that were not satisfied for several data sets. Comparative maximum-likelihood and parsimony optimizations were made in MESQUITE for four suitable phylogenies: Mirbeliaceae-Bossiaeeae (Fabaceae), Casuarinaceae, *Scaevola* (Goodeniaceae) and *Eucalyptus*. For maximum-likelihood optimization we used the MK1 model, shown to be suitable for discrete-state data such as biome occurrences³⁴. Parsimony inferred the same number of biome transitions (eucalypts) or a few more (remaining taxa) in comparison with the maximum-likelihood model (Supplementary Table 5). Therefore, our use of parsimony for the main analyses, rather than maximum likelihood, might have slightly underestimated the extent of biome conservatism. In other words, the degree of phylogenetic biome conservatism could be even more impressive than estimated here, given that parsimony might overestimate transitions.

Interpretation of transoceanic disjunctions. All landmasses in this study are now separated by oceanic gaps. Therefore, disjunct occurrences of sister taxa (inferred by optimization to occur in different landmasses) could have resulted from either vicariance or transoceanic colonization²⁰. By definition, the process of vicariance does not involve a biome transition⁴; therefore, it was necessary to detect likely vicariant disjunctions and eliminate them from the analysis. Colonization and vicariance were distinguished by the estimated age of the disjunct pairs of lineages: those disjunctions that predate the severance of the last connections between the lands were classed as vicariants; those younger could have been established only by transoceanic colonization. Timing of divergences at nodes was taken from molecular dating studies where available. Alternatively, we used fossil evidence directly mapped onto trees following the approach of ref. 35, for example for the Cupressaceae, which have an excellent Southern Hemisphere macrofossil record.

We used the geological estimates of the times of separation of the landmasses by continental drift^{36–38} (Supplementary Table 6). Our approach was conservative, erring on the side of a vicariance interpretation. If the confidence interval of a disjunction age estimate overlapped with that for the corresponding geological separation in Supplementary Table 6, we inferred vicariance and excluded the disjunction from further analysis.

For some taxa, the root (basal) node was dated to a time younger than the geological isolation of the landmass that was inferred as ancestral for the taxon. The relevant geological dates are in Supplementary Table 6. For example, *Chaetanthera* is endemic in South America, which was isolated from 30 Myr ago, but the root node of *Chaetanthera* was dated to 11 Myr ago. In other cases, a taxon was present in a landmass before its isolation but the area of occurrence of its sister taxon could not be determined. For example, the mirbelioid legumes were present in Australia 50 Myr ago. This occurrence is old enough to be vicariant with South America, but its sister group is uncertain and, thus, reconstruction of the ancestral area is not possible. In such cases, the origin of the taxon, whether 'in situ' by vicariance, or by colonization from elsewhere, was undetermined and the basal node was not scored for analysis, although all its descendent nodes were scored.

Tests of biome conservatism. To test whether biome stasis associated with transoceanic colonization was more prevalent than might be expected by chance, we used a null hypothesis that the probability of colonization of a destination in any of the seven biomes (including that of the source) depended on the available area of that biome. For a given biome in a given destination landmass, we assumed that if there were no biome stasis, then all colonizations originating from that biome overseas would be distributed among destination biomes in proportion to their areas. Thus, the expected frequency of stasis was calculated as the proportional area of that biome in the destination landmass (Supplementary Table 3). This calculation was repeated across all 226 observed colonizations, grouped by destination biomes ($n = 28$) and evaluated statistically using the sign test implemented at Simple Interactive Statistical Analysis (SISA, <http://www.quantitativeskills.com/sisa/index.htm>).

Although the test reported above indicated greater-than-expected biome conservatism in the data as a whole, there could have been significant departures from this pattern in colonizations between individual pairs of landmasses. We tested whether biome stasis was consistent across all 30 pairwise combinations of landmasses, in both directions (Fig. 2 and Table 1) using the Wilcoxon matched-pairs signed-rank test, implemented at SISA. The rationale was that each pairwise combination provided an independent test of departure from the null expectation of equal probabilities of biome shift/non-shift during transoceanic colonizations. We used the same rationale and test to ask whether biome stasis in transoceanic colonizations was consistent among biomes.

For 13 individual phylogenies, we tested the hypothesis of phylogenetic biome conservatism using a Monte Carlo approach implemented in MESQUITE. The terminals of each original phylogeny were randomized 100 times and the number of biome transitions estimated by parsimony optimization in each randomized tree. If the number of transitions in the original data fell below the tail of the distribution of values from the randomized trees, then transitions were inferred to be significantly fewer than expected by chance ($P = 0.01$). This test perturbed the clustering of biomes in clades while preserving the tree topology and the number of species in each biome. Thus, rejection of the null hypothesis indicates that closely related species are more likely to occupy the same biome than would be expected on the basis of their phylogenetic relationships.

Tests of bias in biome shifts. Within landmasses, where the great majority of biome shifts were observed (356 of 396), directional bias in biome shifts was evident; for example, it appears that there were many more shifts from sclerophyll into other biomes than vice versa (Fig. 1 and Supplementary Table 1). For each biome, we asked whether there was a significant bias, that is, whether the biome was a net source or sink for transitions. The null expectation is that shifts were equally probable in either direction and the binomial test was used at SISA. We repeated this test, correcting for a correlation between the number of transitions and the species richness of the source biome (Supplementary Fig. 1). Values in Supplementary Table 1 were multiplied by one minus the fractional contribution of source biome to total richness and rescaled to the original total number of transitions (Supplementary Table 2).

29. Burgoyne, P. M., van Wyk, A. E., Anderson, J. M. & Schrire, B. D. Phanerozoic evolution of plants on the African plate. *J. Afr. Earth Sci.* **43**, 13–52 (2005).
30. Barreda, V. & Palazzesi, L. Patagonian vegetation turnovers during the Paleogene–early Neogene: Origin of arid-adapted floras. *Bot. Rev.* **73**, 31–50 (2007).
31. Maddison, W. P. & Maddison, D. R. MESQUITE: A modular system for evolutionary analysis. *Mesquite* (<http://mesquiteproject.org>) (version 2.01, 2007).
32. Omland, K. E., Cook, L. G. & Crisp, M. D. Tree thinking for all biology: the problem with reading phylogenies as ladders of progress. *Bioessays* **30**, 854–867 (2008).
33. Cook, L. G. & Crisp, M. D. Directional asymmetry of long-distance dispersal and colonisation could mislead reconstructions of biogeography. *J. Biogeogr.* **32**, 741–754 (2005).
34. Lewis, P. O. A likelihood approach to estimating phylogeny from discrete morphological character data. *Syst. Biol.* **50**, 913–925 (2001).
35. Crepet, W. L., Nixon, K. C. & Gandolfo, M. A. Fossil evidence and phylogeny: the age of major angiosperm clades based on mesofossil and macrofossil evidence from Cretaceous deposits. *Am. J. Bot.* **91**, 1666–1682 (2004).
36. McLoughlin, S. The breakup history of Gondwana and its impact on pre-Cenozoic floristic provincialism. *Aust. J. Bot.* **49**, 271–300 (2001).
37. Cook, L. G. & Crisp, M. D. Not so ancient: the extant crown group of *Nothofagus* represents a post-Gondwanan radiation. *Proc. R. Soc. Lond. B* **272**, 2535–2544 (2005).
38. Ladiges, P. Y. & Cantrill, D. New Caledonia–Australian connections: biogeographic patterns and geology. *Aust. Syst. Bot.* **20**, 383–389 (2007).

Role of *Jhdm2a* in regulating metabolic gene expression and obesity resistance

Keisuke Tateishi^{1,2,†}, Yuki Okada^{1,2}, Eric M. Kallin^{1,2} & Yi Zhang^{1,2}

Recent studies indicate that the methylation state of histones can be dynamically regulated by histone methyltransferases and demethylases^{1,2}. The H3K9-specific demethylase *Jhdm2a* (also known as *Jmjd1a* and *Kdm3a*) has an important role in nuclear hormone receptor-mediated gene activation and male germ cell development^{3,4}. Through disruption of the *Jhdm2a* gene in mice, here we demonstrate that *Jhdm2a* is critically important in regulating the expression of metabolic genes. The loss of *Jhdm2a* function results in obesity and hyperlipidemia in mice. We provide evidence that the loss of *Jhdm2a* function disrupts β -adrenergic-stimulated glycerol release and oxygen consumption in brown fat, and decreases fat oxidation and glycerol release in skeletal muscles. We show that *Jhdm2a* expression is induced by β -adrenergic stimulation, and that *Jhdm2a* directly regulates peroxisome proliferator-activated receptor α (*Ppara*) and *Ucp1* expression. Furthermore, we demonstrate that β -adrenergic activation-induced binding of *Jhdm2a* to the PPAR responsive element (PPRE) of the *Ucp1* gene not only decreases levels of H3K9me2 (dimethylation of lysine 9 of histone H3) at the PPRE, but also facilitates the recruitment of Ppar γ and Rxra and their co-activators Pgc1 α (also known as Pparg1a), CBP/p300 (Crebbp) and Src1 (Ncoa1) to the PPRE. Our studies thus demonstrate an essential role for *Jhdm2a* in regulating metabolic gene expression and normal weight control in mice.

Using a hypomorphic *Jhdm2a* knockout model, we have previously shown an important role for the H3K9 demethylase *Jhdm2a* in spermatogenesis³. To further characterize the biological function of this demethylase, we created a new mouse line with the catalytic jumonji C domain floxed by *loxP* sites (Supplementary Fig. 1a). Heterozygous mice were generated by crossing *3lox* mice with E1a-Cre transgenic mice (Supplementary Fig. 1a, b). *Jhdm2a*^{1lox/1lox} (knockout) mice were obtained by intercrossing *Jhdm2a*^{1lox/+} mice, and were confirmed by PCR and western blot analysis (Supplementary Fig. 1b, c). Similar to the hypomorphic *Jhdm2a* mice, the complete knockout mice exhibit spermatogenesis defects (data not shown). Interestingly, the *Jhdm2a* knockout mice become obese in adulthood when compared to their wild-type littermates (Fig. 1a and Supplementary Fig. 2). The obese phenotype is also observed in *Jhdm2a* knockout mice backcrossed onto a C57BL/6 background (data not shown), as well as in the hypomorphic *Jhdm2a* mice on a mixed 129SV/Ola and C57BL/6 background (Supplementary Fig. 3), indicating that *Jhdm2a* deficiency leads to obesity irrespective of the genetic background. Consistent with a potential role for *Jhdm2a* in energy homeostasis, *Jhdm2a* is expressed at a relatively higher level in organs responsive to sympathetic nerve activity, such as brown adipose tissue (BAT) and skeletal muscle (Supplementary Fig. 4). In contrast, *Jhdm2a* expression in brain is almost undetectable (Supplementary Fig. 4).

Magnetic resonance imaging (MRI) analysis revealed marked body fat deposition in 4-month-old knockout mice (Supplementary

Fig. 2c). However, non-adipose tissues (lean) were comparable between wild-type and *Jhdm2a* knockout mice (Supplementary Fig. 2c). Similar to that observed in human obesity, large fat droplets are observed in white adipose tissue, as well as in muscle and liver

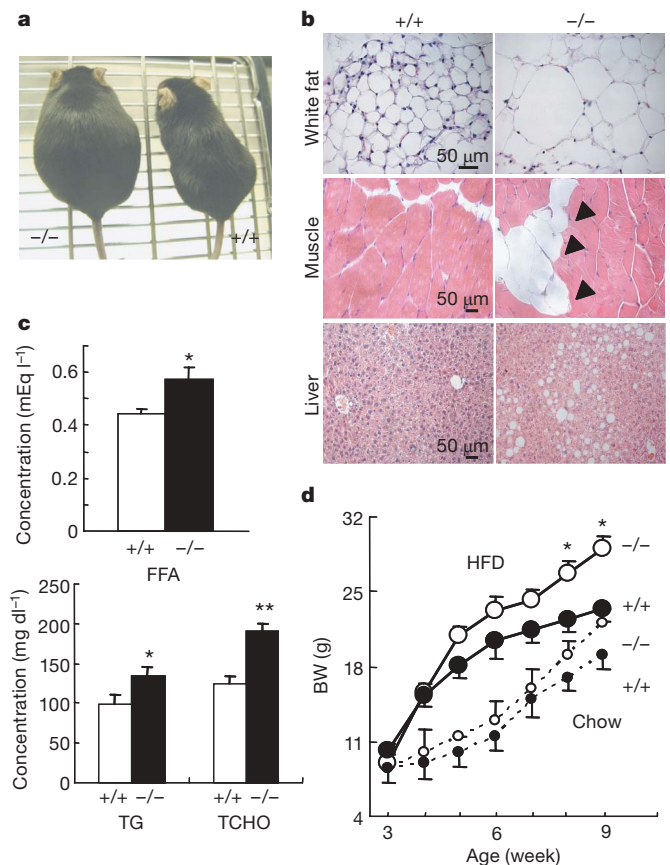


Figure 1 | *Jhdm2a*-deficient mice exhibit obesity phenotypes. **a**, *Jhdm2a* knockout mice exhibit an obesity phenotype. Shown is a representative photograph of 7-month-old littermates. **b**, Abnormal fat accumulation in organs of *Jhdm2a*^{-/-} mice. Haematoxylin and eosin (H&E) staining of white adipose, muscle and liver derived from 7-month-old littermates. Arrowheads indicate the intramuscle fat deposition. Scale bars, 50 μ m. **c**, *Jhdm2a* deficiency results in hyperlipidemia as indicated by the increased levels of serum free fatty acid (FFA), triglyceride (TG) and total cholesterol (TCHO) in *Jhdm2a*^{-/-} ($n = 16$) compared with *Jhdm2a*^{+/+} ($n = 10$) mice. * $P < 0.05$; ** $P < 0.01$. **d**, Growth curve of littermates fed with a high-fat diet (HFD) or normal chow. Solid lines, high-fat diet group; dotted lines, normal chow group. BW, body weight. $n = 4$ per group; * $P < 0.03$. Data are mean and s.e.m.

¹Howard Hughes Medical Institute, ²Department of Biochemistry and Biophysics, Lineberger Comprehensive Cancer Center, University of North Carolina at Chapel Hill, Chapel Hill, North Carolina 27599-7295, USA. †Present address: Department of Gastroenterology, University of Tokyo Hospital, Japan.

(Fig. 1b). In addition, serum lipid content—including free fatty acid, triglyceride and total cholesterol—is significantly higher in the knock-out mice (Fig. 1c). Furthermore, a high-fat diet accelerated the onset of obesity in the knockout mice (Fig. 1d). Collectively, these findings suggest that the loss of *Jhdm2a* function results in abnormal fat metabolism and obesity.

The body weight of an animal is maintained through a balance between food intake and energy expenditure^{5,6}. To understand how *Jhdm2a* deficiency results in obesity, we first analysed food intake before the onset of obesity using 6-week-old mice, and found that caloric intake is not increased in the *Jhdm2a* knockout mice (Supplementary Fig. 5a). Similarly, the 16-week-old *Jhdm2a* knockout mice did not show an increased food intake, regardless of the fat content present in the diet (Supplementary Fig. 5b). In addition, the serum leptin level is not significantly altered in 6-week-old *Jhdm2a* knockout mice before they become obese (Supplementary Fig. 5c).

Given that the human counterpart of mouse *Jhdm2a* has been previously demonstrated to function as a transcriptional co-activator⁴, we compared the gene expression profiles of wild-type and *Jhdm2a* knockout skeletal muscles using Affymetrix microarray technology. We chose to perform the analysis in skeletal muscle because of the high expression of *Jhdm2a* and also its role in energy expenditure. Of the 43,000 probes analysed, 602 probes (1.4%) were downregulated at least twofold and 220 probes (0.05%) were upregulated at least twofold in *Jhdm2a* knockout soleus muscle. Gene ontology enrichment analysis indicated that the largest proportion of downregulated genes were involved in metabolic processes ($P = 0.03$) (Supplementary Fig. 6a), whereas genes involved in lipid metabolism were the most enriched ($P < 1 \times 10^{-4}$) (Supplementary Fig. 6b–e). Interestingly, pathway analysis showed that a significant proportion of the genes involved in PPAR signalling are downregulated in response to the *Jhdm2a* knockout ($P < 1 \times 10^{-11}$) (Supplementary Fig. 7). Quantitative PCR with reverse transcription (qRT–PCR) confirmed the downregulation

of many genes involved in the PPAR pathway, including *Ppara*, *Ucp2*, *MCAD* (also known as *Acadm*), *LCAD* (*Acadl*), *VLCAD* (*Acadvl*) and *Aqp7* but not *Ppard* (Fig. 2a). Consistent with the fact that multiple rate-limiting enzymes for fatty acid oxidation, such as MCAD, LCAD and VLCAD, were downregulated in the *Jhdm2a* knockout skeletal muscle, β -oxidation of palmitic acid was significantly decreased in primary myocytes derived from the *Jhdm2a* knockout newborn (Fig. 2b). Consistent with downregulation of *Aqp7* (Fig. 2a), glycerol release in response to a β -adrenergic agonist is impaired in the *Jhdm2a* knockout soleus muscle (Fig. 2c). These results are consistent with previous demonstrations that PPAR α has an essential involvement in fatty acid metabolism^{7–9}. Notably, the results also indicate that the impaired expression of PPAR α and its downstream target genes might be one of the causes of abnormal fat accumulation in the *Jhdm2a* knockout mice, because previous studies have shown that *Ppara*-deficient mice are prone to diet-induced obesity⁹ and that *Aqp7* deficiency causes obesity in adult mice¹⁰.

To understand how the loss of *Jhdm2a* function results in the downregulation of PPAR α and its target genes, we analysed the presence of *Jhdm2a* around defined PPRE sequences using chromatin immunoprecipitation (ChIP)^{11–14}. Results indicate that *Jhdm2a* binds to the PPRE of *Ppara*, but not to the PPREs of *MCAD*, *Acox1* or *Scp2* (Fig. 2d). Consistent with the function of *Jhdm2a* as an H3K9me2 demethylase, the level of H3K9me2 at the region encompassing the PPRE of the *Ppara* gene is significantly increased in the *Jhdm2a* knockout muscle cells (Fig. 2e). To demonstrate that the reduced PPAR α expression in *Jhdm2a* knockout muscle cells is a cell-intrinsic effect, we performed qRT–PCR and ChIP analysis using *in vitro* cultured primary myocytes derived from newborn wild-type and knockout mice. Results shown in Fig. 2f demonstrate that *Ppara* is decreased by 50% in *Jhdm2a* knockout myocytes. ChIP analysis showed increased levels of H3K9me2 at the PPAR α PPRE of *Jhdm2a* knockout myocytes (Fig. 2g). Notably,

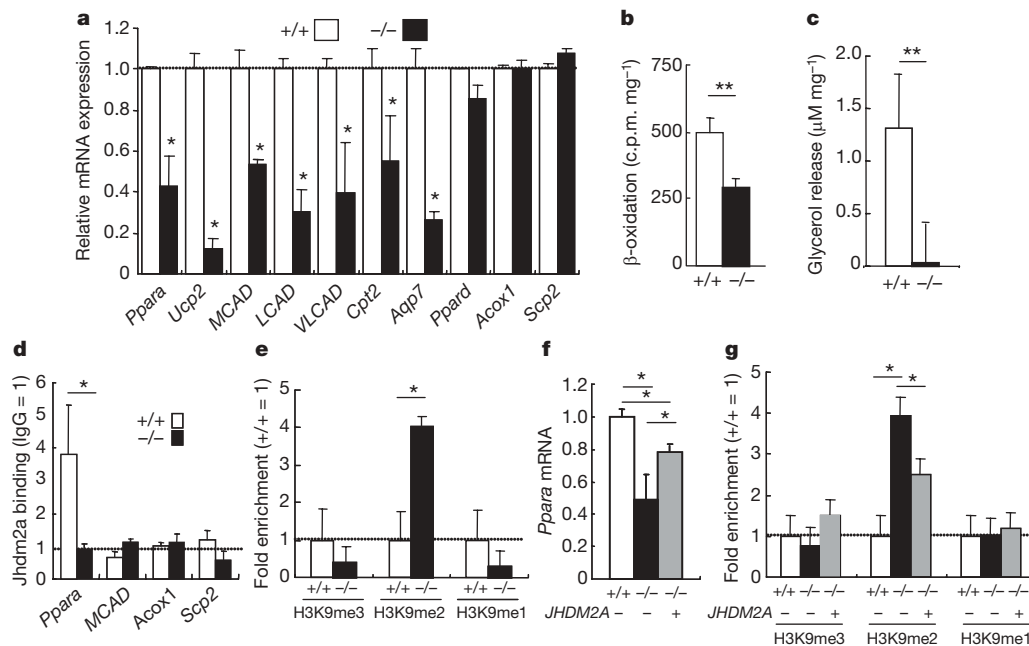


Figure 2 | *Jhdm2a* deficiency affects the expression of metabolic genes and impairs β -oxidation and glycerol release in skeletal muscle. **a**, qRT–PCR analysis confirms the decreased expression of genes that are involved in PPAR signalling in the *Jhdm2a* knockout soleus muscles. $*P < 0.05$. **b**, *Jhdm2a* deficiency results in decreased β -oxidation in primary muscle cells. $n = 5$ per group; $**P < 0.01$. **c**, *Jhdm2a* deficiency results in decreased glycerol release in isolated soleus muscle. $n = 5$ per group; $**P < 0.01$. **d**, *Jhdm2a* directly binds to the PPRE of the *Ppara* enhancer. Soleus muscles were used for ChIP followed by qRT–PCR. Results are normalized to IgG.

$*P < 0.05$. **e**, *Jhdm2a* deficiency results in increased H3K9me2 levels within the *Ppara* enhancer. The signal in wild-type cells is set as 1. $*P < 0.05$. **f**, Cultured *Jhdm2a* knockout myocytes show decreased *Ppara* expression, which can be partially restored by overexpression of the *JHDM2A* gene. Wild-type primary cultured myocytes served as a control for qRT–PCR. $*P < 0.05$. **g**, ChIP analysis in the primary cultured myocytes. *Jhdm2a* deficiency causes the increase of the H3K9me2 level at the PPRE of the *Ppara* enhancer. This change can be partially rescued by overexpression of *Jhdm2a*. The signal in wild-type cells is set as 1. $*P < 0.05$. Data are mean and s.e.m.

both *Ppar α* expression and promoter H3K9me2 levels at PPRE can be partially rescued by overexpression of human *JHDM2A* (Fig. 2f, g). These data collectively support the notion that *Ppara* is a direct target of *Jhdm2a* and that *Jhdm2a* plays an important part in lipid metabolism in skeletal muscle cells.

In addition to skeletal muscle, *Jhdm2a* is also highly expressed in BAT (Supplementary Fig. 4). *Jhdm2a* deficiency resulted in the enlargement and accumulation of lipid droplets in the BAT (Supplementary Fig. 8). Consistent with the BAT abnormalities, *Jhdm2a* knockout mice showed defective adaptive thermogenesis (Fig. 3a). The phenotypic similarity between *Jhdm2a* knockout mice and mice lacking β -adrenergic receptors¹⁵ raises the possibility that *Jhdm2a* might be a critical factor in β -adrenergic signalling. Consistent with this notion, β -adrenergic-stimulated oxygen consumption and glycerol release are greatly reduced in the *Jhdm2a* knockout BAT (Fig. 3b, c). In addition, genes involved in mitochondrial functions including *Ppara*, *Ucp3*, *Cpt2* and *LCAD* are also decreased in the *Jhdm2a* knockout BAT (Fig. 3d). Furthermore, analysis of the expression of *Ucp1* and *Dio2*, two key genes involved in thermogenesis in BAT¹⁶, demonstrated that cold-induced *Ucp1* upregulation is almost completely blocked although *Dio2* induction is not affected (Fig. 3e). Given the critical function of *Ucp1* in cold sensitivity¹⁷, defective activation of *Ucp1* by β -adrenergic signalling is probably one contributing factor of defective thermogenesis in the *Jhdm2a* knockout BAT.

As one of the most important molecules involved in cold-induced thermogenesis in brown fat, the transcriptional regulation of *Ucp1* has been extensively characterized¹⁶. In addition to *Ppar α* and *Ppar γ* , other transcription factors and co-activators known to be involved in *Ucp1* activation include *Rxr α* , *Atf2*, *p300*, *Src1* and *Pgc1 α* . qRT-PCR demonstrates that the expression of these genes is not significantly altered in the *Jhdm2a* knockout BAT (Supplementary Fig. 9), however cold-induced upregulation of *Ppar α* is defective in knockout BAT (Supplementary Fig. 9). This indicates that the defect in cold-induced *Ucp1* induction in *Jhdm2a* knockout BAT might be mediated through *Ppar α* , which is a direct target of *Jhdm2a* in muscle cells

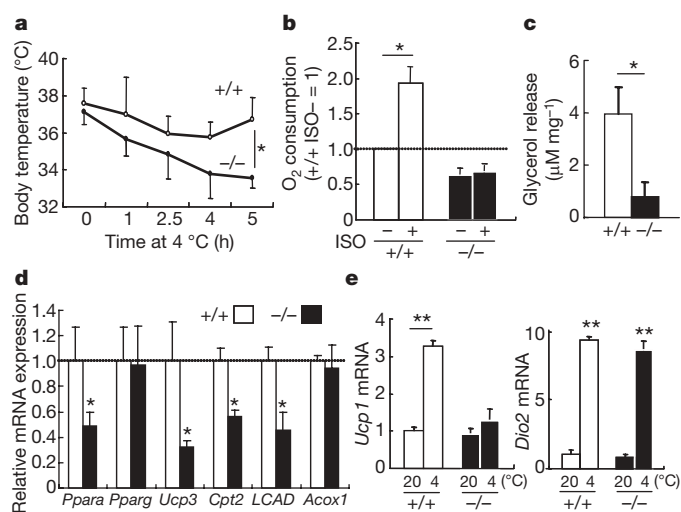


Figure 3 | *Jhdm2a* deficiency results in functional defects in BAT. **a**, *Jhdm2a* deficiency impairs the ability of mice to maintain body temperature when exposed to cold. Shown is the body temperature of 12-week-old mice at different times after cold exposure (4 °C). $n = 5$ per group; $*P < 0.05$. **b**, *Jhdm2a* deficiency impairs ISO-induced oxygen consumption in BAT. $*P < 0.05$. **c**, *Jhdm2a* deficiency results in decreased glycerol release in BAT. $*P < 0.05$. **d**, qRT-PCR analysis demonstrates decreased expression of genes involved in mitochondrial function in the *Jhdm2a* knockout BAT. $*P < 0.05$. **e**, *Jhdm2a* deficiency impairs cold-induced activation of *Ucp1*, but not *Dio2*, in BAT. $n > 4$ per group. The mRNA level is normalized by *36B4* mRNA, and the relative quantity in *Jhdm2a*^{+/+} BAT at 20 °C is defined as 1. $**P < 0.01$. Data are mean and s.e.m.

(Fig. 2d). Given that cold-induced *Ucp1* upregulation is intact in the *Ppar α* deficient mice¹⁸, we explored the possibility that *Jhdm2a* directly regulates *Ucp1* expression in response to cold exposure.

To ascertain that the effect of *Jhdm2a* on *Ucp1* expression is cell intrinsic, we performed short-hairpin RNA (shRNA)-mediated *Jhdm2a* knockdown in the brown adipose cell line HIB1B using lentivirus-based shRNA. Although *Jhdm2a* knockdown does not affect HIB1B differentiation (data not shown), the differentiated knockdown cells have impaired *Ucp1* activation by isoproterenol (ISO), a general β -adrenergic receptor agonist (Fig. 4a), consistent with the result obtained in *Jhdm2a* knockout BAT (Fig. 3e). Importantly, enforced overexpression of human *JHDM2A* in the knockdown cells partially rescued *Ucp1* expression (Fig. 4b). Interestingly, both the messenger RNA and protein levels of *Jhdm2a* are upregulated in response to β -adrenergic receptor activation (Fig. 4c), supporting *Jhdm2a* as an integral component of the β -adrenergic signalling pathway. Similar to that observed in mouse brown fat tissues, the expression of the transcription factors and co-activators involved in *Ucp1* activation is not significantly altered in the HIB1B knockdown cells (Supplementary Fig. 10a). ISO-induced upregulation of *Pgc1 α* is also maintained in HIB1B knockdown cells (Supplementary Fig. 10a). We next explored the possibility that *Jhdm2a* directly regulates *Ucp1* expression. ChIP analysis demonstrated that *Jhdm2a* can bind to the *Ucp1* enhancer region¹⁹ in a β -adrenergic receptor ligand-dependent manner. The binding is site-specific as *Jhdm2a* was not detected within the *Ucp1* coding region (Fig. 4d, amplicon B). As expected, the H3K9me2 levels at the *Jhdm2a* binding site are specifically decreased in response to ISO treatment and this effect is abolished in the *Jhdm2a* knockdown cells (Fig. 4e). Notably, enforced overexpression of human *JHDM2A* in the knockdown cells partially rescued the increased H3K9me2 level in an ISO-dependent manner (Fig. 4e). Collectively, these results indicate that *Jhdm2a* expression is regulated by the β -adrenergic signalling pathway and that *Jhdm2a* contributes to *Ucp1* activation by serving as a co-activator in response to β -adrenergic receptor activation.

Previous studies have indicated that *Ppar γ* - and *Rxr α* -mediated *Ucp1* activation requires the recruitment of co-activators²⁰. In addition to removing the repressive H3K9me2 mark at the *Ucp1* enhancer, *Jhdm2a* could contribute to *Ucp1* activation by affecting the recruitment of transcription factors and co-activators. To examine this possibility, we analysed the effect of the loss of *Jhdm2a* on the recruitment of transcription factors (*Ppar γ* , *Rxr α* and *Atf2*) and co-activators (*Pgc1 α* , *CBP/p300* and *Src1*). We found that the binding of *Ppar γ* , *Rxr α* and *Atf2* to the *Ucp1* enhancer is increased in response to ISO treatment (Fig. 4f). However, the enhanced binding by *Ppar γ* and *Rxr α* disappeared in the *Jhdm2a* knockdown cells (Fig. 4f). Similar results are also observed for the co-activators (Fig. 4g). Given that *Jhdm2a* knockdown does not alter the protein levels of these transcription factors and co-activators (Supplementary Fig. 10b), the simplest explanation of the results is that *Jhdm2a* facilitates their recruitment in response to β -adrenergic stimulation. Our results, together with the previous demonstration that *Ppar γ* recruitment to *Ucp1* enhancer is blocked in *pCip* (also known as *Ncoa3*) and *Src1* double knockout BAT²⁰, indicate that the binding of transcription factors and co-activators to the *Ucp1* enhancer affect one another. Collectively, our data suggest that *Jhdm2a* contributes to β -adrenergic-stimulated *Ucp1* activation by maintaining a low level of H3K9me2 at the *Ucp1* enhancer region, and by augmenting the recruitment of *Ppar γ* and *Rxr α* and their co-activators to the *Ucp1* enhancer element.

In this study we identified *Ppara* and *Ucp1*, two of the important genes involved in controlling energy balance, as direct targets of *Jhdm2a*. Notably, the expression of these two genes, as well as *Jhdm2a*, is induced after β -adrenergic stimulation^{16,21} (Figs 3e, 4c and Supplementary Fig. 9). Thus we propose that *Jhdm2a* mediates β -adrenergic signalling on the basis of the systemic energy demand. Consistent with this notion, *Jhdm2a* knockout mice and mice lacking β -adrenergic receptors have similar phenotypes that include defects

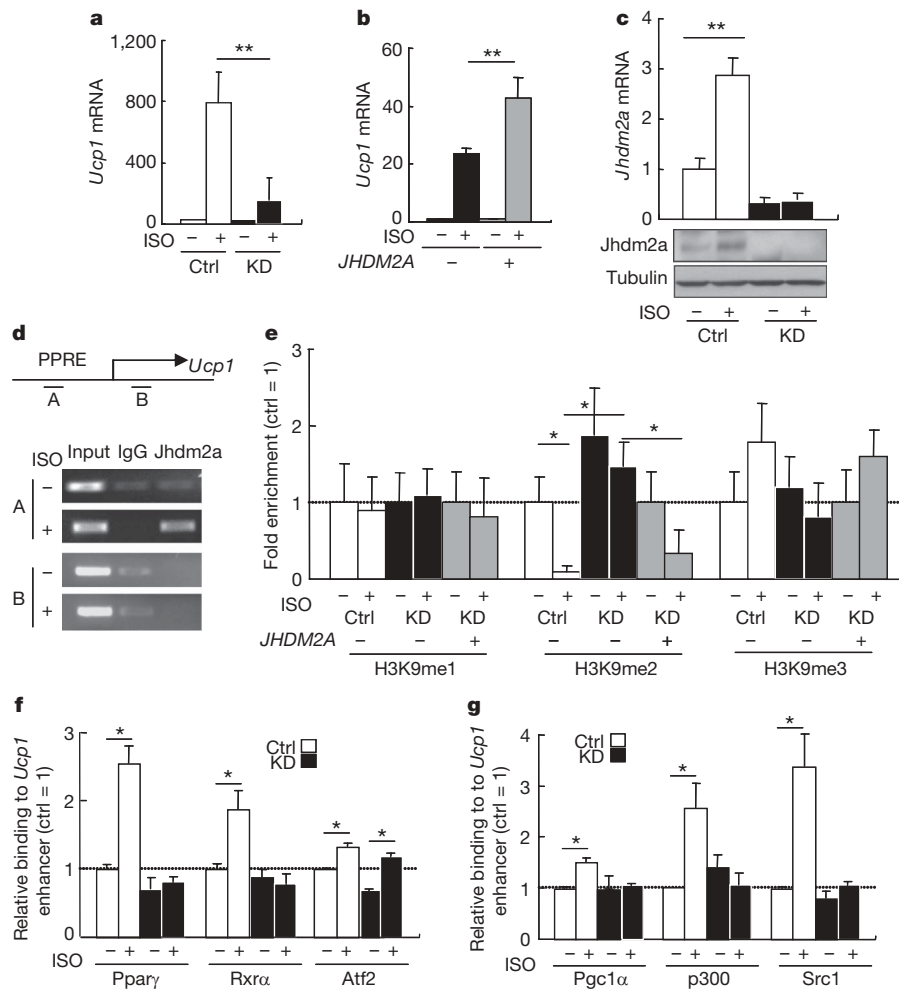


Figure 4 | *Jhdm2a* is induced by β -adrenergic receptor activation and functions as a co-activator of *Ucp1*. **a**, *Jhdm2a* knockdown (KD) impairs ISO-induced *Ucp1* transcriptional activation. Ctrl, control. $^{**}P < 0.01$. **b**, Defective ISO-induced *Ucp1* activation caused by *Jhdm2a* knockdown can be partially restored by *JHDM2A* overexpression $^{*}P < 0.05$. **c**, qRT-PCR (top panel) and western blot analysis (bottom panels) demonstrate that *Jhdm2a* is upregulated by ISO in HIB1B cells. $^{**}P < 0.01$. **d**, ChIP analysis demonstrates that *Jhdm2a* directly binds to PPRES (amplicon A) of the *Ucp1* enhancer after β -adrenergic stimulation. **e**, ChIP analysis demonstrates that H3K9me2 at the *Ucp1* gene enhancer is demethylated by *Jhdm2a* after ISO treatment. The *Jhdm2a* knockdown-induced increase in H3K9me2 level can

be partially rescued by overexpression of *JHDM2A* coupled with ISO treatment. $^{*}P < 0.05$. **f**, ChIP followed by qPCR indicates *Jhdm2a* knockdown impairs β -adrenergic receptor activation-stimulated *Pparg* and *Rxra* recruitment to the PPRES of the *Ucp1* gene enhancer. Results are normalized to IgG, and are shown as the fold-enrichment relative to that in the control cells without ISO. $^{*}P < 0.05$. **g**, ChIP followed by qPCR indicates *Jhdm2a* knockdown impairs β -adrenergic receptor activation-stimulated recruitment of *Pparg* and *Rxra* co-activators *Pgc1 α* , *p300* and *Src1* to the PPRES of the *Ucp1* gene enhancer. Results are normalized to IgG, and are shown as fold of enrichment relative to that in the control cells without ISO. $^{*}P < 0.05$. Data are mean and s.e.m.

in BAT function, cold intolerance, decreased oxygen consumption (Supplementary Fig. 11) and obesity without hyperphagia. Although the *Jhdm2a* deficiency does not affect metabolic hormone levels (Supplementary Fig. 12), the obesity phenotype supports an important role for *Jhdm2a* in regulating systemic metabolic control including *Pparg* and β -adrenergic signalling pathways. Although the entire mechanism underlying the phenotype reported here remains elusive, it is interesting to note that this is a unique mouse model in which a single epigenetic factor deficiency results in obesity.

METHODS SUMMARY

Animal experiments. All animal experiments were performed according to procedures approved by the Institutional Animal Care and Use Committee.

Cell culture, viral infection and differentiation. Primary myoblasts were established from neonatal mice as reported²². To generate a *Jhdm2a* knockdown HIB1B cell line, undifferentiated cells were infected with a lentiviral virus expressing an shRNA for *Jhdm2a* or control. The shRNA sequence for *Jhdm2a* was 5'-GCAGGTGTCAGCTTAAT-3'. The differentiation of HIB1B cells was performed as previously described²³. For the overexpression of the human *JHDM2A* gene, cells were infected with a retroviral vector expressing Flag-JHDM2A or a control before the cells were subjected to differentiation.

Statistics. All results are presented as the mean and standard error. Statistical comparisons were by Student's *t*-tests. Statistical significance was set at $P < 0.05$.

Received 15 December 2008; accepted 19 January 2009.

Published online 4 February 2009.

- Klose, R. J. & Zhang, Y. Regulation of histone methylation by demethylination and demethylation. *Nature Rev. Mol. Cell Biol.* **8**, 307–318 (2007).
- Martin, C. & Zhang, Y. The diverse functions of histone lysine methylation. *Nature Rev. Mol. Cell Biol.* **6**, 838–849 (2005).
- Okada, Y., Scott, G., Ray, M. K., Mishina, Y. & Zhang, Y. Histone demethylase JHDM2A is critical for *Tnp1* and *Prm1* transcription and spermatogenesis. *Nature* **450**, 119–123 (2007).
- Yamane, K. et al. JHDM2A, a JmJc-containing H3K9 demethylase, facilitates transcription activation by androgen receptor. *Cell* **125**, 483–495 (2006).
- Spiegelman, B. M. & Flier, J. S. Obesity and the regulation of energy balance. *Cell* **104**, 531–543 (2001).
- Evans, R. M., Barish, G. D. & Wang, Y. X. PPARs and the complex journey to obesity. *Nature Med.* **10**, 355–361 (2004).
- Reddy, J. K. & Hashimoto, T. Peroxisomal β -oxidation and peroxisome proliferator-activated receptor α : an adaptive metabolic system. *Annu. Rev. Nutr.* **21**, 193–230 (2001).
- Bedu, E., Desplanches, D., Pequignot, J., Bordier, B. & Desvergne, B. Double gene deletion reveals the lack of cooperation between PPAR α and PPAR β in skeletal muscle. *Biochem. Biophys. Res. Commun.* **357**, 877–881 (2007).

9. Finck, B. N. *et al.* A potential link between muscle peroxisome proliferator-activated receptor- α signaling and obesity-related diabetes. *Cell Metab.* **1**, 133–144 (2005).
10. Hibuse, T. *et al.* Aquaporin 7 deficiency is associated with development of obesity through activation of adipose glycerol kinase. *Proc. Natl Acad. Sci. USA* **102**, 10993–10998 (2005).
11. Gulick, T., Cresci, S., Caira, T., Moore, D. D. & Kelly, D. P. The peroxisome proliferator-activated receptor regulates mitochondrial fatty acid oxidative enzyme gene expression. *Proc. Natl Acad. Sci. USA* **91**, 11012–11016 (1994).
12. Lopez, D., Irby, R. B. & McLean, M. P. Peroxisome proliferator-activated receptor α induces rat sterol carrier protein x promoter activity through two peroxisome proliferator-response elements. *Mol. Cell. Endocrinol.* **205**, 169–184 (2003).
13. Pineda Torra, I., Jamshidi, Y., Flavell, D. M., Fruchart, J. C. & Staels, B. Characterization of the human PPAR α promoter: identification of a functional nuclear receptor response element. *Mol. Endocrinol.* **16**, 1013–1028 (2002).
14. Tugwood, J. D. *et al.* The mouse peroxisome proliferator activated receptor recognizes a response element in the 5' flanking sequence of the rat acyl CoA oxidase gene. *EMBO J.* **11**, 433–439 (1992).
15. Bachman, E. S. *et al.* β AR signaling required for diet-induced thermogenesis and obesity resistance. *Science* **297**, 843–845 (2002).
16. Lowell, B. B. & Spiegelman, B. M. Towards a molecular understanding of adaptive thermogenesis. *Nature* **404**, 652–660 (2000).
17. Enerback, S. *et al.* Mice lacking mitochondrial uncoupling protein are cold-sensitive but not obese. *Nature* **387**, 90–94 (1997).
18. Kersten, S. *et al.* Peroxisome proliferator-activated receptor α mediates the adaptive response to fasting. *J. Clin. Invest.* **103**, 1489–1498 (1999).
19. Cassard-Doulcier, A. M. *et al.* Tissue-specific and β -adrenergic regulation of the mitochondrial uncoupling protein gene: control by *cis*-acting elements in the 5'-flanking region. *Mol. Endocrinol.* **7**, 497–506 (1993).
20. Wang, Z. *et al.* Critical roles of the p160 transcriptional coactivators p/CIP and SRC-1 in energy balance. *Cell Metab.* **3**, 111–122 (2006).
21. Lomax, M. A. *et al.* Ontogenic loss of brown adipose tissue sensitivity to beta-adrenergic stimulation in the ovine. *Endocrinology* **148**, 461–468 (2007).
22. Rando, T. A. & Blau, H. M. Primary mouse myoblast purification, characterization, and transplantation for cell-mediated gene therapy. *J. Cell Biol.* **125**, 1275–1287 (1994).
23. Ross, S. R. *et al.* Hibernoma formation in transgenic mice and isolation of a brown adipocyte cell line expressing the uncoupling protein gene. *Proc. Natl Acad. Sci. USA* **89**, 7561–7565 (1992).

Supplementary Information is linked to the online version of the paper at www.nature.com/nature.

Acknowledgements We thank B. M. Spiegelman for the HIB1B cells, L. Xia for construction of the targeting vector, K. E. Gardner for critical reading of the manuscript, D. Pump and K. Hua (UNC Clinical Nutrition Research Unit, DK56350) for calorimetry and MRI, and N. Takahashi for helpful comments. Y.Z. is an investigator of the Howard Hughes Medical Institute.

Author Contributions K.T. and Y.Z. designed the experiments and prepared the manuscript. K.T. performed most of the experiments. Y.O. provided the data for Supplementary Fig. 3. E.K. analysed microarray data and generated Supplementary Figs 6 and 7.

Author Information The primary microarray data is accessible from the NCBI Gene Expression Omnibus repository under the accession number GSE13552. Reprints and permissions information is available at www.nature.com/reprints. Correspondence and requests for materials should be addressed to Y.Z. (yi_zhang@med.unc.edu).

LETTERS

c-Myc suppression of miR-23a/b enhances mitochondrial glutaminase expression and glutamine metabolism

Ping Gao¹, Irina Tchernyshyov², Tsung-Cheng Chang³, Yun-Sil Lee³, Kayoko Kita¹¹, Takafumi Ochi¹¹, Karen I. Zeller¹, Angelo M. De Marzo^{6,7,8}, Jennifer E. Van Eyk^{2,9}, Joshua T. Mendell^{3,4,5} & Chi V. Dang^{1,3,5,6,7,10}

Altered glucose metabolism in cancer cells is termed the Warburg effect, which describes the propensity of most cancer cells to take up glucose avidly and convert it primarily to lactate, despite available oxygen^{1,2}. Notwithstanding the renewed interest in the Warburg effect, cancer cells also depend on continued mitochondrial function for metabolism, specifically glutaminolysis that catabolizes glutamine to generate ATP and lactate³. Glutamine, which is highly transported into proliferating cells^{4,5}, is a major source of energy and nitrogen for biosynthesis, and a carbon substrate for anabolic processes in cancer cells, but the regulation of glutamine metabolism is not well understood^{1,6}. Here we report that the c-Myc (hereafter referred to as Myc) oncogenic transcription factor, which is known to regulate microRNAs^{7,8} and stimulate cell proliferation⁹, transcriptionally represses miR-23a and miR-23b, resulting in greater expression of their target protein, mitochondrial glutaminase, in human P-493 B lymphoma cells and PC3 prostate cancer cells. This leads to upregulation of glutamine catabolism¹⁰. Glutaminase converts glutamine to glutamate, which is further catabolized through the tricarboxylic acid cycle for the production of ATP or serves as substrate for glutathione synthesis¹¹. The unique means by which Myc regulates glutaminase uncovers a previously unsuspected link between Myc regulation of miRNAs, glutamine metabolism, and energy and reactive oxygen species homeostasis.

Oncogenes and tumour suppressors have been linked to the regulation of glucose metabolism, thereby connecting genetic alterations in cancers to their glucose metabolic phenotype^{1,2}. In particular, the *MYC* oncogene produces Myc protein that directly regulates glucose metabolic enzymes as well as genes involved in mitochondrial biogenesis^{9,12}. In this regard, we sought to determine the role of *MYC* in altering the mitochondrial proteome in order to understand further the regulation of tumour metabolism. We studied human P-493 B cells that bear a tetracycline-repressible *MYC* construct, such that tetracycline withdrawal results in rapid induction of Myc and mitochondrial biogenesis, followed by cell proliferation^{12,13}. By comparing the mitochondrial proteomes of tetracycline-treated and untreated cells with high Myc expression, we found eight mitochondrial proteins that are distinctly differentially expressed in response to Myc (Fig. 1a, b and Supplementary Table 1). Mitochondrial glutaminase expression (GLS, molecular mass of ~58 kDa) was increased ~10-fold in response to Myc. As such, we determined the response of glutaminase to Myc induction in a time-course study using anti-GLS antibody¹⁰ (Fig. 1c) and found that GLS levels diminish with decreased Myc expression and recover on Myc re-induction.

However, the level of the mitochondrial protein TFAM remained virtually unaltered. GLS levels also correlate with Myc levels in another human B cell line (CB33) and one (CB33-Myc) with constitutive Myc expression¹⁴. Because human prostate cancer is linked to Myc expression¹⁵, we sought to determine whether reduction of Myc expression by short interfering RNA (siRNA) in the human PC3 prostate cancer cell line is also associated with reduction of GLS expression (Fig. 1d). Similar to the human lymphoid cells, the PC3 cells also displayed a correlation between Myc and GLS levels.

We then sought to determine whether the marked alteration of GLS levels in response to Myc is functionally linked to Myc-induced cell proliferation. Although there are two major known tissue-specific GLS isoforms, GLS1 and GLS2 (refs 16, 17), our data show that only GLS1 is predominantly expressed in P493-6 or PC3 cells (Supplementary Fig. 1). We first determined whether gain of GLS1 function through overexpression in PC3 cells would rescue the diminished growth rate associated with siRNA-mediated reduction of Myc (Supplementary Fig. 2) and found that ectopic GLS1 expression alone is insufficient to stimulate growth. In light of the observation that no single gene could substitute for Myc^{18,19} and that Myc is a pleiotropic transcription factor⁹, this outcome was not particularly surprising. As such, we reduced the expression of GLS1 (hereafter referred to as GLS) by RNA interference (*GLS* siRNA) and found that P-493-6 cell proliferation is markedly attenuated by *GLS* siRNA but not by control siRNA (Fig. 2a). Likewise, proliferation of the human PC3 prostate cancer cell line was diminished by *GLS* siRNA (Fig. 2a), indicating that GLS is necessary for cell proliferation.

Because glutamine is converted by GLS to glutamate for further catabolism by the tricarboxylic acid (TCA) cycle, and previous studies indicate that overexpression of Myc sensitizes human cells to glutamine-withdrawal-induced apoptosis¹¹, we determined the metabolic responses of P493-6 or PC3 cells to glutamine deprivation (Fig. 2b). The growth of both cell lines was diminished significantly by glutamine withdrawal and moderately with glucose withdrawal. Glutamine withdrawal also resulted in a decrease in ATP levels (Fig. 2c) associated with a diminished cellular oxygen consumption rate (Supplementary Fig. 3a, b). Reduction of GLS by RNA interference (RNAi) also reduced ATP levels (Fig. 2d). Because glutamine is a precursor for glutathione²⁰, glutathione levels were measured by flow cytometry and were found to be diminished with glutamine withdrawal or RNAi-mediated reduction of GLS (Supplementary Fig. 4 and Supplementary Table 2) that is also associated with an increase in reactive oxygen species (ROS) levels (Supplementary Fig. 3c) and cell death in the P493-6 cells (Fig. 2e and Supplementary Fig. 5). Of note,

¹Division of Hematology, Department of Medicine, ²Division of Cardiology, Department of Medicine, ³McKusick-Nathans Institute of Genetic Medicine, ⁴Departments of Pediatrics and ⁵Molecular Biology and Genetics, ⁶Departments of Pathology, ⁷Oncology, ⁸Urology, ⁹Biological Chemistry and ¹⁰Cell Biology, Johns Hopkins University School of Medicine, Baltimore, Maryland 21205, USA. ¹¹Laboratory of Toxicology, Faculty of Pharmaceutical Sciences, Teikyo University, Sagamiko, Kanagawa 229-0195, Japan.

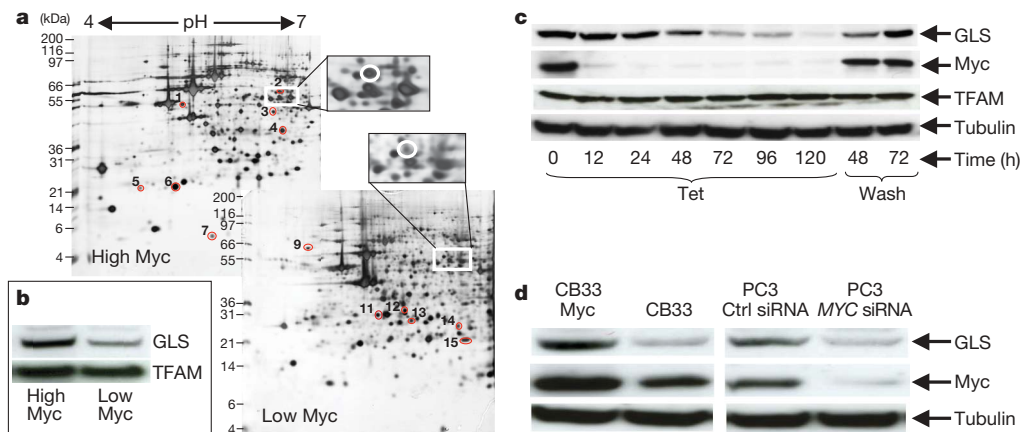


Figure 1 | Myc enhances the expression of mitochondrial protein glutaminase. **a**, The expanded insets of two-dimensional gels reveal the induction of glutaminase (GLS; highlighted by white circles) by Myc in P493-6 B cells. For each condition, 350 μ g of mitochondrial protein lysate was resolved on 18 cm immobilized pH gradient strips as the first dimension followed by 10% Bis-Tris SDS-PAGE as the second dimension, which is marked by molecular mass markers. Protein spots were visualized by silver staining. Six independent biological experiments were performed for each condition. Supplementary Table 1 summarizes the identity of the spots with the same numbering system as depicted in the figure. **b**, Immunoblot with anti-GLS antibody of a one-dimensional SDS-PAGE gel of mitochondrial

proteins (20 μ g per lane) validates the induction of GLS by Myc discovered in **a**. TFAM represents a control mitochondrial protein. **c**, P493-6 cells were treated with tetracycline (Tet) for different lengths of time to inhibit Myc expression or were treated first with tetracycline for 48 h and then washed (Wash) to remove tetracycline, with the times after wash-out indicated. Cells were then harvested for immunoblot assay for GLS or c-Myc. Anti-tubulin antibody and anti-TFAM were used for loading controls. **d**, Human CB33 lymphoblastoid cells, CB33-Myc cells and PC3 cells transfected with siRNA against c-Myc (MYC siRNA) or control siRNA (Ctrl siRNA) were used for immunoblot assays. Experiments were replicated with similar results.

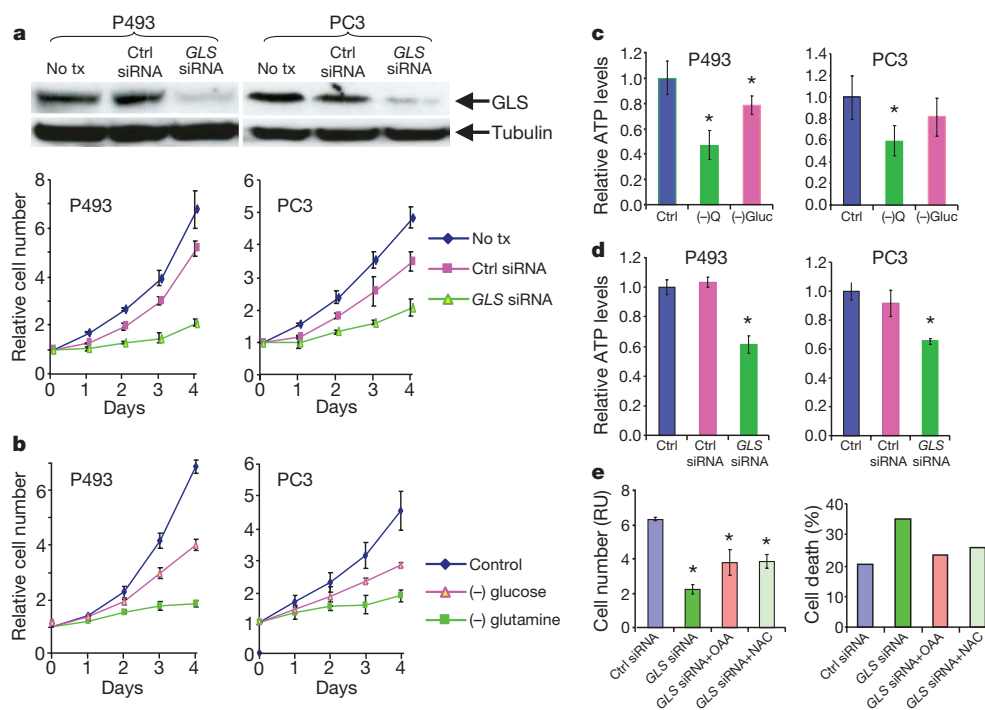


Figure 2 | Glutamine and glutaminase are necessary for Myc-mediated cancer cell proliferation and survival. **a**, Top: immunoblots showing that GLS protein level is diminished by transfecting cells with siRNA for *GLS1* (GLS siRNA) as compared with non transfection (No tx) or control siRNA (Ctrl siRNA). Bottom: growth inhibition of P493 and PC3 cells by GLS siRNA. The results shown are mean \pm s.d., $n = 3$. **b**, Growth inhibition of P493 and PC3 cells cultured under control, glucose- or glutamine-deprived conditions. The results shown are mean \pm s.d., $n = 3$. **c**, Cells were cultured with normal medium or medium without glucose ((-)Gluc) or glutamine ((-)Q) for 48 h and harvested for ATP assay as described in Methods. The results shown (mean \pm s.d., $n = 2$) are relative ATP levels per microgram total protein normalized to the control (Ctrl) normal medium group. **d**, ATP levels in control cells or cells transfected with GLS siRNA or control siRNA. Seventy-two hours after transfection, cells were harvested for ATP assay. The

results shown (mean \pm s.d., $n = 2$) are relative ATP levels per microgram total protein normalized to the non-transfected control group. **e**, Cells were transfected with GLS siRNA or control siRNA and cultured with 10 mM *N*-acetylcysteine (NAC), or 5 mM oxaloacetate (OAA), as indicated. The left panel shows cell counts (relative units (RU)); mean \pm s.d., $n = 5$ of different groups at 72 h after transfection (see Supplementary Fig. 5 for the complete cell growth curve). The right panel shows the percentage cell death at 72 h after transfection. Percentage cell death indicates annexin-positive plus annexin V and 7-AAD-positive cells. Primary data are shown in Supplementary Fig. 4. All experiments in Fig. 2 were repeated at least twice. All experiments with P493 cells were in the absence of tetracycline. Asterisk denotes mean (\pm s.d.) that is significantly different from control ($P < 0.05$, *t* test).

shortly after the *MYC* proto-oncogene was discovered, the MC29 retrovirus which bears the *v-myc* oncogene was found to enhance glutamine catabolism and mitochondrial respiration in transplantable avian liver tumour cells²¹. Thus, our findings functionally link historical observations with *Myc*, glutaminase and glutamine metabolism.

Because *GLS* catabolizes glutamine for ATP and glutathione synthesis, its reduction affects proliferation and cell death presumably through depletion of ATP and augmentation of ROS, respectively. Hence, we sought to rescue the P493-6 cells with the TCA cycle metabolite oxaloacetate (OAA) and the oxygen radical scavenger *N*-acetylcysteine (NAC)¹¹. Both OAA and NAC partially rescued the decreased proliferation and death of P493-6 cells deprived of *GLS* (Fig. 2e and Supplementary Fig. 6). Similarly, OAA and NAC both partially rescued glutamine-deprived P493-6 cells (Supplementary Figs 5 and 6). These findings support the notion that glutamine catabolism through *GLS* is critical for cell proliferation induced by *Myc* and protection against ROS generated by enhanced mitochondrial function in response to *Myc*^{11,20}.

Given that *GLS* is critical for cell proliferation and is induced by *Myc*, we determined the mechanism by which *Myc* regulates *GLS*. Because *Myc* is a transcription factor⁹, we hypothesized that *Myc* transactivates *GLS* directly as a target gene. Despite the presence of a canonical *Myc* binding site (5'-CACGTG-3') in the *GLS* gene intron 1, *GLS* messenger RNA levels do not respond to alterations in *Myc* levels in the P493-6 cells, suggesting that *GLS* is regulated at the post-transcriptional level (Fig. 3a). As such, we hypothesized that *GLS* could be regulated by miRNAs that are in turn directly regulated by *Myc*. The TargetScan algorithm predicts that miR-23a and miR-23b could target the *GLS* 3' untranslated region (UTR) seed

sequence. Notably, our earlier studies uncovered that both miR-23a and miR-23b are suppressed by *Myc* in P493-6 cells⁷, and both miR-23a and miR-23b are decreased in human prostate cancers²², which are associated with elevated *Myc* expression¹⁵.

To verify that miR-23a and miR-23b (hereafter referred to as miR-23a/b) are suppressed by *Myc* and can be diminished by antisense miR-23a/b locked nucleic acid (LNA) oligomers, a northern blot analysis was performed; the results show that miR-23a/b are indeed suppressed by *Myc* and profoundly diminished by antisense miR-23a/b LNAs (Fig. 3b). Quantitative real-time polymerase chain reaction (PCR) assays show (Supplementary Fig. 7) that miR-23a/b levels increase with diminished *Myc* expression and then decrease on *Myc* re-induction in a manner that is compatible with the *GLS* protein levels seen in Fig. 1c. We also found an inverse relationship between *Myc* and the levels of miR-23a/b in the CB33 human lymphoid cells and PC3 prostate cancer cell line (Supplementary Fig. 8). Furthermore, a chromatin immunoprecipitation assay (Fig. 3c) shows that *Myc* directly binds the transcriptional unit, *C9orf3*, encompassing miR-23b, as demonstrated for other *Myc* miRNA targets⁷. Because the transcriptional unit involving miR-23a has not been mapped, we did not study miR-23a in this context. These observations indicate that *Myc* represses miR-23a and miR-23b, which seem to be directly regulated by *Myc*.

We next determined whether miR-23a/b target and inhibit the expression of *GLS* through the 3' UTR. In this regard, we cloned the 3' UTR sequence of *GLS* including the predicted binding site for miR-23a/b to the pGL3 luciferase reporter vector and transfected MCF-7 cells, which are known to express miR-23a/b (ref. 23). The *GLS* 3' UTR inhibited luciferase activity in a fashion that was blocked by co-transfection with the antisense miR-23a/b LNAs, but not with

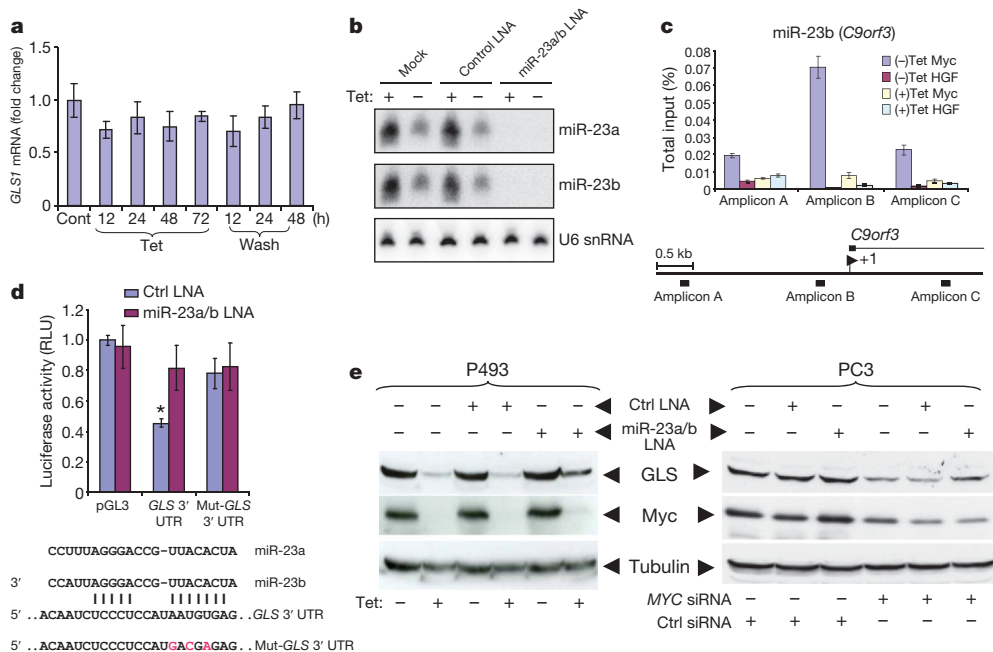


Figure 3 | *Myc* increases *GLS* protein by transcriptionally repressing miR-23a/b that target the *GLS* 3' UTR. **a**, *GLS1* mRNA levels were determined by real-time PCR after treatment of P493 cells with tetracycline or on removal of tetracycline (after 48 h of tetracycline pre-treatment). Data are mean \pm s.d., $n = 3$ PCR reactions. **b**, Northern blot analysis of miR-23a/b expression in P493 cells treated with or without tetracycline for 24 h and then transfected with miR-23a/b LNAs or scrambled control LNA and cultured for 48 h. **c**, Chromatin immunoprecipitation assay with P493 cells showing *Myc* binding to the promoter region of *C9orf3*, whose transcript is processed to miR-23b. The positions of the amplicons are depicted in the cartoon of the *C9orf3* gene below the bar graphs (mean \pm s.d., $n = 3$). Anti-HGF serves as a nonspecific antibody control. **d**, Inhibition of *GLS* 3' UTR luciferase reporter by miR-23a/b. Top: glutaminase reporter (wild-type *GLS*

3' UTR or mutant Mut-*GLS* 3' UTR) or control (pGL3) luciferase constructs were co-transfected with pSV-Renilla into MCF-7 cells, or further co-transfected with miR-23a/b LNAs or control LNA. After 24 h, luciferase activities (relative light units, RLU) were measured. Data shown are RLU normalized to the control group (mean \pm s.d., $n = 4$). Bottom: miR-23a, miR-23b, *GLS* 3' UTR and Mut-*GLS* 3' UTR sequences. **e**, Analysis of *GLS* protein levels in P493 and PC3 cells treated with control or antisense miR-23a/b LNAs. Left: P493 cells were treated with or without tetracycline for 24 h and then transfected with antisense miR-23a/b LNAs or scrambled control LNA. After 72 h, cells were harvested for immunoblot assay. Right: PC3 cells were transfected with *MYC* siRNA or control siRNA. After 24 h, cells were transfected with miR-23a/b LNAs or scrambled control. Cells were cultured for 72 h and then were harvested for immunoblot assay.

control LNAs (Fig. 3d). We next mutated the predicted binding site by a site-directed mutagenesis strategy⁸ and observed that mutant 3' UTR does not inhibit luciferase activity as the wild-type sequence does. Using these reporters in PC3 cells, we observed that diminished expression of Myc via siRNA results in decreased luciferase activity with wild type but not with the mutant 3' UTR reporter (Supplementary Fig. 9). Notably, reduced GLS protein level, a result of decreased Myc expression (Fig. 1c), was rescued by antisense miR-23a/b LNAs (Fig. 3e). The antisense miR-23a/b LNAs also partially rescued the diminished GLS level associated with RNAi-mediated reduction of Myc expression in PC3 cells (Fig. 3e).

We also examined events upstream and downstream of *GLS*²⁴ and found that the glutamine transporter SLC7A5 is induced by Myc in P493-6 cells at the transcriptional level (fivefold by nuclear run-on, with a >7-fold induction of its mRNA level (K.I.Z. and C.V.D., unpublished data). The glutamine transporter ASCT2 (also called SLC1A5) shows a twofold induction by Myc at the mRNA level, whereas glutamate dehydrogenase mRNA levels appear unaltered (K.I.Z. and C.V.D., unpublished data). Furthermore, we found that elevated levels of Myc protein in human prostate cancer correspond to levels of GLS, which are not increased in the accompanying normal tissue from the same patients (Supplementary Fig. 10). Intriguingly, miR-23a and miR-23b are significantly decreased in human prostate cancer as compared with normal prostate tissue²². It is notable that loss of GLS function by antisense suppression significantly inhibits the tumorigenesis of Ehrlich ascites tumour cells *in vivo*²⁵. Our findings uncover a pathway by which Myc suppression of miR-23a/b, which target GLS, enhances glutamine catabolism through increased mitochondrial glutaminase expression. Taken together, these observations provide a regulatory mechanism involving Myc and miRNAs for elevated expression of glutaminase and glutamine metabolism in human cancers.

METHODS SUMMARY

Human cell lines were cultured under standard conditions. Isolation of mitochondria, enrichment for mitochondrial proteins, and proteomic analysis were performed as described^{26–29}. RNA interference experiments and luciferase reporter analysis of miRNA activity were as reported^{8,30}. Flow cytometric analyses of reactive oxygen species, cell death and glutathione level were performed as described^{11,30}. Human samples were acquired with the approval of the Johns Hopkins University School of Medicine Institutional Review Board.

Full Methods and any associated references are available in the online version of the paper at www.nature.com/nature.

Received 20 August 2008; accepted 27 January 2009.

Published online 15 February 2009.

- DeBerardinis, R. J., Sayed, N., Ditsworth, D. & Thompson, C. B. Brick by brick: metabolism and tumor cell growth. *Curr. Opin. Genet. Dev.* **18**, 54–61 (2008).
- Kroemer, G. & Pouyssegur, J. Tumor cell metabolism: cancer's Achilles' heel. *Cancer Cell* **13**, 472–482 (2008).
- DeBerardinis, R. J. *et al.* Beyond aerobic glycolysis: transformed cells can engage in glutamine metabolism that exceeds the requirement for protein and nucleotide synthesis. *Proc. Natl. Acad. Sci. USA* **104**, 19345–19350 (2007).
- Reitzer, L. J., Wice, B. M. & Kennell, D. Evidence that glutamine, not sugar, is the major energy source for cultured HeLa cells. *J. Biol. Chem.* **254**, 2669–2676 (1979).
- Gallagher, F. A., Kettunen, M. I., Day, S. E., Lerche, M. & Brindle, K. M. ¹³C MR spectroscopy measurements of glutaminase activity in human hepatocellular carcinoma cells using hyperpolarized ¹³C-labeled glutamine. *Magn. Reson. Med.* **60**, 253–257 (2008).
- Curthoys, N. P. & Watford, M. Regulation of glutaminase activity and glutamine metabolism. *Annu. Rev. Nutr.* **15**, 133–159 (1995).
- Chang, T. C. *et al.* Widespread microRNA repression by Myc contributes to tumorigenesis. *Nature Genet.* **40**, 43–50 (2008).

- O'Donnell, K. A., Wentzel, E. A., Zeller, K. I., Dang, C. V. & Mendell, J. T. c-Myc-regulated microRNAs modulate E2F1 expression. *Nature* **435**, 839–843 (2005).
- Eilers, M. & Eisenman, R. N. Myc's broad reach. *Genes Dev.* **22**, 2755–2766 (2008).
- Kita, K., Suzuki, T. & Ochi, T. Down-regulation of glutaminase C in human hepatocarcinoma cell by diphenylarsinic acid, a degradation product of chemical warfare agents. *Toxicol. Appl. Pharmacol.* **220**, 262–270 (2007).
- Yuneva, M., Zamboni, N., Oefner, P., Sachidanandam, R. & Lazebnik, Y. Deficiency in glutamine but not glucose induces MYC-dependent apoptosis in human cells. *J. Cell Biol.* **178**, 93–105 (2007).
- Li, F. *et al.* Myc stimulates nuclearly encoded mitochondrial genes and mitochondrial biogenesis. *Mol. Cell. Biol.* **25**, 6225–6234 (2005).
- Schuhmacher, M. *et al.* Control of cell growth by c-Myc in the absence of cell division. *Curr. Biol.* **9**, 1255–1258 (1999).
- Lombardi, L., Newcomb, E. W. & Dalla-Favera, R. Pathogenesis of Burkitt lymphoma: expression of an activated c-myc oncogene causes the tumorigenic conversion of EBV-infected human B lymphoblasts. *Cell* **49**, 161–170 (1987).
- Gurel, B. *et al.* Nuclear MYC protein overexpression is an early alteration in human prostate carcinogenesis. *Mod. Pathol.* **21**, 1156–1167 (2008).
- Perez-Gomez, C. *et al.* Co-expression of glutaminase K and L isoenzymes in human tumour cells. *Biochem. J.* **386**, 535–542 (2005).
- Turner, A. & McGivan, J. D. Glutaminase isoform expression in cell lines derived from human colorectal adenomas and carcinomas. *Biochem. J.* **370**, 403–408 (2003).
- Berns, K., Hijmans, E. M., Koh, E., Daley, G. Q. & Bernards, R. A genetic screen to identify genes that rescue the slow growth phenotype of c-myc null fibroblasts. *Oncogene* **19**, 3330–3334 (2000).
- Nikiforov, M. A. *et al.* Complementation of Myc-dependent cell proliferation by cDNA expression library screening. *Oncogene* **19**, 4828–4831 (2000).
- Lora, J. *et al.* Antisense glutaminase inhibition decreases glutathione antioxidant capacity and increases apoptosis in Ehrlich ascitic tumour cells. *Eur. J. Biochem.* **271**, 4298–4306 (2004).
- Matsuno, T., Satoh, T. & Suzuki, H. Prominent glutamine oxidation activity in mitochondria of avian transplantable hepatoma induced by MC-29 virus. *J. Cell. Physiol.* **128**, 397–401 (1986).
- Porkka, K. P. *et al.* MicroRNA expression profiling in prostate cancer. *Cancer Res.* **67**, 6130–6135 (2007).
- Landgraf, P. *et al.* A mammalian microRNA expression atlas based on small RNA library sequencing. *Cell* **129**, 1401–1414 (2007).
- Bode, B. P. Recent molecular advances in mammalian glutamine transport. *J. Nutr.* **131**, 2475S–2485S (2001).
- Lobo, C. *et al.* Inhibition of glutaminase expression by antisense mRNA decreases growth and tumorigenicity of tumour cells. *Biochem. J.* **348**, 257–261 (2000).
- Rabilloud, T. *et al.* The mitochondrial antioxidant defence system and its response to oxidative stress. *Proteomics* **1**, 1105–1110 (2001).
- Anderson, T. J. *et al.* Discovering robust protein biomarkers for disease from relative expression reversals in 2-D DIGE data. *Proteomics* **7**, 1197–1207 (2007).
- Kersey, P. J. *et al.* The International Protein Index: an integrated database for proteomics experiments. *Proteomics* **4**, 1985–1988 (2004).
- Yates, J. R. III, Eng, J. K., McCormack, A. L. & Schieltz, D. Method to correlate tandem mass spectra of modified peptides to amino acid sequences in the protein database. *Anal. Chem.* **67**, 1426–1436 (1995).
- Gao, P. *et al.* HIF-dependent antitumorigenic effect of antioxidants *in vivo*. *Cancer Cell* **12**, 230–238 (2007).

Supplementary Information is linked to the online version of the paper at www.nature.com/nature.

Acknowledgements The authors want to thank L. Blosser and A. Tam for their help in flow cytometry analysis, and H. Y. Zhang for her help with statistical analysis. This work was partially supported by NIH Awards NHLBI NO1-HV-28180, NCI R01CA051497, NCI R01CA57341, NCI R01CA120185, NCI P50CA58236, Rita Allen Foundation, Leukemia and Lymphoma Society, and Sol Goldman Center for Pancreatic Cancer Research.

Author Contributions P.G., K.K., T.O., A.M.D., J.E.V., J.T.M. and C.V.D. designed experiments. P.G., I.T., T.-C.C., Y.-S.L. and K.I.Z. performed experiments. K.K. and T.O. provided reagents. P.G. and C.V.D. wrote the paper. All authors discussed the results and commented on the manuscript.

Author Information Reprints and permissions information is available at www.nature.com/reprints. Correspondence and requests for materials should be addressed to C.V.D. (cvdang@jhmi.edu) or P.G. (pgao2@jhmi.edu).

METHODS

Cell culture. P493-6 human B lymphoma cells, PC3 human prostate cancer cells, CB33 lymphoblastoid cells, CB33-Myc cells and MCF7 human breast cancer cells were maintained in RPMI 1640 with 10% fetal bovine serum (FBS) and 1% penicillin-streptomycin. HT-29 cells were maintained in McCoy's 5A medium with 10% FBS and 1% penicillin-streptomycin. PC3-GLS1 and control PC3-GFP cells were established by infecting PC3 cells with retroviral supernatants from PQCXIN-GLS1 or PQCXIN-GFP vector-transfected phoenix cells. The cells were selected by and maintained with RPMI 1640 medium containing 500 $\mu\text{g ml}^{-1}$ G418. Experiments under deprived glutamine or glucose culture conditions were performed by using RPMI 1640 without L-glutamine (GIBCO 21870) or RPMI 1640 without D-glucose (GIBCO 11879).

Mitochondrial protein enrichment. To enrich for mitochondrial protein, we adapted protocols as described²⁶. 1×10^9 cells were used for high Myc (no tetracycline treatment) and 1.5×10^9 for tetracycline treated cells. Cells were harvested, washed with cold PBS extensively then washed with cold homogenization buffer (220 mM mannitol, 70 mM sucrose, 2 mM HEPES, pH 7.4 with KOH) to remove PBS. Harvested cell pellets were re-suspended in 8 ml of homogenization buffer with protease inhibitors (Roche), phosphatase inhibitors (EMD Chemicals) and homogenized with 15 strokes by a tight fitting dounce homogenizer. Homogenate was diluted with 60 ml of cold homogenization buffer and centrifuged at 800g for 10 min at 4 °C. The supernatant was collected and centrifuged at 7,000g for 15 min. The resulting pellet was homogenized in 8 ml homogenization buffer, diluted in 60 ml of the same buffer and centrifuged at 800g for 10 min. Supernatant was further centrifuged at 12,000g for 15 min. The mitochondrial pellet after this step was washed once more by re-suspending in 60 ml homogenization buffer and centrifugation for 15 min at 12,000g. Finally, the pellet was re-suspended in 1.5 ml of homogenization buffer, transferred to microcentrifuge tube, centrifuged at 16,000g for 20 min and solubilized in 40 μl of 5% ASB-14 (w/v) and then diluted in an appropriate amount of IEF buffer (8 M urea, 2 M thiourea, 4% w/v CHAPS, 1% w/v dithiothreitol, 0.5% v/v carrier ampholytes pH 4–7, and a trace amount of bromophenol blue) to make 5 mg ml^{-1} protein solution.

Two-dimensional gel electrophoresis and proteomics. Two-dimensional gel electrophoresis and mass spectrometry identification of proteins were performed as described with modifications²⁷. A vMALDI linear ion trap mass spectrometer (vMALDI-LTQ, ThermoElectron) with XCalibur 1.4 SR1 software package was used to perform protein identification. Protein digests were re-suspended in 50% AcCN/0.1% TFA and mixed with an equal volume of 2,5-dihydroxybenzoic acid (2,5-DHB; Laser BioLab) 50 mg ml^{-1} in 50% acetonitrile/0.1% TFA. 0.5 μl of this mixture was spotted on a vMALDI plate. A survey scan from m/z 750 to m/z 4,000 (full MS) was followed by data-dependent MS/MS scans on 30 most intense ions with normalized collision energy value of 40, activation Q value of 0.25, and activation time of 30 ms. Raw data files were searched with BioworkBrowser 3.3 (ThermoElectron) against the IPI human protein sequence database, using search algorithm SEQUEST^{28,29}.

RNAi experiments. siRNAs targeting human *GLS1* (ON-TARGETplus SMARTpool, L-004548-01, target sequences are CCUGAAGCAGUUGGAAUA, CUGAAUAUGUGCAUCGAUA, AGAAAGUGGAGAUCGAAAU and GCACAGACAUGGUUGGUAU), *MYC* (siGENOME SMART pool, J-003282-23, target sequences are ACGGAACUCUUGUGCGUAAUU, GAACACACAA CGUCUUGGAUU, AACGUUAGCUUCACCAACAUU and CGAUGUUGU UUCUGUGGAAUU), or control siRNA (SiControl, D-001210-02, sequence is UAAGGCUAUGAAGAGAUAC) were purchased from Dharmacon Research Inc. Transfection of the siRNAs into P493 or PC3 cells was performed as described previously³⁰.

Knocking-down miR-23a/b with anti-sense LNA oligomers. miRCURY LNA knockdown probes for miR-23a (miRCURY knockdown, 118119-00, target sequence is AUCACAUUGCCAGGGGAUUUCC) and miR-23b (miRCURY knockdown, 138120-00, target sequence is AUCACAUUGCCAGGGGAUU ACC), and for scramble miRNA (miRCURY knockdown, 199002-04, scramble-miR) LNA probes as negative control, were purchased from EXIQON, Inc. The transfection of LNA probes into cells was performed using the same protocol for siRNA transfection as described above.

3' UTR luciferase assays and site-directed mutagenesis. The 3' UTR sequence of human *GLS* was generated by PCR with the following primers: 5'-GCTCTAGACATGTGTATTCTCTCTGTTAGTG-3' and 5'-GCTCTAGACATATCAGCAGATCATCACCATA-3'. The PCR products were digested

with XbaI and then inserted into the PGL3 reporter vector downstream of the luciferase gene. The correct clones were confirmed by sequencing analysis. The mutagenesis of predicted miR-23a/b binding sites (see sequences) was performed using a QuikChange site-directed mutagenesis kit (Stratagene, catalogue number 200519-5) and the following primers: 5'-CAATCTCCCTCCATGACGAGAGCAATATTACCTCG-3' and 5'-GTTAGAGGGAGGTACTGCTCTCGTTATAATGGAGC-3'. For luciferase assay, cells were seeded in 48-well plates. After overnight incubation, cells were co-transfected either with 100 ng reporter vectors and 4 ng pSV-Renilla, or further co-transfected with 10 nM LNA antisense for miR-23a/b or control LNA. After 24 h, luciferase activities were measured using the Dual-Luciferase Reporter Assay System (Promega).

Chromatin immunoprecipitation and real-time PCR. Chromatin immunoprecipitation assay was carried out as described⁷. Chromatin immunoprecipitation primers for *C9orf3* were: amplicon A 5'-ATTCTTCTCTGGCTGTCTTTCC-3', 5'-GAAGCAGCCAATCTGTGGAG-3'; amplicon B 5'-GGAATACTAGGGTACCAGGGCA-3', 5'-GCAGCTTGGCTGGCTAGG-3'; amplicon C 5'-ACTTAGGATCCAATCCACTGTTGAG-3', 5'-CTCAACAGTGGATTGGATCCTAAGT-3'.

For real-time PCR, total RNA was extracted using the RNeasy kit (QIAGEN) followed by DNAase (Ambion) treatment according to the manufacturer's instructions. Primers were designed using Beacon Designer software, and cDNA was prepared using TaqMan Reverse Transcription Reagents (Roche, Applied Biosystems). The primers used were: GLS1-F, 5'-TGGTGGCC TCAGGTGAAAT-3'; GLS1-R, 5'-CCAAGCTAGGTAACAGACCCTGTTT-3'; GLS2-F, 5'-ACGAATCCCCTATCCACAAGTTCA-3'; GLS2-R, 5'-GCAGTCCAGTGGCCTTTAGTG-3'; 18s-F, 5'-CGGCGACGACCCATTCGAAC-3'; 18s-R, 5'-GAATCGAACCCTGATCCCCGTC-3'. Quantitative real-time PCR for GLS1, GLS2 and 18S was performed using the ABI 7500 sequence detection system. All PCRs were performed in triplicate.

Immunoblot analysis. Rabbit antibody for GLS for immunoblots was described previously¹⁰. Rabbit anti-TFAM antibody was a gift from D. Kang. We used monoclonal anti-c-Myc antibody from Santa Cruz (9E10), and mouse antibody for tubulin from CalBiochem (CP06), and performed immunoblot assays according to the manufacturer's instructions.

Northern blot analysis. Northern blotting for miR-23a and miR-23b was performed as described⁷ using Ultrahyb-Oligo (Ambion) and oligonucleotide probes perfectly complementary to the mature miRNA sequences.

Intracellular ATP. ATP levels were measured using a Somatic Cell ATP assay kit (Sigma) according to the manufacturer's instructions. Luminescence was measured using a Wallace microplate luminescence reader (Perkin Elmer) and normalized to the protein concentration.

Flow cytometric measurement of glutathione, ROS and cell death. The measurement of glutathione levels in cells was performed using monobromobimane (Sigma Aldrich) as described previously¹⁹. Intracellular ROS production was measured by staining cells with dichlorodihydrofluorescein diacetate (Molecular Probes). Cell apoptosis was detected using an Annexin V-PE Apoptosis Detection Kit (BD Pharmingen, catalogue number 559763). Stained cells were analysed in FACScan flow cytometers (BD Bioscience).

Measurement of cellular O₂ consumption. Cells were harvested and re-suspended at 1×10^7 per ml in RPMI1640 medium with 10% FBS and 25 mM HEPES buffer. For each experiment, equal numbers of cells suspended in 0.5 ml were pipetted into the chamber of an Oxytherm electrode unit (Hansatech Instrument Ltd), which uses a Clark-type electrode to monitor the dissolved oxygen concentration in the sealed chamber over time. The data were exported to a computerized chart recorder (Oxygraph, Hansatech Instrument Ltd), which calculated the rate of O₂ consumption. The temperature was maintained at 37 °C during the measurement. The O₂ concentration in 0.5 ml of RPMI1640 medium without cells was also measured over time to provide background values. Relative O₂ consumption rate was calculated after correcting for background.

TaqMan microRNA assays. We purchased TaqMan microRNA assay kits for hsa-miR-23a (catalogue number 4373074) and has-miR-23b (catalogue number 4373073) and control probes from Applied Biosystems, and performed real-time PCR assays according to the manufacturer's instructions.

Human prostate cancer samples. Human samples were acquired with the approval of the Johns Hopkins University School of Medicine Institutional Review Board.

LETTERS

piggyBac transposition reprograms fibroblasts to induced pluripotent stem cells

Knut Woltjen¹, Iacovos P. Michael^{1,2}, Paria Mohseni^{1,2}, Ridham Desai^{1,2}, Maria Mileikovsky¹, Riikka Hämäläinen¹, Rebecca Cowling¹, Wei Wang³, Pentao Liu³, Marina Gertsenstein¹, Keisuke Kaji⁴, Hoon-Ki Sung¹ & Andras Nagy^{1,2}

Transgenic expression of just four defined transcription factors (*c-Myc*, *Klf4*, *Oct4* and *Sox2*) is sufficient to reprogram somatic cells to a pluripotent state^{1–4}. The resulting induced pluripotent stem (iPS) cells resemble embryonic stem cells in their properties and potential to differentiate into a spectrum of adult cell types. Current reprogramming strategies involve retroviral¹, lentiviral², adenoviral⁶ and plasmid⁷ transfection to deliver reprogramming factor transgenes. Although the latter two methods are transient and minimize the potential for insertion mutagenesis, they are currently limited by diminished reprogramming efficiencies. *piggyBac* (PB) transposition is host-factor independent, and has recently been demonstrated to be functional in various human and mouse cell lines^{8–11}. The PB transposon/transposase system requires only the inverted terminal repeats flanking a transgene and transient expression of the transposase enzyme to catalyse insertion or excision events¹². Here we demonstrate successful and efficient reprogramming of murine and human embryonic fibroblasts using doxycycline-inducible transcription factors delivered by PB transposition¹³. Stable iPS cells thus generated express characteristic pluripotency markers and succeed in a series of rigorous differentiation assays. By taking advantage of the natural propensity of the PB system for seamless excision¹², we show that the individual PB insertions can be removed from established iPS cell lines, providing an invaluable tool for discovery. In addition, we have demonstrated the traceless removal of reprogramming factors joined with viral 2A sequences¹⁴ delivered by a single transposon from murine iPS lines. We anticipate that the unique properties of this virus-independent simplification of iPS cell production will accelerate this field further towards full exploration of the reprogramming process and future cell-based therapies.

To explore the utility of PB as a vector for somatic cell reprogramming, it was necessary to achieve temporal expression control and transgene silencing, as PB transposons are not purposefully subjected to the same natural silencing process that diminishes retroviral (and less extensively lentiviral) expression¹⁵. The genes for the four mouse factors (*c-Myc*, *Klf4*, *Oct4* and *Sox2*)¹ were transferred into the PB-TET transposon plasmid (hereafter called PB-TET-mF_x; Fig. 1a) under the transcriptional control of the tetO₂ tetracycline/doxycycline inducible promoter¹⁶. All were linked to β geo (a fusion of β -galactosidase and the neomycin resistant gene) through an IRES sequence to allow monitoring the tightness of doxycycline regulation and later demonstration of the reprogrammed cells' capacity for exogenous-factor-independent maintenance. The reverse tetracycline transactivator (rtTA) protein was provided by parental mouse embryonic fibroblasts (rtTA-MEFs) established from 15.5 days post coitum (d.p.c.) ROSA26 rtTA-IRES-GFP knock-in¹⁷ transgenic embryos. rtTA-MEFs were transfected with

circular PB-TET-mF_x plasmid DNA 'cocktails' in conjunction with a PB transposase expression plasmid¹¹. From the time of transfection onwards, fibroblasts were maintained in doxycycline-containing embryonic stem (ES) cell culture conditions without passage. Mouse fibroblasts underwent ES-cell-like colony formation, which resulted in the derivation of self-renewing cell lines displaying key characteristics of reprogramming (Supplementary Fig. 1).

Colonies produced from rtTA-MEFs with PB-TET-mF_x cocktails were scored on the basis of morphology, with early foci formation noted on day 6–8 and colonies forming around day 8–10. These were mostly ES-cell-like (Supplementary Fig. 1a), whereas a handful displayed diverse morphologies (data not shown). Adjusting the doxycycline concentration above or below the standard of 1.5 $\mu\text{g ml}^{-1}$ resulted in subtle declines (150 ng ml^{-1}) or drastic decreases (15 ng ml^{-1} or 15 $\mu\text{g ml}^{-1}$) in colony numbers (Supplementary Fig. 1b), supporting the notion that factor expression level affects reprogramming rates. In the absence of doxycycline, no reprogramming was noted, nor were any cells found positive for alkaline phosphatase staining (data not shown).

Forty-eight PB-TET-mF_x-induced colonies were picked from fibroblast induction fields and passaged on inactivated fibroblast feeder layers. Surviving clones were maintained in doxycycline during establishment, until found to be doxycycline independent in replicate wells. Doxycycline independence occurred as early as day 12 for 3 lines (4D, 4E, 6C), and was achieved by most clones by day 24 (7 out of 39 = 18% on day 15; 21 out of 39 = 54% on day 19; 31 out of 39 = 80% on day 21; 33 out of 39 = 86% on day 23). During establishment, cultures which had not yet achieved autonomous maintenance of reprogramming rapidly flattened and returned to a fibroblast-like state on doxycycline withdrawal (Supplementary Fig. 2a, b) as observed in a prior report⁵. Doxycycline independence was sustained for at least an additional 18 passages, with no apparent disturbance of growth characteristics compared to replica cultures maintained in 1.5 $\mu\text{g ml}^{-1}$ doxycycline. Doubling time and morphology of PB-TET clones were indistinguishable from those of R1 mouse ES cells¹⁸ (data not shown).

Stable reprogramming by exogenous factor expression results in the sequential activation of ES cell markers^{3,5,19}. On day 16 (p2–3, where p indicates passage) the seven doxycycline-independent lines passed the alkaline phosphatase staining criterion (Fig. 1b). These clones tested positive on day 20–22 for the cell-surface marker SSEA1 and nuclear-localized Nanog protein (Fig. 1b). Semi-quantitative reverse transcription polymerase chain reaction (RT-PCR) revealed the expression of ES cell pluripotency markers^{20–22}, such as *Dax1*, *Eras*, *Fbxo*, *Foxd3*, *Nanog*, *Rex1* and *Zfp296* (Supplementary Fig. 2c). Using 3' untranslated region (UTR)-specific reverse primers (Supplementary Table 1), the endogenous counterparts of the four mF_x transgenes were also shown to be active (Fig. 1c).

¹Samuel Lunenfeld Research Institute, Mount Sinai Hospital, Toronto, Ontario M5G 1X5, Canada. ²Department of Molecular Genetics, University of Toronto, Toronto M5S 1A8, Canada. ³The Wellcome Trust Sanger Institute, Wellcome Trust Genome Campus, Hinxton, Cambridgeshire CB10 1SA, UK. ⁴MRC Centre for Regenerative Medicine, Institute for Stem Cell Research, University of Edinburgh, Edinburgh EH9 3JQ, UK.

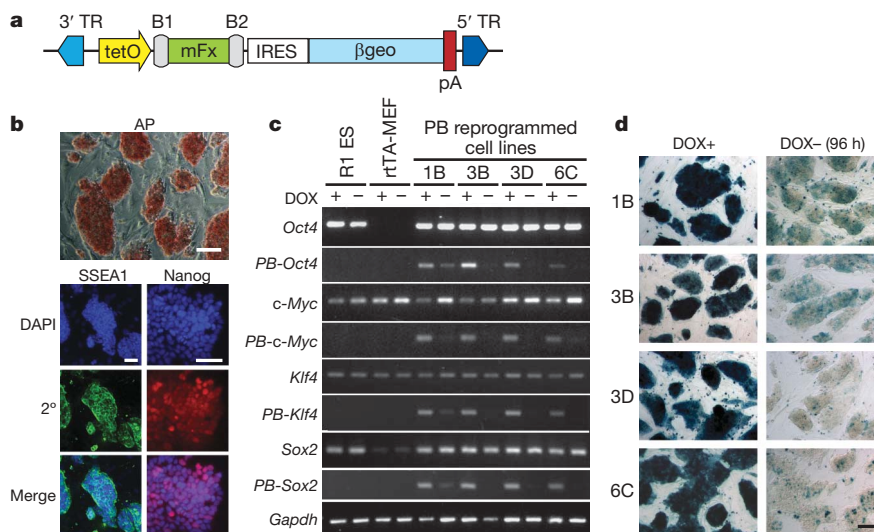


Figure 1 | Cell lines generated by PB-mediated factor transposition are reprogrammed. **a**, The PB-TET transposon vector used to deliver inducible (tetO), reporter-linked (IRES- β geo-pA) mouse factors (mF). 3'/5' TR, PB terminal repeats; B1/B2, post-Gateway cloning sites. **b**, Stable doxycycline-independent cell lines activate alkaline phosphatase (AP), SSEA1 and Nanog. Representative images are from a single cell line (1B). **c**, Doxycycline regulation of PB-delivered factors as monitored by transgene-specific RT-PCR analysis (vector-based reverse primer). Reprogrammed cell lines

PB-TET-reprogrammed clones were screened for LacZ expression to determine general transgene activity in the presence and absence of doxycycline (Fig. 1d). RT-PCR, which allows further distinction of individual transgene activity, revealed variable trace expression levels of some transgenes in the uninduced (dox⁻) state (Fig. 1c). *Oct4* transgene expression could be detected in 1B and to a lesser extent in 3B, and *c-Myc* was maintained minimally in both 1B and 6C. For clones 1B and 3D *Sox2* expression could be detected, whereas *Klf4* appeared silent in all lines except for 1B. Note that RT-PCR detection of *c-Myc*, *Klf4*, *Oct4* and *Sox2* (mF) transcripts reflects average expression levels for each cell population, and does not expose mosaic expression patterns (as revealed in Fig. 1d).

Genomic Southern blot analysis was used to determine transgene copy number in selected doxycycline-independent mouse PB-TET lines (Supplementary Fig. 3a). The average estimated PB transposon copy number was 9, although co-migrating bands which may obscure the exact total could not be ruled out. Line 3D contains only five transposon insertions. As all four PB-TET-mF transgenes are represented in 3D (Fig. 1c), three of the four factors are sufficient in single copy for reprogramming.

Through additional transient transposase expression, we exploited the 'cut' step of transposition to remove the transgenes after complete reprogramming. For clone 1B, a broad range was observed in the mobilization rate for each transposon (Supplementary Figs 3b and 4); transposon 8 was excised only once (1 out of 38 = 2.5%) whereas transposon 9 was excised 11 times (11 out of 38 = 29%). Such high variability suggests that the excision frequency is integration-site-dependent. To simplify complete transgene removal we inserted the MKOS sequence (*c-Myc*, *Klf4*, *Oct4* and *Sox2* ORFs linked with 2A peptide sequences¹⁴) into PB-TET (Fig. 2a). Similar to four-factor reprogramming, induction of rtTA-MEFs with PB-TET-MKOS in the presence of doxycycline yielded colonies after 10–14 days. Out of 48 iPS-cell-like colonies, characterized by pluripotency marker expression and diagnostic Southern analysis (not shown), two single-copy cell lines, designated as scB1 and scC5, were established. Both lines maintained tight regulation of the MKOS reprogramming factors through indirect measurement of the LacZ reporter (Supplementary Fig. 5). Splinkerette PCR¹¹ determined that PB inserted into the first intron of the *Myo1d* gene (chromosome 11)

and controls were grown in the presence (+) or absence (-) of doxycycline for two passages (~96 h). The induction (*Oct4*, *Sox2*) or maintenance (*c-Myc*, *Klf4*) of endogenous gene expression was determined by RT-PCR using 3'-UTR-directed reverse primers. **d**, Residual transgene expression in reprogrammed cell lines visualized as LacZ activity from the transcription-linked β geo reporter gene (Fig. 1a). The level and mosaicism of LacZ after doxycycline withdrawal correlates roughly with basal transcription level detected by RT-PCR. All scale bars are 200 μ m.

in scB1, and into an intragenic region of chromosome 16 in scC5 (Fig. 2b). The insertion events were confirmed by locus-specific genomic PCR (Fig. 2d). For both scB1 and scC5, transient PB transposase expression led to the removal of the linked reprogramming factors in >2% of the exposed cells as estimated by the ratio of LacZ-negative sublines in the presence of doxycycline (Supplementary Fig. 5). Sequence analysis across the original insertion sites revealed that in 10 out of 11 subclones the original transposon integration site was reverted to wild type (Fig. 2c). Complete loss of the PB-TET-MKOS transposon was further confirmed by locus- and transgene-specific genomic PCR revealing subclones which were negative for both genome-transposon junction and internal transposon-specific PCRs (Fig. 2d). Even after the exogenous factors were removed, the endogenous pluripotency genes remained actively expressed (Fig. 2e).

Pluripotency of PB-reprogrammed cell lines (1B, 3D, 6C, scB1 and scC5) was demonstrated by their contribution to chimaera development (Fig. 3a and Supplementary Table 2). Embryos were dissected between 10.5 d.p.c. and 15.5 d.p.c. and scored for GFP fluorescence, indicating contribution of reprogrammed ROSA26-rtTA-IRES-GFP parental MEFs. To reveal chimaeric contribution at the cellular level in tissues representative of the three germ layers we treated recipient dams with doxycycline 20 h before dissection, and then LacZ stained and sectioned embryos (Fig. 3b and Supplementary Table 2). Notably, for cell line 1B, many embryos demonstrated high-level chimaeric contribution despite low-level residual factor expression (Fig. 1c, d), suggesting a threshold that permits differentiation of these cells in the embryonic environment. Pluripotency was stringently confirmed by the production of completely iPS-cell-derived 13.5 d.p.c. embryos (Fig. 3c) via tetraploid embryo complementation assay¹⁸, including germ cell formation detected by Vasa expression²³ in the genital ridge (Fig. 3c). Germ cell formation from iPS cells was also detected in genital ridges of standard diploid chimaeric embryos (Supplementary Fig. 6a). Teratomas containing derivatives from all three embryonic germ layers are additional proof that these cells are pluripotent and able to differentiate to complex tissues (Supplementary Fig. 6b). The chimaeric contribution of iPS cells to postnatal animals (Fig. 3d) is a clear testament to PB transposon-assisted complete reprogramming of fibroblasts to iPS cells (PB-iPS) with the capability of building functional adult tissues.

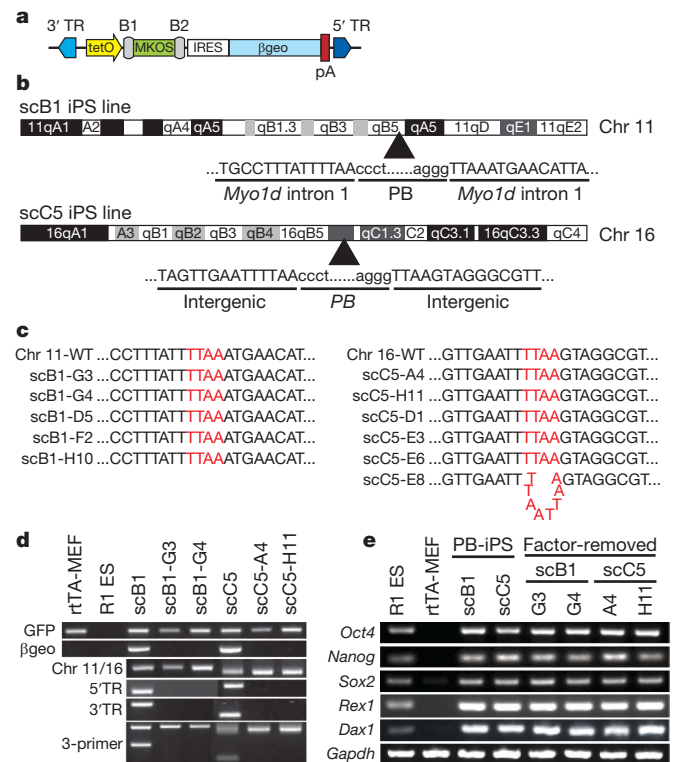


Figure 2 | Seamless factor removal from iPS cells using transposase-stimulated PB excision. **a**, Schematic of the MKOS-containing PB-TET transposon. **b**, Genomic integration site of the individual transposons in scB1 and scC5 lines. Uppercase letters represent flanking genomic sequences whereas lowercase letters are transposon terminal repeat sequences. **c**, Sequence analyses revealed that no mutation was left behind after transposon-mediated removal in most sublines (10 of 11). One single C5 subclone harboured a TTA duplication at the excision site. **d**, Molecular demonstration of transposon removal in representative subclones. From top to bottom: GFP PCR ensures that all cell lines are derivatives of rtTA-MEFs (R1 ES is a negative control); β geo PCR detects the presence of transposons regardless of genomic location; Chr-11- and Chr-16-specific PCR across the TTA tetranucleotide insertion site; 5' and 3' junction PCR; 3-primer PCR for the wild-type allele and the transposon–genome junction. scB1 and scC5 are hemizygous for the transposon and amplify the wild-type allele. **e**, RT-PCR analysis of the single-transposon-induced iPS cell lines and their factor-removed derivatives reveals maintenance of characteristic pluripotency gene expression. R1 ES cells and parental rtTA-MEFs serve as positive and negative controls, respectively.

We successfully used a PB-CAG-rtTA transposon together with PB-TET-mF \times for doxycycline-regulated reprogramming of normal human embryonic fibroblasts. Colonies induced via transposition were picked between day 14 and day 28. Four out of five alkaline-phosphatase-positive clones became doxycycline independent 1 week after isolation. Factor expression in the uninduced state was not detectable by LacZ staining (Supplementary Fig. 7a) and only trace amounts of transcription were detected in colonies by semi-quantitative RT-PCR (Supplementary Fig. 7b). Expression of the endogenous forms of the inducer genes, however, reached levels characteristic of human ES cells (Supplementary Fig. 7b) along with characteristic pluripotency marker genes (Supplementary Fig. 7c) including nuclear-localized NANOG (Supplementary Fig. 8). Spontaneous differentiation after bFGF withdrawal from the medium gave rise to cystic embryoid bodies and to various differentiated cell types, including AFP (endoderm), α SMA and vWF (mesoderm), or β III tubulin and GFAP (ectoderm) positive cells (Supplementary Fig. 9). In accordance to an earlier report²⁴, our observations indicate that mouse factors effectively reprogram human cells, underlining the functional conservation of these transcription factors between the two species.

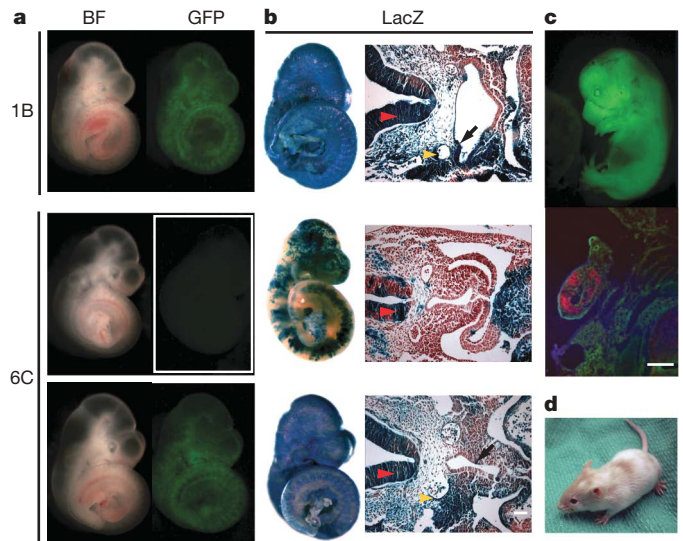


Figure 3 | Cell lines reprogrammed by PB-mediated factor transposition are pluripotent. **a**, Contribution of PB-TET cell lines to embryonic development. Chimaeras dissected at 10.5 d.p.c. with the strongest contribution of PB-iPS-derived cells were easily detected as GFP positive (BF, bright field). **b**, Whole-mount LacZ staining of chimaeric embryos and their sections show contribution of PB-iPS LacZ-positive cells to derivatives of all three embryonic germ layers. Red arrowhead, neural tube (ectoderm); yellow arrowhead, dorsal aorta (mesoderm); black arrow, foregut epithelium (endoderm). **c**, Completely iPS-cell-derived (1B) 13.5 d.p.c. embryo generated by tetraploid embryo complementation. Immunohistochemistry on sections through its genital ridge shows the iPS cell contribution to germ cells (Vasa+, red). **d**, Adult chimaera obtained by aggregating 1B PB-iPS cells with diploid eight-cell-stage ICR (albino) embryos. All scale bars are 100 μ m.

Diploid chimaeras from three mouse iPS cell lines (1B, 6C and 3D) were used to derive secondary MEFs, tracking the iPS-cell-derived component (secondary fibroblast (2 $^{\circ}$ F)/1B, 2 $^{\circ}$ F/6C and 2 $^{\circ}$ F/3D) by GFP expression (Figs 3a and 4). Doxycycline treatment had a marked effect on 2 $^{\circ}$ F/1B and 2 $^{\circ}$ F/6C, which initiated early signs of reprogramming within 2 days, including cellular aggregation (Supplementary Movie). Proliferation also increased markedly, (Fig. 4 and Supplementary Fig. 10a) as initial contribution (10–18% on day 0) reached 90% by day 10. These physical changes were reflected at the molecular level by the activation of alkaline phosphatase (not shown) and SSEA1. The latter showed very rapid activation—detected as early as day 2, expressed by nearly 50% of 2 $^{\circ}$ F/1B and 2 $^{\circ}$ F/6C cells on day 4 and greater than 80% on day 8 (Fig. 4 and Supplementary Fig. 10b). Nanog activation occurred four days earlier (by day 9) in 2 $^{\circ}$ F/1B than in 2 $^{\circ}$ F/6C (Supplementary Fig. S11), highlighting clonal variation and flexibility in the reprogramming process. Overall, PB-iPS-cell-derived fibroblasts displayed a much more rapid initial response to reprogramming factor induction than that previously reported for the doxycycline-inducible lentivirus system²⁵, which may reflect a high level of instability for lentivirus-inserted transgene expression. Single-cell sorting of 2 $^{\circ}$ F/6C cells into 96-well plates revealed that 56 of 192 single cells (29%) were capable of forming colonies. Thirty-nine out of forty-four (89%) established single-cell clones evaluated for Nanog expression were found positive on day 13 of induction. In contrast, line 2 $^{\circ}$ F/3D was inefficient at secondary iPS cell production, as few doxycycline-induced colonies formed and expression of alkaline phosphatase and SSEA1 was delayed (not shown). The PB-TET-Oct4 transgene was noticeably less active in 2 $^{\circ}$ F/3D as compared to 2 $^{\circ}$ F/1B and 2 $^{\circ}$ F/6C (Supplementary Fig. 10c), signifying the need for a sufficient level of Oct4 expression even in secondary iPS cell induction.

Successful transposon-based reprogramming of fibroblasts to iPS cells represents a significant advance in current methods of transgene delivery. First, PB transposition permits technical simplification and

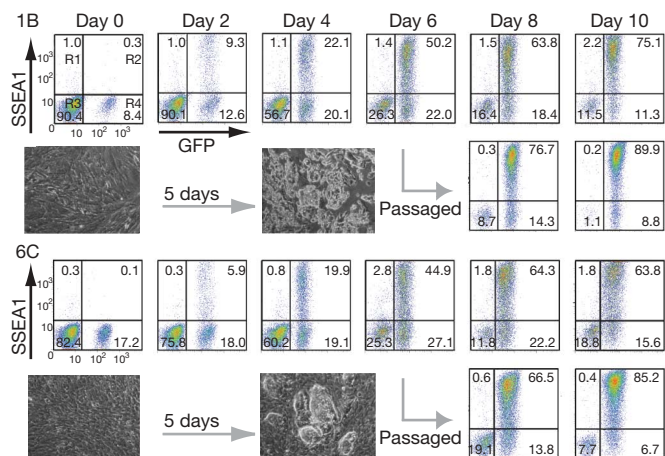


Figure 4 | Properties of secondary fibroblast reprogramming.

Fluorescence-activated cell sorting (FACS) analysis establishing the dynamics of SSEA1 activation in 2^oF/1B and 2^oF/6C cell lines. The inset shows colony formation as early as day 5. On day 6 of reprogramming gene induction, the cultures were also passed by standard trypsinization and analysed in parallel to eliminate the negative effect of cell overgrowth.

improved accessibility of reprogramming methodology by making use of effortless plasmid DNA preparation and commercial transfection products for delivery. This eliminates the need for specialized biohazard containment facilities or the production of high-titre, limited-lifetime viral stocks²⁶. Second, the range of somatic cell types that could be used for reprogramming is not limited by a decreased susceptibility to viral infection²⁶. Third, PB-mediated delivery will allow the option of xeno-free production of human iPS cells contrary to current viral production protocols that use xenobiotic conditions. Finally, accurate transgene removal through transposase expression has been demonstrated in various cell lines^{8,11,12,27–29}. We have harnessed this potential and show here that the reprogramming factors can be removed without a trace from iPS cells once exogenous expression becomes dispensable. These four key characteristics of PB transgenesis mark important advances towards achieving clinically acceptable methods of deriving reprogrammed cells. Complementary, secondary fibroblasts or alternative secondary cell types with a combinatorial removal of proven reprogramming transgene insertions may provide an enormously powerful tool for high-throughput screening to explore further the mechanisms that have roles in the reprogramming process.

METHODS SUMMARY

PB expression vectors were generated using standard cloning procedures, whereas reprogramming factors were shuttled from retroviral sources using Gateway cloning (Invitrogen). Plasmid DNA for fibroblast transfection was prepared using a QIAprep Spin Miniprep Kit (Qiagen).

MEFs were isolated from 15.5 d.p.c. ROSA26 knock-in rTA-IRES-GFP¹⁷ embryos. HEFs were derived from 12-week abortions. Fibroblasts were seeded in ES media at 1.25×10^5 cells per 10 cm^2 (MEFs) or 6.25×10^4 cells per 10 cm^2 (HEFs) and transfected with PB-mF_x transposon vectors and PB transposase expression plasmid 24 h later. For PB-TET-mF_x transfections, expression was induced with $1.5\ \mu\text{g ml}^{-1}$ doxycycline the following day. Forty-eight hours after transfection, cells were fed with fresh ES media daily without passage. The resulting colonies were picked on day 10–12. iPS clones were maintained on inactivated feeders, or gelatin-coated dishes.

LacZ staining was performed overnight on 0.25% glutaraldehyde-fixed cells. Alkaline phosphatase staining was done according to the manufacturer's specifications (Vector Labs). RT-PCR used cDNA prepared with the QuantiTect Reverse Transcription Kit (Qiagen). Southern blotting was carried out using standard methods and DIG-labelled probes for immunodetection (Roche). Immunostaining was performed on cells grown and fixed on chambered slides (Nunc) or 4-well dishes. Flow cytometry used live cells stained with SSEA1.

Mouse PB-TET clones were grown in the absence of doxycycline for at least three passages before aggregation with diploid or tetraploid Hsd:ICR(CD-1) or diploid C57BL/6 host embryos³⁰. The prenatal embryos were dissected, scored

for GFP and then further processed to perform immunohistochemistry or to derive secondary MEFs. Embryos prepared for LacZ staining and sectioning were treated with doxycycline *in utero* 20 h before dissection. Teratoma formation using PB-TET clones was performed as previously described¹. Differentiation of human iPS was spontaneous on Matrigel following plating of embryoid bodies formed in AggreWell (SCI) dishes.

Full Methods and any associated references are available in the online version of the paper at www.nature.com/nature.

Received 6 November 2008; accepted 12 February 2009.

Published online 1 March 2009.

- Takahashi, K. & Yamanaka, S. Induction of pluripotent stem cells from mouse embryonic and adult fibroblast cultures by defined factors. *Cell* **126**, 663–676 (2006).
- Maherali, N. *et al.* Directly reprogrammed fibroblasts show global epigenetic remodeling and widespread tissue contribution. *Cell Stem Cell* **1**, 55–70 (2007).
- Okita, K., Ichisaka, T. & Yamanaka, S. Generation of germline-competent induced pluripotent stem cells. *Nature* **448**, 313–317 (2007).
- Meissner, A., Wernig, M. & Jaenisch, R. Direct reprogramming of genetically unmodified fibroblasts into pluripotent stem cells. *Nature Biotechnol.* **25**, 1177–1181 (2007).
- Brambrink, T. *et al.* Sequential expression of pluripotency markers during direct reprogramming of mouse somatic cells. *Cell Stem Cell* **2**, 151–159 (2008).
- Stadtfield, M., Nagaya, M., Utikal, J., Weir, G. & Hochedlinger, K. Induced pluripotent stem cells generated without viral integration. *Science* **322**, 945–949 (2008).
- Okita, K., Nakagawa, M., Hyenjong, H., Ichisaka, T. & Yamanaka, S. Generation of mouse induced pluripotent stem cells without viral vectors. *Science* **322**, 949–953 (2008).
- Ding, S. *et al.* Efficient transposition of the piggyBac (PB) transposon in mammalian cells and mice. *Cell* **122**, 473–483 (2005).
- Wu, S. C. *et al.* piggyBac is a flexible and highly active transposon as compared to sleeping beauty, Tol2, and Mos1 in mammalian cells. *Proc. Natl Acad. Sci. USA* **103**, 15008–15013 (2006).
- Cadinanos, J. & Bradley, A. Generation of an inducible and optimized piggyBac transposon system. *Nucleic Acids Res.* **35**, e87 (2007).
- Wang, W. *et al.* Chromosomal transposition of PiggyBac in mouse embryonic stem cells. *Proc. Natl Acad. Sci. USA* **105**, 9290–9295 (2008).
- Fraser, M. J., Ciszczon, T., Elick, T. & Bauser, C. Precise excision of TTAA-specific lepidopteran transposons piggyBac (IFP2) and tagalong (TFP3) from the baculovirus genome in cell lines from two species of Lepidoptera. *Insect Mol. Biol.* **5**, 141–151 (1996).
- Cary, L. C. *et al.* Transposon mutagenesis of baculoviruses: analysis of *Trichoplusia ni* transposon IFP2 insertions within the FP-locus of nuclear polyhedrosis viruses. *Virology* **172**, 156–169 (1989).
- Kaji, K. *et al.* Virus-free induction of pluripotency and subsequent excision of reprogramming factors. *Nature* doi:10.1038/nature07864 (this issue).
- Ellis, J. Silencing and variegation of gammaretrovirus and lentivirus vectors. *Hum. Gene Ther.* **16**, 1241–1246 (2005).
- Agha-Mohammadi, S. *et al.* Second-generation tetracycline-regulatable promoter: repositioned tet operator elements optimize transactivator synergy while shorter minimal promoter offers tight basal leakiness. *J. Gene Med.* **6**, 817–828 (2004).
- Belteki, G. *et al.* Conditional and inducible transgene expression in mice through the combinatorial use of Cre-mediated recombination and tetracycline induction. *Nucleic Acids Res.* **33**, e51 (2005).
- Nagy, A., Rossant, J., Nagy, R., Abramow-Newerly, W. & Roder, J. C. Derivation of completely cell culture-derived mice from early-passage embryonic stem cells. *Proc. Natl Acad. Sci. USA* **90**, 8424–8428 (1993).
- Stadtfield, M., Maherali, N., Breault, D. T. & Hochedlinger, K. Defining molecular cornerstones during fibroblast to iPS cell reprogramming in mouse. *Cell Stem Cell* **2**, 230–240 (2008).
- Kaji, K. *et al.* The NuRD component Mbd3 is required for pluripotency of embryonic stem cells. *Nature Cell Biol.* **8**, 285–292 (2006).
- Kim, J. B. *et al.* Pluripotent stem cells induced from adult neural stem cells by reprogramming with two factors. *Nature* **454**, 646–650 (2008).
- Mikkelsen, T. S. *et al.* Dissecting direct reprogramming through integrative genomic analysis. *Nature* **454**, 49–55 (2008).
- Fujiwara, Y. *et al.* Isolation of a DEAD-family protein gene that encodes a murine homolog of *Drosophila* vasa and its specific expression in germ cell lineage. *Proc. Natl Acad. Sci. USA* **91**, 12258–12262 (1994).
- Huangfu, D. *et al.* Induction of pluripotent stem cells from primary human fibroblasts with only Oct4 and Sox2. *Nature Biotechnol.* **26**, 1269–1275 (2008).
- Wernig, M. *et al.* A drug-inducible transgenic system for direct reprogramming of multiple somatic cell types. *Nature Biotechnol.* **26**, 916–924 (2008).
- Takahashi, K., Okita, K., Nakagawa, M. & Yamanaka, S. Induction of pluripotent stem cells from fibroblast cultures. *Nature Protocols* **2**, 3081–3089 (2007).
- Dafa'alla, T. H. *et al.* Transposon-free insertions for insect genetic engineering. *Nature Biotechnol.* **24**, 820–821 (2006).

28. Wilson, M. H., Coates, C. J. & George, A. L. Jr. PiggyBac transposon-mediated gene transfer in human cells. *Mol. Ther.* **15**, 139–145 (2007).
29. Mitra, R., Fain-Thornton, J. & Craig, N. L. piggyBac can bypass DNA synthesis during cut and paste transposition. *EMBO J.* **27**, 1097–1109 (2008).
30. Nagy, A. *Manipulating the Mouse Embryo: A Laboratory Manual* 3rd edn (Cold Spring Harbor Laboratory Press, 2003).

Supplementary Information is linked to the online version of the paper at www.nature.com/nature.

Acknowledgements We thank J. Moffat for time-lapse image acquisition, P.-A. Pentilla for cell sorting, M.-S. Eiyomo for assisting with initial PB test vector construction, J. Ure and M. Kownacka for technical assistance, M. Kibschull for establishing human embryonic fibroblasts, A. Cheung for discussions, and K. Vintersten for critical reading of the manuscript. This work was supported by the Wellcome Trust to P.L., and grants awarded to A.N. from the Canadian Stem Cell Network and JDRF.

Author Contributions K.W. designed the experiments, cloned the transposon vectors, isolated and transfected fibroblasts, cultured mouse PB-iPS lines, performed alkaline phosphatase, LacZ and immunostaining, FACS analysis,

dissected embryos, prepared DNA and performed Southern blotting, collected, analysed and interpreted data, and wrote the manuscript. I.P.M. designed experiments and assisted with initial cloning. P.M. and R.D. isolated fibroblasts, and assisted with cell culture, immunostaining and embryo dissections. M.M. transfected human fibroblasts, cultured human PB-iPS lines, performed alkaline phosphatase staining, immunostaining and differentiation assays. R.H. and K.W. performed the single transposon reprogramming studies and the removal of factors from iPS cells. R.C. carried out RT-PCR reactions. W.W. and P.L. provided the *PB-PGK-neo-bpA* and pCyl43 transposase plasmids, and guidelines for their use. M.G. generated and coordinated the iPSC chimaera production. K.K. performed immunostaining on induced secondary fibroblasts. H.-K.S. and I.P.M. performed teratoma assays and collected microscopy images. A.N. was responsible for the project concept, supervised the experiment design and data interpretation, and wrote the manuscript. All authors were involved in initial project design, discussed the results and contributed to the manuscript preparation.

Author Information Reprints and permissions information is available at www.nature.com/reprints. Correspondence and requests for materials should be addressed to A.N. (nagy@lunenfeld.ca).

METHODS

Plasmid vector construction. PB-TET was constructed by exchanging the 5'/3'-TR-flanked *PGK-neo* cassette of *PB-PGK-neo-bpA*¹¹ with a blunt NotI/HindIII fragment containing tetO₂ (provided by S. Mohammadi) via digestion with NheI and HindIII (both polished), resulting in PB-tetO₂. The NheI and SalI (polished) IRES- β geo-bpA element from pIFS (provided by J. Dixon) was ligated into PB-tetO₂ prepared by NheI and SmaI digestion to yield PB-tetO₂-IRES- β geo. Finally, a Gateway RfA cassette (Invitrogen) maintained in the polished NotI site of pBluescriptKS+ (Stratagene) was inserted by digestion with SacII and SpeI into PB-tetO₂-IRES- β geo digested with SacII and NheI. For PB-CAG, the *PGK-neo* cassette was removed by digestion with NheI (polished) and HindIII and replaced with a CBA-RfA-r β gpA cassette released by OsiI and HindIII digestion from a constitutive gene expression construct (I.P.M., K.W. and A.N., unpublished data). The four reprogramming factors were Gateway cloned from retroviral backbones (Addgene) into the PB-TET transposon vector using pDONR221 (Invitrogen) as an intermediate. The Tet transactivator was amplified from pTet-On Advanced (Clontech) using *attB1/2* primers (Supplementary Table 2) and similarly Gateway cloned into PB-CAG. The MKOS element from pCAG2LMKOSimO (ref. 14) was cloned into pENTR2B using EcoRI before Gateway shuttling. The Tet transactivator was amplified from pTet-On Advanced (Clontech) using *attB1/2* primers (Supplementary Table 1). **Fibroblast isolation.** 15.5 d.p.c. ROSA26-rTA-IRES-GFP embryos (from *Gt(ROSA)26So^{tm1.1}(rtTA,EGFP)^{Ng}*) were decapitated, eviscerated, dissociated with 0.25% trypsin, 0.1% EDTA and plated in DMEM, 10% FBS, penicillin-streptomycin and glutamax. HEFs were isolated from 12-week-old abortuses and maintained in DMEM, 15% human serum, 10 ng ml⁻¹ bFGF, penicillin-streptomycin, glutamax, β -mercaptoethanol and NEAA.

PB transfection and cell culture. MEFs were seeded in DMEM, 15% FBS, penicillin-streptomycin, glutamax, β -mercaptoethanol, sodium-pyruvate, non-essential amino acids and LIF on gelatinized (0.1%) 6-well dishes at a density of 1.25×10^5 cells per 10 cm². After 24 h culture, FugeneHD (Roche) was used to transfect cells with 10 ng, 100 ng, or 400 ng of each mF_x transposon (25 ng, 50 ng, or 100 ng for PB-TET-MKOS) plus 100 ng of pCyl43 PB transposase plasmid¹¹ (normalized to 2 μ g total DNA with empty pBluescriptKS+) at a Fugene:DNA ratio of 8 μ l:2 μ g. After 24 h, the media was supplemented with doxycycline (day 0), and changed entirely 48 h after transfection. Cells were fed daily with doxycycline-containing media (1.5 μ g ml⁻¹, unless otherwise indicated). Colonies were picked in 96-well format over days 10–14 and cultivated on mitomycin-c-arrested MEFs. For PB-TET induced clones, doxycycline treatment was maintained until day 16–24. iPS cells for DNA or RNA preparation were grown on gelatin. Established iPS cells were passaged 1:6 every 48 h. Transfection of HEFs was performed similarly, except fibroblasts were initially seeded in DMEM supplemented with 15% human serum, 10 ng ml⁻¹ bFGF, penicillin-streptomycin, glutamax and non-essential amino acids at a density of 6.25×10^4 cells per 10 cm², and grown in HEScGRO (Millipore) 48 h after transfection. Doxycycline (1.5 μ g ml⁻¹) was added 24 h after transfection and withdrawn a week after picking. Colonies were initially passaged mechanically 1:2, and later with TripLE Select (Invitrogen) 1:4 every 7 days. Human iPS cells were maintained on inactivated MEFs in KO-DMEM, 20% serum replacement, 10 ng ml⁻¹ bFGF, penicillin-streptomycin, glutamax and non-essential amino acids.

Southern blotting. Ten micrograms of genomic DNA from R1 ES cells, PB-iPS lines or rtTA-MEFs was digested with BamHI overnight, resolved by gel electrophoresis, and transferred to Hybond N+ (GE Healthcare). A *neo* probe PCR fragment prepared with DIG High Prime DNA Labelling and Detection Kit II (Roche) was used to detect transposon insertions (~25 ng probe per ml hybridization solution).

Splinkerette, genomic and RT-PCR. Splinkerette PCR to determine PB genomic integration sites was performed as described¹¹. TA-cloned PCR products were sequenced bidirectionally with M13 forward and reverse primers. PB insertion loci were determined using BLAST. Genomic PCR on factor-removed PB-iPS lines was performed using primers described in Supplementary Table 1. Approximately 100 ng of genomic template DNA was amplified using Qiagen Taq (Qiagen) with the inclusion of Q-Solution. Highly repetitive sequences on chromosome 16 required nested PCR. Three-primer PCR amplification used PB-3F in conjunction with the chromosome-specific primer set. Standard PCR conditions were: 95 °C for 30 s, 55 °C for 30 s, 72 °C for 45 s; $\times 35$ cycles. RNA was collected using the RNeasy Mini Kit (Qiagen), quantified and treated with gDNA

WipeOut and cDNA prepared with the QuantiTect Reverse Transcription Kit (Qiagen). For each RT-PCR reaction, we used 50–100 ng of cDNA and primers listed in Supplementary Table 1. Standard PCR conditions were: 94 °C for 30 s, 58–62 °C for 30 s, 72 °C for 15–30 s; $\times 30$ –35 cycles.

PB transgene removal. Stable PB-TET clones were transiently transfected with pCyl43 transposase (2 μ g DNA:8 μ l FugeneHD). After puromycin (1 μ g ml⁻¹) treatment for 3 days to eliminate non-transfected cells, the cells were plated at clonal density (~500–1,000 cells per 60 cm²) on inactivated MEFs. Clones were picked after 5 days further culture.

LacZ/alkaline phosphatase staining. Cells and embryos were fixed with 0.25% glutaraldehyde, rinsed in wash buffer (2 mM MgCl₂, 0.01% sodium deoxycholate, and 0.02% Nonidet-P40 in PBS) and stained overnight (~16 h) in LacZ staining solution: 20 mM MgCl₂, 5 mM K₃Fe(CN)₆, 5 mM K₄Fe(CN)₆ and 1 mg ml⁻¹ X-gal in PBS. Embryos were embedded in paraffin, sectioned and counterstained with neutral red. Staining for alkaline phosphatase activity was performed on cells without fixation using the Vector Red Kit (Vector Labs).

Immunostaining and flow cytometry. Cells were grown on inactivated MEFs on gelatin-coated Lab-Tek borosilicate glass slides (Nunc) or 4-well dishes containing gelatinized or Matrigel-treated glass coverslip inserts. Samples were washed with PBS, fixed in 4% PFA/PBS for 10 min at 25 °C, permeabilized with 0.3% Triton X-100 in PBS for 10 min at 25 °C, blocked in 5% goat serum for 1 h, and primary antibody was added overnight at 4 °C (mNanog, AB5731, Chemicon, 1:1,000; hNanog, 0002P-F, ReproCell, 1:200; SSEA1, SSEA4, Tra1-60, Tra1-81, 1:5, provided by P. Andrews; muscle actin, M0635, DakoCytomation, 1:100; β III-tubulin, TU-20, Millipore, 1:100; HNF-3 β , sc-9187, Santa Cruz, 1:100; GFAP, Z0334, DakoCytomation, 1:200; AFP, MAB1369, R&D Systems, 1:200; vWF, A 0082, DakoCytomation, 1:200). Samples were washed in PBS and secondary antibody (cy3 IgG, 1:1,000; Alexa488 IgG or IgM, 1:400; Alexa594 IgG, 1:200) was added for 1 h at 25 °C. After washing, samples were mounted in Vectashield with DAPI (Vector Labs). Genital ridges were pre-fixed with 4% paraformaldehyde in PBS for 1 h at 25 °C, embedded and cryosectioned at 30 μ m thickness, washed, blocked and incubated overnight at 4 °C with rabbit anti-primordial germ cell marker (DDX4/MVH, ab13840, abcam, 1:400). Sections were washed in PBS and secondary antibody (cy3 IgG, 1:500) was added for 2 h at 25 °C. Immunofluorescence was visualized and acquired using a Zeiss LSM 510 confocal microscope. Doxycycline-induced fibroblast pools from PB-iPS chimaeric mice were diluted to ~15% GFP positive 2^F/1B and 2^F/6C representation with wild-type ICR MEFs before seeding. Cells were washed once in PBS containing 5% FBS, incubated with anti-SSEA1 antibody (1:200) for 30 min on ice, washed twice in PBS:5% FBS, incubated with Alexa647-conjugated secondary antibody for 30 min on ice, washed twice and resuspended in PBS:5% FBS for analysis on a FACS-Calibur. Single GFP-positive cell plating from PB-iPS chimaeric MEF pools was done with a FACS-Aria.

In vitro differentiation assays. Human PB-iPS lines were dissociated and used to generate embryoid bodies by aggregation in AggreWell 400 plates (StemCell Technologies) in 15% FBS DMEM with all additives except LIF and bFGF, in the absence of doxycycline. After 14 days growth, embryoid bodies were plated on Matrigel-coated coverslips or 4 chamber slides. Immunohistochemistry was performed after an additional 10 days culture.

Teratoma formation. Cell lines were suspended in DMEM containing 10% FBS, and 100 μ l (1×10^6 cells) injected subcutaneously into both dorsal flanks of nude mice (CByJ.Cg-Foxn1nu/J) anaesthetized with isoflurane. Six weeks after injection, teratomas were dissected, fixed overnight in 10% buffered formalin phosphate and embedded in paraffin. Sections were stained with haematoxylin and eosin.

Generation of chimaeras. Doxycycline-independent PB-TET iPS clones were collected as cell clumps of ~8–15 cells from gelatinized dishes by gentle trypsinization. For diploid chimaeras, 2.5 d.p.c. Hsd:ICR(CD-1) or C57BL/6 embryos were aggregated with PB-iPS cell clumps, and cultured overnight at 37 °C in 5% CO₂ in KSOM medium (Millipore). For tetraploid embryo complementation, two-cell-stage Hsd:ICR(CD-1) embryos (1.5 d.p.c.) were electrofused with a CF-150B Pulse Generator (BLS) and cultured overnight, and aggregated as described above. All embryos were transferred into pseudopregnant recipient ICR females 24 h later³⁰. Dissected embryos were examined for GFP using a Leica MZ16 FA stereomicroscope, or left to term to verify coat colour contribution. For LacZ detection, pregnant dams were treated with doxycycline (1.5 μ g ml⁻¹ doxycycline; 5% sucrose in water) 20 h before dissection.

Virus-free induction of pluripotency and subsequent excision of reprogramming factors

Keisuke Kaji¹, Katherine Norrby¹, Agnieszka Paca¹, Maria Mileikovsky², Paria Mohseni^{2,3} & Knut Woltjen²

Reprogramming of somatic cells to pluripotency, thereby creating induced pluripotent stem (iPS) cells, promises to transform regenerative medicine. Most instances of direct reprogramming have been achieved by forced expression of defined factors using multiple viral vectors^{1–7}. However, such iPS cells contain a large number of viral vector integrations^{1,8}, any one of which could cause unpredictable genetic dysfunction. Whereas *c-Myc* is dispensable for reprogramming^{9,10}, complete elimination of the other exogenous factors is also desired because ectopic expression of either Oct4 (also known as Pou5f1) or Klf4 can induce dysplasia^{11,12}. Two transient transfection-reprogramming methods have been published to address this issue^{13,14}. However, the efficiency of both approaches is extremely low, and neither has been applied successfully to human cells so far. Here we show that non-viral transfection of a single multiprotein expression vector, which comprises the coding sequences of *c-Myc*, *Klf4*, *Oct4* and *Sox2* linked with 2A peptides, can reprogram both mouse and human fibroblasts. Moreover, the transgene can be removed once reprogramming has been achieved. iPS cells produced with this non-viral vector show robust expression of pluripotency markers, indicating a reprogrammed state confirmed functionally by *in vitro* differentiation assays and formation of adult chimaeric mice. When the single-vector reprogramming system was combined with a *piggyBac* transposon^{15,16}, we succeeded in establishing reprogrammed human cell lines from embryonic fibroblasts with robust expression of pluripotency markers. This system minimizes genome modification in iPS cells and enables complete elimination of exogenous reprogramming factors, efficiently providing iPS cells that are applicable to regenerative medicine, drug screening and the establishment of disease models.

Efficient multiprotein expression has been reported in a variety of cell types, including human embryonic stem (ES) cells, using the 2A peptide sequence of foot and mouth disease virus (F2A) or 2A-like sequences from other viruses^{17,18}. Recently, this multiprotein expression strategy has also been applied for reprogramming with transient transfection¹⁴ and a doxycycline (dox)-inducible lentiviral vector^{19,20}. Here we have taken advantage of the strategy to generate virus-free, factor-removable iPS cells using a single plasmid with a 2A-peptide-linked reprogramming cassette, *c-Myc-Klf4-Oct4-Sox2* (MKOS)-*IRES-mOrange*, flanked by *loxP* sites, pCAG2LMKOSimO (Supplementary Fig. 1). Initially we investigated whether the 2A-peptide-mediated multiprotein expression could achieve robust expression of *c-Myc*, *Klf4*, *Oct4* and *Sox2* when transcribed from the ubiquitously expressed synthetic CAG enhancer/promoter²¹. When a vector pCAGMKOSiE, which carries the same 2A-peptide-linked MKOS reprogramming cassette, was transfected into HEK293 cells, expression of *Klf4*, *Oct4* and *Sox2* could be detected by immunoblotting (Supplementary Fig. 2a). Whereas high expression of

endogenous *c-Myc* in HEK293 cells precluded clear identification of exogenous *c-Myc*, a phosphorylated form at Thr58 that was subjected to subsequent ubiquitination²² was enriched in the transfectants, indicating that excess *c-Myc* was degraded (Supplementary Fig. 2a, b). Appropriate nuclear localization of exogenous Oct4 and Sox2 was also observed in the transfected HEK293 cells (Supplementary Fig. 2c).

When the vector pCAG2LMKOSimO was introduced into mouse embryonic fibroblasts (MEFs), some mOrange-positive cells converted to an ES-cell-like morphology at day 5–6, and by day 9 colonies containing alkaline-phosphatase-positive cells appeared (data not shown). Moreover, morphologically ES-cell-like colonies picked between days 20 and 30 succeeded to grow maintaining an ES-cell-like morphology on gelatin (Supplementary Fig. 3a). We then went on to estimate the reprogramming efficiency using Nanog reactivation as a marker of reprogramming^{3,4}. MEFs from TNG mice, which have a green fluorescent protein (GFP) reporter inserted at the Nanog start codon²³, and MEFs from wild-type 129 mice were transfected with the pCAG2LMKOSimO plasmid and cultured on either irradiated MEFs or gelatin. The number of transiently transfected mOrange-positive cells was measured by flow cytometry at day 2. The number of reprogrammed colonies judged by GFP positivity (TNG MEFs) or anti-Nanog immunofluorescence (129 MEFs) (Supplementary Fig. 3b) was scored on day 28 (Table 1). By comparing stable transfection efficiency with nucleofection (3.6% of transiently transfected cells, see Supplementary Fig. 3c for details) and the number of reprogrammed colonies, we calculated overall reprogramming efficiency to be an average of 2.5% (Supplementary Table 1). Although the estimation method is different from that used in viral reprogramming systems (efficiency of ~0.1%^{2,3,7}), this relatively high efficiency may depend on several factors in this non-viral method, including expression of the four reprogramming factors from a single transcript and use of the CAG enhancer/promoter, which may be less prone to silencing.

Stable cell lines were established by picking colonies derived from transfection of 129 MEFs (8 out of 12 morphologically ES-cell-like colonies picked) and TNG MEFs (5 out of 9 GFP-positive colonies picked) with pCAG2LMKOSimO. We examined the expression of the reprogramming factors in eight cell lines, imO1–imO8. All cell lines showed robust reactivation of endogenous *Oct4* and *Sox2*, comprising most of total *Oct4* and *Sox2* transcripts detected by common primers for endogenous and exogenous cDNAs (Fig. 1a). Endogenous *c-Myc* expression, which was higher in MEFs than in ES cells, became similar to levels in ES cells in all cell lines, whereas there was no large change in endogenous *Klf4* expression levels (Fig. 1a). Total *c-Myc* and *Klf4* expression were high relative to expression in ES cells, but total *Oct4* and *Sox2* expression were not, although the exogenous transcript encodes all four genes. This observation could be explained by the fact

¹MRC Centre for Regenerative Medicine, Institute for Stem Cell Research, University of Edinburgh, Edinburgh EH9 3JQ, UK. ²Samuel Lunenfeld Research Institute, Mount Sinai Hospital, Toronto, Ontario M5G 1X5, Canada. ³Department of Molecular Genetics, University of Toronto, Toronto, Ontario M5S 1A8, Canada.

Table 1 | Nucleofection conditions and number of Nanog-GFP/Nanog-positive colonies

Nucleofection condition				Two days after nucleofection			Number of Nanog-GFP/Nanog-positive colonies at day 28	
Mice	Experiment number	Passage number	DNA (μ g)	Cells per well	mOrange-positive (%)	Positive cells per well	On γ MEFs	On gelatin
TNG	1	4	2	100,000	8.2	8,200	—	6
	2	3	2	35,000	13.3	4,655	—	3.5*
129	1	3	2	30,000	21.0	6,300	—	3.3†
	2	4	2	20,000	18.6	3,720	6	2
	3	5	5	50,000	10.4	5,200	8	1
	4	5	10	50,000	12.0	6,000	7	6

2×10^6 MEFs from TNG or 129 mice (passage number is shown) were transfected using the indicated amount of linearized DNA in each experiment. mOrange-positive cell number at day 2 was estimated from the collected cell number from one well and the percentage of mOrange-positive cells. The number of Nanog-GFP colonies from TNG MEFs or Nanog-positive colonies (by immunofluorescence) from 129 MEFs at day 28 on irradiated MEFs (γ MEFs) or on gelatin is shown.

—, no data; *, average of two wells; †, average of three wells.

that the expression level of *c-Myc* and *Klf4* is lower than that of *Oct4* and *Sox2* in ES cells ($c-Myc < Klf4 < Oct4 \approx Sox2$, quantified by real-time polymerase chain reaction (PCR), data not shown). The total amount of the four reprogramming factor proteins was also comparable to that in ES cells in all cell lines examined (Supplementary Fig. 4a). In conjunction with *Oct4* and *Sox2*, 13 additional pluripotent markers, which are highly enriched in both ES cells and iPS cells^{1,4,24}, were reactivated in all cell lines screened (Fig. 1b). Bisulphite genomic sequencing analyses revealed that the promoter region of *Oct4* and *Nanog* is highly unmethylated in the iPS cells (Supplementary Fig. 4c). These results indicate that efficient reprogramming had occurred due to the non-viral single vector.

The number of vector-integration sites was analysed by Southern blotting in cell lines imO1–imO8, as well as in five TNG iPS cell lines, TNGimO1–TNGimO5 (strategy shown in Fig. 2a). Of the 13 cell lines, imO7 and TNGimO5 were found to have a single-vector integration in one site, indicating that a stable single-copy insertion of the non-viral expression vector can achieve direct reprogramming, effectively minimizing genome modification in iPS cells (Fig. 2b). We did not find reprogrammed cell lines without vector integration. The

integration sites of imO1, imO3 and imO7, as well as the tandem repeats in imO1 and imO3, were identified by inverse PCR and confirmed by genomic PCR (Fig. 2c and Supplementary Fig. 5). All integration sites of the individual cell lines were different, supporting the notion that reprogramming does not depend on vector integration at specific loci⁸. Expression of the genes at the integration sites was detectable in MEFs, ES cells and all examined iPS cell lines, without significant influence imposed by vector integration (Supplementary Fig. 5d). Adult cells (footpad fibroblasts) were also successfully reprogrammed by means of definite single-copy vector integration (Supplementary Fig. 6).

To remove the exogenous reprogramming factors, we performed transient *Cre* transfection and tracked the loss of fluorescent reporter expression. Many of the mOrange-negative colonies started to differentiate after *Cre* transfection (Supplementary Fig. 7a). This excision-mediated differentiation was prevented by culturing the cells in the presence of the fibroblast growth factor (Fgf) receptor inhibitor PD173074, which inhibits mouse ES cell differentiation²⁵ (Fig. 3a). The percentage of differentiated colonies after *Cre*-mediated excision differed among clones, possibly reflecting variable stability of the

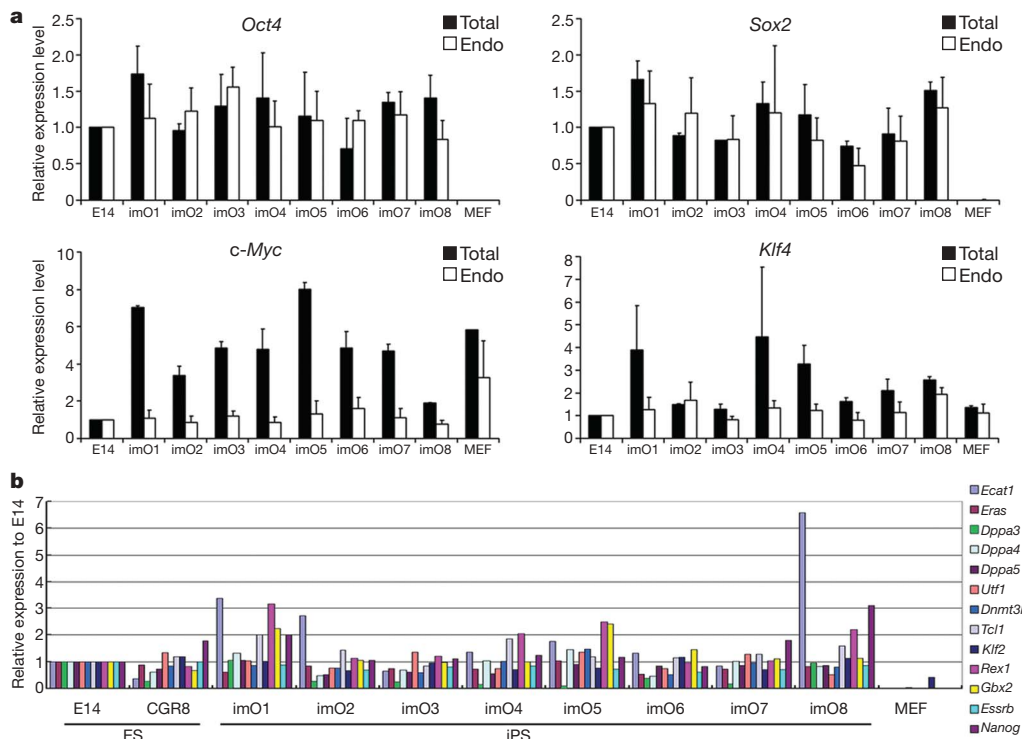


Figure 1 | Efficient reactivation of pluripotent markers in iPS cells generated by a non-viral multiprotein expression vector. **a**, Quantitative PCR for total and endogenous *c-Myc*, *Klf4*, *Oct4* and *Sox2* expression. Data are shown as relative expression to an ES cell line, E14Tg2a (E14). Error bars indicate the s.d. generated from triplicates. **b**, Quantitative PCR for

pluripotent markers. Two independent ES cell lines, E14Tg2a (E14) and CGR8, were analysed together with iPS cell lines. Data are shown as relative expression to E14Tg2a, and represent one of two independent experiments. *Ecat1* (also known as 2410004A20Rik), *Dppa5* (*Dppa5a*), *Rex1* (*Zfp42*).

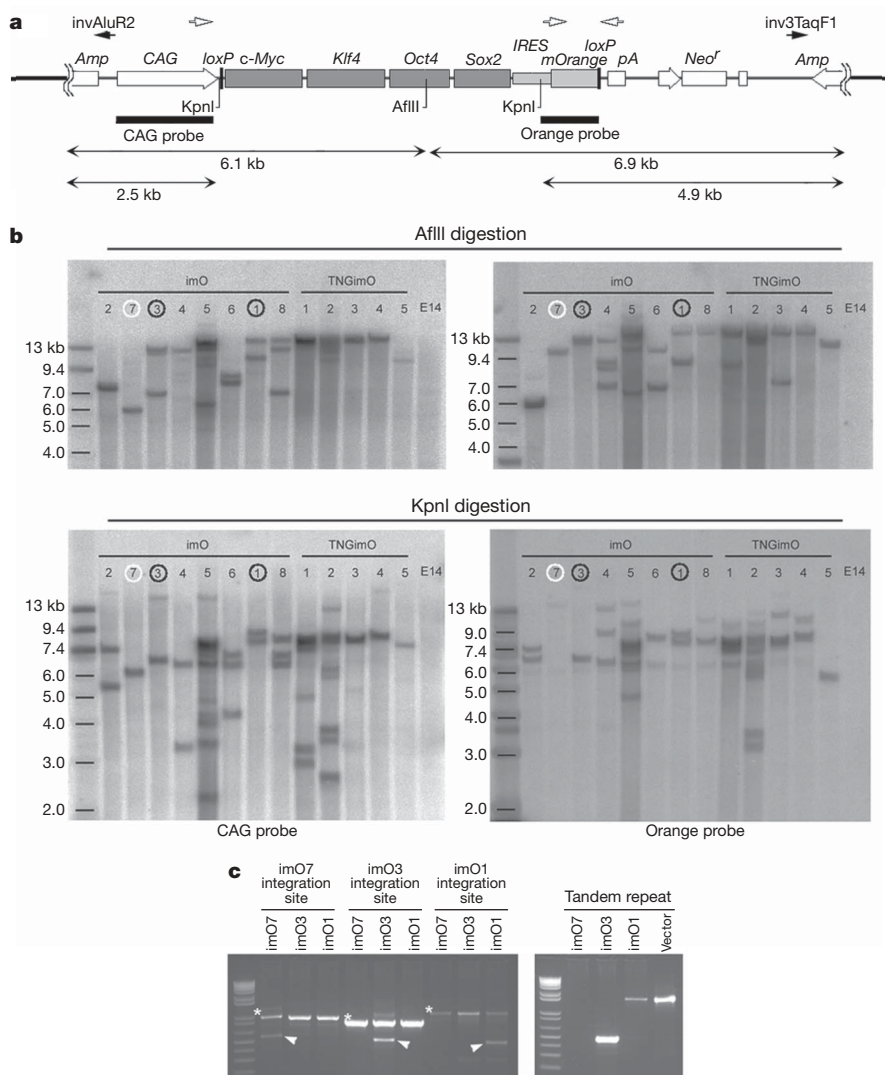


Figure 2 | Non-viral iPS cells with a single-vector integration site.

a, Schematic diagram of restriction enzyme sites, AflIII and KpnI, in pCAG2LMKOSimO and two probes, CAG probe and Orange probe, used for Southern blotting (bars). Black arrows (invAluR2, inv3TaqF1) indicate the position of primers used to detect tandem repeat integration in **c**. pA, Amp and Neo^r represent polyA signal, ampicillin-resistant gene and neomycin-resistance gene, respectively. **b**, Southern blotting analysis for the AflIII- (top) and KpnI- (bottom) digested genome of imO1–imO8 and TNGimO1–TNGimO5 using the CAG probe (left panels) and Orange probe

(right panels). **c**, Validation of the integration site and tandem repeat integration. A single integration site of imO7 (white circle in **b**) and a single integration site with tandem integration (same orientation) of imO1 and imO3 (black circles in **b**) was identified by inverse PCR (data not shown) and validated by genomic PCR. Asterisks, band from wild-type allele. Arrowheads, integration-site-specific band. Detail of the integration site is shown in Supplementary Fig. 5. The different band size of tandem repeats is caused by vector degradation accompanied by random integration.

reprogrammed state (Fig. 3b). All tested reprogramming-cassette-excised clones, which were generated from imO2, imO3, imO7 and TNGimO5 and expanded in the presence of PD173074, could subsequently maintain an undifferentiated morphology for at least five passages after removal of PD173074 (data not shown). The presence of PD173074 may allow cells to adapt upon rapid loss of exogenous reprogramming factors at single colony density. Whereas Cre-excised cell lines from imO7 and TNGimO5 could be maintained over 20 passages while maintaining an undifferentiated morphology, cell lines derived from imO2 and imO3 were prone to generate more differentiated cells at later passages in the absence of PD173074 (data not shown). The endogenous gene expression of *c-Myc*, *Klf4*, *Sox2* and *Oct4* was maintained in the Cre-excised cell lines imO2Ec3 derived from imO2 with additional constitutive enhanced GFP (eGFP) expression (imO2E1), imO3c8 and imO7c8, which are derived from imO3 and imO7, respectively (Supplementary Fig. 8a). Expression of other pluripotency genes was also sustained (Supplementary Fig. 8b), indicating that our single-vector system has enabled complete

elimination of exogenous genes without disturbing maintenance of the iPS cell state.

We next examined the differentiation ability of the cell lines before and after reprogramming-cassette excision. Cre-excised cell lines imO3c8 and imO7c8 downregulated the pluripotency markers *Oct4*, *Nanog* and *Rex1* and upregulated markers of all three germ layers in embryoid bodies, thus behaving in the same way as ES cells²⁶ (Supplementary Fig. 9a). Furthermore, β -tubulin-positive neurons were generated efficiently in a monolayer neural differentiation protocol²⁷ (Supplementary Fig. 9b). Differentiation of the factor-retained parental cell lines imO3 and imO7 was less efficient (Supplementary Fig. 9a, b). Both imO7 and imO7c8 produced teratocarcinomas when transplanted to the kidney capsule, although imO7 tumours contained more undifferentiated cells than did imO7c8 tumours (Fig. 3c). Finally, we injected the reprogramming-vector-free iPS cells into C57BL/6 blastocysts (results summarized in Supplementary Table 2). To identify chimaeric embryos, two cell lines with constitutive eGFP expression, imO3Ec5 and imO7Ec3, were used, and high-contribution

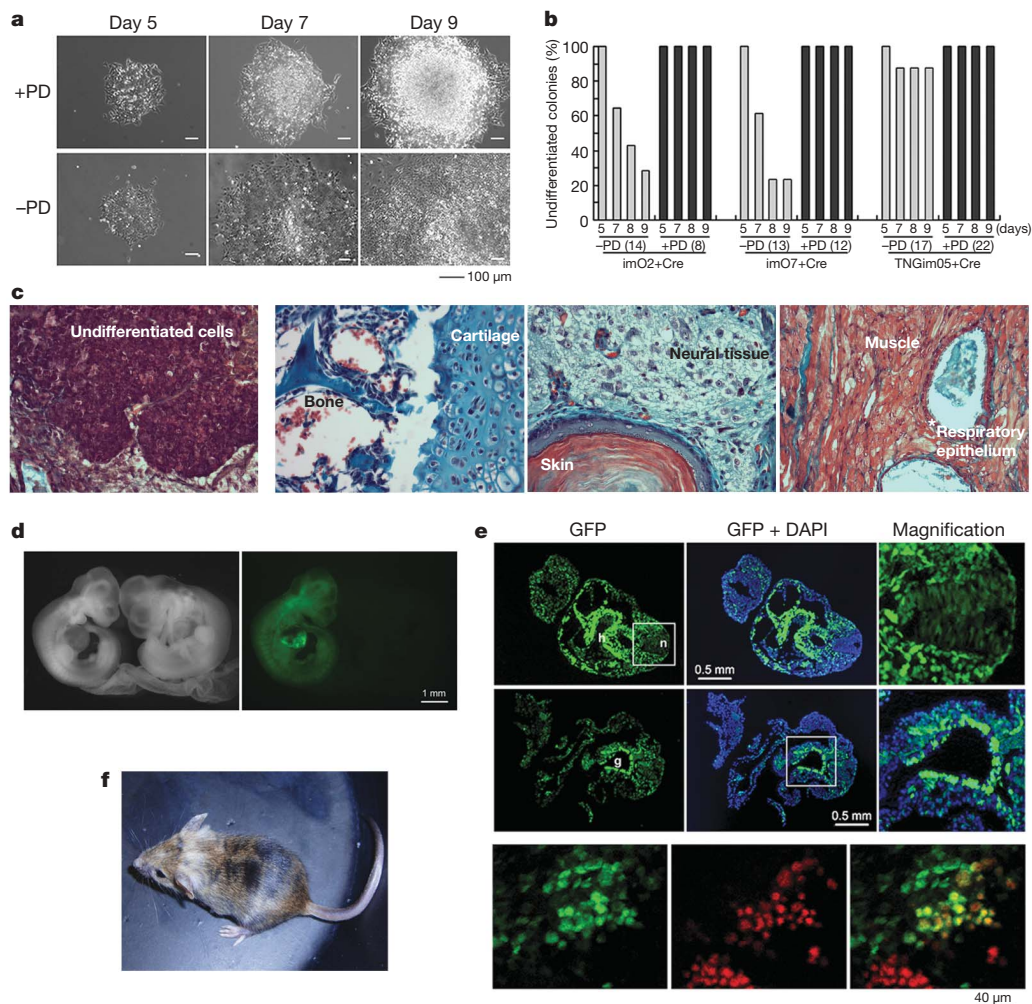


Figure 3 | Reprogramming cassette excision and pluripotency of the non-viral iPS cells. **a**, Many of the undifferentiated colonies at 5 days post *Cre* transfection differentiated by day 9 in the absence of the fibroblast growth factor receptor inhibitor PD173074 (bottom). **b**, Percentage of reprogramming-cassette-free undifferentiated colonies in the absence ($-PD$) and presence ($+PD$) of PD173074. Numbers of monitored reprogramming-cassette-excised colonies are indicated in parentheses. Experiments were performed in three cell lines, imO2, imO7 and TNGimO5. **c**, Undifferentiated cells in imO7 teratoma (left) and various tissues in

chimaeric embryos were generated at high frequency from both cell lines (Fig. 3d and Supplementary Table 2). Contribution to all three germ layers—ectoderm, mesoderm and endoderm—was observed, in addition to Oct4-positive germ cells in the 12.5 days post coitum (d.p.c.) genital ridge (Fig. 3e). Three *Cre*-excised iPS cell lines, imO1c5, imO7c8 and TNGimO3cC5, gave rise to live chimaeras, indicating that iPS cells derived with the non-viral multiprotein expression vector are genuinely pluripotent (Fig. 3f).

To address the reprogramming ability of the non-viral single-vector system in human cells, we enhanced stable transfection efficiencies using a *piggyBac* (PB) transposon gene-delivery system¹⁵. Co-transfection of two PB transposons carrying a dox-inducible *MKOS-IRES-geo* cassette and a constitutively active *CAG-rtTA* transactivator construct¹⁶ was applied to human embryonic fibroblasts (Supplementary Fig. 10a). In this design, on genomic integration, the two transposons allow dox-inducible activation of *MKOS* expression in wild-type cells. We observed iPS-like colony formation 14 days post transfection (d.p.t.) when the cells were maintained in human ES cell culture conditions supplemented with dox. In total, 15 colonies were picked from 14–25 d.p.t. from 4 wells of 6-well plates, initially containing either

imO7c8 teratoma (the other three panels). **d**, imO3Ec5-derived chimaeric embryos (green) at 10.5 d.p.c. **e**, Transversal sections at 9.5 d.p.c. (upper six panels) and genital ridge at 12.5 d.p.c. (bottom panels). imO3Ec5 contributed to ectoderm (neural tissue, n; the boxed regions are magnified on the right), mesoderm (heart; h), endoderm (gut, g; the boxed regions are magnified on the right) and germ cells (red staining with anti-Oct4 antibody). DAPI, 4,6-diamidino-2-phenylindole. **f**, An adult imO7c8-derived chimaeric mouse.

3.2×10^4 or 6.4×10^4 fibroblasts per well. When dox was withdrawn on 32 d.p.t., 3 clones successfully propagated as stable cell lines, whereas the exogenous factor expression was uninduced as indicated by negative staining for lacZ activity (Supplementary Fig. 10b). All clonal lines displayed human ES cell morphology (Supplementary Fig. 10b) and were positive for alkaline phosphatase (not shown). Robust expression of endogenous pluripotency markers SSEA4, NANOG, TRA-160 and TRA-181 was confirmed in all three cell lines (Supplementary Fig. 10c). These results demonstrate that the non-viral single-vector system can reprogram human fibroblasts, and strongly indicate that it can also be applied to the production of exogenous-factor-free, non-viral human iPS cells.

We demonstrate that a single non-viral vector with 2A-peptide-linked reprogramming factors can achieve reprogramming efficiently and that the exogenous reprogramming factors can be completely removed from the iPS cells using subsequent *Cre* transfection. Absolute avoidance of unpredictable exogenous reprogramming factor reactivation is important not only for clinical applications but also for drug screening, because some small molecules affect epigenetic genome modification²⁸, which could cause unexpected reactivation

and unreliable screening results. Cre recombinase boasts the most efficient *in vivo* and *in vitro* recombination system currently known, and a part of the vector backbone remaining in the integration site following Cre-mediated factor deletion would be a tolerable remnant for *in vitro* iPS applications. We also demonstrated the single-vector reprogramming system combined with a PB transposon delivery system for human cell reprogramming. PB transposons are completely removable from their integration site without any residual change in the original DNA sequence^{15,16}. This PB-based single-vector reprogramming system will enable the generation of non-genetically modified human iPS cells as shown in the mouse¹⁶, which is ideal for regenerative medicine.

METHODS SUMMARY

A vector, pCAG2LMKOSimO, which has *c-Myc*, *Klf4*, *Oct4* and *Sox2* coding regions linked with 2A peptide sequences driven by CAG enhancer/promoter^{18,21}, was constructed as described in the Methods. The vectors were introduced into MEFs using Nucleofector II (Amaxa) and cells were cultured in ES cell culture conditions for up to four weeks. Colonies showing ES-cell-like morphology were picked and cultured on either irradiated MEFs (γ MEFs) or gelatin after trypsinization. Gene expression was analysed by quantitative PCR. Protein expression was analysed by immunoblotting. Integration number of the vector and the integration site in the established cell lines were analysed by Southern blotting and inverse PCR, respectively. The reprogramming cassette was excised by Cre transient transfection in the presence or absence of a fibroblast growth factor receptor inhibitor PD173074 (100 ng ml⁻¹), and pluripotency of the cell lines was examined *in vitro* (embryoid body formation, neural differentiation) and *in vivo* (teratoma formation, blastocyst injection).

Full Methods and any associated references are available in the online version of the paper at www.nature.com/nature.

Received 28 December 2008; accepted 12 February 2009.

Published online 1 March 2009.

- Takahashi, K. & Yamanaka, S. Induction of pluripotent stem cells from mouse embryonic and adult fibroblast cultures by defined factors. *Cell* **126**, 663–676 (2006).
- Wernig, M. *et al.* *In vitro* reprogramming of fibroblasts into a pluripotent ES-cell-like state. *Nature* **448**, 318–324 (2007).
- Maherali, N. *et al.* Directly reprogrammed fibroblasts show global epigenetic remodeling and widespread tissue contribution. *Cell Stem Cell* **1**, 55–70 (2007).
- Takahashi, K. *et al.* Induction of pluripotent stem cells from adult human fibroblasts by defined factors. *Cell* **131**, 861–872 (2007).
- Yu, J. *et al.* Induced pluripotent stem cell lines derived from human somatic cells. *Science* **318**, 1917–1920 (2007).
- Park, I. H. *et al.* Reprogramming of human somatic cells to pluripotency with defined factors. *Nature* **451**, 141–146 (2008).
- Okita, K., Ichisaka, T. & Yamanaka, S. Generation of germline-competent induced pluripotent stem cells. *Nature* **448**, 313–317 (2007).
- Aoi, T. *et al.* Generation of pluripotent stem cells from adult mouse liver and stomach cells. *Science* **321**, 699–702 (2008).
- Nakagawa, M. *et al.* Generation of induced pluripotent stem cells without Myc from mouse and human fibroblasts. *Nature Biotechnol.* **26**, 101–106 (2008).
- Wernig, M., Meissner, A., Cassady, J. P. & Jaenisch, R. *c-Myc* is dispensable for direct reprogramming of mouse fibroblasts. *Cell Stem Cell* **2**, 10–12 (2008).
- Hochedlinger, K., Yamada, Y., Beard, C. & Jaenisch, R. Ectopic expression of Oct-4 blocks progenitor-cell differentiation and causes dysplasia in epithelial tissues. *Cell* **121**, 465–477 (2005).
- Foster, K. W. *et al.* Induction of KLF4 in basal keratinocytes blocks the proliferation–differentiation switch and initiates squamous epithelial dysplasia. *Oncogene* **24**, 1491–1500 (2005).
- Stadtfeld, M., Nagaya, M., Utikal, J., Weir, G. & Hochedlinger, K. Induced pluripotent stem cells generated without viral integration. *Science* **322**, 954–959 (2008).
- Okita, K., Nakagawa, M., Hyenjong, H., Ichisaka, T. & Yamanaka, S. Generation of mouse induced pluripotent stem cells without viral vectors. *Science* **322**, 949–953 (2008).
- Wang, W. *et al.* Chromosomal transposition of PiggyBac in mouse embryonic stem cells. *Proc. Natl Acad. Sci. USA* **105**, 9290–9295 (2008).
- Woltjen, K. *et al.* piggyBac transposition reprograms fibroblasts to induced pluripotent stem cells. *Nature* doi:10.1038/nature07863 (this issue).
- Hasegawa, K., Cowan, A. B., Nakatsuji, N. & Suemori, H. Efficient multicistronic expression of a transgene in human embryonic stem cells. *Stem Cells* **25**, 1707–1712 (2007).
- Szymczak, A. L. *et al.* Correction of multi-gene deficiency *in vivo* using a single ‘self-cleaving’ 2A peptide-based retroviral vector. *Nature Biotechnol.* **22**, 589–594 (2004).
- Sommer, C. A. *et al.* iPS cell generation using a single lentiviral stem cell cassette. *Stem Cells* doi:10.1634/stemcells.2008-1075 (2008).
- Carey, B. W. *et al.* Reprogramming of murine and human somatic cells using a single polycistronic vector. *Proc. Natl Acad. Sci. USA* **106**, 157–162 (2009).
- Niwa, H., Yamamura, K. & Miyazaki, J. Efficient selection for high-expression transfectants with a novel eukaryotic vector. *Gene* **108**, 193–199 (1991).
- Yeh, E. *et al.* A signalling pathway controlling *c-Myc* degradation that impacts oncogenic transformation of human cells. *Nature Cell Biol.* **6**, 308–318 (2004).
- Chambers, I. *et al.* Nanog safeguards pluripotency and mediates germline development. *Nature* **450**, 1230–1234 (2007).
- Mikkelsen, T. S. *et al.* Dissecting direct reprogramming through integrative genomic analysis. *Nature* **454**, 49–55 (2008).
- Kunath, T. *et al.* FGF stimulation of the Erk1/2 signalling cascade triggers transition of pluripotent embryonic stem cells from self-renewal to lineage commitment. *Development* **134**, 2895–2902 (2007).
- Kaji, K. *et al.* The NuRD component Mbd3 is required for pluripotency of embryonic stem cells. *Nature Cell Biol.* **8**, 285–292 (2006).
- Ying, Q. L., Stavridis, M., Griffiths, D., Li, M. & Smith, A. Conversion of embryonic stem cells into neuroectodermal precursors in adherent monoculture. *Nature Biotechnol.* **21**, 183–186 (2003).
- Brueckner, B., Kuck, D. & Lyko, F. DNA methyltransferase inhibitors for cancer therapy. *Cancer J.* **13**, 17–22 (2007).

Supplementary Information is linked to the online version of the paper at www.nature.com/nature.

Acknowledgements We thank A. Tsakiridis for advice on using the 2A peptide sequence and A. Nagy for providing data from his laboratory on generating human reprogrammed cell lines by combining the PB transposon system and the 2A-sequence-joined reprogramming factors (or MKOS single vector reprogramming system) as well as for his comments on the manuscript. We also thank I. Chambers for providing TNG MEFs and for discussion and comments on the manuscript, V. Wilson for advice on teratoma analysis, T. Kunath, S. Lowell, C. Blackburn and K. Vintersten for discussions and comments on the manuscript, and B. Hendrich for permission to start preliminary experiments of this work in his laboratory. We also thank J. Ure, L. Robertson, R. McLay and R. Wilkie for technical assistance, and Biomed unit staff for mouse husbandry. K.K. is the recipient of MRC career development fellowship in stem cell research. A.P. is the recipient of a BBSRC CASE PhD studentship. M.M., P.M. and K.W. were supported by grants from the Canadian Stem Cell Network and Juvenile Diabetes Research Foundation.

Author Contributions K.K. conceived the study, designed and executed the experiments, interpreted data and wrote the manuscript. K.N. performed immunoblotting and karyotype checking, and assisted with manuscript preparation. A.P. performed real-time PCR and *in vitro* differentiation experiments. M.M. generated human reprogrammed cells. P.M. performed immunostaining for human reprogrammed cells. K.W. constructed the PB/MKOS system, assisted human cell reprogramming experiments and analysis, and helped to prepare the manuscript.

Author Information Reprints and permissions information is available at www.nature.com/reprints. Correspondence and requests for materials should be addressed to K.K. (keisuke.kaji@ed.ac.uk).

METHODS

Plasmid construction. The sequences of all primers used for plasmid construction are listed in Supplementary Table 3. The *c-Myc* coding region plus *F2A* 5' 50 bp (*c-Myc-F2A* 5'), the *F2A* 3' 54 bp plus *Klf4* coding region plus *T2A* (*F2A* 3'-*Klf4-T2A*), the *Oct4* coding region plus *E2A* 5' 50 bp (*Oct4-E2A* 5'), and the *E2A* 3' 50 bp plus *Sox2* coding region (*E2A* 3'-*Sox2*) fragments were separately amplified by PCR using mouse ES cell complementary DNA as a template. *c-Myc-F2A-Klf4-T2A* fragment was amplified by PCR using EcoRI *Koz* 5'-*Myc* and *Klf4*-3' GSG *T2A* Xho primers after annealing and extension of *c-Myc-F2A* 5' and *F2A* 3'-*Klf4-T2A* fragment taking advantage of the complimentary *F2A* peptide region. The *Oct4-E2A-Sox2* fragment was amplified by PCR using Xho5'-*Oct4* and *Sox2*-3' EcoRI Xho primers after annealing and extension of *Oct4-E2A* 5' and *E2A* 3'-*Sox2* fragment. The individual fragments were subcloned into pTOPO-bluntII (Invitrogen), and the *Oct4-E2A-Sox2* fragment was transferred into a XhoI site located after *c-Myc-F2A-Klf4-T2A*, resulting in *c-Myc-F2A-Klf4-T2A-Oct4-E2A-Sox2* (MKOS) in pTOPO-bluntII. pCAGMKOSiE was constructed by inserting the MKOS fragment into the EcoRI site of pCIG2, which is generated by replacing CMV promoter of pIRES2-EGFP (BD Biosciences Clontech) with CAG enhancer/promoter²¹. The *IRES* fragment was amplified by NotIRES and mOrangeIRES primers using pIRES2-eGFP as a template. The *mOrange* fragment was amplified by IRESmOrange and XbaBamloxPmOrange primers using pmOrange (BD Biosciences Clontech) as a template. The *IRES-mOrange-loxP* fragment (imOloxP) was amplified using these fragments and the flanking primers, and subcloned into pTOPO-bluntII. MKOS was inserted into the EcoRI site of pcDNA3 (Invitrogen), and then annealed KpnBamloxPBamX F/R oligonucleotides was inserted before *c-Myc*, and imOloxP was inserted after *Sox2* (pCMV2LMKOSimO). pCAG2LMKOSimO was constructed by transferring a BamHI–BamHI fragment containing MKOSimO flanked by two *loxP* sites from pCMV2LMKOSimO into the pCAGDNA3 vector, which was made by replacing its CMV promoter with CAG enhancer/promoter²¹. Full sequence information of the vector and PCR conditions is available on request.

Southern blotting. Ten micrograms of genomic DNA digested with AflIII or KpnI was separated in 0.8% of agarose gel in TAE buffer, and hybridized with ³²P-labelled probes in PerfectHyb Plus Hybridization Buffer (Sigma) at 65 °C after transfer onto Hybond-XL (GE Healthcare). The expected band size from tandem integration is: same orientation, <13.0 kb, and opposite orientation, <13.8 kb or <12.2 kb in AflIII digestion; same orientation, <6.4 kb, and opposite

orientation, <9.8 kb or <5.1 kb, in KpnI digestion using either the CAG or Orange probe.

Nucleofection and reprogramming efficiency estimation. MEF Nucleofector Kit 2 (Amaxa) and program T-20 were used for nucleofection according to the manufacturer's instructions. We transfected 2×10^6 MEFs with 2–10 µg of linearized DNA, and 10^5 cells were seeded in 6-well plates on either γ MEFs or gelatin in the presence of LIF. Forty-eight hours later, viable cells were collected from one gelatin well, and after counting cell number the mOrange-positive population was measured by flow cytometry (CyAn ADP, Dako). mOrange-positive cell numbers per well were estimated using the results in each experiment as shown in Table 1. The rest of the wells were kept for 4 weeks, with medium changed every 2–3 days. Nanog-GFP-positive colonies from TNG MEFs were picked and seeded on γ MEFs after trypsinization. Colonies from 129 MEFs were fixed with 4% PFA and stained with anti-Nanog antibody (ab21603, Abcam) followed by Alexa-Fluor-488-conjugated anti-rabbit IgG antibody (Molecular Probes).

Reprogramming cassette excision. Cells were cultured in the presence and absence of 100 ng ml^{-1} PD173074 (Sigma) for 24 h before *Cre* transfection with Lipofectamine2000 (Invitrogen). Forty-eight hours after *Cre* transfection, cells were collected and seeded at 10^3 cells per 10 cm dish with gelatin in the presence or absence of PD173074. Undifferentiated mOrange-negative colonies were marked 5 days post *Cre* transfection, and morphology of the colonies was monitored to day 9. Colonies were picked between days 12 and 14, propagated in 96-well plates, and reprogramming cassette excision in each clone was verified by genomic PCR using CAG F, IRES mOrange and BGH R primers (Supplementary Fig. 8b, c; primer sequences are in Supplementary Table 4). Reprogramming-cassette-positive colonies by genomic PCR, which had undetectable mOrange expression by microscopy, were excluded from the total colony numbers indicated in parentheses in Fig. 3b. Differentiated colonies, which failed to grow after being picked, were considered as reprogramming-cassette-excised colonies and counted in the total colony numbers.

Quantitative PCR. Each quantitative PCR used 1% of cDNA made from 1 µg of total RNA in Light-Cycler 480 system with SYBR Green (Roche). See Supplementary Table 5 for the gene-specific primers. Data are shown as relative expression to an ES cell line, E14Tg2a, after normalization with TATA binding protein (*Tbp*) expression. Details of PCR conditions are available on request. Data represent one of two independent experiments. Error bars in *c-Myc*, *Klf4*, *Oct4* and *Sox2* PCR represent standard deviation of duplicate samples.

LETTERS

Hedgehog signalling is essential for maintenance of cancer stem cells in myeloid leukaemia

Chen Zhao^{1*}, Alan Chen^{1*}, Catriona H. Jamieson³, Mark Fereshteh¹, Annelie Abrahamsson³, Jordan Blum¹, Hyog Young Kwon¹, Jynho Kim⁴, John P. Chute², David Rizzieri², Michael Munchhof⁵, Todd VanArsdale⁶, Philip A. Beachy⁴ & Tannishtha Reya¹

Although the role of Hedgehog (Hh) signalling in embryonic pattern formation is well established¹, its functions in adult tissue renewal and maintenance remain unclear, and the relationship of these functions to cancer development has not been determined. Here we show that the loss of Smoothed (Smo), an essential component of the Hh pathway², impairs haematopoietic stem cell renewal and decreases induction of chronic myelogenous leukaemia (CML) by the BCR-ABL1 oncoprotein³. Loss of Smo causes depletion of CML stem cells—the cells that propagate the leukaemia—whereas constitutively active Smo augments CML stem cell number and accelerates disease. As a possible mechanism for Smo action, we show that the cell fate determinant Numb, which depletes CML stem cells, is increased in the absence of Smo activity. Furthermore, pharmacological inhibition of Hh signalling impairs not only the propagation of CML driven by wild-type BCR-ABL1, but also the growth of imatinib-resistant mouse and human CML. These data indicate that Hh pathway activity is required for maintenance of normal and neoplastic stem cells of the haematopoietic system and raise the possibility that the drug resistance and disease recurrence associated with imatinib treatment of CML^{4,5} might be avoided by targeting this essential stem cell maintenance pathway.

CML arises owing to a translocation between the BCR serine/threonine kinase gene and the ABL1 tyrosine kinase³. Imatinib mesylate, which binds to the ABL1 kinase domain and inhibits phosphorylation of substrates, has been used to treat CML, but it is not curative because the cancer stem cells that propagate the leukaemia are resistant to therapy and are not eradicated^{5–7}. Furthermore, imatinib resistance due to mutations in the drug-binding site can occur, especially in advanced stage disease, leading to disease relapse and progression⁴. The design of effective new therapies thus critically depends on the identification of signals that are required for CML propagation and in particular signals required for CML cancer stem cell maintenance.

Given the parallels in signalling between development and cancer^{8,9}, we examined whether Hh signalling, an important regulator of development and oncogenesis in many tissues^{1,10}, might also have a role in CML. To this end we conditionally deleted Smo—a protein that is essential for Hh signal transduction². Smo is negatively regulated by the Hh receptor Patched (Ptch) in the absence of Hh protein signals. This inhibition is relieved when Ptch is bound by the Hh proteins Shh, Ihh or Dhh. Subsequently, Smo causes activation of Hh pathway targets via the Gli family of transcriptional effectors².

Smo was deleted in the haematopoietic system by crossing mice carrying a *loxP*-flanked *Smo* allele¹¹ to mice in which Cre is driven by

Vav regulatory elements¹². Smo was efficiently deleted in haematopoietic cells of *Vav-Cre;Smo^{loxP/loxP}* mice as compared to control *Smo^{loxP/loxP}* mice lacking Cre (Fig. 1a, b). Although the frequency of haematopoietic stem cells (HSCs) and differentiated cells was unchanged in the Smo-deficient (*Smo^{-/-}*) mice (Supplementary Fig. 1), these animals had a clear defect in long-term HSC function in primary and secondary transplants (Fig. 1c and Supplementary Fig. 1). Decreased reconstitution was not due to decreased homing or to a preferential loss of any specific lineage (Supplementary Figs 1 and 2), and could be recapitulated with whole bone marrow transplants (Supplementary Fig. 3). Cumulatively, these data indicate that Smo is required for HSC renewal *in vivo*.

We next investigated the role of Hh signalling in CML initiation and propagation. CML can be modelled by transplanting BCR-ABL1-transduced haematopoietic progenitors into irradiated mice¹³. Whereas control cells transduced with BCR-ABL1 caused CML in 94% (16 out of 17) of recipients within 3 months, similarly transduced *Smo^{-/-}* cells caused CML in only 47% (8 out of 17) of recipients (Fig. 1d), and these tumours showed an increased latency. The reduced CML incidence was not due to altered homing or engraftment (Supplementary Fig. 4). These data suggest that Hh activity is required for the initiation and propagation of CML. The propagation of several cancers has been shown to depend on cancer stem cells, a critical subset of cancer cells that are capable of transferring the disease to a new host⁸. Because deletion of Smo led to impaired CML growth, we postulated that the loss of Smo might affect CML stem cells. As shown in Fig. 1e, f, the frequency of c-Kit⁺ Lin⁻ Sca-1⁺ (KLS) cells (which have previously been shown to be responsible for propagating CML⁶) was significantly reduced in the absence of Smo.

The fact that loss of Smo led to decreased numbers of CML stem cells led us to investigate whether activation of the Hh pathway might lead to an increased frequency of CML stem cells and acceleration of disease. To test this, we used a transgenic mouse expressing an activated form of Smo (*SmoM2*) fused to yellow fluorescent protein (YFP)¹⁴; expression of this gene from the Rosa26 locus promoter is blocked by a *loxP*-flanked stop sequence, and is thus inducible by Cre. When *SmoM2*-YFP mice were crossed with *Vav-Cre* mice, progeny expressed YFP in >70% of c-Kit⁺ Lin^{-/lo} Sca-1⁺ Flk2⁻ (KLSF) cells (Fig. 2a). Although the infection of both control and *SmoM2* KLSF cells with BCR-ABL1 resulted in CML, the frequency of CML stem cells in animals receiving *SmoM2* cells was fourfold greater than in mice receiving control cells (Fig. 2b, c). As expected, *SmoM2* was expressed in transgenic but not in control CML stem cells (Fig. 2d). Most importantly, the increased CML stem cell frequency led to a

¹Department of Pharmacology and Cancer Biology, ²Department of Medicine, Division of Cellular Therapy, Duke University Medical Center, Durham, North Carolina 27710, USA. ³Department of Medicine, Stem Cell Research Program, Moores UCSD Cancer Center La Jolla, California 92093, USA. ⁴Department of Developmental Biology Institute of Stem Cell Biology and Regenerative Medicine, Howard Hughes Medical Institute, Stanford University Medical Center, Stanford, California 94305, USA. ⁵Division of Medicinal Chemistry, Pfizer Laboratories, Groton, Connecticut 06340, USA. ⁶Division of Oncology, Pfizer Laboratories, La Jolla, California 92121, USA.

*These authors contributed equally to this work.

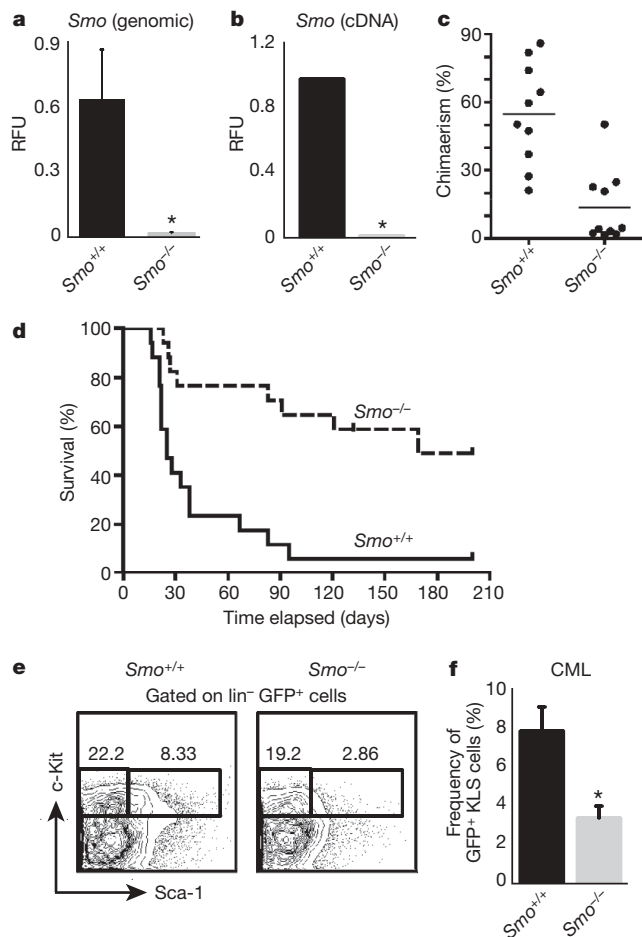


Figure 1 | Conditional deletion of *Smo* impairs the development of BCR-ABL1-induced CML and depletes CML stem cells. **a, Real-time PCR (rtPCR) using primers specific for the *loxP* sites was carried out on *Smo*^{-/-} or *Smo*^{+/+} bone marrow genomic DNA ($n = 3$, $*P = 0.03$). RFU, relative fluorescent units. **b**, rtPCR for *Smo* using complementary DNA from *Smo*^{-/-} or *Smo*^{+/+} KLSF cells ($n = 7$, $*P < 0.00001$). **c**, KLSF cells from *Smo*^{-/-} or *Smo*^{+/+} mice were transplanted together with competing bone marrow cells into congenic recipients and donor-derived chimaerism was monitored. The graph shows the average donor-derived chimaerism after long-term reconstitution ($n = 2$ with 20 mice, $P = 0.0002$). **d**, Survival curve of mice transplanted with BCR-ABL1-infected *Smo*^{-/-} or *Smo*^{+/+} KLSF cells ($n = 3$ with 34 mice, $P = 0.0002$). **e**, Representative example of CML stem cells (*GFP*⁺ *Lin*⁻ *c-Kit*⁺ *Sca*⁺) in the bone marrow of mice transplanted with BCR-ABL1-infected *Smo*^{-/-} or *Smo*^{+/+} KLS cells. **f**, Graph of the average percentage of CML stem cells in mice receiving BCR-ABL1-infected *Smo*^{+/+} (8 mice) or *Smo*^{-/-} KLS cells (9 mice). Frequency shows *c-Kit*⁺ *Sca*⁺ cells as a percentage of the *GFP*⁺ *Lin*⁻ population. $*P = 0.006$. Error bars in all bar graphs are s.e.m.**

significant acceleration of CML progression (Fig. 2e). *Smo*M2 expression also accelerated CML growth when activated post-embryonically (Supplementary Fig. 5). Thus genetic loss- and gain-of-function experiments indicate that Hh pathway activity controls the frequency and maintenance of CML stem cells, and consequently the incidence and latency of CML formation.

Our previous studies suggested that in normal haematopoietic stem cells, maintenance of the undifferentiated state depends on low levels of the cell fate determinant Numb¹⁵. We therefore tested whether Numb may act similarly in CML stem cells, and whether the effects of loss of *Smo* might be due to altered levels of Numb. We found that a greater frequency of *Smo*^{-/-} CML KLS cells had high levels of Numb as compared to control CML KLS cells (Fig. 3a–c). Additionally, ectopically expressed Numb inhibited *in vitro* propagation of BCR-ABL1-infected haematopoietic cells (Fig. 3d) and of CML stem cells from established leukaemias (Fig. 3e). These data

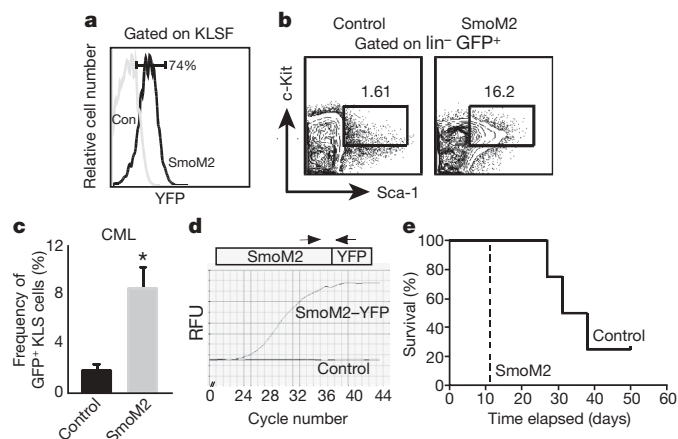


Figure 2 | The presence of constitutively active *Smo* increases the frequency of CML stem cells and accelerates disease. **a, Analysis of YFP fluorescence, which reflects *Smo*M2 expression in control (con) and *Smo*M2 KLSF cells ($n = 4$). **b**, Analysis of CML stem cells (*GFP*⁺ *KLS*) in mice transplanted with BCR-ABL1-infected control (left) and constitutively activated *Smo* (*Smo*M2, right) KLSF cells. **c**, The average percentage of CML stem cells in mice receiving BCR-ABL1-transduced control ($n = 4$) and *Smo*M2 KLSF cells ($n = 12$). Error bars are s.e.m., $*P = 0.048$. **d**, rtPCR analysis of *Smo*M2 expression in CML stem cells. **e**, Survival curve of mice receiving BCR-ABL1 transduced control (solid line) or *Smo*M2 KLSF cells (dashed line; $n = 2, 16$ mice, $P = 0.0082$).**

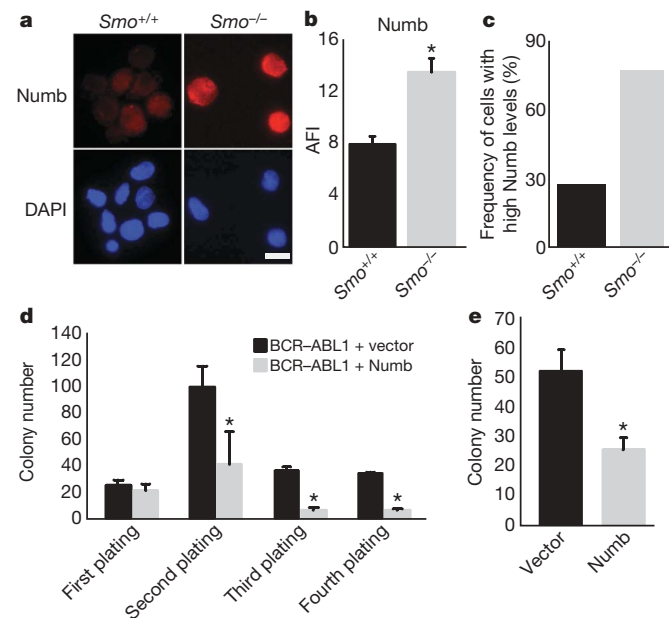


Figure 3 | Loss of *Smo* increases frequency of cells with high levels of Numb and contributes to decreased CML growth. **a, CML stem cells from *Smo*^{+/+} and *Smo*^{-/-} leukaemias were stained with Numb (red, top panel) and 4,6-diamidino-2-phenylindole (DAPI; blue, bottom panel). Scale bar, 10 μ m. **b**, The average fluorescence intensity (AFI) was determined by dividing the overall mean fluorescence intensity by the area of the cell ($P = 0.002$). **c**, The frequency of cells with high expression levels of Numb was calculated by designating cells above a mean fluorescence intensity value of 1,000 as high expressors ($n = 3$, using either CML KLS or CML *c-Kit*⁺ cells). **d**, KLSF cells were infected with MSCV-BCR-ABL1-IRES-GFP and either vector MSCV-IRES-YFP or MSCV-Numb-IRES-YFP. GFP and YFP double-positive cells were plated in methylcellulose, colonies were counted and cells were serially replated ($n = 2$, $*P < 0.006$). **e**, CML KLS cells were infected with viruses expressing control vector or Numb IRES-YFP. Infected cells were sorted and plated in methylcellulose ($n = 2$, $P = 0.03$). Error bars in **b–e** are s.e.m.**

suggest that increased Numb expression may contribute to the loss of CML stem cells in the absence of Smo.

Our genetic data showing that CML stem cells depend on Hh pathway activity raised the possibility that these cells might be targeted by pharmacological blockade of this pathway. We therefore tested the effect of cyclopamine, which inhibits Hh signalling by stabilizing Smo in its inactive form¹⁶. Exposure of CML stem cells to cyclopamine at a dose determined to minimize off-target effects and toxicity (Supplementary Fig. 6) led to a twofold inhibition of colony growth (Fig. 4a). This could be recapitulated using the Hh-blocking antibody 5E1 (Supplementary Fig. 7), suggesting that Hh pathway activation in CML may be ligand dependent^{17,18}. We also delivered cyclopamine to animals transplanted with BCR-ABL1-infected HSCs; whereas all of the control animals succumbed to CML within 4 weeks, 60% of the cyclopamine-treated mice were still alive after 7 weeks (Fig. 4b and Supplementary Fig. 8). Furthermore cyclopamine-treated mice had up to a 14-fold reduction in the CML stem cell population (Fig. 4c, d); consistent with this depletion, leukaemias from cyclopamine-treated mice were unable to propagate disease effectively when transplanted (Supplementary Fig. 9). These data suggest that cyclopamine can target the CML stem cell compartment critical for propagation of CML. Notably cyclopamine was most effective when initiated at early stages after CML establishment (Supplementary Fig. 10).

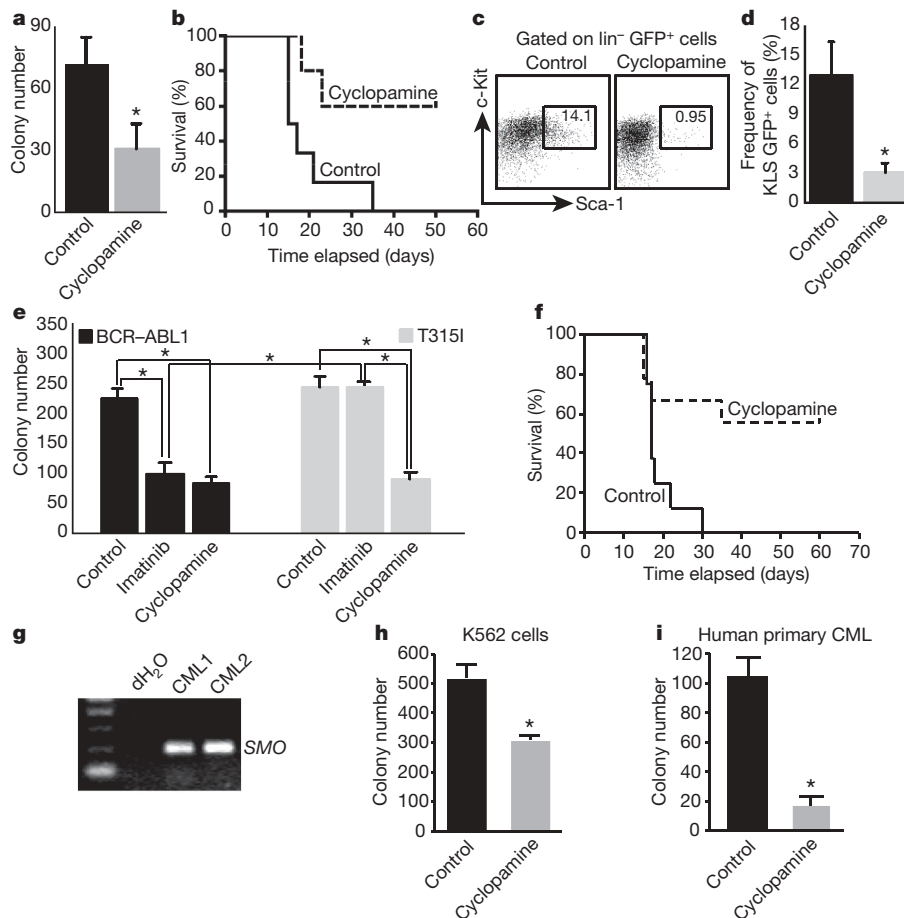


Figure 4 | Pharmacological inhibition of Smo impairs CML development and propagation. **a**, CML stem cells were plated in methylcellulose in the presence of 1 μ M tomatidine (control) or cyclopamine ($n = 2$, $*P = 0.005$). **b**, Survival curve of mice transplanted with BCR-ABL1-infected KLS cells in the presence of vehicle or cyclopamine ($n = 3$ with 32 mice, $P = 0.02$). **c**, Representative example of CML stem-cell frequency in vehicle- or cyclopamine-treated CML. **d**, Average CML stem cell frequency in vehicle- or cyclopamine-treated mice ($n = 4$, $*P = 0.03$). **e**, KLSF cells were infected with wild-type BCR-ABL1 or the imatinib-resistant T3151 mutant BCR-ABL1, and plated in methylcellulose with imatinib (2 μ M) or

One rationale for identifying new pathways involved in CML is that targeting these pathways may be used to prevent or overcome imatinib resistance¹⁹. To test whether cyclopamine could impair the growth of imatinib-resistant CML, we infected cells with virus encoding either wild-type BCR-ABL1 or the T3151 mutant^{4,6,20} that is resistant to imatinib and other tyrosine kinase inhibitors used at present. Cells infected with mutant BCR-ABL1 were unresponsive to imatinib (Fig. 4e), but their growth was reduced 2.5-fold by cyclopamine (Fig. 4e). Progression of drug-resistant CML *in vivo* was also significantly impaired in the presence of cyclopamine (Fig. 4f) as well as in the genetic absence of *Smo* (Supplementary Fig. 11). These data indicate that Hh pathway activity is required for maintenance of CML stem cells, and raise the possibility that small molecule inhibitors of the pathway could be useful for targeting both normal and imatinib-resistant CML.

Finally we tested whether targeting this pathway could inhibit the growth of human CML. Freshly isolated primary human blast crisis CML samples expressed *SMO* (Fig. 4g). To determine whether *SMO* may functionally contribute to human CML growth, we tested the effect of cyclopamine on both a human CML cell line and patient samples in a methylcellulose assay. Cyclopamine decreased colony formation in an imatinib-resistant human CML cell line (Fig. 4h) and in three independent primary patient samples (Fig. 4i and

cyclopamine (1 μ M) ($n = 2$, $*P < 0.004$). **f**, Survival curve of mice receiving T3151 BCR-ABL1-infected KLSF cells and either vehicle or cyclopamine, 7 days after transplantation ($n = 2$ with 16 mice, $P = 0.021$). **g**, *SMO* PCR on primary uncultured human CML samples. **h**, Imatinib-resistant K562 blast crisis CML cells were plated in methylcellulose in the presence of 1 μ M tomatidine or cyclopamine ($n = 2$, $*P < 0.01$). **i**, CD34⁺ cells were sorted from primary uncultured human blast crisis CML samples and plated in methylcellulose in the presence of 1 μ M tomatidine or cyclopamine ($n = 3$, $*P < 0.05$). Error bars in all bar graphs are s.e.m.

Supplementary Fig. 12), but not in untransformed cord blood cells (Supplementary Fig. 13). Consistent with this, inhibition of SMO by the delivery of a new SMO antagonist also impaired the propagation of imatinib-resistant human CML cells in xenografts (A.A., M.M., T.V.A. and C.H.J., manuscript in preparation). Cumulatively, these data suggest that Hh signalling is important for human CML growth and that it may continue to have a role even as the disease progresses into blast crisis phase.

The studies discussed earlier demonstrate a dependence of normal and neoplastic stem cells on Hh signalling. Previously, mammalian Hh proteins have been reported to preserve and increase the short-term repopulating capacity of human HSCs²¹. Our genetic loss-of-function studies indicate that intact Hh signalling is needed for HSC renewal. This requirement may be shared with the nervous system, in which progenitor development is dependent on Hh pathway activation^{22,23}. Just as Hh signalling seems to be required for stem cells, its aberrant activation has been associated with the development of several solid cancers^{17,18,24,25}. In the haematopoietic system, Hh signalling has been implicated in the growth of B cell lymphoma²⁶ and multiple myeloma²⁷. Our observations provide critical genetic evidence for a role of Hh signalling in myeloid leukaemia, and together with previous work, suggest that this pathway may have a broader role in haematological malignancies. Our data are also unique in demonstrating that loss of endogenous cancer stem cells impairs *in vivo* cancer progression, supporting the notion that the leukaemia stem cells identified by transplantation are the relevant drivers of endogenous cancer growth^{28–30}. The real impetus for identification of new pathways that drive cancer is the opportunity to inhibit these pathways instead of, or in addition to, conventional therapies. This is especially true for CML, in which imatinib is incapable of eradicating the disease, not only necessitating its continual use but also increasing the likelihood of resistance and relapse. Our findings that the pharmacological inhibition of Hh signalling can impair growth of CML driven by wild-type and imatinib-resistant BCR-ABL1, as well as human CML, raise the possibility that Hh antagonists may be useful as a therapy for normal and drug resistant CML.

METHODS SUMMARY

For CML assays, HSCs were infected with MSCV-BCR-ABL1-IRES-GFP or MSCV-IRES-GFP (control) and transplanted into recipient mice. CML was assessed by flow cytometry and histopathology. Pharmacological inhibition of Hh was initiated 6–8 days after transplantation by delivering 25 mg kg⁻¹ of cyclopamine twice a day by oral gavage. Treatment was continued for five consecutive days, stopped for two days and then continued once a day until the mice were analysed after signs of leukaemia. For human CML studies, peripheral blood CD34⁺ cells were sorted and plated in methylcellulose in tomatidine or cyclopamine.

Full Methods and any associated references are available in the online version of the paper at www.nature.com/nature.

Received 10 June; accepted 18 December 2008.

Published online 25 January 2009.

- Ingham, P. W. & Placzek, M. Orchestrating ontogenesis: variations on a theme by sonic hedgehog. *Nature Rev. Genet.* **7**, 841–850 (2006).
- Rohatgi, R. & Scott, M. P. Patching the gaps in Hedgehog signalling. *Nature Cell Biol.* **9**, 1005–1009 (2007).
- Ren, R. Mechanisms of BCR-ABL in the pathogenesis of chronic myelogenous leukaemia. *Nature Rev. Cancer* **5**, 172–183 (2005).
- Gorre, M. E. *et al.* Clinical resistance to STI-571 cancer therapy caused by BCR-ABL gene mutation or amplification. *Science* **293**, 876–880 (2001).
- Graham, S. M. *et al.* Primitive, quiescent, Philadelphia-positive stem cells from patients with chronic myeloid leukemia are insensitive to STI571 *in vitro*. *Blood* **99**, 319–325 (2002).
- Hu, Y. *et al.* Targeting multiple kinase pathways in leukemic progenitors and stem cells is essential for improved treatment of Ph⁺ leukemia in mice. *Proc. Natl Acad. Sci. USA* **103**, 16870–16875 (2006).

- Jorgensen, H. G., Allan, E. K., Jordanides, N. E., Mountford, J. C. & Holyoake, T. L. Nilotinib exerts equipotent antiproliferative effects to imatinib and does not induce apoptosis in CD34⁺ CML cells. *Blood* **109**, 4016–4019 (2007).
- Reya, T., Morrison, S. J., Clarke, M. F. & Weissman, I. L. Stem cells, cancer, and cancer stem cells. *Nature* **414**, 105–111 (2001).
- Taipale, J. & Beachy, P. A. The Hedgehog and Wnt signalling pathways in cancer. *Nature* **411**, 349–354 (2001).
- Evangelista, M., Tian, H. & de Sauvage, F. J. The hedgehog signaling pathway in cancer. *Clin. Cancer Res.* **12**, 5924–5928 (2006).
- Long, F., Zhang, X. M., Karp, S., Yang, Y. & McMahon, A. P. Genetic manipulation of hedgehog signaling in the endochondral skeleton reveals a direct role in the regulation of chondrocyte proliferation. *Development* **128**, 5099–5108 (2001).
- Zhao, C. *et al.* Loss of β -catenin impairs the renewal of normal and CML stem cells *in vivo*. *Cancer Cell* **12**, 528–541 (2007).
- Daley, G. Q., Van Etten, R. A. & Baltimore, D. Induction of chronic myelogenous leukemia in mice by the P210^{bcr/abl} gene of the Philadelphia chromosome. *Science* **247**, 824–830 (1990).
- Mao, J. *et al.* A novel somatic mouse model to survey tumorigenic potential applied to the Hedgehog pathway. *Cancer Res.* **66**, 10171–10178 (2006).
- Wu, M. *et al.* Imaging hematopoietic precursor division in real time. *Cell Stem Cell* **1**, 541–554 (2007).
- Chen, J. K., Taipale, J., Cooper, M. K. & Beachy, P. A. Inhibition of Hedgehog signaling by direct binding of cyclopamine to Smoothened. *Genes Dev.* **16**, 2743–2748 (2002).
- Thayer, S. P. *et al.* Hedgehog is an early and late mediator of pancreatic cancer tumorigenesis. *Nature* **425**, 851–856 (2003).
- Watkins, D. N. *et al.* Hedgehog signalling within airway epithelial progenitors and in small-cell lung cancer. *Nature* **422**, 313–317 (2003).
- O'Hare, T., Corbin, A. S. & Druker, B. J. Targeted CML therapy: controlling drug resistance, seeking cure. *Curr. Opin. Genet. Dev.* **16**, 92–99 (2006).
- Azam, M., Latek, R. R. & Daley, G. Q. Mechanisms of autoinhibition and STI-571/imatinib resistance revealed by mutagenesis of BCR-ABL. *Cell* **112**, 831–843 (2003).
- Bhardwaj, G. *et al.* Sonic hedgehog induces the proliferation of primitive human hematopoietic cells via BMP regulation. *Nature Immunol.* **2**, 172–180 (2001).
- Balordi, F. & Fishell, G. Mosaic removal of hedgehog signaling in the adult SVZ reveals that the residual wild-type stem cells have a limited capacity for self-renewal. *J. Neurosci.* **27**, 14248–14259 (2007).
- Han, Y. G. *et al.* Hedgehog signaling and primary cilia are required for the formation of adult neural stem cells. *Nature Neurosci.* **11**, 277–284 (2008).
- Goodrich, L. V., Milenkovic, L., Higgins, K. M. & Scott, M. P. Altered neural cell fates and medulloblastoma in mouse patched mutants. *Science* **277**, 1109–1113 (1997).
- Johnson, R. L. *et al.* Human homolog of patched, a candidate gene for the basal cell nevus syndrome. *Science* **272**, 1668–1671 (1996).
- Dierks, C. *et al.* Essential role of stromally induced hedgehog signaling in B-cell malignancies. *Nature Med.* **13**, 944–951 (2007).
- Peacock, C. D. *et al.* Hedgehog signaling maintains a tumor stem cell compartment in multiple myeloma. *Proc. Natl Acad. Sci. USA* **104**, 4048–4053 (2007).
- Kelly, P. N., Dakic, A., Adams, J. M., Nutt, S. L. & Strasser, A. Tumor growth need not be driven by rare cancer stem cells. *Science* **317**, 337 (2007).
- Kennedy, J. A., Barabe, F., Poeppl, A. G., Wang, J. C. & Dick, J. E. Comment on "Tumor growth need not be driven by rare cancer stem cells". *Science* **318**, 1722, doi: 10.1126/science.1149590 (2007).
- Adams, J. M., Kelly, P. N., Dakic, A., Nutt, S. L. & Strasser, A. Reply. *Science* **318**, 1722, doi: 10.1126/science.1149672 (2007).

Supplementary Information is linked to the online version of the paper at www.nature.com/nature.

Acknowledgements We wish to thank R. Wechsler-Reya for critical advice, D. Kioussis for Vav-Cre transgenic mice, A. M. Pendergast, A. Means and B. Hogan for review of the manuscript, S. Li for advice on mouse CML experiments, G. Daley, M. Azam and S. Li for the T3151 BCR-ABL1 construct, B. Harvat for cell sorting, and J. Harris, B. Zimdahl, N. D'Amato and S. Honeycutt for experimental help. T.R. is a recipient of a CRI Investigator Award, an EMF New Scholar award and a Leukemia and Lymphoma Society Scholar Award. M.F. is supported by the Duke Molecular Cancer Biology Training grant and C.H.J. is funded by the California Institute of Regenerative Medicine and a sponsored research agreement with Pfizer. This work was also supported by National Institutes of Health grants DK63031, DK072234, AI067798 and the Lisa Stafford Memorial Prize to T.R.

Author Information Reprints and permissions information is available at www.nature.com/reprints. The authors declare competing financial interests: details accompany the full-text HTML version of the paper at www.nature.com/nature. Correspondence and requests for materials should be addressed to T.R. (t.reya@duke.edu).

METHODS

Mice. The *Smo*^{-/-} and *Smo*^{+/+} mice used were in a mixed 129X1/SvJ and C57BL/6J background. Transplant recipients (C57BL/6 CD45.1) were 8–10 weeks of age. All mice were bred and maintained on acidified, antibiotic water in the animal care facility at Duke University Medical Center. All animal experiments were performed according to protocols approved by the Duke University Institutional Animal Care and Use Committee.

HSC isolation and analysis. Isolation of HSCs from bone marrow and their transplantation for *in vivo* analysis of function were performed as described¹². For analysis of lineage markers, bone marrow cells from control or *Smo*^{-/-} mice were incubated with antibodies to murine Ter119 (also known as Ly76), Mac-1 (Itgam), B220 (Ptpcr) and CD3 (Cd3e) (eBiosciences), and analysed by FACS. For the reconstitution assays, bone marrow cells from control, *Smo*^{-/-} or SmoM2 mice were stained and analysed for the KLSF cells¹², and 500 control or *Smo*^{-/-} KLSF cells were injected along with 200,000 competing bone marrow cells into lethally irradiated CD45.1 recipients. Multilineage repopulation was assessed at 20 weeks. Secondary repopulation assays were carried out by isolating whole bone marrow from primary recipients originally transplanted with control or *Smo*^{-/-} KLSF cells. Recipient mice were killed and analysed for donor chimaerism at 24 weeks.

Generation and analysis of diseased mice. HSCs from *Smo*^{-/-}, SmoM2 or control mice were isolated and cultured overnight in X-vivo with 10% fetal bovine serum (FBS), 100 ng ml⁻¹ stem cell factor (SCF, also known as KITLG) and 20 ng ml⁻¹ thrombopoietin (THPO) in a 96-well U-bottom plate (50,000 per well). Subsequently, cells were infected with MSCV-BCR-ABL1-IRES-GFP or MSCV-IRES-GFP as a control. After 48 h, different cell doses ranging from 15,000–20,000 *Smo*^{-/-} or 5,000–8,000 limiting SmoM2 cells were transplanted retro-orbitally along with 200,000 whole bone marrow cells into lethally irradiated allelically mismatched recipients. After transplantation, recipient mice were evaluated daily for signs of morbidity, weight loss, failure to groom and splenomegaly. Premorbid animals were killed and relevant tissues were collected and analysed by flow cytometry and histopathology. For flow cytometric analysis of CML stem cells, leukaemic cells were stained for KLS and analysed on FACS-Vantage (BD Biosciences) and Flowjo software (Tree Star, Inc.).

Cyclopamine treatment of diseased mice. Mice were given 25 mg kg⁻¹ of cyclopamine twice a day by oral gavage beginning 6–8 days after transplantation. Treatment was continued for five consecutive days, stopped for two days, and then continued once a day until the end of the monitoring period. Mice were

visually assessed daily for signs of distress. In mice that showed signs of distress treatment was stopped and continued when they showed recovery.

Methylcellulose colony formation assays. For the colony formation assays CML KLS GFP⁺ cells, or KLSF cells infected with wild-type BCR-ABL1 or T315I BCR-ABL1 were sorted into a 24-well plate with complete methylcellulose medium (Stem Cell Technologies) containing cyclopamine (Toronto Research Chemicals) and/or imatinib (Sequoia Research Chemicals). Colonies were counted 8–10 days after plating. For the serial replating assay, cells were collected and counted, and 10,000 cells were replated into 12-well plates.

Immunofluorescence staining. Primary CML cells collected from bone marrow and spleen were sorted for KLS and GFP⁺ cells by FACS. Cells were cytospun, airdried and fixed in 4% paraformaldehyde. The primary antibody used was goat anti-Numb (Novus Biologicals), and the secondary antibody used was donkey anti-goat-Alexa Fluor 594 (Molecular Probes). DAPI (Molecular Probes) was added as a nuclear counterstain. Slides were viewed on the Axio Imager (Zeiss) at ×630 magnification. Fluorescence intensity analysis was quantified using Metamorph software (Molecular Devices).

Real-time PCR analysis. RNA was isolated using RNAqueous-Micro (Ambion) and converted to cDNA using Superscript II (Invitrogen). cDNA concentrations were measured with a fluorometer (Turner Designs) using RiboGreen reagent (Molecular Probes). Quantitative rtPCR was performed using an iCycler (BioRad) by mixing equal amounts of cDNAs, iQ SYBR Green Supermix (BioRad) and gene specific primers. Primer sequences are available on request. All real-time data was normalized to actin.

Human CML samples. All experiments on human CML samples were carried out with approval from the Duke University Institutional Review Board. Patient samples were either obtained from the Duke Adult Bone Marrow Transplant Clinic, or purchased from Open Biosystems. Mononuclear cells were isolated from peripheral blood samples using density-gradient centrifugation. RNA was isolated using RNAqueous-Micro (Ambion) and was converted to cDNA using Superscript II (Invitrogen). PCR with reverse transcription (RT-PCR) was performed (DNA Engine DYAD) with primer sequences specific to human *SMO*. Primer sequences are available on request. For all colony formation assays, samples were sorted for hCD34⁺ cells and plated into a 12-well plate (100,000 cells per well) with complete methylcellulose medium (Stem Cell Technologies) in the presence of tomatidine or cyclopamine (1 μM, Toronto Research Chemicals). Colony numbers were counted 14–17 days after plating.

LETTERS

Association of reactive oxygen species levels and radioresistance in cancer stem cells

Maximilian Diehn^{1,2*}, Robert W. Cho^{2,3*}, Neethan A. Lobo², Tomer Kalisky⁸, Mary Jo Dorie¹, Angela N. Kulp², Dalong Qian², Jessica S. Lam², Laurie E. Ailles², Manzhi Wong², Benzion Joshua⁴, Michael J. Kaplan⁴, Irene Wapnir⁵, Frederick M. Dirbas⁵, George Somlo⁹, Carlos Garberoglio¹⁰, Benjamin Paz¹⁰, Jeannie Shen¹⁰, Sean K. Lau¹¹, Stephen R. Quake⁸, J. Martin Brown¹, Irving L. Weissman^{2,6} & Michael F. Clarke^{2,7}

The metabolism of oxygen, although central to life, produces reactive oxygen species (ROS) that have been implicated in processes as diverse as cancer, cardiovascular disease and ageing. It has recently been shown that central nervous system stem cells^{1,2} and haematopoietic stem cells and early progenitors^{3–6} contain lower levels of ROS than their more mature progeny, and that these differences are critical for maintaining stem cell function. We proposed that epithelial tissue stem cells and their cancer stem cell (CSC) counterparts may also share this property. Here we show that normal mammary epithelial stem cells contain lower concentrations of ROS than their more mature progeny cells. Notably, subsets of CSCs in some human and murine breast tumours contain lower ROS levels than corresponding non-tumorigenic cells (NTCs). Consistent with ROS being critical mediators of ionizing-radiation-induced cell killing^{7,8}, CSCs in these tumours develop less DNA damage and are preferentially spared after irradiation compared to NTCs. Lower ROS levels in CSCs are associated with increased expression of free radical scavenging systems. Pharmacological depletion of ROS scavengers in CSCs markedly decreases their clonogenicity and results in radiosensitization. These results indicate that, similar to normal tissue stem cells, subsets of CSCs in some tumours contain lower ROS levels and enhanced ROS defences compared to their non-tumorigenic progeny, which may contribute to tumour radioresistance.

We began by addressing whether the low ROS concentrations that seem to be critical for self-renewal of haematopoietic stem cells (HSCs)^{3,5} are also a property of mammary epithelial stem cells^{9,10}. We isolated CD24^{med}CD49^{high}Lin[−] mammary cells—a population enriched for mammary repopulating units (MRUs)—and CD24^{high}CD49^{low}Lin[−] progenitor cells by flow cytometry (Supplementary Fig. 1), and then measured the intracellular concentrations of prooxidants using 2′-7′-dichlorofluorescein diacetate (DCF-DA) staining³. Cells in the MRU-enriched population contained significantly lower concentrations of ROS than the progenitor-enriched cells in two different strains of mice (Fig. 1a–c). Specifically, the MRU-enriched populations showed low to intermediate ROS levels, whereas the progenitor-enriched populations contained more uniformly high levels. Similarly, analysis of the two populations using MitoSOX Red—a highly selective detection method for mitochondrial superoxide—demonstrated lower superoxide levels in the MRU-enriched population (Fig. 1d). To assess whether mammary repopulating activity was related to intracellular concentrations of ROS, we transplanted CD24^{med}CD49^{high}Lin[−] cells on the basis of their

DCF-DA staining levels. Mammary stem cells with low and intermediate ROS levels gave rise to epithelial outgrowths when transplanted into cleared fat pads (Supplementary Table 1). Similar heterogeneity of ROS concentrations was recently demonstrated in HSC-enriched populations^{5,11}, where it may have functional importance in modulating the HSC-niche interaction¹².

Given the conservation of low ROS levels in several types of normal tissue stem cells, we proposed that CSCs in some tumours may also contain lower concentrations of ROS than their non-tumorigenic progeny. To investigate ROS biology in human CSCs, we began by examining the expression of genes involved in ROS metabolism in primary human breast CSCs and NTCs. Using microarray data from human breast CSC-enriched populations and NTCs¹³, and a curated list of genes involved in ROS metabolism⁵ (see Methods), gene set enrichment analysis (GSEA)¹⁴ revealed that the expression of ROS genes was highly over-represented in the CD44⁺CD24^{−/low}Lin[−] breast CSC-enriched population compared to the NTCs ($P < 0.001$; Supplementary Fig. 2). The ROS genes identified as the core-enriched genes by GSEA included several important antioxidant genes (Supplementary Table 2). Thus, gene expression profiles of human breast CSC-containing populations suggest that they contain higher levels of antioxidant defence systems than NTCs.

Next we directly assessed ROS levels in human tumour subpopulations. To do this the CD44⁺CD24^{−/low}Lin[−] breast CSC-enriched population and the corresponding ‘not CD44⁺CD24^{−/low}Lin[−]’ NTC population were purified from surgically resected breast tumours (Supplementary Fig. 3). DCF-DA staining showed that the CSC-enriched population in the human breast tumours we examined contained considerably lower levels of prooxidants than the NTC population. In some breast tumours, most of the cells in the CSC-containing fraction displayed a low ROS phenotype compared to the NTCs (Fig. 1e), whereas in others it was restricted to a significant subset of CSCs (Supplementary Fig. 4). We found a similar enrichment of cells with low ROS concentrations in a head and neck tumour (Supplementary Fig. 4). Thus, CSC-enriched populations from some human tumours contain lower average intracellular ROS levels than corresponding NTC populations.

Recently, we have demonstrated that Thy1⁺CD24⁺Lin[−] cells in most spontaneously developing breast tumours from mouse mammary tumour virus (MMTV)-Wnt1 mice are highly enriched for tumorigenic activity¹⁵ (Supplementary Fig. 5a). We therefore addressed whether the CSC-enriched population in this model system also shows a low ROS phenotype. ROS analysis using DCF-DA demonstrated that in tumours

¹Department of Radiation Oncology, ²Stanford Institute for Stem Cell Biology and Regenerative Medicine, ³Department of Pediatrics Division of Stem Cell Transplantation, ⁴Department of Otolaryngology—Head and Neck Surgery, ⁵Department of Surgery, ⁶Departments of Pathology and Developmental Biology, ⁷Department of Medicine, Stanford University School of Medicine, Stanford, California 94305, USA. ⁸Department of Bioengineering and Howard Hughes Medical Institute, Stanford University, Stanford, California 94305, USA. ⁹Department of Medical Oncology and Therapeutics Research, ¹⁰Department of Surgery, ¹¹Department of Pathology, City of Hope National Medical Center, Duarte, California, California 91010, USA.

*These authors contributed equally to this work.

in which the $\text{Thy1}^+ \text{CD24}^+ \text{Lin}^-$ population was enriched for CSCs, this population contained a significantly higher fraction of cells with low prooxidant levels than the 'not $\text{Thy1}^+ \text{CD24}^+$, Lin^- non-tumorigenic population (Fig. 1f). $\text{Thy1}^+ \text{CD24}^+ \text{Lin}^-$ cells contained two main subpopulations of cells on the basis of ROS concentration, with the low ROS subpopulation being significantly over-represented compared to NTCs (Supplementary Fig. 5b). To confirm the presence of CSCs within the low ROS subpopulation, we transplanted CSCs on the basis of their DCF-DA staining and found that both the low and the high ROS subsets of $\text{Thy1}^+ \text{CD24}^+ \text{Lin}^-$ cells gave rise to tumours in recipient animals (Supplementary Table 3). Thus, a subset of CSCs from these MMTV-Wnt1 tumours had lower baseline levels of ROS compared to NTCs.

It is well established that cell killing after exposure to ionizing radiation and a subset of cytotoxic chemotherapeutics is partially mediated by free radicals¹⁶. Given our observations of increased

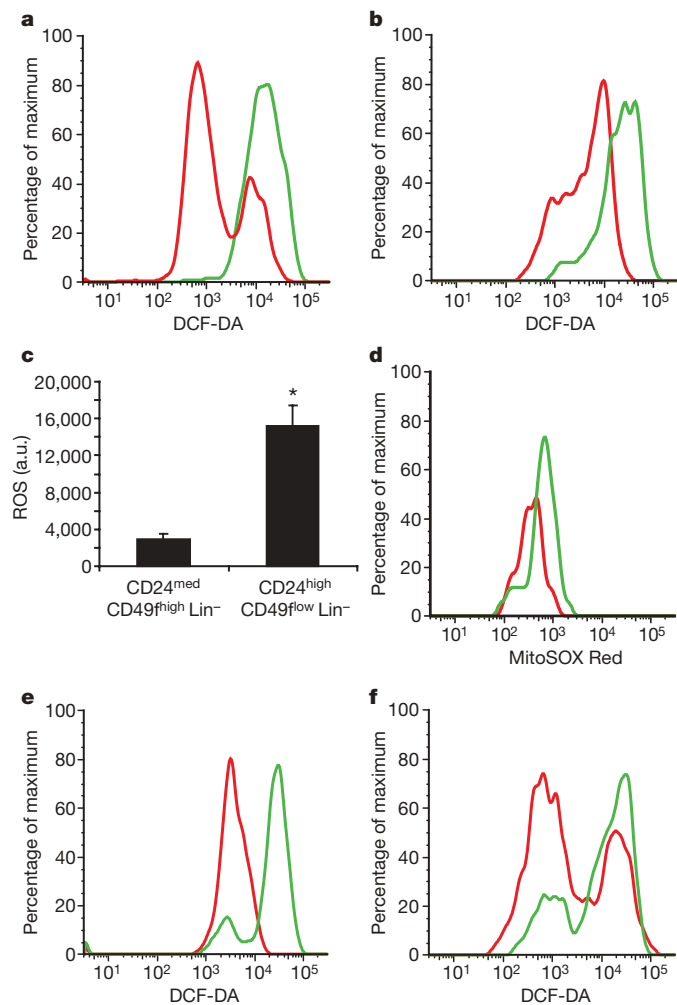


Figure 1 | Analysis of ROS levels in normal mammary and breast cancer stem cells and their progeny. **a**, $\text{CD24}^{\text{med}} \text{CD49}^{\text{high}} \text{Lin}^-$ mammary cells (mammary stem-cell-containing population; red) and $\text{CD24}^{\text{high}} \text{CD49}^{\text{low}} \text{Lin}^-$ mammary cells (progenitor cell-containing population; green) were isolated from C57BL/6J female mice using flow cytometry, and intracellular ROS concentrations were measured by DCF-DA staining. **b**, As in **a** except using 29S1/SvImJ mice. **c**, The mean and s.e.m. for replicates of **a** and **b** are shown ($n = 6$, $*P = 0.001$). a.u., arbitrary units. **d**, As in **b** but using MitoSOX Red instead of DCF-DA. Data shown are representative of two independent experiments. **e**, $\text{CD44}^+ \text{CD24}^{-/\text{low}} \text{Lin}^-$ breast cancer cells (CSC-containing population; red) and 'not $\text{CD44}^+ \text{CD24}^{-/\text{low}}, \text{Lin}^-$ cells (non-tumorigenic population; green) were isolated from a primary human breast tumour by flow cytometry and ROS levels were analysed using DCF-DA. **f**, As in **e** but using murine $\text{Thy1}^+ \text{CD24}^+ \text{Lin}^-$ breast cancer cells (CSC-containing population; red) and 'not $\text{Thy1}^+ \text{CD24}^+, \text{Lin}^-$ cells (non-tumorigenic population; green) isolated from an MMTV-Wnt1 breast tumour.

expression of ROS defence genes in CSCs, we were interested in testing whether CSC-enriched populations develop less DNA damage than NTCs after ionizing radiation. To examine DNA damage immediately after irradiation, we purified $\text{Thy1}^+ \text{CD24}^+ \text{Lin}^-$ cells and NTCs from MMTV-Wnt1 tumours by flow cytometry and irradiated them on ice. Cells were then either left on ice or incubated at 37 °C, before being analysed using the alkaline comet assay¹⁷. Although untreated cells did not show significantly different levels of DNA damage, there were fewer DNA strand breaks in the $\text{Thy1}^+ \text{CD24}^+ \text{Lin}^-$ cells than in the NTCs immediately after exposure to ionizing radiation (Fig. 2a, b). These findings are consistent with the hypothesis that the enhanced expression of ROS defences in CSCs contributes to reduced levels of DNA damage after irradiation.

Because the alkaline comet assay mainly measures single-strand breaks, and as double-strand breaks are important for ionizing-radiation-induced lethality¹⁸, we also analysed the levels of double-strand breaks as reflected by phosphorylated histone 2AX (H2AX, also known as H2AFX) nuclear foci after *in vitro* irradiation. As with the comet assay, we again observed significantly lower levels of DNA damage in $\text{Thy1}^+ \text{CD24}^+ \text{Lin}^-$ CSC-enriched cells than in NTCs (Supplementary Fig. 6). We also measured phosphorylated H2AX foci after *in vivo* irradiation of MMTV-Wnt1 tumours, and again found that $\text{Thy1}^+ \text{CD24}^+ \text{Lin}^-$ cells contained fewer foci than NTCs (Fig. 2c). Thus, consistent with their lower baseline levels of ROS, $\text{Thy1}^+ \text{CD24}^+ \text{Lin}^-$ CSC-enriched cells isolated from these tumours developed less DNA strand breaks than NTCs after exposure to ionizing radiation.

Given these findings, CSCs would be expected to preferentially survive exposure to ionizing radiation in intact tumours. Mice bearing MMTV-Wnt1 tumours were therefore treated with short, fractionated courses of ionizing radiation and the percentage of the $\text{Thy1}^+ \text{CD24}^+ \text{Lin}^-$ CSC-enriched population before and after irradiation was analysed using flow cytometry. On average, we found an

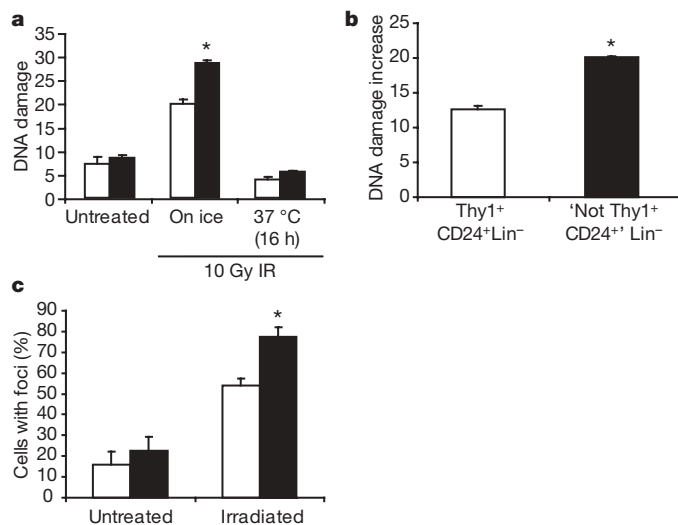


Figure 2 | $\text{Thy1}^+ \text{CD24}^+ \text{Lin}^-$ CSC-enriched cells develop less DNA damage after irradiation than non-tumorigenic cells. **a**, $\text{Thy1}^+ \text{CD24}^+ \text{Lin}^-$ cells (CSC-enriched population; open bars) and 'not $\text{Thy1}^+ \text{CD24}^+, \text{Lin}^-$ non-tumorigenic cells (filled bars) were isolated from MMTV-Wnt1 breast tumours by flow cytometry and irradiated with 10 Gy of ionizing radiation (IR). DNA damage was measured before irradiation, immediately after irradiation, and 16 h later using the alkaline comet assay. Data are the mean of median tail moments and s.e.m. ($n = 3$, $*P = 0.05$). **b**, Using the data from **a**, the difference in median tail moments between the untreated and 'on ice' time points was calculated. Data are mean and s.e.m. ($n = 3$, $*P = 0.004$). **c**, $\text{Thy1}^+ \text{CD24}^+ \text{Lin}^-$ cells (open bars) and 'not $\text{Thy1}^+ \text{CD24}^+, \text{Lin}^-$ non-tumorigenic cells (filled bars) from MMTV-Wnt1 tumours that were processed and collected 15 min after being irradiated *in vivo* with 1 Gy of ionizing radiation were immunostained for $\gamma\text{-H2AX}$, a marker of DNA double-strand breaks. Data are mean and s.e.m. ($n = 2$, $*P = 0.04$).

approximately twofold increase in the percentage of the $\text{Thy1}^+ \text{CD24}^+ \text{Lin}^-$ CSC-enriched population compared with the 'not $\text{Thy1}^+ \text{CD24}^+ \text{Lin}^-$ NTCs in the irradiated tumours, suggesting that CSCs are relatively radioresistant compared with NTCs (Fig. 3a, b). We found a similar increase in the fraction of the $\text{CD44}^+ \text{Lin}^-$ CSC-enriched population when we irradiated human head and neck cancer xenografts grown in immunodeficient mice (Fig. 3c). Other investigators have documented similar radioresistance of CSCs in brain tumours¹⁹ and a breast cancer cell line²⁰. Thus, CSCs in some murine and human tumours are relatively radioresistant compared to their NTC counterparts.

Because a significant fraction of murine breast CSCs contained relatively low levels of ROS, we proposed that these cells may express enhanced levels of ROS defences compared to their NTC counterparts. We were particularly interested in glutathione (GSH), a critical cellular reducing agent and antioxidant that has been implicated in chemotherapy and radiotherapy resistance of cancer cells²¹. As our previous analyses demonstrated heterogeneity in CSC-enriched populations, and because single-cell gene expression studies have shown significant variations in gene expression in other stem cell populations²², we investigated the expression of critical GSH biosynthesis genes in MMTV-Wnt1 CSCs and NTCs using single-cell quantitative PCR with reverse transcription (qRT-PCR). This analysis showed significant overexpression of *Gclm* ($P < 0.001$) and *Gss* ($P < 0.005$) in a large fraction of cells within the CSC-enriched population, the former of which encodes the regulatory subunit of the enzyme (glutamate-cysteine ligase) that catalyses the rate-limiting step of GSH synthesis (Fig. 4a)²³. Furthermore *Foxo1*, a transcription factor implicated in the regulation of an anti-ROS gene expression program in HSCs⁵, was also overexpressed in CSCs compared to NTCs ($P < 0.001$; Fig. 4a). Other genes, including *Hif1a*, *Epas1* and *Foxo4*, were not differentially expressed. Thus, genes controlling GSH biosynthesis were overexpressed by many cells within the CSC-enriched population isolated from this tumour.

To pharmacologically manipulate ROS levels separately in CSCs and NTCs, we used *in vitro* culture conditions that allowed both cell

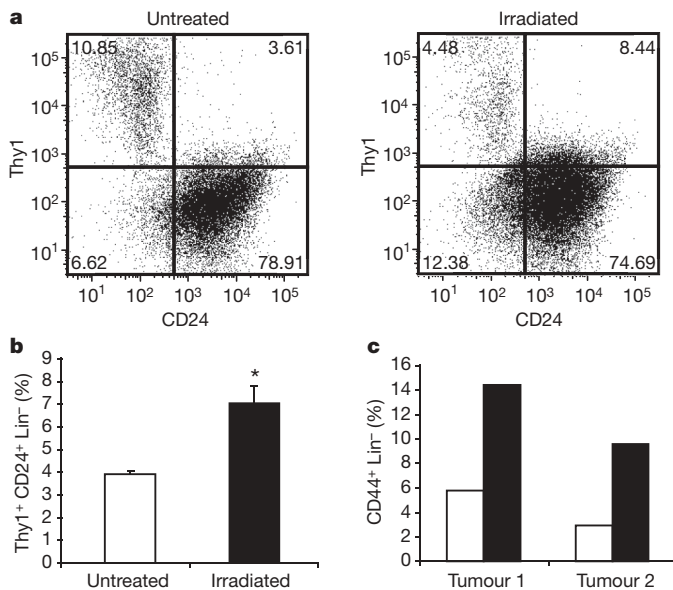


Figure 3 | Enrichment of CSCs after *in vivo* irradiation. **a**, Breast tumours from MMTV-Wnt1 mice were irradiated *in vivo* with 3×5 Gy or 5×2 Gy. The percentage of $\text{Thy1}^+ \text{CD24}^+ \text{Lin}^-$ cells in untreated and irradiated tumours was quantified by flow cytometry 72 h after the last fraction was delivered. **b**, The mean and s.e.m. for replicates of **a** are shown ($n = 6$, $*P = 0.008$). **c**, First generation xenografts established from two different primary human head and neck cancers were irradiated *in vivo* with 2×3 Gy (filled bars) or with untreated control (open bars). The percentage of $\text{CD44}^+ \text{Lin}^-$ cells was quantified as above.

populations to produce colonies after co-culture with irradiated feeder cells. We found that $\text{Thy1}^+ \text{CD24}^+ \text{Lin}^-$ CSC-enriched cells were relatively radioresistant compared with NTCs (Fig. 4b and Supplementary Fig. 7). When exposed to 2 Gy—a dose commonly administered clinically during daily treatments of breast cancer patients—twofold ± 0.2 more CSC-enriched colonies survived than NTC colonies. Next, we attempted to radioprotect NTCs by exposing them to the nitroxide antioxidant tempol²⁴. Pretreatment with tempol radioprotected NTCs, and resulted in survival levels similar to those seen in the CSC-enriched population (Fig. 4c).

Given the overexpression of genes involved in GSH synthesis by CSCs, we wished to assess the sensitivity of these cells to ROS increase by pharmacological depletion of GSH. Exposure of $\text{Thy1}^+ \text{CD24}^+ \text{Lin}^-$ CSC-enriched cells to L-S,R-buthionine sulphoximine (BSO), which inhibits glutamate-cysteine ligase²⁵, decreased their colony forming ability by approximately threefold (Fig. 4d). Finally, we addressed whether GSH depletion would radiosensitize CSCs. As shown in Fig. 4e, BSO pretreatment of $\text{Thy1}^+ \text{CD24}^+ \text{Lin}^-$ CSC-enriched cells led to significant radiosensitization. These data demonstrate the importance of low ROS levels and antioxidant defences to CSC survival and radiosensitivity in these tumours.

Our data indicate that normal breast stem cells and a subset of CSCs in some tumours arising in both mice and humans contain lower levels of

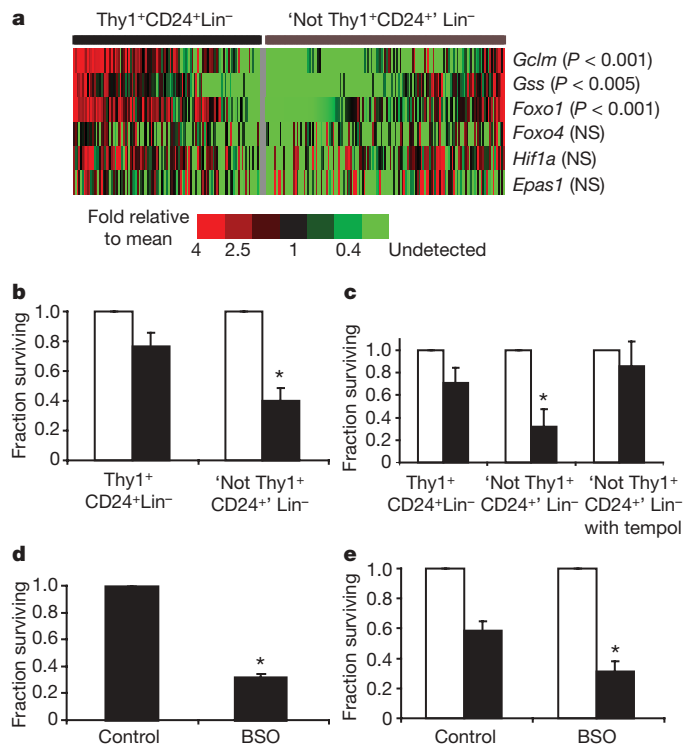


Figure 4 | $\text{Thy1}^+ \text{CD24}^+ \text{Lin}^-$ cells overexpress genes involved in ROS scavenging and pharmacological modulation of ROS levels affects the radiosensitivity of $\text{Thy1}^+ \text{CD24}^+ \text{Lin}^-$ and 'not $\text{Thy1}^+ \text{CD24}^+ \text{Lin}^-$ cells. **a**, Single-cell qRT-PCR analysis of gene expression in $\text{Thy1}^+ \text{CD24}^+ \text{Lin}^-$ CSC-enriched cells and 'not $\text{Thy1}^+ \text{CD24}^+ \text{Lin}^-$ non-tumorigenic cells. The heatmap displays the mean centred cycling threshold (C_t) values. **b**, Clonogenic survival of $\text{Thy1}^+ \text{CD24}^+ \text{Lin}^-$ CSC-enriched cells and 'not $\text{Thy1}^+ \text{CD24}^+ \text{Lin}^-$ non-tumorigenic cells before (open bars) and after (filled bars) 2 Gy of ionizing radiation ($n = 3$, $*P = 0.001$). **c**, Clonogenic survival of 'not $\text{Thy1}^+ \text{CD24}^+ \text{Lin}^-$ non-tumorigenic cells before (open bars) and after (filled bars) 2 Gy of ionizing radiation, and in the presence of 10 mM of the ROS scavenger tempol ($n = 2$, $*P = 0.03$). **d**, Clonogenic survival of $\text{Thy1}^+ \text{CD24}^+ \text{Lin}^-$ CSC-enriched cells in the presence or absence of 24-h pretreatment with 1 mM of the glutathione synthesis inhibitor BSO ($n = 3$, $*P = 0.002$). **e**, Clonogenic survival of $\text{Thy1}^+ \text{CD24}^+ \text{Lin}^-$ CSC-enriched cells before (open bars) or after (filled bars) 3 Gy of ionizing radiation, with or without BSO pretreatment ($n = 3$, $P = 0.03$). All data are mean and s.e.m.

ROS than their cellular descendants. Taken together with previous reports of low ROS concentrations in other normal tissue stem cells, these findings indicate that stem cells in diverse systems have conserved this attribute, which probably helps to protect their genomes from endogenous and exogenous ROS-mediated damage. The mechanism leading to low ROS levels in some CSCs seems to be at least partially due to the increased production of free radical scavengers. Notably, there seems to be marked heterogeneity of ROS levels in both normal stem cell and CSC-enriched populations, which could indicate that the enriched populations contain both stem and non-stem cells, and/or that ROS levels in stem cells can differ on the basis of environmental factors that alter the balance of endogenous production and the expression of scavenging pathways. The low ROS subset found in the various stem cell populations may also represent a quiescent subpopulation. Heterogeneity of ROS levels may influence the extent to which CSC-enriched populations are resistant to therapies such as ionizing radiation.

In light of recent findings that CSCs in glioblastoma multiforme display enhanced DNA repair capabilities¹⁹, it seems that CSCs may resist standard cytotoxic therapies through a combination of mechanisms, and that these may be unique to a given tumour. In the case of human CSCs, the frequency with which these cells show low ROS levels or enhanced DNA repair remains to be determined, particularly as the normal transformation precursor may be either stem or progenitor cells^{26,27} and because ROS concentration (Fig. 1 and refs 5, 28) and increased DNA repair capabilities seem to partially reflect differentiation state. Clinical therapies could probably be optimized by patient- and tumour-specific identification of CSC-resistance mechanisms, and overcoming low ROS levels in CSCs may be a useful method for improving local and systemic oncological therapies.

METHODS SUMMARY

Cells were analysed, collected by FACS and injected into recipient mice as described with minor modifications from mouse mammary glands¹⁰, human breast²⁹ cancers, human head and neck³⁰ cancers and MMTV-Wnt1 mouse tumours¹⁵. For human samples, informed consent was obtained after the approval of protocols by the Stanford University and City of Hope Institutional Review Boards. For intracellular ROS analysis, cells were loaded with 10 μ M DCF-DA (Invitrogen), incubated at 37 °C for 30 min, and immediately analysed by flow cytometry. Cells were resorted on the basis of their level of DCF-DA staining for transplant experiments. For MitoSOX Red experiments, cells were loaded with 5 μ M MitoSOX Red at 37 °C for 20 min. DNA damage was evaluated using the single-cell gel electrophoresis assay under alkaline conditions¹⁷. For γ -H2AX immunostaining, purified cells were cytospun onto poly-L-lysine coated slides, fixed, permeabilized and stained with a phospho-specific (Ser 139) histone H2AX antibody (Cell Signaling Technology) followed by a secondary Alexa Fluor 488-conjugated antibody (Invitrogen). For single-cell gene expression analysis, cells were sorted into 96-well plates containing CellsDirect qRT-PCR mix (Invitrogen). After reverse transcription, genes were pre-amplified (22 cycles) using the same Taqman primers (Applied Biosystems) used for quantification. Products were analysed using qPCR DynamicArray microfluidic chips (Fluidigm). For *in vitro* colony assays, cells were cultured in Epicult B medium (StemCell Technologies) with 5% serum in the presence of \sim 13,000 cm^{-2} irradiated NIH-3T3 cells. After 24–48 h, the media was replaced with serum-free Epicult B, and colonies were counted \sim 7 days later. GSEA¹⁴ was performed using previously published microarray data¹³ of CSCs and NTCs from primary breast tumour samples and a curated list of ROS genes (Supplementary Table 4). Levels of significance were determined by Student's *t*-tests using $\alpha = 0.05$.

Full Methods and any associated references are available in the online version of the paper at www.nature.com/nature.

Received 6 September 2007; accepted 18 December 2008.

Published online 4 February 2009; corrected 9 April 2009 (details online).

- Smith, J., Ladi, E., Mayer-Proschel, M. & Noble, M. Redox state is a central modulator of the balance between self-renewal and differentiation in a dividing glial precursor cell. *Proc. Natl Acad. Sci. USA* **97**, 10032–10037 (2000).
- Tsatmali, M., Walcott, E. C. & Crossin, K. L. Newborn neurons acquire high levels of reactive oxygen species and increased mitochondrial proteins upon differentiation from progenitors. *Brain Res.* **1040**, 137–150 (2005).
- Ito, K. *et al.* Regulation of oxidative stress by ATM is required for self-renewal of haematopoietic stem cells. *Nature* **431**, 997–1002 (2004).

- Ito, K. *et al.* Reactive oxygen species act through p38 MAPK to limit the lifespan of hematopoietic stem cells. *Nature Med.* **12**, 446–451 (2006).
- Tothova, Z. *et al.* FoxOs are critical mediators of hematopoietic stem cell resistance to physiologic oxidative stress. *Cell* **128**, 325–339 (2007).
- Miyamoto, K. *et al.* Foxo3a is essential for maintenance of the hematopoietic stem cell pool. *Cell Stem Cell* **1**, 101–112 (2007).
- Powell, S. & McMillan, T. J. DNA damage and repair following treatment with ionizing radiation. *Radiat. Oncol.* **19**, 95–108 (1990).
- Ward, J. F. Biochemistry of DNA lesions. *Radiat. Res.*, Suppl. 8, S103–S111 (1985).
- Shackleton, M. *et al.* Generation of a functional mammary gland from a single stem cell. *Nature* **439**, 84–88 (2006).
- Stingl, J. *et al.* Purification and unique properties of mammary epithelial stem cells. *Nature* **439**, 993–997 (2006).
- Jang, Y. Y. & Sharkis, S. J. A low level of reactive oxygen species selects for primitive hematopoietic stem cells that may reside in the low-oxygenic niche. *Blood* **110**, 3056–3063 (2007).
- Hosokawa, K. *et al.* Function of oxidative stress in the regulation of hematopoietic stem cell-niche interaction. *Biochem. Biophys. Res. Commun.* **363**, 578–583 (2007).
- Liu, R. *et al.* The prognostic role of a gene signature from tumorigenic breast-cancer cells. *N. Engl. J. Med.* **356**, 217–226 (2007).
- Subramanian, A. *et al.* Gene set enrichment analysis: a knowledge-based approach for interpreting genome-wide expression profiles. *Proc. Natl Acad. Sci. USA* **102**, 15545–15550 (2005).
- Cho, R. W. *et al.* Isolation and molecular characterization of cancer stem cells in MMTV-Wnt1 murine breast tumors. *Stem Cells* **26**, 364–371 (2008).
- Riley, P. A. Free radicals in biology: oxidative stress and the effects of ionizing radiation. *Int. J. Radiat. Biol.* **65**, 27–33 (1994).
- Dorie, M. J. *et al.* DNA damage measured by the comet assay in head and neck cancer patients treated with tirapazamine. *Neoplasia* **1**, 461–467 (1999).
- Cohen-Jonathan, E., Bernhard, E. J. & McKenna, W. G. How does radiation kill cells? *Curr. Opin. Chem. Biol.* **3**, 77–83 (1999).
- Bao, S. *et al.* Glioma stem cells promote radioresistance by preferential activation of the DNA damage response. *Nature* **444**, 756–760 (2006).
- Phillips, T. M., McBride, W. H. & Pajonk, F. The response of CD24^{low}/CD44⁺ breast cancer-initiating cells to radiation. *J. Natl. Cancer Inst.* **98**, 1777–1785 (2006).
- Estrela, J. M., Ortega, A. & Obrador, E. Glutathione in cancer biology and therapy. *Crit. Rev. Clin. Lab. Sci.* **43**, 143–181 (2006).
- Warren, L., Bryder, D., Weissman, I. L. & Quake, S. R. Transcription factor profiling in individual hematopoietic progenitors by digital RT-PCR. *Proc. Natl Acad. Sci. USA* **103**, 17807–17812 (2006).
- Griffith, O. W. Biologic and pharmacologic regulation of mammalian glutathione synthesis. *Free Radic. Biol. Med.* **27**, 922–935 (1999).
- Hahn, S. M. *et al.* Potential use of nitroxides in radiation oncology. *Cancer Res.* **54**, 2006s–2010s (1994).
- Bailey, H. H. L-S-R-buthionine sulfoximine: historical development and clinical issues. *Chem. Biol. Interact.* **111–112**, 239–254 (1998).
- Jamieson, C. H. *et al.* Granulocyte-macrophage progenitors as candidate leukemic stem cells in blast-crisis CML. *N. Engl. J. Med.* **351**, 657–667 (2004).
- Akala, O. O. *et al.* Long-term haematopoietic reconstitution by *Trp53^{-/-}p16Ink4a^{-/-}p19Arf^{-/-}* multipotent progenitors. *Nature* **453**, 228–232 (2008).
- Saretzki, G. *et al.* Downregulation of multiple stress defense mechanisms during differentiation of human embryonic stem cells. *Stem Cells* **26**, 455–464 (2008).
- Al-Hajj, M., Wicha, M. S., Benito-Hernandez, A., Morrison, S. J. & Clarke, M. F. Prospective identification of tumorigenic breast cancer cells. *Proc. Natl Acad. Sci. USA* **100**, 3983–3988 (2003).
- Prince, M. E. *et al.* Identification of a subpopulation of cells with cancer stem cell properties in head and neck squamous cell carcinoma. *Proc. Natl Acad. Sci. USA* **104**, 973–978 (2007).

Supplementary Information is linked to the online version of the paper at www.nature.com/nature.

Acknowledgements We thank D. Spitz for helpful discussions and D. Menke, D. Rossi, and J. Seita for technical assistance. This work was supported by grants from the National Institutes of Health (M.F.C., G.S. and I.L.W.), the Virginia and D.K. Ludwig Foundation (M.F.C. and I.L.W.), the Breast Cancer Research Foundation (M.F.C.), the Machiah foundation (T.K.), the American Society for Therapeutic Radiology and Oncology (M.D.), and the Radiological Society of North America (M.D.). M.D. is a recipient of the Leonard B. Holman Research Pathway fellowship.

Author Contributions M.D. and R.W.C. contributed equally to this work. M.D., R.W.C., N.A.L., T.K., M.J.D., A.N.K., D.Q., J.S.L., L.A. and M.W. performed the experiments. B.J., M.J.K., I.W., F.D., G.S., C.G., B.P., J.S. and S.K.L. aided in human tumour tissue acquisition. G.S. designed a pre-operative protocol allowing for tissue acquisition. M.D., R.W.C. and M.F.C. designed the experiments and wrote the manuscript. S.R.Q., J.M.B. and I.L.W. provided intellectual input and aided in experimental design.

Author Information Reprints and permissions information is available at npg.nature.com/reprintsandpermissions. The authors declare competing financial interests: details accompany the full-text HTML version of the paper at www.nature.com/nature. Correspondence and requests for materials should be addressed to M.F.C. (mfclarke@stanford.edu).

METHODS

Murine mammary stem cell isolation. Mammary glands from 6–12-week-old female C57BL/6j or 129S1/SvImJ mice were dissociated as described¹⁰ with minor modifications. Specifically, mammary fat pads were collected and placed directly into Medium 199 (Gibco BRL) supplemented with 20 mM HEPES and penicillin, streptomycin and actinomycin. Tissue was minced using sterile razor blades and 4 Wünsch units of Liberase Blendzyme 4 (Roche) and 100 Kunitz units of DNase I (Sigma) were added. Tissue was incubated for 60–90 min in a 37 °C and 5% CO₂ incubator, during which the cells were mechanically aspirated every 30 min. Cells were pelleted by centrifugation for 5 min at 4 °C and 350g. After lysis of the red blood cells with ACK lysis buffer (Gibco BRL), a single-cell suspension was obtained by further enzymatic digestion for ~2 min in 0.25% trypsin, followed by another ~2 min in 5 mg ml⁻¹ dispase II (StemCell Technologies) plus 200 Kunitz units DNase I (Sigma). Cells were then filtered through 40-µm nylon mesh, pelleted and resuspended in staining media (HBSS and 2% heat-inactivated calf serum (HICS)). Cells were counted using trypan blue dye exclusion.

Tumour dissociation. Human and mouse tumours were dissociated as previously described¹⁵ with minor modifications. Depending on the time of the surgical case, some of the human tumours were kept overnight at 4 °C before dissociation. Tumours from patients or from MMTV-Wnt1 tumour-bearing FVB/NJ female mice were minced with a razor blade and suspended in 20 ml of Medium 199 (Gibco BRL) supplemented with 20 mM HEPES. The dissociation enzyme cocktail consisted of 100 Kunitz units of DNase I (Sigma), 8 Wünsch units of Liberase Blendzyme 2 (Roche) and 8 Wünsch units Liberase Blendzyme 4 (Roche). Tumours were digested to completion (1.5–2.5 h at 37 °C and 5% CO₂) with pipetting every 30 min for manual dissociation. Once digested, 30 ml of RPMI (BioWhittaker) with 10% HICS was added to the digestion solution to inactivate the collagenases. A 40-µm nylon filter was used to filter the sample. After pelleting, cells were resuspended in 5 ml of ACK buffer for red blood cell lysis. HBSS (BioWhittaker) with 2% HICS was used to dilute the ACK buffer and the cells were again filtered through a 40-µm nylon filter. The filtered cells were spun down and resuspended in HBSS with 2% HICS.

Cell staining and flow cytometry. Cells were stained at a concentration of 1 × 10⁶ cells per 100 µl of HBSS with 2% HICS (staining media). Cells were blocked with rabbit or mouse IgG (1 mg ml⁻¹) at 1:100 dilution and antibodies were added at appropriate dilutions determined from titration experiments. For the normal mammary stem cell experiments, antibodies included CD49f, CD31, CD45, Ter119 (BD Pharmingen), CD24, Thy1.2 and CD140a (eBioscience). For the murine MMTV-Wnt1 breast cancer experiments, antibodies included CD24, Thy1.1, CD140a (eBioscience), CD45 and CD31 (BD Pharmingen). For the human breast cancer experiments, antibodies included CD44, CD24, CD45, CD3, CD20, CD10, glycophorin A (BD Pharmingen), CD31 (eBioscience) and CD64 (Dako). For the primary human head and neck cancer experiment, antibodies included CD44, CD45 (BD Pharmingen) and CD31 (eBioscience), and for the xenograft experiments, antibodies included CD44, mCD45 (BD Pharmingen), mCD31 (Abcam) and H-2K^d (eBioscience). Cells were stained for 20 min on ice and washed with staining media. When biotinylated primary antibodies were used, cells were further stained with streptavidin-conjugated fluorophores and washed. Ultimately, cells were resuspended in staining media containing 7-aminoactinomycin D (1 µg ml⁻¹ final concentration) or 4'-6-diamidino-2-phenylindole (DAPI, 1 µg ml⁻¹ final concentration) to stain dead cells.

For all experiments, cells were analysed and sorted using a FACSAria cell sorter (BD Bioscience). Side scatter and forward scatter profiles were used to eliminate debris and cell doublets. Dead cells were eliminated by excluding DAPI⁺ cells, whereas contaminating human or mouse Lin⁺ cells were eliminated by excluding cells labelled with the fluorophore used for the lineage antibody cocktail. In cell-sorting experiments, cell populations underwent two consecutive rounds of purification (double sorting) when the initial purity was not deemed high enough and a sufficient number of cells were available. Final purities ranged from ~60% to >95%.

MMTV-Wnt1 breast tumour radiation experiments. For *in vivo* irradiation experiments, tumour-bearing animals were irradiated on consecutive days with the indicated doses of ionizing radiation using a 160 kVp cabinet irradiator (Faxitron). Tumours were grown on the ventral surface of mice in the vicinity of the second mammary fat pad and the delivered dose was adjusted to compensate for attenuation by overlying tissues. Seventy-two hours after the final fraction was delivered, tumours were collected, dissociated and analysed by flow cytometry as above. For each experiment, at least one untreated control tumour was analysed in parallel. When multiple control tumours were available, the percentage of Thy1⁺ CD24⁺ Lin⁻ cells in these tumours was averaged to define the baseline percentage of Thy1⁺ CD24⁺ Lin⁻ cells for that experiment. In other experiments, tumours were irradiated and these tumours along with controls

were collected 15 min after irradiation. Tumours were dissociated as above and cells were stained with a phospho-specific (Ser 139) histone H2AX antibody (Cell Signaling Technology) as described in the Methods Summary.

Human breast and head and neck cancer primary specimens. Primary tumour specimens were obtained with informed consent after approval of protocols by the Stanford University and City of Hope Institutional Review Boards. Tumours were from untreated patients, except for the two breast cancer tumours shown in Supplementary Fig. 2a–d, which had been treated with neoadjuvant chemotherapy before resection.

Human head and neck cancer xenograft radiation experiments. Tumours were grown subcutaneously on the backs of Rag2/cytokine receptor common γ -chain double knockout (Rag2 γ DKO) mice as previously described³⁰. Mice were irradiated as described earlier, except that for each fraction half of the dose was delivered from the left side of the animal and half from the right. The non-tumour-bearing portions of each animal were shielded using custom-made lead chambers.

MMTV-Wnt1 DCF-DA transplant experiments. Lin⁻ or Thy1⁺ CD24⁺ Lin⁻ cells from tumours were sorted as described above. Cells were loaded with 10 µM DCF-DA (Invitrogen), incubated at 37 °C for 30 min, and sorted into 'ROS low' and 'ROS high' sub-populations on the basis of their DCF-DA staining profile. Sorted cells were injected into FVB female mice in Matrigel (BD Bioscience) in the vicinity of the second mammary fat pad at the indicated cell numbers.

Normal mammary stem cell DCF-DA transplant experiments. CD24^{med} CD49^{high} Lin⁻ mammary cells (enriched for mammary repopulating units) were isolated from mammary fat pads from C57BL/6j female mice as described above. Cells were loaded with 10 µM DCF-DA (Invitrogen), incubated at 37 °C for 30 min, and sorted into 'ROS low' and 'ROS mid' sub-populations on the basis of their DCF-DA staining profile (in comparison to that of CD24^{high} CD49^{low} Lin⁻ progenitor cells, which showed an 'ROS high' profile). Mammary glands of 21-day-old female C57BL/6j mice were cleared of endogenous epithelium as previously described¹⁰, and sorted cells were injected into each cleared fat pad using a Hamilton syringe. Injected glands were removed for wholemount analysis after 5–6 weeks. Transplants were scored as positive if epithelial structures consisting of ducts with lobules and/or terminal end buds and that arose from a central point were present.

In vitro colony assay. Sorted tumour cells were cultured in Epicult B medium (StemCell Technologies) with 5% serum in the presence of ~13,000 cm⁻² irradiated NIH-3T3 cells. After 24–48 h, the media was replaced with serum-free Epicult B, and ~7 days later, colonies were fixed with acetone:methanol (1:1), stained with Giemsa and counted. Colonies were counted if they contained \geq 30 cells and the number of colonies in control wells was in the range of 30–100, depending on how many cells were sorted and the plating efficiency of a given tumour. For the BSO experiments, cells were cultured for 24 h in modified mammosphere medium³¹ in the presence or absence of 1 mM BSO, and the drug was removed immediately before irradiation. For the tempol experiments, cells were treated with 10 mM tempol for 15 min before irradiation, after which the drug was removed. For all drug experiments, 'drug only' controls were run in parallel to adjust for effects of each drug on baseline colony counts.

Gene set enrichment analysis. To define a list of genes involved in ROS metabolism and regulation, we began with a previously generated list⁵. In brief, this list was initially generated by these authors using the Gene Ontology GO:TERMFINDER program (<http://search.cpan.org/dist/GO-TermFinder/>) to classify genes by biological process, molecular function, or cellular component. The biological process terms included were: response to oxidative stress; response to reactive oxygen species; response to hydrogen peroxide; response to oxygen radical; and response to superoxide. We manually curated this list by performing PubMed-based literature searches for each gene and only retaining those that had published evidence of involvement in ROS metabolism or regulation (that is, removing genes that seemed to be included solely owing to electronic curation with inferred evidence). This trimmed the ROS gene list from 55 to 36 unique symbols (Supplementary Table 4). GSEA was then applied as previously described¹⁴. The 'core enriched genes' shown in Fig. 4 were defined by the algorithm.

Single-cell gene expression analysis. For the single-cell gene expression experiments we used qPCR DynamicArray microfluidic chips (Fluidigm). Single MMTV-Wnt1 Thy1⁺ CD24⁺ Lin⁻ CSC-enriched cells and 'not Thy1⁺ CD24⁺ Lin⁻ non-tumorigenic cells were sorted by FACS into 96-well plates containing PCR mix (CellsDirect, Invitrogen) and RNase inhibitor (SuperaseIn, Invitrogen). After hypotonic lysis, we added qRT-PCR enzymes (SuperScript III RT/Platinum Taq, Invitrogen), and a mixture containing a pool of low-concentration assays (primers/probes) for the genes of interest (Gclm-Mm00514996_m1, Gss-Mm00515065_m1, Foxo1-Mm00490672_m1, Foxo4-Mm00840140_g1, Hif1a-Mm00468875_m1, Epas1-Mm00438717_m1). Reverse transcription (15 min at 50 °C, 2 min of 95 °C) was followed by pre-amplification for 22 PCR cycles (each

cycle: 15 s at 95 °C, 4 min at 60 °C). Total RNA controls were run in parallel. The resulting amplified cDNA from each one of the cells was inserted into the chip sample inlets with Taqman qPCR mix (Applied Biosystems). Individual assays (primers/probes) were inserted into the chip assay inlets (two replicates for each). The chip was loaded for 1 h in a chip loader (Nanoflex, Fluidigm) and then transferred to a reader (Biomark, Fluidigm) for thermocycling and fluorescent quantification.

To remove low quality gene assays, we discarded gene assays in which the qPCR curves showed non-exponential increases. To remove low quality cells (for example, dead cells) we discarded cells that did not express the housekeeping genes *Actb* (beta-actin) and *Hprt1* (hypoxanthine guanine phosphoribosyl transferase 1). This resulted in a single-cell gene expression data set consisting of 248 cells (109 tumorigenic and 139 non-tumorigenic) from a total of seven chip-runs. A two-sample Kolmogorov–Smirnov (K-S) statistic was calculated to test whether genes were differentially expressed in the two populations. We generated *P* values by permuting the sample labels (that is, Thy1⁺ CD24⁺ Lin⁻ CSC-enriched cells versus ‘not Thy1⁺ CD24⁺ Lin⁻ non-tumorigenic cells) and comparing the actual K-S statistic to those in the permutation-derived null distribution. The *P* values were further corrected by Bonferroni correction to adjust for multiple hypothesis testing.

31. Liao, M. J. *et al.* Enrichment of a population of mammary gland cells that form mammospheres and have in vivo repopulating activity. *Cancer Res.* **67**, 8131–8138 (2007).

LETTERS

Structure and function of the 5'→3' exoribonuclease Rat1 and its activating partner Rai1

Song Xiang¹, Amalene Cooper-Morgan¹, Xinfu Jiao², Megerditch Kiledjian², James L. Manley¹ & Liang Tong¹

The 5'→3' exoribonucleases (XRN2s) comprise a large family of conserved enzymes in eukaryotes with crucial functions in RNA metabolism and RNA interference^{1–5}. XRN2, or Rat1 in yeast⁶, functions primarily in the nucleus and also has an important role in transcription termination by RNA polymerase II (refs 7–14). Rat1 exoribonuclease activity is stimulated by the protein Rai1 (refs 15, 16). Here we report the crystal structure at 2.2 Å resolution of *Schizosaccharomyces pombe* Rat1 in complex with Rai1, as well as the structures of Rai1 and its murine homologue Dom3Z alone at 2.0 Å resolution. The structures reveal the molecular mechanism for the activation of Rat1 by Rai1 and for the exclusive exoribonuclease activity of Rat1. Biochemical studies confirm these observations, and show that Rai1 allows Rat1 to degrade RNAs with stable secondary structure more effectively. There are large differences in the active site landscape of Rat1 compared to related and PIN (PIT N terminus) domain-containing nucleases^{17–20}. Unexpectedly, we identified a large pocket in Rai1 and Dom3Z that contains highly conserved residues, including three acidic side chains that coordinate a divalent cation. Mutagenesis and biochemical studies demonstrate that Rai1 possesses pyrophosphohydrolase activity towards 5' triphosphorylated RNA. Such an activity is important for messenger RNA degradation in bacteria²¹, but this is, to our knowledge, the first demonstration of this activity in eukaryotes and suggests that Rai1/Dom3Z may have additional important functions in RNA metabolism.

The XRN2s share two regions of sequence conservation, corresponding to residues 1–390 and 590–751 in *S. pombe* Rat1²² (Fig. 1a and Supplementary Fig. 1). The segment between them and the segment following the second region are poorly conserved (Fig. 1a). The XRN2s display processive and exclusive exoribonuclease activity towards RNA substrates with a 5' monophosphate, whereas they are essentially inactive towards RNAs with a 5' triphosphate^{15,23}. They require divalent cations (Mg²⁺ or Mn²⁺) for activity, and contain seven conserved acidic residues in the first region that are essential for function^{7,24,25}. It has been suggested that these acidic residues may be located in the active site of XRN2s, equivalent to those in other Mg²⁺-dependent nucleases such as T4 RNase H²⁵. However, XRN2s and RNase H share no sequence homology besides these motifs. No structural information is currently available on any of the XRN2s.

Rai1 has strong sequence homologues in other fungal species, including *S. pombe*²². A weak sequence homologue, known as Dom3Z, exists in mammals¹⁶, although it probably does not associate with XRN2 (ref. 13). The Rai1 proteins share no recognizable sequence homology with other proteins.

We have determined the crystal structure of the *S. pombe* Rat1–Rai1 complex at 2.2 Å resolution. The expression constructs contain residues 1–885 of Rat1 (101 kDa) and full-length Rai1 (41 kDa),

respectively. Although the last 106 residues of Rat1 are not included in the construct, deletion of the carboxy-terminal 125 residues does not affect cell viability²². The refined structure has excellent agreement with the crystallographic data and the expected geometric parameters (Supplementary Table 1). Most of the residues (90%) are in the most favoured region of the Ramachandran plot.

The structure of Rat1 shows that its two conserved regions constitute a single, large domain (Fig. 1b and Supplementary Fig. 2). The active site of Rat1 is formed primarily by residues in the first region, which has several weak structural homologues in the Protein Data Bank. All of these homologues are nucleases, including RNase H (Supplementary Fig. 3)^{17,18}. Like RNase H, Rat1 contains a cluster of acidic residues in the active site (Supplementary Fig. 4)²⁵, although there are differences in the positions of some of the equivalent acidic residues (Supplementary Fig. 5). The structural analysis suggests that Rat1 shares the same catalytic mechanism as these related nucleases²⁶.

The second conserved region of Rat1 introduces large differences in the overall landscape of the active site as compared with other related nucleases. This region makes few direct contributions to the active site but generally surrounds it, such that the active site of Rat1 is mostly a pocket (Fig. 1c and Supplementary Figs 2 and 4), whereas the equivalent region in the other nucleases is much more open (Supplementary Fig. 3). Therefore, an endonuclease activity for Rat1 is incompatible with the structure of its active site, providing the molecular basis for the exclusive exonuclease activity of the XRN2s.

Helix αD in the first conserved region is exceptionally long (Supplementary Fig. 1), and its C-terminal end is projected 30 Å away from the rest of the structure (Fig. 1b and Supplementary Fig. 2). We have named this feature of the Rat1 structure the 'tower' domain. The N-terminal region of this helix contributes several conserved residues to the active site (Supplementary Fig. 4). In comparison, the XRN1 homologues have a deletion in the C-terminal region of this helix (Supplementary Fig. 1), suggesting that the tower domain may be unique to XRN2 and serve XRN2-specific functions, for example RNA polymerase II (Pol II) termination.

Notably, the poorly conserved segment following the second conserved region (Fig. 1a) has intimate interactions with the first conserved region (Fig. 1b and Supplementary Fig. 2). Most importantly, residues 840–863 form a long loop that traverses the bottom of the first region, and are located in the centre of the interface with Rai1 (see below). A deletion mutant lacking the last 204 residues of *S. pombe* Rat1 (and therefore missing this C-terminal loop) is non-functional²², and our biochemical data showed that deletion of this loop abolished interaction with Rai1 (Supplementary Information). This C-terminal segment is located on the opposite face of Rat1 from the active site (Fig. 1b) and does not make any direct contribution to it (Supplementary Fig. 4), suggesting that it may instead be important for stabilizing the conformation of Rat1 for catalysis (see below).

¹Department of Biological Sciences, Columbia University, New York, New York 10027, USA. ²Department of Cell Biology and Neuroscience, Rutgers University, Piscataway, New Jersey 08854, USA.

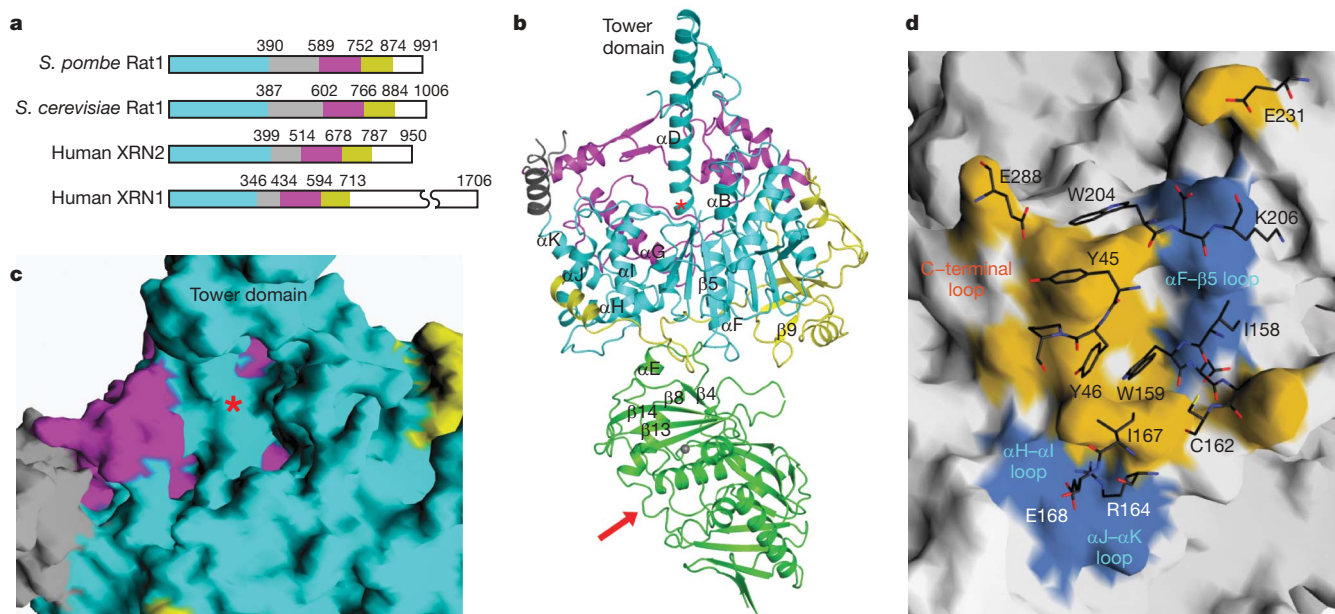


Figure 1 | Structure of the Rat1–Rai1 complex. **a**, Domain organization of *S. pombe* Rat1, *S. cerevisiae* Rat1, human XRN2 and human XRN1. The first conserved region is coloured in cyan, the second in magenta and the linker segment between them in grey. A poorly conserved segment in the C terminus that is also observed in our structure is shown in yellow. **b**, Schematic drawing of the structure of *S. pombe* Rat1–Rai1 complex. The structure of Rat1 is coloured as in **a**, and the structure of Rai1 is in green. The active site of Rat1 is indicated with the red star, and the red arrow points to

the opening of the Rai1 active site pocket. A bound divalent cation in the active site of Rai1 is shown as a grey sphere. **c**, Molecular surface of the active site region of Rat1, coloured as in **a**. **d**, Good surface complementarity at the interface between Rat1 and Rai1. Rat1 is shown as a molecular surface, and residues in the interface with Rai1 are coloured in light blue and yellow for the first conserved region and the C-terminal segment, respectively. Rai1 is shown in stick representation, with carbon atoms in black. All the structure figures were produced with PyMOL²⁹ or Grasp³⁰.

Rai1 is bound about 30 Å away and on the opposite face from the active site of Rat1 (Fig. 1b). The primary interactions involve the poorly conserved C-terminal segment of Rat1 and the β8–αE segment and strand β4 of Rai1 (Fig. 1d and Supplementary Fig. 6). Approximately 800 Å² of the surface area of Rat1 and Rai1 are buried in this interface, and the two surfaces at the interface are highly complementary to each other, with a shape correlation score of 0.76 (ref. 27), consistent with the stability of the Rat1–Rai1 complex (see below)^{15,16}.

Our structural data, together with earlier biochemical data, indicate that the activating effect of Rai1 is due at least in part to its stabilization of Rat1 structure. Rat1 alone is relatively unstable *in vitro*¹⁵ and loses nuclease activity on pre-incubation, whereas the Rat1–Rai1 complex is more stable and can retain most of its activity¹⁶. This should produce higher apparent activity for the Rat1–Rai1 complex than Rat1 alone in exoribonuclease assays. Although Rai1 does not make any direct contribution to the Rat1 active site, the C-terminal loop at the centre of the interface is essential for Rat1 activity²², suggesting that Rai1 could also stimulate Rat1 by indirectly affecting its catalysis.

Residues in the Rat1–Rai1 interface are generally conserved among the fungal proteins (Supplementary Figs 1 and 7), consistent with the fact that this interaction has been observed in *Saccharomyces cerevisiae* and *S. pombe*^{15,16,22}. However, these residues in Rai1 are not conserved in the mammalian homologue, as there is a 7-residue deletion between β8 and αE in Dom3Z (Supplementary Fig. 7). Our structure of Dom3Z alone confirms that the β8–αE region has a different conformation (Supplementary Fig. 8), and there is no evidence that Dom3Z associates with mammalian XRN2 by gel filtration (data not shown).

To assess the importance of individual residues for the stability of the Rat1–Rai1 complex, we introduced mutations in the interface and characterized their effects on the complex using gel filtration chromatography. The presence of wild-type Rai1 gave rise to a clear shift of the Rat1 peak (Fig. 2a), corresponding to the formation of the Rat1–Rai1 complex, whereas mutation of Rai1 residues in the

interface, including W159A, R164A and W204A (Fig. 1d and Supplementary Fig. 6), greatly reduced the interactions with wild-type Rat1 (Fig. 2b). Similarly, mutation of Rat1 residues in the interface also abolished interaction with wild-type Rai1 (data not shown). The migration behaviour of the mutants alone was similar to that of the wild-type protein (Fig. 2b), indicating that the mutation did not disrupt the structure of Rai1. As a control, we created the K256A mutant of Rai1. This residue is outside the interface with Rat1, and the mutation did not affect the interaction (data not shown).

To assess the functional significance of the Rat1–Rai1 interaction, we next carried out exoribonuclease assays with Rat1 alone and with Rat1 plus Rai1. We initially used three different RNA substrates (at 1 nM concentration), each labelled at the 3' end and containing a 5' monophosphate. Notably, Rat1 alone (50 nM) degraded all three substrates, but only partially, and in each case generated major intermediates that were 30–100 nucleotides smaller than the substrate (Fig. 2c, lanes 2, 6, 10). This may reflect stalling of Rat1 caused by secondary structure features in the substrates, as suggested by previous results^{15,28} (Supplementary Information). However, all three RNAs were degraded significantly more efficiently in the presence of equal molar amounts of Rai1, with roughly 60% of the substrate completely digested for each of the RNAs (Fig. 2c, lanes 3, 7, 11), whereas Rai1 alone did not show any RNase activity (Fig. 2c, lanes 4, 8, 12).

To provide evidence that Rat1 stalling was indeed due to RNA secondary structure, we used two additional substrates containing three MS2 binding sites, which form stable stem loops, very near the 5' end (1 nM concentration). With both substrates, Rat1 alone (50 nM) displayed at best weak activity, consistent with a block at the 5' MS2 hairpins (Fig. 2d, lanes 2 and 7; note that the SV40 and SV40-3MS2 substrates are identical except for the MS2 sites). In contrast, significant fractions (roughly 60%) of both RNAs were completely digested in the presence of equal molar amounts of Rai1 (Fig. 2d, lanes 3 and 8), whereas the W159A mutation abolished the stimulatory effects of Rai1 (Fig. 2d, lanes 5 and 10). Overall, these experiments indicate that Rai1 allows Rat1 to degrade RNAs with

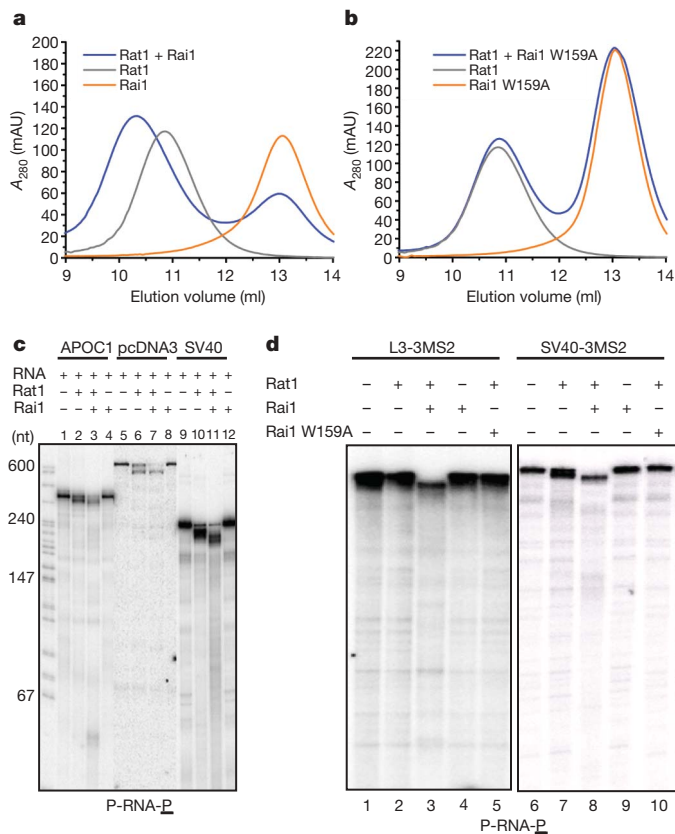


Figure 2 | Biochemical and functional characterization of the Rat1-Rai1 interaction. **a**, Gel filtration profiles for wild-type Rat1 (full length) alone, wild-type Rai1 (full length) alone, and their mixture (with Rai1 present in roughly twofold molar excess). mAU, milliabsorption unit. **b**, Gel filtration profiles for wild-type Rat1 alone, the W159A mutant of Rai1 alone, and their mixture. **c**, Cleavage of three different 5'-phosphorylated, 3'-labelled RNA substrates by Rat1 and the Rat1-Rai1 complex. The RNA substrate is indicated at the bottom of the figure, with the radiolabelled phosphate group underlined. nt, nucleotides. **d**, Cleavage of two other RNA substrates, each with three MS2 binding sites, by Rat1 and the Rat1-Rai1 complex.

stable secondary structure more effectively, and confirm the functional importance of the Rat1-Rai1 interface.

The structures of Rai1 and Dom3Z contain two highly twisted, mixed β -sheets, and several helices cover up some of the exposed surfaces of the two β -sheets (Fig. 3a). Consistent with the unique sequences of these proteins, the structures do not seem to have a close homologue in the Protein Data Bank, and they may represent a new protein fold.

Unexpectedly, the structures suggest a catalytic function for these proteins. Strikingly, there is a large pocket in their surface (Fig. 3b), and many of the side chains in this pocket are highly conserved among Rai1 homologues (Supplementary Fig. 7). Most importantly, there is a cluster of four acidic residues (Glu 150, Glu 199, Asp 201 and Glu 239 in Rai1) at the bottom of the pocket (Fig. 3a), and three of them (Glu 150, Asp 201 and Glu 239), together with the main chain carbonyl of Leu 240 and two water molecules, form the octahedral coordination sphere of a cation (Fig. 3c and Supplementary Fig. 9). In a Rat1-Rai1 crystal soaked with 50 mM $MnCl_2$, a strong difference electron density feature is observed at this position, confirming that it is a binding site for divalent cations.

The structural analysis therefore suggests that this pocket could be an active site of Rai1 and Dom3Z. This active site is distinct from the interface with Rat1, which involves a separate surface area of Rai1 (Figs 1b and 3a). In addition, the conformation of the active site region of Dom3Z is essentially the same (Supplementary Fig. 9), even though it cannot interact with Rat1, providing further evidence that

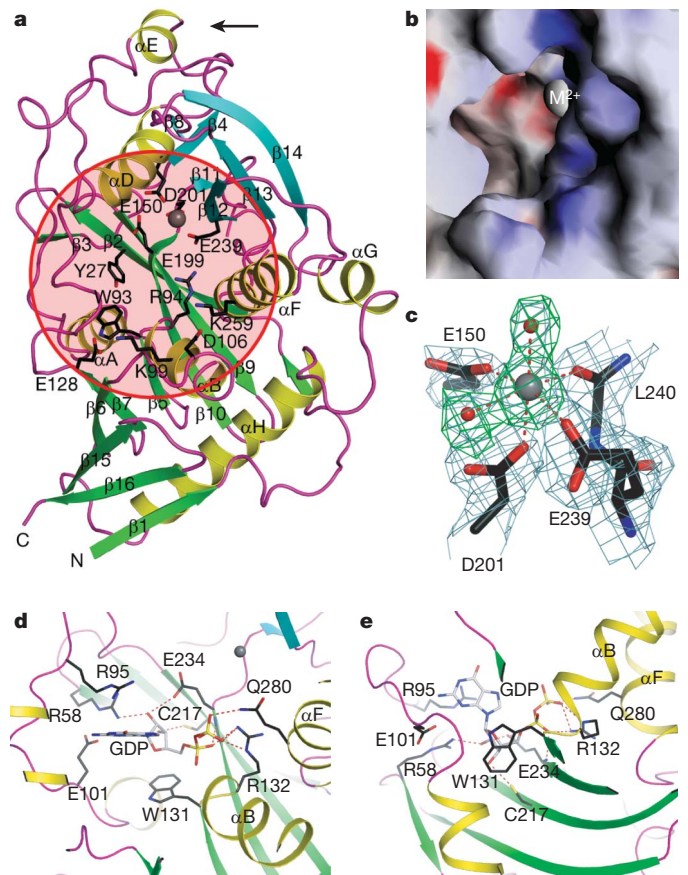


Figure 3 | Structure of Rai1. **a**, Schematic drawing of the structure of *S. pombe* Rai1. Strands in the large β -sheet are shown in green, and those in the small β -sheet in cyan. Side chains of some of the conserved residues in the large pocket in the structure are shown in black, and the pocket is highlighted in light pink. A bound divalent cation is shown as a grey sphere. The arrow indicates the interface region with Rat1. **b**, Molecular surface of Rai1, showing the large pocket in the structure. The divalent cation is labelled as M^{2+} . **c**, Final $2F_o - F_c$ electron density (in light blue) at 2.2 Å resolution for the divalent cation and its ligands in the large pocket in Rai1, contoured at 1.5 σ . Omit $F_o - F_c$ electron density for the cation and the two water molecules is shown in green, contoured at 3 σ . **d**, Schematic drawing of the detailed interactions between GDP (in light grey) and Dom3Z (side chains in black). **e**, Panel **d** after 90° rotation around the horizontal axis.

this active site may function independently of Rat1 binding. However, no enzymatic activity has been reported for Rai1 (ref. 16).

During the course of examining the effects of Rai1 on Rat1 activity, we obtained the first evidence that Rai1 possesses catalytic activity. Specifically, when we used as a substrate a 3'-labelled RNA containing a 5' triphosphate (1 nM), Rat1 alone (50 nM) displayed very weak activity (Fig. 4a, lane 2). Notably, addition of Rai1 (50 nM) resulted in efficient degradation of this substrate (Fig. 4a, lane 3). To determine whether this required the active site of Rai1, we mutated two of the conserved acidic residues in this region, E199A and D201A. Notably, the double mutation abolished the degradation of the RNA substrate with a 5' triphosphate (Fig. 4a, lane 7), but did not disrupt the stimulatory effect on hydrolysis of the RNA with a 5' monophosphate (Supplementary Fig. 10, lane 7). As a control, the K256A mutation, located outside the Rat1-Rai1 interface and the active site of Rai1, did not affect hydrolysis of either substrate (Fig. 4a, lane 5; Supplementary Fig. 10, lane 5).

These experimental data suggest that Rai1 could possess RNA 5' pyrophosphohydrolase activity, which would convert the 5' triphosphate group to a single phosphate, making the RNA a substrate for Rat1. To obtain additional evidence for this, we pre-incubated a 3'-labelled RNA substrate containing a 5' triphosphate

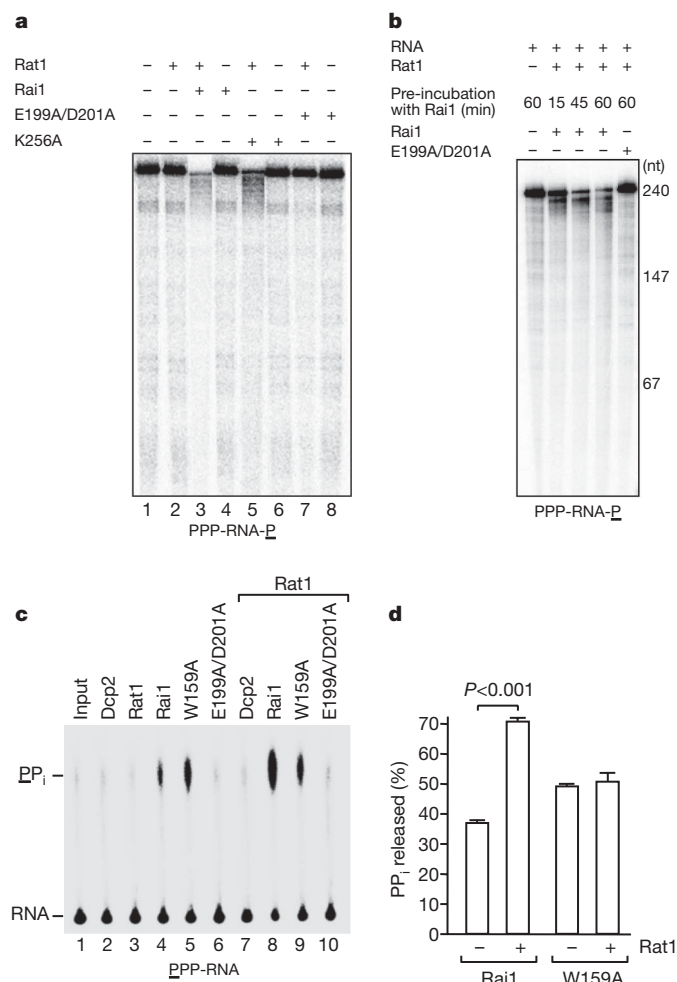


Figure 4 | Biochemical evidence for pyrophosphohydrolase activity of Rai1. **a**, Cleavage of 5'-triphosphorylated, 3'-labelled RNA substrate by Rat1 and the Rai1–Rai1 complex. Rat1 does not show ribonuclease activity towards this RNA in the absence of Rai1. The E199A/D201A mutant does not enable this ribonuclease activity. **b**, Pre-incubation of 5'-triphosphorylated RNA with wild-type Rai1, but not E199A/D201A mutant, allows Rat1 to degrade the substrate. **c**, Rai1 can release pyrophosphate (PP_i) from RNA with 5' triphosphate. The assays were carried out in the absence (lanes 1–6) or presence (lanes 7–10) of Rat1. Human Dcp2 decapping protein was used as a negative control. The pyrophosphate marker is indicated on the left and was generated by RNA polymerase during *in vitro* transcription, and could be clearly distinguished from free phosphate. **d**, Quantification of the percentage of pyrophosphate generated by Rai1 from four independent experiments. The error bars represent standard error of the mean.

with wild-type Rai1 or the E199A/D201A double mutant (50 nM) and then re-purified the RNA. Subsequent exoribonuclease assays with Rat1 demonstrated that the RNA pre-incubated with wild-type Rai1 was efficiently degraded, whereas the RNA pre-incubated with the mutant was not (Fig. 4b). Longer pre-incubation with Rai1 resulted in more of the RNA substrate being degraded by Rat1 (Fig. 4b), also consistent with Rai1 having a catalytic activity on its own.

To obtain direct evidence for the release of pyrophosphate from 5' triphosphorylated RNA, we used a substrate carrying a ³²P label at the γ position (at 50 nM concentration). Strikingly, both the wild-type Rai1 and the W159A mutant (50 nM) were able to hydrolyse the triphosphate linkage and release pyrophosphate (Fig. 4c, lanes 4 and 5). In contrast, the E199A/D201A double mutant at the same concentration lacked detectable activity (Fig. 4c, lane 6) as did Rat1 (lane 3) and the Dcp2 decapping enzyme (lane 2), confirming that the pyrophosphohydrolase activity is due to Rai1. Notably, Rat1 (50 nM) displayed a stimulatory effect on Rai1-mediated pyrophosphohydrolase activity, and this stimulation was not observed with

the W159A mutant (Fig. 4c lanes 8 and 9, and 4d). Pre-incubation experiments confirmed that this stimulation was not due to simple stabilization of Rai1 by Rat1 (data not shown). Instead, the stimulatory effect of Rat1 could be due to its RNA binding property, bringing the substrate near the active site of Rai1. These data confirm that Rai1 possesses an intrinsic RNA 5' pyrophosphohydrolase activity. In comparison, Rai1 displayed no pyrophosphohydrolase activity towards GTP (Supplementary Fig. 11), suggesting that this activity is limited to RNA substrates (Fig. 3b).

To define the substrate binding mode in the active site of Rai1 or Dom3Z, we soaked their crystals with various nucleotides and observed the binding of GDP in the active site of DOM3Z (Supplementary Fig. 12). Only the diphosphate group of GDP has strong electron density. The α phosphate is situated near the N terminus of helix α B, having favourable interactions with the dipole of this helix (Fig. 3d). It also interacts with the side chain of conserved Arg 132 (Arg 94 in *S. pombe* Rai1, Supplementary Fig. 7). The β phosphate interacts with Arg 132 and the conserved Gln 280 in helix α F (Gln 263 in Rai1). In comparison, although the ribose has van der Waals interactions with the conserved Trp 131 (Trp 93 in Rai1, Fig. 3e), its hydroxyls as well as the guanine base are not recognized by conserved residues. The conserved Glu 234 residue (Glu 199 in Rai1) is located near the phosphates of GDP and could serve a catalytic role in the pyrophosphohydrolase reaction.

Our structural and biochemical studies have shown that Rai1 possesses catalytic activity, acting as a pyrophosphohydrolase on RNA substrates with a 5' triphosphate. Although an RNA 5' pyrophosphohydrolase activity is important for mRNA degradation in bacteria²¹, ours is the first demonstration of such an activity in eukaryotes. Rai1 shares neither sequence nor structural homology with the bacterial 5' pyrophosphohydrolase RppH. Rai1 and Dom3Z homologues therefore have two distinct functions: (1) stimulation of Rat1 exoribonuclease activity, by a mechanism independent of Rai1 catalytic activity; and (2) a pyrophosphohydrolase activity towards selected RNA substrates. The former is involved in Pol II termination and RNA metabolism, and seems to be restricted to the fungal Rai1 homologues. The latter probably applies to both the fungal Rai1 and the animal Dom3Z homologues, and this activity seems to be unrelated to Pol II termination. Our studies have identified a novel eukaryotic enzyme that is likely to have important catalytic functions in RNA metabolism. For example, Rai1/Dom3Z may be part of an RNA quality control system in the nucleus, promoting the degradation of 5' triphosphorylated (that is, uncapped) RNA.

METHODS SUMMARY

Crystallography. *S. pombe* Rat1 and Rai1 were overexpressed separately in *Escherichia coli*. The bacterial cells were mixed together and lysed, and the Rai1–Rat1 complex was purified. Crystals were obtained by the sitting-drop vapour diffusion method, and the structures were determined by the selenomethionyl single-wavelength anomalous diffraction method.

Rat1 exoribonuclease assays. RNA substrates were produced by *in vitro* transcription, purified and labelled at the 5' or 3' end. Exoribonuclease assays were performed at 37 °C for 15 min. The RNA products were isolated and fractionated by 6% PAGE in 7 M urea. The assays were repeated several times to ensure reproducibility.

Pyrophosphohydrolase assays. An RNA substrate with 5' triphosphate labelled at the γ position was produced by *in vitro* transcription in the presence of [γ -³²P]GTP. The products from the pyrophosphohydrolase reaction were resolved by polyethyleneimine-cellulose thin layer chromatography plates developed in 1.5 M KH₂PO₄ (pH 7.5).

Full Methods and any associated references are available in the online version of the paper at www.nature.com/nature.

Received 4 October; accepted 18 December 2008.

Published online 4 February 2009.

1. Parker, R. & Song, H. The enzymes and control of eukaryotic mRNA turnover. *Nature Struct. Mol. Biol.* 11, 121–127 (2004).

2. Newbury, S. F. Control of mRNA stability in eukaryotes. *Biochem. Soc. Trans.* **34**, 30–34 (2006).
3. Bousquet-Antonelli, C., Presutti, C. & Tollervey, D. Identification of a regulated pathway for nuclear pre-mRNA turnover. *Cell* **102**, 765–775 (2000).
4. Gatfield, D. & Izaurralde, E. Nonsense-mediated messenger RNA decay is initiated by endonucleolytic cleavage in *Drosophila*. *Nature* **429**, 575–578 (2004).
5. Gazzani, S., Lawrenson, T., Woodward, C., Headon, D. & Sablowski, R. A link between mRNA turnover and RNA interference in *Arabidopsis*. *Science* **306**, 1046–1048 (2004).
6. Amberg, D. C., Goldstein, A. L. & Cole, C. N. Isolation and characterization of *RAT1*: an essential gene of *Saccharomyces cerevisiae* required for the efficient nucleocytoplasmic trafficking of mRNA. *Genes Dev.* **6**, 1173–1189 (1992).
7. Kim, M. *et al.* The yeast Rat1 exonuclease promotes transcription termination by RNA polymerase II. *Nature* **432**, 517–522 (2004).
8. West, S., Gromak, N. & Proudfoot, N. J. Human 5'→3' exonuclease Xrn2 promotes transcription termination at co-transcriptional cleavage sites. *Nature* **432**, 522–525 (2004).
9. Connelly, S. & Manley, J. L. A functional mRNA polyadenylation signal is required for transcription termination by RNA polymerase II. *Genes Dev.* **2**, 440–452 (1988).
10. Luo, W. & Bentley, D. A ribonucleolytic Rat torpedoed RNA polymerase II. *Cell* **119**, 911–914 (2004).
11. Buratowski, S. Connections between mRNA 3' end processing and transcription termination. *Curr. Opin. Cell Biol.* **17**, 257–261 (2005).
12. Luo, W., Johnson, A. W. & Bentley, D. L. The role of Rat1 in coupling mRNA 3'-end processing to transcription termination: implications for a unified allosteric-torpedo model. *Genes Dev.* **20**, 954–965 (2006).
13. Kaneko, S., Rozenblatt-Rosen, O., Meyerson, M. & Manley, J. L. The multifunctional protein p54nrb/PSF recruits the exonuclease XRN2 to facilitate pre-mRNA 3' processing and transcription termination. *Genes Dev.* **21**, 1779–1789 (2007).
14. West, S. & Proudfoot, N. J. Human Pcf11 enhances degradation of RNA polymerase II-associated nascent RNA and transcriptional termination. *Nucleic Acids Res.* **36**, 905–914 (2008).
15. Stevens, A. & Poole, T. L. 5'-exonuclease-2 of *Saccharomyces cerevisiae*. Purification and features of ribonuclease activity with comparison to 5'-exonuclease-1. *J. Biol. Chem.* **270**, 16063–16069 (1995).
16. Xue, Y. *et al.* *Saccharomyces cerevisiae* RAI1 (YGL246c) is homologous to human DOM3Z and encodes a protein that binds the nuclear exonuclease Rat1p. *Mol. Cell. Biol.* **20**, 4006–4015 (2000).
17. Mueser, T. C., Nossal, N. G. & Hyde, C. C. Structure of bacteriophage T4 RNase H, a 5' to 3' RNA-DNA and DNA-DNA exonuclease with sequence similarity to the RAD2 family of eukaryotic proteins. *Cell* **85**, 1101–1112 (1996).
18. Devos, J. M., Tomanicek, S. J., Jones, C. E., Nossal, N. G. & Mueser, T. C. Crystal structure of bacteriophage T4 5' nuclease in complex with a branched DNA reveals how Flap endonuclease-1 family nucleases bind their substrates. *J. Biol. Chem.* **282**, 31713–31724 (2007).
19. Glavan, F., Behm-Ansmant, I., Izaurralde, E. & Conti, E. Structures of the PIN domains of SMG6 and SMG5 reveal a nuclease within the mRNA surveillance complex. *EMBO J.* **25**, 5117–5125 (2006).
20. Clissold, P. M. & Ponting, C. P. PIN domains in nonsense-mediated mRNA decay and RNAi. *Curr. Biol.* **10**, R888–R890 (2000).
21. Deana, A., Celesnik, H. & Belasco, J. G. The bacterial enzyme RppH triggers messenger RNA degradation by 5' pyrophosphate removal. *Nature* **451**, 355–358 (2008).
22. Shobuike, T., Tatebayashi, K., Tani, T., Sugano, S. & Ikeda, H. The *dhp1⁺* gene, encoding a putative nuclear 5'→3' exonuclease, is required for proper chromosome segregation in fission yeast. *Nucleic Acids Res.* **29**, 1326–1333 (2001).
23. Kenna, M., Stevens, A., McCammon, M. & Douglas, M. G. An essential yeast gene with homology to the exonuclease-encoding *XRN1/KEM1* gene also encodes a protein with exonuclease activity. *Mol. Cell. Biol.* **13**, 341–350 (1993).
24. Page, A. M., Davis, K., Molineux, C., Kolodner, R. D. & Johnson, A. W. Mutational analysis of exonuclease I from *Saccharomyces cerevisiae*. *Nucleic Acids Res.* **26**, 3707–3716 (1998).
25. Solinger, J. A., Pascolini, D. & Heyer, W.-D. Active-site mutations in the Xrn1p exonuclease of *Saccharomyces cerevisiae* reveal a specific role in meiosis. *Mol. Cell. Biol.* **19**, 5930–5942 (1999).
26. Yang, W., Lee, J. Y. & Nowotny, M. Making and breaking nucleic acids: Two-Mg²⁺-ion catalysis and substrate specificity. *Mol. Cell* **22**, 5–13 (2006).
27. Lawrence, M. C. & Colman, P. M. Shape complementarity at protein/protein interfaces. *J. Mol. Biol.* **234**, 946–950 (1993).
28. Poole, T. L. & Stevens, A. Structural modifications of RNA influence the 5' exonucleolytic hydrolysis by XRN1 and HKE1 of *Saccharomyces cerevisiae*. *Biochem. Biophys. Res. Commun.* **235**, 799–805 (1997).
29. DeLano, W. L. *PyMOL Users Manual* (DeLano Scientific, 2002).
30. Nicholls, A., Sharp, K. A. & Honig, B. Protein folding and association: insights from the interfacial and thermodynamic properties of hydrocarbons. *Proteins* **11**, 281–296 (1991).

Supplementary Information is linked to the online version of the paper at www.nature.com/nature.

Acknowledgements We thank R. Abramowitz and J. Schwanof for setting up the X4A and X4C beamlines and H. Robinson for setting up the X29A beamline at the NSLS, and S. Jia for providing the *S. pombe* genome. This research is supported in part by grants from the NIH to L.T. (GM077175), J.L.M. (GM28983) and M.K. (GM67005).

Author Information The atomic coordinates have been deposited at the Protein Data Bank with accession numbers 3FQD, 3FQG, 3FQI and 3FQJ. Reprints and permissions information is available at www.nature.com/reprints. Correspondence and requests for materials should be addressed to L.T. (ltong@columbia.edu).

METHODS

Protein expression and purification. DNA fragment corresponding to residues 1–885 of *S. pombe* Rat1 was amplified from the genome and inserted into the pET24d vector (Novagen). The recombinant Rat1 protein carries a hexa-histidine tag at the C terminus. Full-length *S. pombe* Rai1 was cloned into the pET26b vector, and the recombinant protein does not carry any affinity tag. The plasmids were transformed separately into *E. coli* BL21 (DE3) Rosetta cells. After induction with 0.3 mM IPTG, the cells were allowed to grow at 20 °C for 14–16 h. Cells expressing Rat1 and Rai1 were mixed and lysed by sonication, and the Rat1–Rai1 complex was purified by Ni-NTA (Qiagen) and gel filtration (Sephacryl S-300, GE Healthcare) chromatography. Purified protein was concentrated to 10 mg ml⁻¹ in a buffer containing 20 mM Tris (pH 7.5), 200 mM NaCl, 2 mM dithiothreitol (DTT) and 5% (v/v) glycerol, flash frozen in liquid nitrogen and stored at -80 °C. The C-terminal His tag on Rat1 was not removed for crystallization.

The selenomethionyl protein sample was produced in minimal media supplemented with specific amino acids to inhibit endogenous methionine biosynthesis, and the bacteria were grown in the presence of selenomethionine³¹. The purification procedure is the same as for the native protein except that the DTT concentration in the storage buffer was increased to 10 mM.

To study Rai1 alone, *S. pombe* Rai1 was cloned into the pET26b vector and overexpressed in *E. coli*. The recombinant protein, with a C-terminal His tag, was purified following the same protocol as that for the Rat1–Rai1 complex.

Mouse DOM3Z was cloned into vector pET28a. The recombinant protein contains an N-terminal His tag. Native and selenomethionine proteins were expressed and purified following the same protocol as for the Rat1–Rai1 complex.

Protein crystallization. Plate-like crystals of the Rat1–Rai1 complex were obtained with the sitting-drop vapour diffusion method at 23 °C. The reservoir solution contained 0.3 M sodium malonate (pH 5.0), 10 mM DTT and 14% (w/v) PEG 3350. Before crystallization setup the protein was supplemented with 60 mM of Gly-Gly-Gly (Hampton Research). The quality of the crystals was improved by micro seeding. The crystals belong to space group *P*₂₁₂₁, and there is one Rat1–Rai1 heterodimer in the asymmetric unit.

Crystals of Rai1 alone were obtained with the sitting-drop vapour diffusion method at 23 °C. The reservoir solution contained 0.2 M sodium citrate tribasic (pH 5.0) and 20% (w/v) PEG 3350. The crystals belong to space group *C*₂, and there is one Rai1 molecule in the asymmetric unit.

Crystals of DOM3Z were obtained with the sitting-drop vapour diffusion method at 23 °C. Two different crystal forms were characterized. Rod-like crystal form 1 was obtained with a reservoir buffer containing 0.1 M HEPES (pH 7.5) and 20% (w/v) PEG8000. The crystals belong to space group *P*₂₁, and there is one DOM3Z molecule in the asymmetric unit. Rod-like crystal form 2 was obtained with a reservoir buffer containing 25% (w/v) PEG3350 and 0.2 M KH₂PO₄. 10 mM DTT was added to the reservoir for the selenomethionine protein. The crystals belong to space group *P*₂₁₂₁, and there is one molecule in the asymmetric unit.

The crystals were cryo-protected by the reservoir solution supplemented with 25% (v/v) glycerol and flash-frozen in liquid nitrogen for data collection.

To obtain the GDP complex of DOM3Z, the crystals (in form 2) were soaked with reservoir buffer supplemented with 25 mM GDP and 10 mM MgCl₂ overnight.

Data collection and structure determination. The structures of the Rat1–Rai1 complex and DOM3Z were determined by the selenomethionyl anomalous diffraction method³². For the Rat1–Rai1 complex, a single-wavelength anomalous diffraction (SAD) data set to 2.5 Å resolution was collected on a selenomethionyl-substituted crystal at the NSLS beamline X4A. A native reflection data set to 2.2 Å resolution was collected at the X4C beamline. The diffraction data were processed and scaled with the HKL package³³. The data processing statistics are summarized in Supplementary Table 1. The diffraction pattern of this crystal is anisotropic beyond 2.5 Å resolution, contributing to the relatively lower completeness of the data at the high resolution shell.

The Se atoms were located with the program BnP³⁴, and the reflections were phased with the program Solve³⁵. Most of the residues in the complex were built automatically by the program Resolve, and the model was completed by manual building with the program O³⁶. The structure refinement was carried out with the programs CNS³⁷ and Refmac³⁸, and water molecules were added with the program ARP³⁹.

Free-enzyme crystals of the Rat1–Rai1 complex were soaked overnight in a solution containing 50 mM MnCl₂, and a diffraction data set to 2.5 Å resolution was collected at the X4C beamline. After structure refinement with the protein atoms only, a strong peak (12σ in the difference electron density map) was observed at the divalent cation position in the putative active site of Rai1, which was modelled as a Mn²⁺ ion.

A native diffraction data set to 2.0 Å resolution for Rai1 alone was collected at the X4C beamline. The structure was solved by the molecular replacement method with the program Molrep⁴⁰, and the structure refinement was carried out with Refmac³⁸.

For DOM3Z, a SAD data set to 2.6 Å resolution was collected on a selenomethionyl crystal in crystal form 2 on NSLS beamline X29A. Native data sets for the free enzyme in crystal form 1 to 2.0 Å resolution and the GDP complex (in crystal form 2) to 2.6 Å resolution were collected at NSLS beamlines X4A and X4C, respectively. The diffraction data were processed by the HKL package (Supplementary Table 1)³³. The Se atoms were located by BnP³⁴, and the reflections were phased with the program Solve³⁵. The atomic model was completed with the program O³⁶. The structure of crystal form 1 was solved by the molecular replacement method with the program Molrep⁴⁰. The structure refinement was carried out with the programs CNS³⁷ and Refmac³⁸, and water molecules were added with the program ARP³⁹.

All diffraction data were collected near the Se edge, with X-ray wavelength of 0.98 Å.

Rat1–Rai1 interactions. Rat1 and Rai1 mutants were made with the QuikChange kit (Stratagene) and verified by sequencing. The mutant proteins were expressed and purified following the same protocol as that for the wild-type protein. All the proteins carry a hexa-histidine tag at the N terminus.

Analytical gel filtration experiments were carried out on a Superose-12 10/30 column (GE Healthcare), with a buffer containing 20 mM Tris (pH 7.5) and 200 mM NaCl. 400 μg of Rat1 and Rai1 were mixed and diluted to a final volume of 120 μl with the gel filtration buffer. The mixture was incubated on ice for 30 min before being loaded onto the column. The proteins were also run separately on the column to determine their migration behaviour alone.

Rat1 exoribonuclease assays. pGEM SVL was linearized with DraI and transcribed with Sp6 RNA polymerase (Promega) for 2 h at 37 °C. The RNA transcripts were gel purified using standard procedures. The 5' termini of unlabelled SVL pre-mRNA were dephosphorylated by calf intestinal phosphatase (New England Biolabs) for 1 h at 37 °C. SVL pre-mRNAs were subsequently labelled at their 5' ends with T4 polynucleotide kinase (NEB) and [γ-³²P]ATP at 37 °C for 1 h, or at their 3' ends with ³²P Cp and T4 RNA ligase (Promega) for 1 h at 37 °C. Exoribonuclease assays were performed at 37 °C for 15 min. The reaction mixtures contained ~1 ng labelled pre-mRNA, 50 mM NaCl, 5 mM MgCl₂, 20 mM Tris (pH 8.0), 0.5 mM DTT, 500 ng BSA and the indicated amounts of recombinant Rat1 and Rai1. The RNA products were isolated and fractionated by 6% PAGE in 7 M urea. The data were analysed by Phosphor Imager. The assays were repeated several times to ensure reproducibility.

pGEM APOC1 was cut with PstI and *in vitro* transcribed by T7 RNA polymerase (Promega). pcDNA3 was cut with NdeI and *in vitro* transcribed by Sp6 RNA polymerase (Promega).

Rai1 pre-incubation experiments. SVL pre-mRNA carrying 5' triphosphate and 3' ³²P phosphate was incubated for 15, 45 and 60 min at 30 °C with wild-type Rai1 or the E199A/D201A double mutant. The treated RNA was purified by phenol/chloroform extraction and ethanol precipitation, and used in exoribonuclease assays with Rat1.

Pyrophosphohydrolase assays. The pcDNA3 polylinker (pcP) was amplified by PCR with a forward primer corresponding to the SP6 promoter primer and a 3' primer consisting of the T7 promoter sequences containing 16 cytosines at the 5' end. The PCR product was used as template to transcribe RNA with SP6 RNA polymerase in the presence of [γ-³²P]GTP as described⁴¹. The resulting RNA is exclusively labelled at the 5' end at the first phosphate within the 5' triphosphate and contains a 3' terminal 16 guanoses to stabilize the 3' end. The indicated recombinant proteins were incubated with ³²P 5'-end-labelled RNA in RNA decapping buffer (10 mM Tris-HCl (pH 7.5), 100 mM KOAc, 2 mM MgOAc, 0.5 mM MnCl₂ and 2 mM DTT) at 37 °C for 30 min as previously described⁴². The reaction products were resolved by polyethyleneimine-cellulose thin layer chromatography plates developed in 1.5 M KH₂PO₄ (pH 7.5) and exposed to a PhosphorImager. Molecular Dynamics PhosphorImager (Storm860) and ImageQuant-5 software were used for product quantifications. The data were analysed with GraphPad Instat software.

31. Double, S. *et al.* Crystallization and preliminary X-ray analysis of the 9 kDa protein of the mouse signal recognition particle and the selenomethionyl-SRP9. *FEBS Lett.* **384**, 219–221 (1996).
32. Hendrickson, W. A. Determination of macromolecular structures from anomalous diffraction of synchrotron radiation. *Science* **254**, 51–58 (1991).
33. Otwinowski, Z. & Minor, W. Processing of X-ray diffraction data collected in oscillation mode. *Methods Enzymol.* **276**, 307–326 (1997).
34. Weeks, C. M. & Miller, R. The design and implementation of SnB v2.0. *J. Appl. Crystallogr.* **32**, 120–124 (1999).
35. Terwilliger, T. C. SOLVE and RESOLVE: Automated structure solution and density modification. *Methods Enzymol.* **374**, 22–37 (2003).

36. Jones, T. A., Zou, J. Y., Cowan, S. W. & Kjeldgaard, M. Improved methods for building protein models in electron density maps and the location of errors in these models. *Acta Crystallogr. A* **47**, 110–119 (1991).
37. Brunger, A. T. *et al.* Crystallography & NMR System: A new software suite for macromolecular structure determination. *Acta Crystallogr. D* **54**, 905–921 (1998).
38. Murshudov, G. N., Vagin, A. A. & Dodson, E. J. Refinement of macromolecular structures by the maximum-likelihood method. *Acta Crystallogr. D* **53**, 240–255 (1997).
39. Lamzin, V. S., Perrakis, A. & Wilson, K. S. in *Crystallography of Biological Macromolecules. International Tables for Crystallography Vol. F* (eds Rossmann, M. G. & Arnold, E.) 720–721 (Kluwer, 2001).
40. Vagin, A. A. & Teplyakov, A. An approach to multi-copy search in molecular replacement. *Acta Crystallogr. D* **56**, 1622–1624 (2000).
41. Jiao, X., Wang, Z. & Kiledjian, M. Identification of an mRNA-decapping regulator implicated in X-linked mental retardation. *Mol. Cell* **24**, 713–722 (2006).
42. Piccirillo, C., Khanna, R. & Kiledjian, M. Functional characterization of the mammalian mRNA decapping enzyme hDcp2. *RNA* **9**, 1138–1147 (2003).

NEWS

Early intervention

Fifty of the United States' most promising early-career biomedical scientists now have the chance to pursue their research dreams without the corresponding nightmare of trying to find funding.

Under the new Early Career Scientist initiative at the Howard Hughes Medical Institute (HHMI) in Chevy Chase, Maryland, the 50 — 9 women and 41 men from 33

institutes — will receive a full salary and benefits along with \$1.5 million each in research funds over the course of their six-year appointment.

"This is a time when money is tight for everyone, and I'm extremely lucky to have this measure of financial security for my lab for the next few years," says appointee Rachel Wilson, a neurobiologist at Harvard Medical School in Boston, Massachusetts. "This kind of grant allows us to do research that's more adventurous and risky."

More than 2,000 scientists flooded the HHMI's offices with applications when the institute announced the programme in March 2008. Applicants had to be 2–6 years into their first independent position and could not hold more than one early-career award from anywhere else.

Wilson, who is studying how fruitfly brains process information about odours, will now extend her work to investigate how the brains deal with other sensory stimuli. Ultimately she hopes to uncover fundamental information about the human brain. "I don't claim that what I do in my lab today is going to cure human brain disease tomorrow, but this work will shed



Rachel Wilson.

light on fundamental questions about how the human brain works," says Wilson. "It's a shameful truth that we, as a field of neuroscience, don't understand how patterns of electricity in the human brain affect perception, thoughts and actions."

Appointee Joe Thornton, a molecular evolutionary biologist at the University of Oregon in Eugene, identifies the genetic mutations by

which ancient hormone receptor proteins took on modern-day functions. He is excited about the chance to research more thoroughly.

"We've resurrected ancient proteins to understand how they've evolved new functions," he says. "But I want to know if what we've observed is of general importance or if there are different rules for different gene families to evolve. Now we can develop new models."

Tom Cech, who was president of the HHMI when the scheme launched, says that on a fact-finding mission last year, he and other HHMI officials found the greatest need for funding support was among those at the early stage of their careers.

Funding difficulties for early-career scientists include short-term grants that aren't renewable, which can be compounded by a drop in success rates. "When a researcher has their lab up and running and has great ideas and lots of energy, instead of being in the lab working, they're writing grant application after grant application trying to get continuous funding," Cech says. "We decided this was an area of opportunity and we should invest in this particular stage." ■

Karen Kaplan

POSTDOC JOURNAL

Kidding around

Shortly after getting married in 2000, my wife and I decided to have three kids. It seemed like the perfect-size family for us — not too big, not too small. We figured three would still allow us to give each plenty of attention. Recently, we discussed the prospect of having our third. However, our hands are already full with a bright-eyed three-year-old daughter and an inquisitive one-year-old son. We are beginning to reconsider the notion of having that sought-after trio.

This is perhaps the most difficult of the important

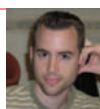
personal and professional decisions looming before me, as graduate school fades away behind me and my career stands facing me. The decision to have a third child falls during this transitory period of my life as a postdoc.

Job changes can occur quickly, and moving to another city with an infant is not ideal. So what is the solution? Procrastinate. We can afford to wait to have another child because my wife and I are still relatively young, although I think the longer we wait, the less likely we are to have another child.

We would both love to have a third child eventually, but at the moment we must make the tough decision to put family growth on hold. Right now I need to focus on my career: on publishing, publishing, publishing and then looking for a job.

For the time being this is my next priority — raise a paper and nurture a career. Then think about raising another little one. ■

Bryan Venters is a postdoctoral fellow at the Center for Eukaryotic Gene Regulation at Pennsylvania State University, University Park.



IN BRIEF

Vietnam pay complaints

The most significant impediments to science in Vietnam are low pay and a paucity of research funding, according to a report by the International Foundation for Science, a research council in Sweden that supports scientists in developing nations. Sixty per cent of respondents in a poll published in the document said that salary was a "serious" or "obstructive" problem. "Vietnamese scientists' salaries are very low and [they] find it difficult to live on their government salaries alone," the report says, adding that 83% of all scientists consider their salary to be inadequate to support a family. For female scientists, it's 89%. The report also cited a lack of funding for research equipment and fieldwork as a significant obstacle to doing good science.

Bioscience park launched

Plans for a biosciences park in Minnesota are under way along with the creation of a venture-capital fund worth up to US\$1 billion to support the state's biotech sector. The 940-hectare Elk Run site in Pine Island includes the BioBusiness Park that aims to create and attract bioscience and biomedical firms to this south-eastern part of the state. It is supported by property developer Tower Investments, based in Woodland, California, and venture capitalist Steven Burrill. Tower and Burrill are also creating the fund to support development of new technologies created by the University of Minnesota, the Mayo Clinic, a medical research institute in nearby Rochester, and private research organizations.

BP Solar cuts 620 jobs

Solar technology firm BP Solar said this week that it will cut about 140 jobs at an assembly plant in Frederick, Maryland, and another 480 at manufacturing and assembly plants in Madrid. The cuts are part of an effort to reduce costs and refocus its global manufacturing operations. The company is phasing out its photovoltaic module assembly in Maryland and closing its photovoltaic-cell manufacturing and module assembly operations in Spain. Chief executive Reyad Fezzani says solar markets have been hit hard by three major interrelated factors: the economic downturn, oversupply and increased competition. BP Solar is a subsidiary of UK-based global energy company BP.

PREVENTION BY NUMBERS

Researchers who study environmental influences on cancer tend to receive a fraction of the funds available to those researching cancer cures. But career opportunities exist — and may even be expanding. **Heidi Ledford** reports.

The locals call it ‘Cancer Alley’ — a sweltering stretch of the Mississippi River from Baton Rouge, Louisiana, to New Orleans, where more than a hundred chemical plants and oil refineries share a home with some of poorest people in the United States. In truth, no one has proved a link between the local industry and the few, sporadic reports of rare-cancer clusters along Cancer Alley. But the region’s bad reputation is well deserved: the state of Louisiana has a major cancer problem. In 2005, the state had 214.9 cancer deaths for every 100,000 people, second only to Kentucky in the United States; the national average is 184.1.

It was against this backdrop that Maureen Lichtveld, head of Tulane University’s department of environmental health sciences in New Orleans, and her colleagues decided it was time to create an environmental-oncology programme. It draws on the resources and faculty members at Tulane’s expanding cancer centre, and at nearby Louisiana State University in Baton Rouge and Xavier University of Louisiana in New Orleans (see ‘Epidemiologists in demand’). Funding provided by Tulane University and the Louisiana Cancer Research Consortium allowed Lichtveld to hire five new faculty members, two of whom have not yet been recruited.

Forming the programme was a practical decision, Lichtveld says. “I saw a real opportunity in terms of where the research is going,” she says. “We’re seeing a new emphasis on health disparities across the board.”

According to the US National Institutes of Health (NIH), environmental factors such as pollution, cigarette smoke and diet contribute to 80–90% of all cancers. Despite these numbers, research in environmental oncology — which aims to track down environmental contributions to cancer — receives only a fraction of the amount spent on the hunt for cures. “We would get more bang for our buck, although the outcome is not immediate and not as sexy, if we invest in early detection and screening,” says Lichtveld.

This attitude may be changing with the

recent emphasis on early disease diagnosis and personalized health care. “It is now being realized that an exclusive focus on genetic aspects of cancer is not providing solutions,” says Soterios Kyrtopoulos, director of the chemical carcinogenesis and genetic toxicology programme at the National Hellenic Research Foundation in Athens, Greece. “So the pendulum is swinging back again to studying the environment.”

Patchwork of grants

Funding for environmental cancer research in the United States is available as a patchwork of governmental and private foundation programmes. The NIH spent US\$171 million on environmental cancer research in fiscal year 2008, and as of February, the American Cancer Society, based in Atlanta, Georgia, had eight grants totalling \$5 million for environmental carcinogenesis research. Meanwhile, President Barack Obama has pledged to double the NIH budget for cancer research over the next five years.

“We anticipate significant increases in funding,” says Linda Birnbaum, director of the National Institute of Environmental Health Sciences (NIEHS), although she

says she can’t yet predict the likely number of grants. Environmental oncologists are scrambling to assemble applications for the dozens of relevant ‘challenge grants’ made available under the recent US economic stimulus package. These grants of up to \$1 million, including salaries for students and postdocs, are intended as jump-start funds and will last for only two years.

Large studies increasingly present opportunities for qualified researchers in environmental oncology. In 2003, the NIEHS and the National Cancer Institute jointly created a network of four centres to investigate the relationship between breast cancer and early-life environmental exposures. The NIEHS is also enrolling 50,000 sisters of breast-cancer sufferers in a decade-long prospective study looking at the possible risk effects of factors such as genetics and diet.

Investigating both genes and the



R. LLEWELLYN/CORBIS



M. BOTSIVALI

Soterios Kyrtopoulos (front row, third from right) was part of the mid-March inaugural meeting of an ‘Envirogenomarkers’ project at the National Hellenic Research Foundation in Athens, Greece.

EPIDEMIOLOGISTS IN DEMAND

In compiling the special mix of skills inherent to the environmental oncologist, epidemiology is an often over-looked component. Indeed, the researchers behind the newly founded environmental oncology programme at Tulane University in New Orleans, Louisiana, made sure to house their degree in the university's School of Public Health and Tropical Medicine for that very reason. There, environmental oncology graduate students are required to

study epidemiology.

"We were pretty adamant that we wanted a population studies component in there," says Charles Miller, who studies carcinogenesis and DNA damage at Tulane University. "Ultimately, you have to know what to do with the data."

And yet the number of cancer researchers with epidemiology training often fails to meet the demand. They are in short supply in Europe, says Richard Sullivan, a cancer researcher at King's

College London and chairman of the European Cancer Research Manager forum.

Data compiled by the foundation suggest that most epidemiologists in cancer prevention are in the later stages of their careers, and the pipeline of young epidemiologists has dwindled. "Where are the next team leaders and mentors?" says Sullivan. "Where are they going to come from?"

The problem, he says, is often the length of epidemiological

studies, which can take decades to complete and publish. That timescale does not mesh well with how researchers are judged in the short term by the academy. Nevertheless, he says, fellowships are available to those with training in epidemiology and an interest in environmental oncology, and often have only a small pool of applicants.

"In the United Kingdom, these positions are underfilled," says Sullivan. "We never get enough good people applying."

H.L.

environment has piqued the interest of many: in 2006, the NIH created the Genes, Environment and Health Initiative, which receives \$40 million a year and will continue until 2010. One component of the initiative is to develop technology to monitor environmental exposures that could contribute to disease. It receives \$19.5 million each year, and has funded 32 investigators, including some in a project that aims to find biomarkers of exposure to environmental carcinogens. Continuation of these programmes beyond 2010 is under review.

European interest

Environmental oncology is thriving in Europe as well. In 2005, the European Union launched the Environmental Cancer Risk, Nutrition, and Individual Susceptibility (ECNIS) network of excellence under its Sixth Framework Programme for research. This programme, intended to unite European researchers in the field of environmental oncology, has received €11 million (US\$14.7 million) over five years.

The Seventh Framework Programme also provides for a number of environmental oncology projects, says Kyrtopoulos. For example, it has awarded €3.5 million of the €4.7 million needed for his collaboration with ten other research groups in Europe to find biomarkers linking environmental exposures and disease, including some cancers. The project will create positions for about ten students and five postdocs, says Kyrtopoulos.

Biomarker discovery remains both a focus and a source of frustration. Finding robust clinical biomarkers can enable early detection of disease — a goal both in academia and in the burgeoning diagnostics industry. But researchers have struggled with irreproducibility when they attempt

to use biomarkers discovered in small-scale experiments to larger, clinically relevant populations. This is especially a problem when high-throughput technologies such as proteomics or transcriptomics are used, says Kyrtopoulos. But the problem may be ironed out as researchers learn how to adapt the technology to the rigours of working with large, highly variable populations.

In some cases, the easiest route to funding may be to appeal to the environmental concerns that prevail in certain countries. Australia, for instance, is particularly well known for exploring the effects of ultraviolet light on skin cancer. In Norway, the past decade has seen an overall shift away from epidemiology and cancer prevention, but the government is devoting considerable funds towards monitoring the effects of pollution, in large part due to interests in the Arctic and the oil industry, says epidemiologist Eiliv Lund of the University of Tromsø, Norway. "As long as you work in pollution, it's still not so difficult to get funding."

In Japan, the exposures to target are asbestos, radiation and air pollution, says Tetsuo Noda, director of the Cancer Institute of the Japanese Foundation for Cancer Research in Tokyo. Still, environmental oncologists in Japan are struggling. The Japanese funding system, in which results that have a demonstrated societal benefit are presented to the funding agency every five years, does not mesh well with epidemiological studies, which tend to be long-term. "Because of that, we cannot get

enough money to make progress in environmental oncology," says Noda.

It's a worldwide problem, as students of cancer epidemiology often fail to appreciate the major funding and study-length demands of the field, notes Shine Chang, an associate professor of epidemiology and director of research training at the University of Texas M. D. Anderson Cancer Center in Houston.

But the interest is there, although

dedicated programmes such as Tulane's are rarities. Roger Giese, director of the Environmental Cancer Research Program at Northeastern University in Boston, Massachusetts, says that graduate students and postdocs come from a variety of scientific backgrounds; they go on to pursue careers in numerous fields, from regulatory agencies to industry to academia. Fellowships such as the ones at the American Cancer Society, help postdocs make the transition to their first faculty appointment. And the NIH offers an international fellowship programme for

cancer-prevention researchers.

"I'm very hopeful that cancer-prevention research continues to gain strength," says Bill Chambers, scientific programme director of the American Cancer Society. "Traditionally we've focused on curing the patient, but it is much more cost-effective and far better for our lifestyle to really robustly pursue prevention."

Heidi Ledford writes for Nature from Cambridge, Massachusetts.



"We anticipate significant increases in funding."

— Linda Birnbaum

Manifesto

The sin of self.

João Ramalho-Santos

We know who you are.
We know what you do.

In heated basements and garages where translucent tubes pump fluids and gases into converted aquaria. Media, flasks, enzymes, growth factors, hormones, antibiotics — you buy online, have them delivered, trade in makeshift markets. The equipment is discreetly cleaned out on Sundays, after waxing the car; the protocols you lazily download and follow like gospel until someone posts a better recipe. And, in the same dark corners where once homemade beer and short-wave radios were your grandest projects, clusters of cells fruitfully multiply under your proud gaze.

It started years ago, with Dolly the martyr sheep, another sacrificial lamb to human greed. Not bothering with particulars (do you ever?), you found the general principles seductive, bought the hype, began thinking about 'experiments'. Therapeutic cloning. Somatic-cell nuclear transfer. Pluripotency. The words rolled off your tongue like poems. Unfortunately, expensive equipment was needed, precise skills, an iron will. All the things you lack. Until the news came that someone had made it easy, incredibly easy.

Easy.

That was probably the only thing you understood. Induced pluripotency, stem cells grown out of modified adult tissue. Cells that could be propagated indefinitely, be made into any other cells. No need for embryos, oocytes or micromanipulation stations, just the forced expression of a few factors. Maybe you didn't fully grasp the science at first. (Who are you kidding? You still don't.) Vectors, transfection, transduction, transcription control, reprogramming. But, after the kits became available, anyone could use the technology. That's the true beauty of democracy in your eyes, isn't it? The ability to be as effortlessly smart as the smartest, while remaining utterly dumb.

So you tearfully sacrificed a piece of skin into a Petri dish, added in the factors with some culture media, made that fragment of you immortal. The modified cells grew, pluripotent and strong, and

you contemplated them as a deity gazing down on its ancient self. People with white lab coats and prophetic gazes had talked about all-encompassing cures, cell-based therapies, regenerative medicine. You can say that some such Grand Purpose was at the back of your mind. Perhaps distant relatives suffered from Parkinson's or diabetes or stroke, and you feared bad genes would fail you. But you lie. The fascination was the sin of self, the secrets of plasticity, the possibility of contemplating a miraculous endless rebirth, even if in a limited form. You differentiated your cells, not to cure, but to see if it could be done. And then you allowed your idle mind to set free its twisted imagination. Or, much more likely, you borrowed imagination from others, downloaded a few more protocols.

Easy.

In carefully controlled cultures you prime tiny haemangioblast islands (do you even know what haemangioblasts are?) until they bloom red into the culture. You brew litres of your own blood to share in rituals without metaphor or pain. "Drink, for this is my blood," you say in abandoned churches and vandalized cemeteries; failing to understand that comfortable literalism shatters any possible ancient meaning. You grow cardiomyocytes, wear them in medallions that synchronize their beat to iPods and Club

DJs. "Wear your heart on your sleeve," says the pirate online commercial, hinting that this is a just a wonderful new fad gadget, a novel pulsating plastic.

We know. We know more than you realize. Hushing in upscale restaurants, ordering off-off-menu with ever changing codes you pick up from message boards, snickering at the witty dish names, commenting that the differentiated muscle tissue marinated in lemongrass "tastes just like chicken", wondering "who it is" as you lay down platinum cards. Congratulations. You have found yet another way of selling yourselves.

"Know thy cell, know thyself," you hide beneath slick mottos. When neurons are differentiated from your own pluripotent stem cells you truly believe you will be able to see yourselves think, gazing into the dish in search of profound answers to all possible questions. As none are forthcoming you hurry your cultures to oracle interpreters that carefully fondle your artificially expatriated brain cells, measure current activities, calcium bursts, nitric oxide synthesis; use these cryptic signs to tell you what you crave to know. Anything at the service of your insecurities and platinum cards. At least electrophysiology PhDs have found

welcome new employment, patch-clamping confused aggregates of cells, cells trying desperately to create meaning from a context of your making, not their own.

You were always partial to slavery. First towards other human beings, then animals, now, fittingly, your own cells. You have shown no restraint, no shame. This is your last warning.

We know who you are.

We know what you do.

We will let others know. On your walls, in your blogs, in your favourite bars, in your congregations, in your children's schools. We will be as ruthless as you have been heartless.

We are coming. And we will not rest until all cells are set free.

People for the Ethical Treatment of All Life.

João Ramalho-Santos lives in Coimbra, Portugal. He often wonders why.



JACEY